Cape Peninsula
University of Technology

DESIGN, MODELLING AND SIMULATION OF A NOVEL MICRO-ELECTRO-MECHANICAL GYROSCOPE WITH OPTICAL READOUTS

by

Bo Zhang

Thesis submitted in fulfilment of the requirements for the degree

Doctor of Technology: Electrical Engineering

in the Faculty of Engineering

at the Cape Peninsula University of Technology

Supervisor: Prof. Dr. Bohua Sun
Co-supervisor: Prof. Dr. MTE Kahn

Bellville
October 2007

DECLARATION

I, Bo Zhang, declare that the contents of this thesis represent my own unaided work, and that the thesis has not previously been submitted for academic examination towards any qualification. Furthermore, it represents my own opinions and not necessarily those of the Cape Peninsula University of Technology.

张博

Signed

2008. 03. 26

Date

ABSTRACT

Micro Electro-Machnical Systems (MEMS) applications are fastest development technology present. MEMS processes leverage mainstream IC technologies to achieve on chip sensor interface and signal processing circuitry, multi-vendor accessibility, short design cycles, more on-chip functions and low cost. MEMS fabrications are based on thin-film surface microstructures, bulk micromaching, and LIGA processes. This thesis centered on developing optical micromaching inertial sensors based on MEMS fabrication technology which incorporates bulk *Si* into microstructures. Micromachined inertial sensors, consisting of the accelerometers and gyroscopes, are one of the most important types of silicon-based sensors. Microaccelerometers alone have the second largest sales volume after pressure sensors, and it is believed that gyroscopes will soon be mass produced at the similar volumes occupied by traditional gyroscopes.

A traditional gyroscope is a device for measuring or maintaining orientation, based on the principle of conservation of angular momentum. The essence of the gyroscope machine is a spinning wheel on an axle. The device, once spinning, tends to resist changes to its orientation due to the angular momentum of the wheel. In physics this phenomenon is also known as gyroscopic inertia or rigidity in space. The applications are limited by the huge volume.

MEMS Gyroscopes, which are using the MEMS fabrication technology to minimize the size of gyroscope systems, are of great importance in commercial, medical, automotive and military fields. They can be used in cars for ABS systems, for anti-roll devices and for navigation in tall buildings areas where the GPS system might fail. They can also be used for the navigation of robots in tunnels or pipings, for leading capsules containing medicines or diagnostic equipment in the human body, or as 3-D computer mice. The MEMS gyroscope chips are limited by high precision measurement because of the unprecision electrical readout system.

The market is in need for highly accurate, high-G-sustainable inertial measuring units (IMU's). The approach optical sensors have been around for a while now and because of the performance, the mall volume, the simplicity has been popular. However the production cost of optical applications is not satisfaction with consumer. Therefore, the MEMS fabrication technology makes the possibility for the low cost and micro optical devices like light sources, the waveguide, the high thin fiber optical, the micro photodetector, and vary demodulation measurement methods. Optic sensors may be defined as a means through which a measurand interacts with light guided in an optical fiber (an intrinsic sensor) or guided to (and

returned from) an interaction region (an extrinsic sensor) by an optical fiber to produce an optical signal related to the parameter of interest. During its over 30 years of history, fiber optic sensor technology has been successfully applied by laboratories and industries worldwide in the detection of a large number of mechanical, thermal, electromagnetic, radiation, chemical, motion, flow and turbulence of fluids, and biomedical parameters. The fiber optic sensors provided advantages over conventional electronic sensors, of survivability in harsh environments, immunity to Electro Magnetic Interference (EMI), light weight, small size, compatibility with optical fiber communication systems, high sensitivity for many measurands, and good potential of multiplexing. In general, the transducers used in these fiber optic sensor systems are either an intensity-modulator or a phase-modulator. The optical interferometers, such as Mach-Zehnder, Michelson, Sagnac and Fabry-Perot interferometers, have become widely accepted as a phase modulator in optical sensors for the ultimate sensitivity to a range of weak signals. According to the light source being used, the interferometric sensors can be simply classified as either a coherence interferometric sensor if a the interferometer is interrogated by a coherent light source, such as a laser or a monochromatic light, or a lowcoherence interferometric sensor when a broadband source a light emitting diode (LED) or a superluminescent diode (SLD), is used.

This thesis proposed a novel micro electro-mechanical gyroscope system with optical interferometer readout system and fabricated by MEMS technology, which is an original contribution in design and research on micro opto-electro-mechanical gyroscope systems (MOEMS) to provide the better performances than the current MEMS gyroscope. Fiber optical interferometric sensors have been proved more sensitive, precision than other electrical counterparts at the measurement micro distance. The MOMES gyroscope system design is based on the existing successful MEMS vibratory gyroscope and micro fiber optical interferometer distances sensor, which avoid large size, heavy weight and complex fabrication processes comparing with fiber optical gyroscope using Sagnac effect. The research starts from the fiber optical gyroscope based on Sagnac effect and existing MEMS gyroscopes, then moving to the novel design about MOEMS gyroscope system to discuss the operation principles and the structures.

In this thesis, the operation principles, mathematics models and performances simulation of the MOEMS gyroscope are introduced, and the suitable MEMS fabrication processes will be discussed and presented. The first prototype model will be sent and fabricated by the manufacture for the further real time performance testing.

There are a lot of inventions, further research and optimize around this novel MOEMS gyroscope chip. In future studying, the research will be putted on integration three axis

gyroscopes in one micro structure by optical sensor multiplexing principles, and the new optical devices like more powerful light source, photosensitive materials etc., and new demodulation processes, which can improve the performance and the interface to co-operate with other inertial sensors and navigation system.

ACKNOWLEDGEMENTS

TABLE OF CONTENTS

LIST OF FIGURES

LIST OF TABLE

GLOSSARY

Acronyms	Explanation
MEMS	Micro-Electro-Mechanical Systems
EMS	Engine Management Systems
RLG	Ring Laser Gyroscopes
FOG	Fiber Optical Gyroscopes
R-FOG	Resonance-Fiber Optical Gyro
FET	Field-Effect Transistor
IFOGs	Interferometric Fiber-Optic Gyros
RRG	Ring Resonator Gyros
CCW	Counter-Clockwise
CW	Clockwise
BPSK	Phase Shift Keying Modulation
MQW	Multi-Quantum Well
MIG	Interferometric MOEMS Gyroscope
AFIT	Air Force Institute Of Technology
ZRO	Zero Rate Output
INS	Inertial Navigation System
FPI	Fabry-Perot Interferometer
EFPI	Extrinsic FP Interferometers
FBG	Fiber Bragg Grating
EDFA	Erbium-Doped Fiber Amplifier
SMD	Surface Mount Device
OPD	Optical Path Difference
EMI	Electromagnetic Interference
RFI	Radio-Frequency Interference
LPF	Low Pass Filter
TEC	Thermoelectric Cooling
SMF	Single Model Fiber
BJT	Bipolar Junction Transistor
BMM	Bulk Micromachining

CHAPTER ONE

INTRODUCTION

This introductory chapter creates the context for this research project. In it is discussed the awareness of the research problems, research objectives, research motivation and research aims. The thesis will follow the research scope and provide the solutions for those research problems.

1.1 Awareness of the problem

Monitoring environmental parameters is an important aspect of many electrical and mechanical systems. Manufacturing systems, aerospace vehicles, civil structure monitoring systems, and medical devices depend on accurate and reliable sensors. Information from sensors is used for active control, calibration, and failure prevention in these systems. Therefore, the system design must include a cost-effective sensor network to monitor environmental parameters.

The inertial sensors are very broad useful for objects gesture measurement devices, designed to convert, or transducer, a physical phenomenon into a measurable signal. The physical phenomenon is an inertial force. This force is often transducer into a linearly scaled voltage output with a given sensitivity. The methodologies used for macroscopic inertial sensors can and have been utilized for micro machined sensors in many applications. The gyroscopes are the complex and most important device for inertial monitoring. The gyroscope can be plentiful used for navigation system, stability controller, unmanned vehicles, and medical treatment etc. The miniaturization techniques like the Micro-Electro-Mechanical systems and Nano-Electro-Mechanical systems (MEMS/NEMS) fabrication technology give the potential, probability to the conventional gyroscopes more advantages and convenient features (Soderkvist, J., 1994).

Gyroscopes are devices, which are used to measure angular rotation rate. They are widely used in airplanes, spacecrafts, missiles, automobiles and even consumer electronics. Traditional gyroscopes with spinning wheels employed in the present aerospace and military industries are bulky, need lubricant and eventually wear out. Gyroscope is required with a sensitivity as low as 10-100°/s for land transport vehicles, attitude and heading reference systems in the airplanes require 1°/s gyroscopes, while precision inertial navigation systems (Barbour N., Schmidt G., 2001), such us military airplanes and ships, spacecrafts and satellites, need a sensitivity value as high as 0.01-0.001°/s. The micro applications require micro integration micro motion sensors.

Reducing the size, the cost and increasing performances of a gyroscope are the problems, which need a novel solution and MEMS fabrication technology, can be used to solve it.

The optical sensing technology is universal method to use and giving major improvements to many areas. The optical sensors possess important status and depending on excellent performances, the optical sensors have attached importance to develop in many fields. Even after nearly 30 years since its first introduction, the new ideas in applications and sensing techniques are evolving for optical fibre sensors. The use of optical fibre sensors is increasing widely in civil, industrial, and military applications mainly due to their, (a) miniature size and light weight, (b) high sensitivity, (c) immunity from electro-magnetic interference, (d) resistance to harsh environments, (e) remote signal processing abilities, and, (f) multiplexing capabilities.

The optical gyroscope is the most sensitivity and high accuracy angular rate sensing system based on the Sagnac effect. The only problem is the huge size and high manufacturing cost. A Ring laser gyroscope (RLG) typically weights about 4 kg. Researching to integrate the optical gyroscopes and MEMS fabrication technology has increased and become more recognition. MEMS technology is the fabrication technology to reduce conventional devices and sensors to micro size to provide high performance, low cost, and micro applications. MEMS technology is enabling part of inexpensive, autonomous sensor nodes with volumes ranging from cubic mm to several cubic *cm* on the Silicon chips. In this research, the challenge is to develop a novel sensing method and MEMS structures to provide micro size and high performances gyroscopes that could match the performance of FOG with that of MEMS devices.

1.2 Statement of the problem

Traditional gyroscopes with spinning wheels employed in the present aerospace and military industries are bulky, need eventually wear out. Ring laser gyroscopes (RLG's) are also expensive and heavy. We need tiny gyroscopes with the low power consumption and long life span. It is particularly useful in micro-satellites and micro air vehicles due to long time of flight to measure angular rotation rate.

MEMS technology is enabling the development of inexpensive, autonomous sensor nodes with volumes ranging from cubic mm to several cubic cm on the Silicon chips. Studies are being conducted on various types of gyroscopes for the different application size. Traditionally MEMS based gyroscopes are based on Coriolis force sensing and capacitive electronic readout systems. This has proved effective and simple to implement but not very

accurate and are susceptible to electromagnetic interference. Fibre optic gyroscopes, although very sensitive, are however bulky and not easily manufactured.

In this research, the challenge was to develop a MEMS based gyroscope with an optical read out system. The research problem statement: Is it feasible to have MEMS gyroscope that would have the simple manufacturing strategy of a MEMS gyroscope, without the drawbacks of the readout system that creates poor sensitivity. Is it possible to develop an optical readout schema that would be more sensitive than the present MEMS gyros but that could be integrated on the MEMS substrate?

1.3 Research Objectives

Much literature is available on the study of gyroscopes including mechanical gyroscopes, fibre optical gyroscopes (FOG), ring laser gyroscopes (RLG), and recently MEMS gyroscopes. But there are few relating to MEMS optical technology, which in particular and more recently is allowing a dramatic increasing the sensitivity and reduction in the size and power consumption of sensors, actuators, communication components and power systems. More research is needed to develop the feasibility of MOEMS gyroscopes.

The proposed studying aim is to develop an effective and efficient MEMS gyroscope with optical read-out. This has hitherto not yet been done. The following objectives would be realised in the thesis, which includes a study of:

1.3.1 MEMS Gyroscopes with Optical Readout

Combining these two methods in one silicon substrate would reduce the size and improve the sensitivity considerably. In this design a fibre optic interferometer is envisaged as the sensing unit instead of the capacitive sensors used in current MEMS gyroscopes. MEMS technology gyroscopes has as its back bone many successful structures based on Coriolis force designs. It was proposed in this research to add a sensitive optical readout to the mems design.Based on these two methods, a new type of MEMS gyroscope with optical read-out system would then result.

In order for the main objective to be met and adequately addressed, several sub-objectives need to be addressed and these include:

3

1.3.1.1 Studying Sagnac Effect and Coriolis Effect Theories

The Sagnac effect is based on interferometry using for the optical gyroscope. This effect was first demonstrated in 1911 by Harress and in 1913 by Sagnac, so it is now often called the Sagnac effect. Harress (1912) and then Sagnac (1913) studied the question of how electromagnetic radiation like light would behave in a rotating system.

The Coriolis Effect is the apparent deflection of moving objects from a straight path when they are viewed from a rotating frame of reference. The effect is named after Gustave Coriolis, a French scientist who described it in 1835, though the mathematics appeared in the tidal equations of Pierre-Simon Laplace in 1778. The Coriolis effect is caused by the Coriolis force, which appears in the equation of motion in a rotating frame of reference. The Coriolis effect exists only when using a rotating reference frame. It is mathematically deduced from the law of inertia. The Coriolis effect set up the relation between the rotation rate and Coriolis force, while the rotation rate measurement becomes to the force measurement, which make the rotation rate sensor method easier. Most MEMS vibration gyroscopes are based on the Coriolis effect.

1.3.1.2 Development of a MOEMS Gyroscope Mathematical Model

The rotation rate is difficult to detect directly. Most MEMS gyroscopes are detecting the differential phase distortion or elastic distortion, indirectly calculating rotation speed based on Coriolis effect. So the sensing of the deformation of the MEMS gyroscope is playing a decisive role in the sensitivity of the rotation rate. The optical phase shift sensing techniques are proven to be more acurate than the capacitive electronic techniques. There are however no existing mathematical model between the light intensity and rotation rate. In order to proceed with the research aims, it was reuired that a mathematical model be developedto indicate the relationship between the rotation rate and changing light intensity These mathematical evolutions would ten be be tested by simulation as a MOEMS gyroscope.

1.3.1.3 Software simulation and program development

The department of mechanical engineering's MEMS software platform in CoventerWare was selected for the software development. This together with Matlab would be implemented to develop models of the design and to evaluate theoretical models. The theoretical models will be developed in Matlab and the simulation models in CoventerWare. The electronic detector part will be simulated in Matlab. Because the objective involves optical, electrical and machine devices, the software development deals with multi-design routines.

1.3.1.4 Discussion and Evaluation

Since all the fabrication of MEMS devices are at micrometer level, this research only investigates a rigourous theoretical design, modelling and simulation of a new type of MOEMS gyroscope. However enough data will be gathered for in order to supply the possibility for manufacturers to make the product.

1.5 Motivation of the research project

MEMS components are currently replacing conventionally designed and built devices because of their small size, relatively low cost, and relatively high performance. The small size of the MEMS devices is an advantage because it saves space, allowing the "real estate" to be used more efficiently, and thus saves money. Due to the fact that MEMS devices are batch fabricated, where hundreds or thousands are produced at the same time, the cost of a MEMS based gyroscope sensor would be expected to go down, making the devices less expensive than conventionally fabricated devices including fibre optic gyroscopes (Clark, Howe, Horowitz, 1996).

The motivation for undertaking research in this cross disciplinary field of MOEMS (Micro-Opto-Electrical-Mecahnical-Systems) are discussed below. Guidance, navigation and control systems both in aircrafts and spacecrafts require gyroscopes to maintain orientation in flight even in case of undesired interference. In particular, the measurement of the angular motion of a satellite in the space is essential for the control and stabilization of its attitude. In those micro systems, the size, mass and sensitive is attached important position. Systems employing a gyroscope include the control and processing electronics to provide the most direct method for sensing inertial angular velocity. To date fibre-optic gyroscopesbased on the Sagnac effect are the most accurate and is not susceptible to electromagnetic interference. However, MEMS based gyros using the Coriolis force are inexpensive as explained above but are susceptible to erroneous readout and less sensitivity due to EM effects.

It is hoped hereby that enough evidence from the design of a MOEMS gyroscope would be produced that would enable a truly generally applicable autonomous system sensor that would overcome the drawbacks of traditional MEMS and fibre optic gyroscope techniques.

5

1.6 Outline of the Literature Study

MEMS technology has grown rapidly in the last ten years and its applications range broadly from consumer electronics, sensors, entertainment applications, automobiles and medicine to health care. The compatibility of MEMS fabrication with mainstream IC-CMOS technologies (eg: CMOS micromachining or CMOS-MEMS), provides not only high sensitivity , on-chip "smart" conditioning circuitry and low cost, but also has such advantages as scalability, multi-vendor accessibility and short design cycles (Geiger, W., *et al.*, 1998).

Micro-electro-mechanical systems technology is a revolutionary enabling technology, which is based on manufacturing processes that have their roots in photolithographic processing used in microelectronics for fabrication of integrated circuits. Today, MEMS defines both the methodologies to make the MEMS systems and the systems themselves (Pryputniewicz R. J., 1999). MEMS are combing mechanical and electrical components into single devices or sensors (Steward V., Grabbe D. G., Furlong C., and Pryputniewicz R. J., 2003). MEMS fabrication is based on the capability of making controllable mechanical structures that are moveable, and the required electronic components out of silicon and its derivatives using modified IC fabrication techniques. The first MEMS device was made by R. T. Howe in 1982, who demonstrated a technique of how to fabricate micro beams from polycrystalline silicon films. Using this technique, a prototype of the first fully integrated MEMS chemical vapour sensor, where both the mechanical and electrical components were fabricated on the same substrate, was built. This development provided a basis for more research that became the broad field of MEMS (Greiff, Boxenhorn, King, Niles, 1991).

There are numerous possible applications for MEMS and Nanotechnology. As a breakthrough technology, allowing unparalleled synergy between previously unrelated fields such as biology and microelectronics, many new MEMS and Nanotechnology applications are emerging, expanding beyond that which is currently identified or known. Below is discussed a few applications of current interest in the literature:

a) Biotechnology

MEMS and Nanotechnology is enabling new discoveries in science and engineering such as the Polymerase Chain Reaction (PCR) microsystems for DNA amplification and identification, micromachined Scanning Tunneling Microscopes (STMs), biochips for detection of hazardous chemical and biological agents, and microsystems for high-throughput drug screening and selection.

b) Communications

High frequency circuits is expected to benefit considerably from the advent of the RF-MEMS technology. Electrical components such as inductors and tunable capacitors can be improved significantly compared to their integrated counterparts if they are made using MEMS and Nanotechnology. With the integration of such components, the performance of communication circuits will improve, while the total circuit area, power consumption and cost will be reduced. In addition, the mechanical switch, as developed by several research groups, is a key component with huge potential in various microwave circuits. The demonstrated samples of mechanical switches have quality factors much higher than anything previously available. Reliability and packaging of RF-MEMS components seem to be the two critical issues that need to be solved before they receive wider acceptance by the market.

c) Accelerometers

MEMS accelerometers are quickly replacing conventional accelerometers for crash air-bag deployment systems in automobiles. The conventional approach uses several bulky accelerometers made of discrete components mounted in the front of the car with separate electronics near the air-bag. MEMS and Nanotechnology has made it possible to integrate the accelerometer and electronics onto a single silicon chip at a cost between R35 to R80. These MEMS accelerometers are much smaller, more functional, lighter, more reliable, and are produced for a fraction of the cost of the conventional macroscale accelerometer elements.

Figure 1.1 illustrates where MEMS are being used in automobiles. This include drive strain/torque sensors, engine timing/position sensors, antilock brakes/acceleration sensors, engine management systems (EMS)/mass airflow sensors, temperature sensors, transmission sensors, air conditioning/humidity, sun/light sensors, automatic headlight control sensors, airbag deployment sensors, seat control/load/force sensors, emission control/oxygen sensors, and active suspension/speed and pressure sensors (Tanaka, Mochida, Sugimoto, Moriya, Hasegawa, Atsuchi, and Ohwada, 1995). The development micro gyroscope system with high performances is amajor research object in this thesis.

Drive Train
Torque Sensor

Engine Timing
Position Sensor

Antilock Brakes
Accelerometer
Position Sensor

Engine Management
System (EMS)
Mass Air Flow Sensor
Temperature Sensors
Position Sensor

Automatic Headlight
Control
Sun / Light Sensor

Air Bag System
Accelerometer

Seat Control
Temperature Sensor
Load / Force Sensor

Emissions Control
Oxygen Sensor

Transmission
Position Sensor

Air Conditioning
Temperature
Humidty
Sun / Light

Active Suspension
Accelerometer
Position / Speed
Pressure Sensor
Load/Force Sensor

Figure 1.1: Possible MEMS sensor applications in automobiles

The largest market for inertial sensors is the automotive industry; inertial sensors are used in the antilock brakes, traction control, airbag deployment, stability control, and safety control systems of a car. There are also many applications outside the automotive world; they include virtual reality, smart toys, industrial motion control, hard drive head protection systems, image stabilization, GPS receivers, and inertial navigational systems (Sparks, Slaughter, Beni, Jordan, Chia, Rich, Johsnon, Vas, 1998).

There are two basic inertial MEMS sensors: the MEMS accelerometers, which measure linear acceleration, and the micro gyroscope which measures rotational accelerations (Juneau, Pisano, Smith, 1997). Gyroscopes are the inertial measurement devices, which are used to detect angular rotation rate of the objects. Gyroscopes are widely used for guidance, navigation and control systems in airplanes, spacecrafts, missiles, automobiles, and even consumer electronics to maintain orientation, measure the angular motion of essential

8

objects for the control and stabilization of its attitude. These inertial sensors can measure accelerations about a single axis or about multiple axes. Examples of a single axis MEMS accelerometer and gyroscope are illustrated in figure 1.2 and 1.3, respectively. The accelerometer in figure 1.2 measures forces defined by Newton second law caused by a linear acceleration. The tuning fork configuration micro gyroscope, illustrated in figure 1.3, measures angular acceleration due to the Coriolis forces acting on the vibrating masses.
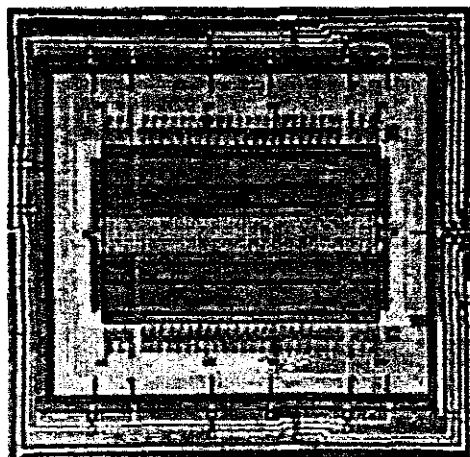
Figure 1.2: Example of a Single Axis Accelerometer ADXL190
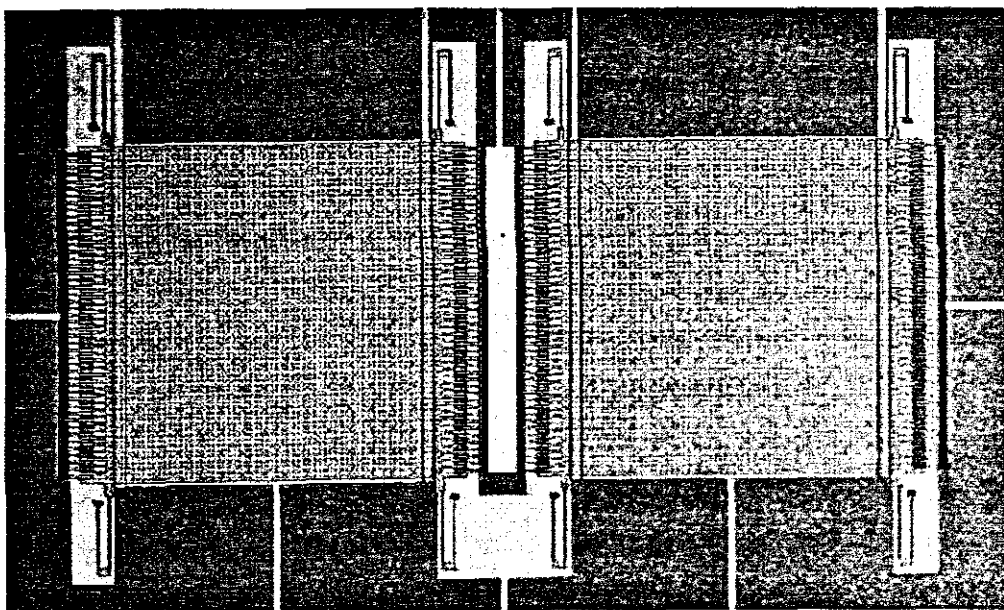
Figure 1.3: A Dual Mass Tuning Fork Micro Gyroscope

When the inertial sensors are minisize in size and cost, the applications increase exponentially. As the accuracy and stability of these miniatures, low-cost devices increases, higher performance systems are being introduced into lower cost items and consumer goods such as automobiles, thereby enhancing safety and functionality. Inertial sensors are made up of a combination of parts: proof masses, elastic springs, dampers, actuators, and a method for measuring displacements of the proof masses. The purpose of the elastic springs

is to provide the proof masses with support and to return the masses back to their original positions after linear acceleration, or rotation, has stopped. The dashpot provides the damping for the system; this is usually done one of two ways: thin film and shear damping. Thin film damping is achieved by using a thin gas film between two vibrating plates; through compression and friction, the film disperses the excess energy, thus adding damping to the system (Geiger, Merz, Fischer, Folkmer, Sandmaier, and Lang, 1999). In other systems that have plates vibrating parallel to one another the film produces shear forces that dissipate energy; this type of damping is known as shear.

There are several methods for determining displacements of the proof masses that are used in the micro inertial sensors. There are: piezoresistive, resonant frequency modulation, capacitive, floating-gate field-effect transistor (FET), strain FET, and tunneling-based. Piezoresistive sensing is used for inertial sensors that make use of single crystals or that are micromachined in bulk quantities. The resonant frequency modulation method of sensing is used mostly for inertial sensors with very high sensitivities. The capacitive sensing method is most commonly used for industrial purposes due to its relative insensitivity to temperature. The floating-gate FET method of sensing is used to measure inertial forces, while the strain FET method measures strains in the packages of the inertial sensors. Both methods have proven difficult to implement in industry. The electron tunneling method is used when displacement must be measured accurately; this method however is still in developmental stages (Geen, Sherman, Chang and Lewis, 2002).

The traditional gyroscopes with spinning wheels employed in the present aerospace and military industries are bulky, which need lubricant and wear out, as stability control system, and navigation system etc. Ring laser gyroscopes, fiber optical gyroscopes are high precision. MEMS gyroscope has the ideal size but not performance.

The gyroscope development is going through the processes from the macro size to the micro size. Traditional gyroscopes with spinning wheels employed in the present aerospace and military industries are bulky, which need lubricant and wear out, as stability control system, and navigation system etc. Ring laser gyroscopes (RLG), fiber optical gyroscopes (FOG) are high precision. But they are expensive and heavy. The micro applications requires the body structures transformed from the huge spin wheel mass to the tiny light vibration mass or optical interferometer measurement system fabricated by MEMS (Micro-electro-Mechanical system) technology like MEMS vibratory gyroscopes and fiber optical gyroscopes.

The MEMS inertial sensors have the following advantages compared with the conventional inertial instruments.

a) Smaller volume and lighter weight

The advanced semiconductor manufacturing processes make the volume smaller and weight of the micro inertial mechanical sensors lighter.

b) Mass production and lower production cost

Thousands of micro inertial devices in a 3 inch or 4 inch silicon chip could be yielded with the mature technique and batch production, which will improve the rate of finished products and reducing the cost. The cost of micro inertial devices, then, will depend on the packaging, testing and accessory circuits. It is undoubted that the cost would drop greatly when the true integration of electromechanical is accomplished.

c) Anti-harsh environments and wider applications

With the small testing proof mass, a micro mechanical accelerometer is adapted to measure the high acceleration. The measurement range could be extended widely by the micro mechanical gyroscopes without rotating parts.

d) Lower consumption, higher sensitivity and efficiency

When performing the same task, the consumption of micro mechanical devices is only one tenth of the traditional ones or even less, while the operation speed could be improved ten times. Certain reasons, for example, the no delay performance of integrated micro mechanical devices result in their wide use in high speed application.

e) Multi-function and intelligence

Most micro mechanical devices integrated the transducer, actuator and electronic circuits. It is easier to realize the multi-function and intelligence of micro mechanical devices after using the intelligent materials and structures.

The operating principles of MEMS vibratory gyroscopes involve the rotation induced energy transfer between two principal modes of the mechanical structure. Resonant motion of the proof mass in the drive mode induces motion in the sense mode upon rotation due to Coriolis force. The measure of this Coriolis force generated displacement in the sense mode is used

to find the rotation rate. MEMS gyroscopes system sense in only one axis, but angular rate is requiring a vector, measuring all three-axis rotations. Assembling three gyroscopes together is needed, which will increase the package size, and the complexity of packaging cost. The capacitance readout electronic circuits have the essential shortcoming at the sensitivity, responding time, bandwidth etc. Therefore, the current MEMS gyroscopes only occupy the low and middle sensitivity scales markets.

An interferometer, as suggested by its name, is a device that uses interference between two beams of collimated light to make measurements. In principle, these measurements can be made to great precision, typically on the order of nanometers, since interferometric technique uses the interference of nanometer wavelengths. The restriction to 100's of nanometers is not due to just the properties of interferometers but to the precision of the translation stages used to make the very small distance changes. The simple concept of the fiber optical interferometer shows in figure 1.4.
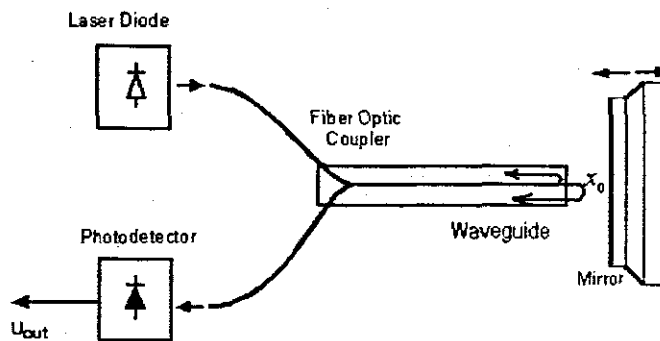
Figure 1.4: Basic Structure of Micro Fiber Optical Interferometer

Modern inertial navigation systems require sensors that are highly reliable and have a wide dynamic range. These objectives are not easily achieved with mechanical gyroscopes. The optical gyroscope systems are all worked by Sagnac effect, which is one type of interferometers. The ring laser gyroscope (RLG) products have already existed that offer major advantages over their mechanical predecessors in the areas of reliability, cost, power consumption, startup time, shelf life. The fiber optical gyroscopes (FOGs) are well developed at this stage. The size of the FOG gyroscope is limited however by the long light path. The novel MOEMS gyroscope system proposed in this thesis attempts at integrating the advantages of MEMS gyroscope and optical Sagnac gyroscope systems, which has the micro vibration structure to transform the rotation rates to linear vibration movement and use high precision light interferometric read-out system to measurement the displacement of the static mass.

Based on the Sagnac effect, ring laser gyroscopes (RLG), fiber optical gyroscopes (FOG), and other optical gyroscopes are too large and heavy for many applications. The large size comes from the long distance light path to create the enough interference and the lack of MEMS fabrication technology for the micro optical devices.

In the commercial area, there is an urgent need for micro size, low cost, and high performances rotation rate measurement devices or sensors. Optical sensors have advantages in that the sensitivity, performance, response time, lifetime, and bandwidth are better than electronic or mechanical sensors. They occupy the high sensitivity and precision sensors markets.

The novel micro gyroscope system with optical read-out system is proposed in this dissertation. This particular micro optical gyroscope system inherits the advantages of original MEMS gyroscope and the optical interferometric is introduced at the signal readout system, which is first time about optical measurement method used for micro gyroscope system.

1.7 Research Methodology

The methodology used to develop the proposed sensor would be to conduct a thourough study of the state of the art developments and operating principles of both MEMS and other optical gyroscopes.

The propsed concept, of joining the two technologies on a single substrate, would then be modelled and a suitable mathematical proof of its viability established. The best solution would then be taken to build on a physical model development that can be accurately simulated, by means of Matlab and CoventorWare software. The software simulations will then be compared to the analytical model of the proposed sensor. The following steps were envisaged in the sensor development.

The table 1.1 describes the major research methodology to meet the stated research objectives. The cross sectional model of the MOEMS gyroscope chip shown in figure 1.5 is according to the operating principles developed in this thesis which is further described in the body text.

Table 1.1: Design of MOEMS Gyroscope Chip

	The operating principle	Material	Fabrication Processes
Micro Vibration Structure Part	Coriolis effect	Polysilicon PMMA Au	MEMS fabrication like surface etch, bulk deposition, LIGA
Optical Part	Light Interferometry	Semiconductor Photoelectric material	MEMS fabrication like LIGA waveguide
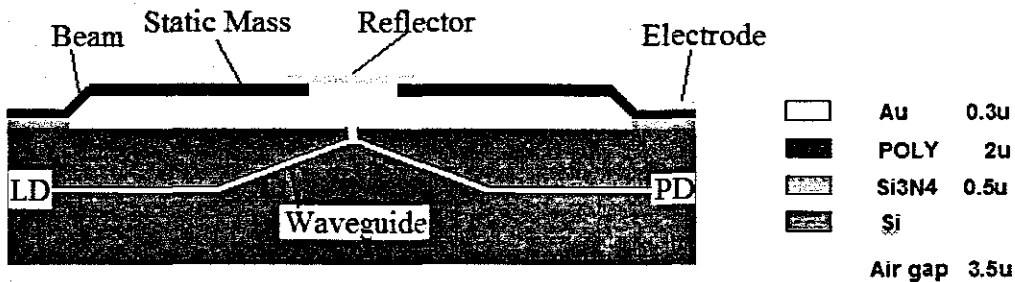
Figure 1.5: Cross section view of MOEMS Gyroscope system developed in the thesis

This novel MOEMS gyroscope system is estimated as cheaper and much smaller than any other optical gyroscope, but provide much higher precision measurement and sensitivity than the traditional MEMS gyroscope technology.

1.8 Outline of the Dissertation

Pursuant to the introduction in chapter one, the research objectives are developing and improving micro gyroscope system based on MEMS fabrication technology and novel measurement methods, which is rotation rate measurement sensor. The rotation movement is most complex motion in inertial reference forms. The development of micro gyroscope systems has great significant for motion controller either in military or civilization areas.

In chapter two, a detailed literature review of the different gyroscopes is given. A numerical typical gyroscope based on the mechanical, optical theoretical and MEMS technology is introduced about their design parameters and characteristic, which shows a development direction of the gyroscopes and easy to compare the different operation principles. That gives the development background and significantly methods to improve the performance of the micro gyroscope systems.

Chapter three introduced all kinds of phase shift optical sensing technologies including the Sagnac effect using to all optical gyroscopes and providing the high precision measurement result. Through the optical sensing technology review, the optical sensing method is proved with the better sensitivity and high accuracy on micro displacement measurment comparing with electron method like capacitive method, piezoelectricity etc. This is giving the ideal to develop MEMS gyroscope with optical readout system. With the further studying about MEMS technology and fiber optical interferometric measurement method, it is possible to integrate those high technologies in one micro system to provide the micro size and high performances sensor.

After the literature review of the different gyroscope systems and optical sensing, the research method has been proposed in chapter four, which is how to develop micro size and high precision gyroscope sensor based on MEMS vibration structure and optical read-out system. The answer is using MEMS fabrication technology to produce solid micro vibration structure, which convert one direction rotation rate to another direction vibration movement based on Coriolis force theory, and building micro fiber optical interferometer based on optical interferometric, which gives high precision measurement about amplitude of vibration created by rotation rate. The operation principles and mathematics model of MEMS vibration structure and the details of how to combine the fiber optical interferometer with MEMS vibration structures are described in detail.

Chapter five designs and builds the MEMS vibration structures including single mass, dual mass with the straight beams and folded beams, which are typtical vibration structure used in MEMS fabrication technology, based on operation principles and functions described in chapter 4. Based on the solid models, the performances of the vibration structures are simulated in Matlab and CoventorWare, which is professional software for MEMS design. About fiber optical interferometer readout system, the structure of interferometer, optical components and component features are introduced. Through chapter four and chapter five, this novel MOEMS gyroscope system is presented including the theories discussion, operation methods description, and model design, performances simulation etc. Although, many aspects of this MOEMS gyroscope system need further study and optimize, this design organically integrates the optical and MEMS technology creating the interface between optic and electro-mechanic, which expand the intersection of various subjects, provide the ideology of sensors design.

The MEMS fabrication technology is new manufactory approaches for micro devices, and rapidly developing in last decade years. There is not everybody familiar with this rising technology. In chapter six, the basic MEMS conceptions, principles and fabrication methods

are introduced. There are recommendatory MEMS fabrication processes for MOEMS gyroscope system.

The dissertation ends with a list of major contributions and some suggestions for future improvement of the performances of the MOEMS gyroscope system, given in the last chapter 7. The micro gyroscope system is a systemic, multi-subjects, complex device, which is involved with mechanics, electrics, optic, and MEMS fabrication technology etc. In last three years studying about the rotation rate sensor, I studied from the basic rotation rate measurement theories to the present MEMS gyroscope system. Finally, the MOEMS gyroscope system is proposed. In this dissertation, the main part is focused on the novel MOEMS gyroscope system description, can not contain all the outcomes and applications.

1.9 Summary

This chapter introduced the background the reseach objectives, stated the research problems, and gave the research scope. The chapter concluded the thesis outline. The research will follow the scope and identified problems.

CHAPTER TWO
GYROSCOPES DEVELOPMENT AND OPERATING PRINCIPLES

In this chapter, various types of gyroscopes are introduced including the conventional mechnical gyroscopes, pure optical gyroscope systems, and MEMS gyros in detail. For each of them, the operating principles, device structures, fabrication technology, specifications, open issues related to the design, packaging and interface electronics are discussed. This provides a detailed background to the study and development of the MOEMS gyroscope to be discussed in the main text of the thesis.

2.1 Gyroscope Concepts and Development History

The inertial Sensors are widely used in many applications in the aerospace, military, automotive and marine industries such as accelerometers and gyroscopes. In the aerospace industry, these devices are used in the basic flight stabilization of aircraft and rockets as well as in navigation. Military applications include the same usages in air to air missiles, air to ground missiles, ground to air missiles, ground to ground missiles, barrage rounds and hypersonic projectiles. Automotive applications include vehicle stability systems and rollover prevention systems. Naval and marine applications include ship stabilization and navigation. The navigation systems require gyroscopes with a sensitivity as low as 10-100°/s for land transport vehicles, attitude and heading reference systems in the airplanes use 1°/s gyroscopes, while precision inertial navigation systems (Barbour, Schmidt, 2001), such us military airplanes and ships, spacecrafts and satellites, need a sensitivity value as high as 0.01-0.001°/s. To date micro accelerometers are in a mature state of developement and large numbers used in the motorcar industries. However the same cannot be said of micro rotation based sensors.

Gyroscopes are devices for measuring rotation rate or maintaining orientation, based on the principle of conservation of angular momentum. There are three classes of gyroscopes with performance rationgs from low to high. These are known as rate grade, tactical grade and inertial grade respectively. Recently, markets in automotive and consumer electronic products are demanding low-cost gyroscopes with rate-grade performance for driving security and comfort, and motion stability control. The performance requirements for these applications include a full-scale range of at least $50\,^0/s$ and a resolution of $0.1\,^0/s$ in a bandwidth of $50Hz$. In physics this is also known as gyroscopic inertia or rigidity in space. The essential operating principle of the device is a spinning wheel on an axle. The device, once spinning, tends to resist changes to its orientation due to the angular momentum of the wheel.

Gyroscopes can, on the face of it, be very perplexing objects to understand because they move in peculiar ways and even seem to defy gravity. An illustartion of a signal axis gyroscope is shown in figure 2.1. The special properties of these devices make gyroscopes extremely important in navigation systems. A typical airplane uses about a dozen gyroscopes in everything from its compass to its autopilot. The Russian Mir space station used eleven gyroscopes to keep its orientation to the sun, and the Hubble Space Telescope has a batch of navigational gyros as well.
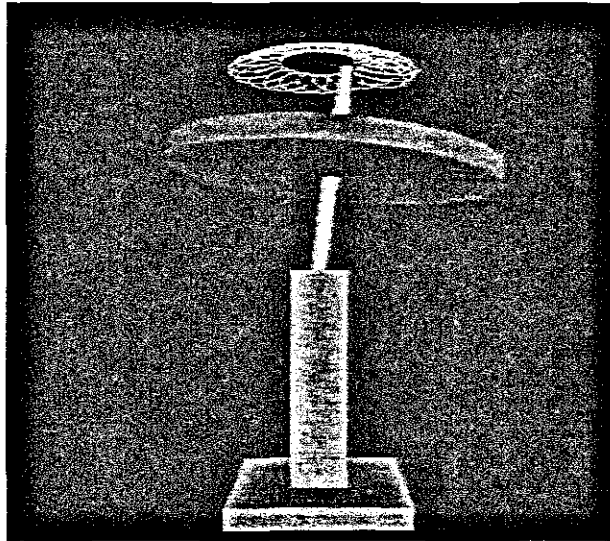
Figure 2.1: Simple Gyroscope Model Demonstration

A gyroscope exhibits a number of behaviors including precession and nutation, so it is an important feedback sensor to control the attitude of objects. Since the 1960s, gyroscopes have been advancing by the processes of development from mechanical gyroscopes to optical gyroscopes. The development of laser and fiber optical technology had an immense effect on this development. But the optical gyroscope systems are still macro measurement devices. In the last 10 years miniaturization is turning into a main consideration in gyroscope development (Madni, Wan, 1998). These innovations are expected to bring wider advantages and lower cost for a new generation of inertial navigation systems.

Gyroscope's operate differently depending on their type. The spinning gyroscopes work on the basis that a spinning object that is tilted perpendicularly to the direction of the spin will have a precession. The precession keeps the device oriented in a vertical direction so the angle relative to the reference surface can be measured (Yazdi, Ayazi, and Najafi, 1998). Optical gyroscopes are most commonly ring laser gyroscopes working based on Sagnac effect. These devices send two lasers around a circular path in opposite directions. If the path spins, a phase shift can be detected since the speed of light always remain constant.

Usually the rings are triangles or rectangles with mirrors at each corner. Optical gyroscopes are a great improvement to the spinning mass gyroscopes because there is no wear, greater reliability and smaller size and weight. With development MEMS fabrication technology, the micro gyroscope is fabricated based on Coriolis effects, which is used for micro applications and provide enough sensitivity for low level sensing requirements.

Draper Lab proposed the first silicon micromachined vibration gyroscope in 1991. After that, various fabrication technologies, structural designs and drive/sense mechanisms have been investigated. During the early 1990s, bulk micromachining and metal electroforming were mostly used to form large masses. Draper Lab's single-crystal-silicon-on-glass tuning fork gyroscope demonstrated a resolution of 1.5°/s in a 60 Hz bandwidth in 1993. U-Michigan's metal electroforming vibrating ring gyroscope achieved a resolution of 0.5°/s in a 10 Hz bandwidth in 1994 (Greiff, Boxenhorn, King, and Niles, 1991). In mid-90's, surface micromachined gyroscopes enabled the read-out circuits to be easily integrated on the same chip. Murata demonstrated a polysilicon surface micromachined vibratory gyroscope with a resolution of 7°/s in 1995 (Mochida, Tamura, Ohwada, 1999). Delco's electroformed vibrating metal ring gyroscope achieved 0.5°/s resolution in 1997 (Suzuki, Takiguchi, Hotate, 2000). UC-Berkeley's surface micromachined z-axis gyroscope achieved a noise floor of 1°/s/Hz$^{1/2}$ in 1996, which were improved to 0.2°/s/Hz$^{1/2}$ in 1997. Samsung investigated a surface micromachining gyroscope made from 7.5μm thick polysilicon and achieved 0.1°/s resolution in 1997. HSG-IMIT reported a surface micromachined gyroscope with a resolution of 0.05°/s at a bandwidth of 50 Hz in 1999. Carnegie Mellon demonstrated both lateral-axis and z-axis gyroscopes using the maskless post-CMOS micromachining process. Analog Devices Inc. reported an integrated zaxis gyroscope with 0.05°/s/Hz$^{1/2}$ noise floor in 2002 (Shearwood, Williams, Mellor, Yates, Gibbs, and Mattingley, 1995,).

Bulk micromachined gyroscopes also made noticeable progress after 1995. The microgyroscope with a clover-leaf shape and a metal post attached to the center and provided an angle random walk of 0.1°/s/Hz$^{1/2}$ and a bias stability of 70°/hr in 1997. Murata reported a deep RIE gyroscope with decoupling of the sense and drive modes and a resolution of 0.07°/s at bandwidth of 10 Hz in 1999 (Sparks, Slaughter, Beni, Jordan, Chia, Rich, Johnson, and Vas 1998).

2.2 Mechanical Spinning Mass Gyroscopes

The spinning mass gyroscopes are the classical gyroscope, which have a mass spinning steadily within free movable axis called gimbals. When the gyro is tilted, gyroscopic effect causes precession, motion orthogonal to the direction tilt sense on the rotating mass axis,

hence letting us know the angle moved. Because mechanical constraints cause numerous error factors, the idea came up such that fixing the axis with springs and the spring tension is proportional to the precession speed. By integrating the spring tension one would get the angle. Angular velocity, which is rate of turn, sensor is rate-gyroscope. Nowadays most gyroscopes are actually rate-gyroscopes. Dry tuned gyro, dynamically tuned gyro, is a type of spinning mass gyro, which has been designed to cause very small mechanical constraints once the spinning speed reaches to specific speed.

People often confuse with Gyrocompass, which is also a spinning mass gyro usually very big, but its axis is made to rotate and maintain same direction as that of the earth rotation all the time, hence giving you *True North* all the time: gyroscope gives you info on relative change of angles.

The gyroscope effect was discovered in 1817 by Johann Bohnenberger and invented and named in 1852 by Léon Foucault for an experiment involving the rotation of the Earth. Foucault's experiment to see the Earth's rotation was unsuccessful due to friction, which effectively limited each trial to 8 to 10 minutes, too short a time to observe significant movement. In the 1860s, however, electric motors made the concept feasible, leading to the first prototype gyrocompasses; the first functional marine gyrocompass was developed between 1905 and 1908 by German inventor Hermann Anschütz-Kaempfe. The American Elmer Sperry followed with his own design in 1910, and other nations soon realized the military importance of the invention in an age in which naval might was the most significant measure of military power and created their own gyroscope industries. The most Gyroscope Companies quickly expanded to provide aircraft and naval stabilizers as well, and other gyroscope developers followed suit (Wikipedia: Gyroscope).

In the first several decades of the 20th century, other inventors attempted to use gyroscopes as the basis for early black box navigational systems by creating a stable platform from which accurate acceleration measurements could be performed in order to bypass the need for star sightings to calculate position. Similar principles were later employed in the development of inertial guidance systems for ballistic missiles.

A gyroscope exhibits a number of behaviours including precession and nutation. Gyroscopes can be used to construct gyrocompasses which complement or replace magnetic compasses in ships, aircraft and spacecraft, vehicles in general, to assist in stability for the bicycle, Hubble Space Telescope, ships, vehicles in general or be used as part of an Inertial guidance system (Wagner, 1990). Gyroscopic effects are used in toys like yo-yos and dynabees. Many other rotating devices, such as flywheels, behave gyroscopically although the gyroscopic effect is not used.
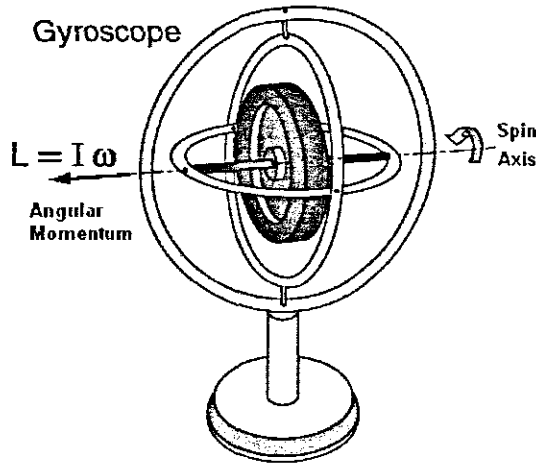
Figure 2.2: Typical Mechanical Wheel Mass Gyroscopes

In figure 2.2, the fundamental equation describing the behaviour of the gyroscope is:

$$\tau = \frac{dL}{dt} = \frac{d(I\omega)}{dt} = I\alpha \qquad (2.1)$$

where the vectors τ and L are, respectively, the torque on the gyroscope and its angular momentum, the scalar I is its moment of inertia, the vector ω is its angular velocity, and the vector α is its angular acceleration.

It follows from this that a torque τ applied perpendicular to the axis of rotation, and therefore perpendicular to L, results in a motion perpendicular to both τ and L. This motion is called *precession*. The angular velocity of precession Ω_P is given by

$$\tau = \Omega_p \times L \qquad (2.2)$$

Precession can be demonstrated by placing a spinning gyroscope with its axis horizontal and supported loosely at one end. Instead of falling, as might be expected, the gyroscope appears to defy gravity by remaining with its axis horizontal, even though one end of the axis is unsupported. The free end of the axis slowly describes a circle in a horizontal plane. This effect is explained by the above equations. The torque on the gyroscope is supplied by a couple of forces: gravity acting downwards on the device's centre of mass, and an equal force acting upwards to support one end of the device. The motion resulting from this torque is not downwards, as might be intuitively expected, causing the device to fall, but perpendicular to both the gravitational torque (downwards) and the axis of rotation (outwards

21

from the point of support), i.e. in a forward horizontal direction, causing the device to rotate slowly about the supporting point.

As the second equation shows, under a constant torque due to gravity, the gyroscope's speed of precession is inversely proportional to its angular momentum. This means that, as friction causes the gyroscope's spin to slow down, the rate of precession increases. This continues until the device is unable to rotate fast enough to support its own weight, when it stops precessing and falls off its support.

2.3 Optical Gyroscopes

The optical gyroscopes described in the following subsections are: fiber optic gyros (FOG), resonant fiber optic gyros (RFOGs), ring resonator gyros (RRG), integrated optic ring laser gyro and micro-optical-electro-mechanical-system gyros, which are all working based on Sagnac Effect.

2.3.1 Fiber Optic Gyros (FOG)

The FOGs were first proposed in '60s and developed rather slowly because appropriate laser sources and photoconductive components were not available. Interferometric fiber-optic gyros (IFOGs) are based on the Sagnac effect (Andronova, Malykin, 2002). In particular they are phase sensitive devices. Sagnac effect generates an optical phase difference, $\Delta\Phi s$, between two counterpropagating waves in a rotating fiber coil, optical paths (Komachia, Sonobe, Oho, Ohbu, Yuhara, Izuka, 1996):

$$\Delta\phi_s = S\Omega = \frac{4\pi RL}{\lambda c}\Omega \qquad (2.3)$$

where S is the scale factor, Ω is the angular velocity around the rotation axis, R is the fiber coil radius, L is the optical path length, λ is the optical wave length and c is the velocity of light in vacuum. The effect is non-reciprocal: the counterpropagating beams acquire Sagnac phase shift of opposite sign and different value. In a general formulation, the phase shift depends only on the light frequency and on the dot product of the equivalent area vector A of the average optical path and the rotation rate vector Ω:

$$\Delta\phi_S = \frac{8\pi A}{c\lambda}\Omega \qquad (2.4)$$

As it is shown in the previous equations, the phase shift is an indirect measurement of the rotation rate Ω. Some design considerations can also be derived from Eqns (2.3) and (2.4). In fact, both longer and larger coils increase sensitivity, which is the capability of the output photocurrent to follow the variation of the input rate, because sensitivity is proportional both to diameter and total length of the optical path. However, it should be considered that larger coils are more sensitive to temperature variations and vibrations.

If P_D is the power that impinges on photodiode, expressed as

$$P_D = \frac{1}{2} P_0 (1 + \cos \Delta \phi_S)$$

(2.5)

The sensitivity is given by:

$$\frac{dP_D}{d\Omega} = -\frac{1}{2} P_0 sen \Delta \phi_S \frac{4\pi LR}{\lambda c}$$

(2.6)

where P_D is the input power. The maximum value is obtained for $\Delta \Phi_s = \pi/2$, i.e. where the fringe slope of the interferometer is at the maximum value. A further consideration is that sensitivity is also inversely proportional to wavelength, but increasing sensitivity by using shorter wavelength results also in a reduction of the radiation resistance of the optical fibers.

The uncertainty in the measurement (that is also the minimum detectable rotation rate) is $d(\Delta \Phi_s)$ = shot noise/fringe slope. The design of IFOG is, then, focused on reducing all noise sources below the photon noise at the detector.

Interferometric FOG can operate with two different configurations: open loop and closed loop. In the open loop configuration the information about the angular rate is obtained directly by the electrical signal at the output. In the closed loop a non-reciprocal phase shift is generated in the feedback loop to null the total phase shift. The applied opposite phase shift gives the information about the rotation rate.

Figure 2.3 represents an open loop configuration scheme and clarifies the principle of operation of this kind of sensor.
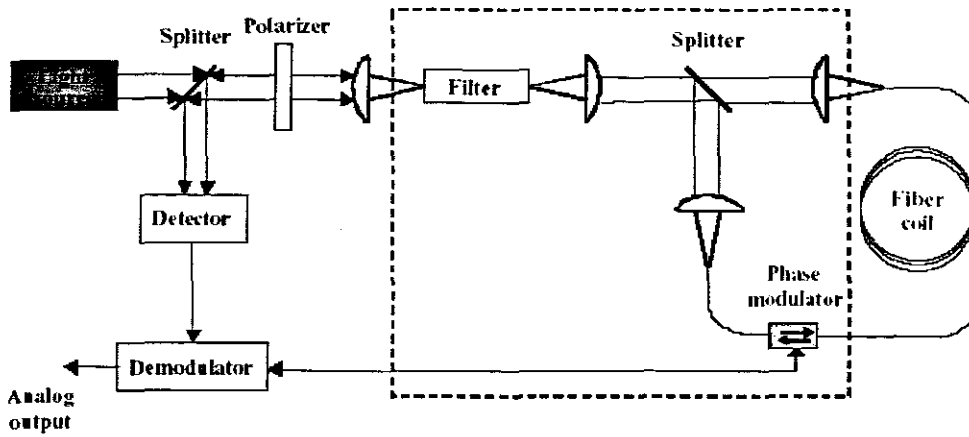
Figure 2.3: Architecture of open loop IFOG

As in any interferometric device, the output signal is the result of the interference between two waves that, in this case, are counterpropagating in the optical fiber. This scheme is called "minimum configuration" which means it is able to guarantee the reciprocity of the system. To accurately measure the Sagnac effect and, then, increase the gyroscope quality, it is necessary to reduce any phase differences different from that induced by the rotation. Thus, reciprocity is the fundamental requirement for IFOG. The dashed block shows the components that usually are integrated on a single chip.

The source beam is coupled into an optical path. The light pass through an optical system composed by a filter and polarizers to select and guarantee the presence of just one mode in the structure. This is because each mode in the structure has an independent light path that can experience environmental perturbations, different from those relevant to another mode. If the clockwise (CW) and counterclockwise (CCW) beams correspond to different modes, reciprocity is not achieved. Also, the fiber in the coil is required to be polarization-maintaining to ensure that just one mode does exist in the structure. The second splitter is used to create, in the fiber, two counterpropagating waves that sense Sagnac effect. After the coil the two beams recombine into the interferometer, the light passes again through the polarizat ion control system and is directed on the photodetector by the second splitter. The phase modulator is used to apply a dynamic phase bias generated by a sinusoidal wave to the light path, thus increasing sensitivity (Lefevre, Marten, Morrise, Simonpieti, Vivenot and Arditty, 1990). If the modulation frequency f_m is sufficiently high, the electronic noise is avoided. The signal at the output of the photodiode is demodulated and processed for producing an output corresponding to the magnitude and sense of the rotation.

The optical sources used in an IFOG is a broadband multi-mode laser or a super-luminescent source to reduce the gyro signal noise due to coherent Rayleigh scattering

generated by the counterpropagating beams (Bergh, Lefevre, Shaw, 1984). Either semiconductor or doped fiber sources can be used, depending on the desired performance of the gyroscope.

The main advantages for the open loop scheme are: low-price due to the use of a small number of commercial components, both electronic and optics, good sensitivity, and long lifetime and high reliability. Furthermore it has a low power consumption due to the low power consumption of the electronics and low driving power required by the laser; it is also insensitive to shocks and vibrations due to the interferometric structure, and insensitive to gravity or acceleration because it is not based on inertial forces and it doesn't need any tight control of the fiber length with respect to a frequency sensitive device. Disadvantages are the use of a very long single mode fiber to increase sensitivity, the drift caused by the analog components and the influence of temperature and environmental conditions.

To overcome the main issues of the open loop configuration, a closed loop device can be used (Dyott, Bennett, Allen, Brunner, 2002). Very high performance has been obtained with respect to open loop devices. The general scheme of a closed loop IFOG is in figure 2.4.

In the scheme the demodulator output passes through a servo amplifier which drives a phase transducer placed in the interferometer. The total phase shift becomes equal to zero because the phase transducer introduces a non reciprocal phase shift that is equal, but opposite in sign, to that generated by the Sagnac effect when the device rotates. The output of the system is then the output of the phase transducer. Advantages of this scheme with respect to the open loop one is insensitivity to light source intensity variations and to gain variations of single component, because the system is always operated at zero. This implies a very small drift 0.001 to 0.01°/h. The output linearity and stability depend only on the phase transducer.
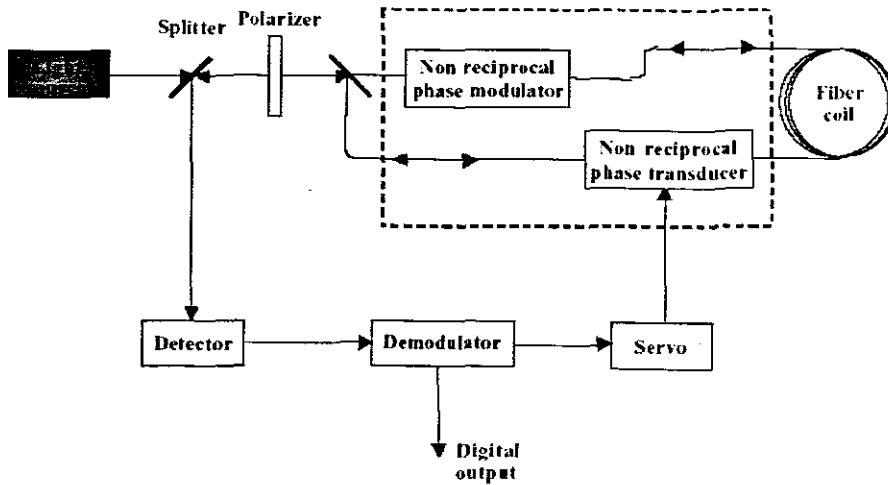
Figure 2.4: Architecture of closed loop IFOG

The typical performance reported for the interferometric fiber-optic gyros are an input range of ±100°/s, a drift (bias) between 0.001 and 0.2°/ h with a drift stability ranging from 0.0005 and 0.01°/ h. Random walk is in the range 0.004-0.04°/ h and the bandwidth changes from 20 to 100 Hz. IFOGs have long been used for terrestrial applications. These gyro systems are extremely robust and they are commercially available for use in space due to their relatively high reliability and cost effectiveness (Dollon *et.al.* 2002).

2.3.2 Resonant Fiber Optic Gyros (RFOGs)

A resonant fiber optic gyro configuration is illustrated in figure 2.5. It is a frequency sensitive device in which the Sagnac effect generates a frequency difference between two resonant beams in the ring fiber cavity, locked to the resonant clockwise and counterclockwise frequencies. Resonance condition is $\beta \pm L = 2m\pi$ that can be rewritten in terms of wavelength as $(2\pi / \pm \lambda)n(\pm L) = 2\pi m$. From this last equation, $\pm f = mc / n(\pm L)$ can be derived, where $L = 2\pi R$, $+L$ and $-L$ are the path lengths for clockwise (CW) and counter-clockwise (CCW) conterpropagating beams, respectively, and $+f$ and $-f$ are the corresponding frequencies. When the device is rotated, these changes in length result in a change of the resonant frequencies in the cavity.

The output from a laser at frequency f_0 is split into two beams, each of them passing through an acoustooptic frequency shifter. The frequencies of the two beams are shifted by f_1 and f_2 to coincide with the CW and CCW resonant modes.
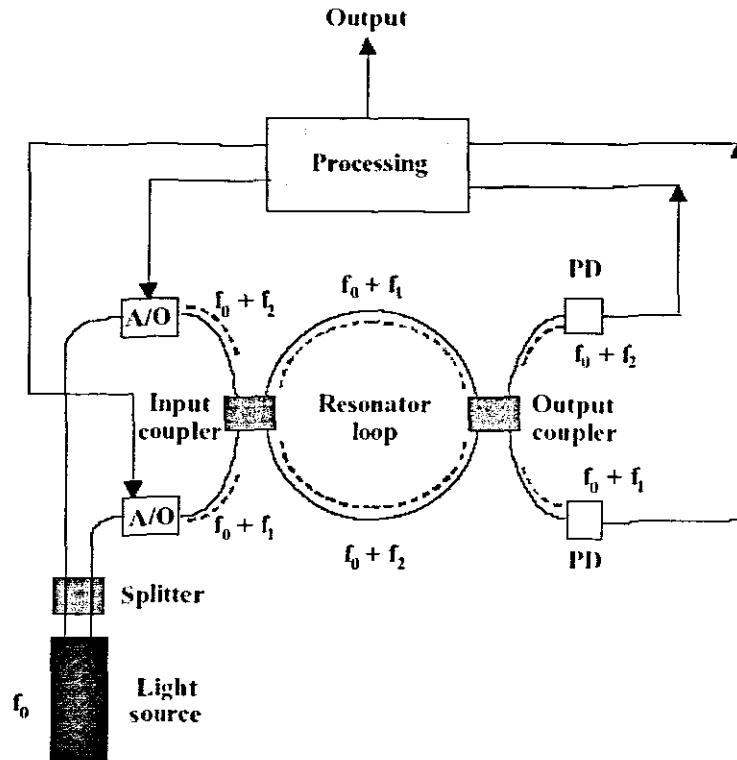
Figure 2.5: Resonant Fiber-Optic Gyro Scheme

A fiber coupler is used to couple the beams into counterrotating waves in the fiber cavity. Without any rotation, the cavity resonant modes have the same frequency, the initial frequency shift values for both CW and CCW beams are equal. A second fiber coupler is used to couple the counterrotating waves to the two photodetectors. The photodetector outputs are used to calculate feedback signals to drive the acoustooptic frequency shifters. If the two detectors reveal the maximum value of the expected power this means that the two input beams are perfectly locked to the resonance frequencies inside the cavity. If it doesn't happen, the processing unit caluculates the optimal frequency values to obtain the locking and calculate the signals to rearrange the shifters. The feedback loops lock the frequencies $f_0 + f_1$ and $f_0 + f_2$ to the CW and CCW resonances of the fiber cavity (Sanders, Strandjord, Mead, 2002). The frequency difference between the imposed frequency shifts is a meaurement of the rotation rate:

$$\Delta f = \frac{4A}{\lambda P} \Omega$$ (2.7)

where A is the area enclosed by the coil, $.$ is the wavelength of light, P is the perimeter of the fiber coil and $.$ is the rotation rate.

The measurement uncertainty on the frequency-sensitive fiber devices is:

27

$$dΩ = \frac{λP}{4A} \frac{\sqrt{2Γ}}{SNR}$$ (2.8)

where $Γ$ is the width of the resonant peaks of the fiber and SNR is the signal-to-noise ratio at the photodiode.

The main advantages of RFOG are high reliability and small amount of fiber with respect to the interferometric device due to the larger scale factor. Disadvantages are mainly represented by the need of a highly coherent laser source to increase sensitivity because, as it is shown in Eqn. (2.7), the measurement uncertainty is proportional to the line width of the resonant modes. The sensitivity can be increased by using some matching techniques between the frequency of optical beams and the resonant frequencies of the cavity, and low-loss components because a higher optical power results in a higher sensitivity. No significant experimental results have been obtained so far.

2.3.3 Ring Resonator Gyros (RRG)

They are based on the same principle of the resonant fiber-optic gyro seen in the previous subsection. Two main categories can be identified, both based on frequency shift, which is Sagnac effect, generated by the rotation: active ring resonator gyros and passive ring resonator gyros (Chow, Gea-Banacloche, Pedrotti, Sanders, Schleich, Scully, 1985).

For a circular ring, the round trip path difference between CW and CCW counterrotating beams is $ΔL = cΔt = 4πR_2Ω/c$. At the same time, for a path length of L at $λ$, the resonance condition can be expressed as $m(±λ) = ±L$, i.e. $±ω = mc/±L$ (integer m). The frequency difference between the two CW and CCW beams is:

$$ΔΩ = Ω_+ - Ω_- = mcΔL/L^2 ≈ ΩΔL/L$$ (2.9)

The scale factor of the frequency sensitive devices is larger than that of the phase sensitive ones.

2.3.3.1 Active Ring Resonator Gyros

In an active ring resonator gyro an active medium is introduced inside the ring cavity. The general scheme of the cavity, which includes a laser emitting on both sides and an optical path formed by mirrors is reported in figure 2.6.

These active sensors show a wide dynamic range ($>10^9$) and a fast update rate. They are vibration insensitive and have a long and reliable lifetime ($>30,000$hours). Disadvantages are, mainly, a not high sensitivity and some performance limitations as null shift and lock-in effect (Haus, Tatz, Smith, 1985).
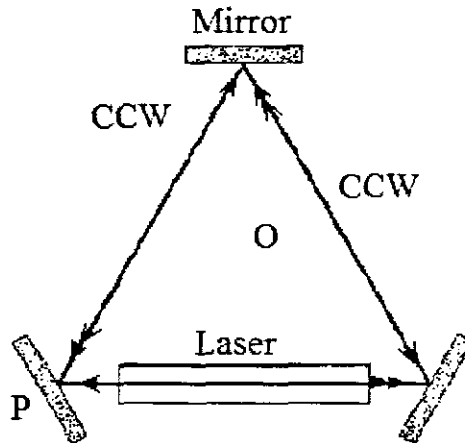
Figure 2.6: Active Ring Resonator Gyro Scheme

The output characteristics of an active ring resonator gyro are reported in figure 2.7. The ideal behavior of the gyro output is in figure 2.7(a).
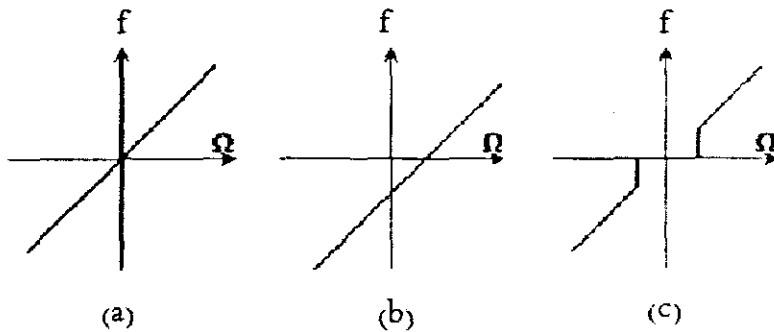
Figure 2.7: Output characteristics of an active ring resonator gyro

In Figure 2.7(b), one can observe that a non zero frequency difference, null shift, can be obtained at zero input rate. This is due to the anisotropy of the cavity with respect to radiation travelling in the two directions. If repeatable it can be measured and compensated and constant bias of opposite value by means of a continuous rotation. Figure 2.7(c) describes the lock-in effect: at very small rotation rates frequency difference is zero, defining a dead-

band. It is mainly due to the weak coupling effects between independent counter-rotating beams. This effect results in a backscattering from one wave into the other one at the mirrors or inside the cavity (Armenise, Armenise, Passaro, De Leonardis, 2000). The problem is solved by using mechanical optical dithering alternating bias: the gyro is rotated in alternating way in one direction and in the opposite one.

It is possible to calculate the lock-in threshold and, hence, the minimum detectable rotation rate Ω_{th} when just the lock-in effect is taken into account:

$$\Omega_{th} = \frac{b}{S} = \frac{Lb\lambda}{8\pi A} \tag{2.10}$$

where b is the backscattering coefficient .

Drift stability of 0.02°/h, scale factor of 1.164.352*ps/rev* with stability equal to 20*ppm* have been reported (Online reference). Random walk is 0.02°/h, operation temperature range is -54 to +85°C and the power consumption 0.37 W at 5 *Vdc*. The gyro seems to be mainly devoted to tactical applications.

2.3.3.2 Passive Ring Resonator Gyros

The second category of ring resonator gyros is the passive one. The main feature is that the source is external to the cavity as shown in figure 2.8.
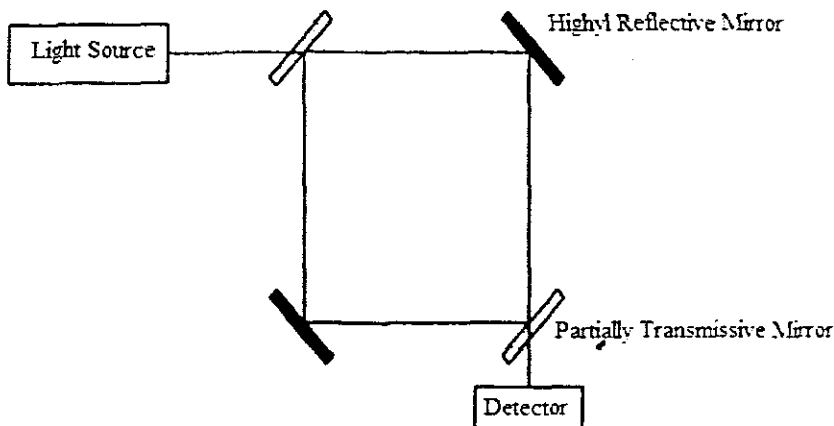
Figure 2.8: Scheme of Passive Ring Resonator Gyro

As the case of fiber ring resonator, light is split into two beams coupled into the cavity. At the output, the frequency difference between the beams carries the information about the rotation rate.

Advantages are a high sensitivity due to the absence of gain variations of the laser, low cost of fabrication, shock and vibration immunity due to the absence of moving parts, low power consumption for the small number of the components, high polarization selection in guided-wave structures that avoids polarization fluctuation induced noise and Kerr effect that are present in IFOG devices, high reliability. Moreover, passive structures solve problems of the active configuration such us lock-in effect and mode competition. Disadvantages are the need of low-loss waveguides and large ring radius to obtain high finesses and low quantum limit.

Two examples of passive ring resonator gyros are reported in the following. First configuration, reported in figure 2.9, is silicon integrated optic waveguide chip (Armenise, Passaro, De Leonardis, Armenise, 2001).
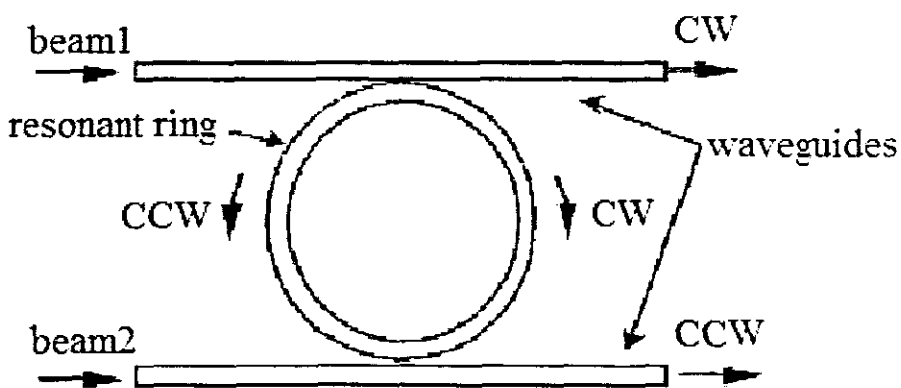
Figure 2.9: Scheme of silicon integrated optic waveguide passive ring resonator gyro

A semiconductor laser source is split into two waveguides. The beams 1 and 2 produce the CCW and CW modes inside the ring. The information about rotation rate is in the phase difference between the output signals. Rate response has been obtained in the range of 1 to 200°/s.

In the scheme reported in figure 2.10, a directional coupler, which launches light into the resonator, is composed of a Mach-Zehnder interferometer with a thermooptic phase shifter (Monovoukas, Swiecki, Maseeh, 2000).
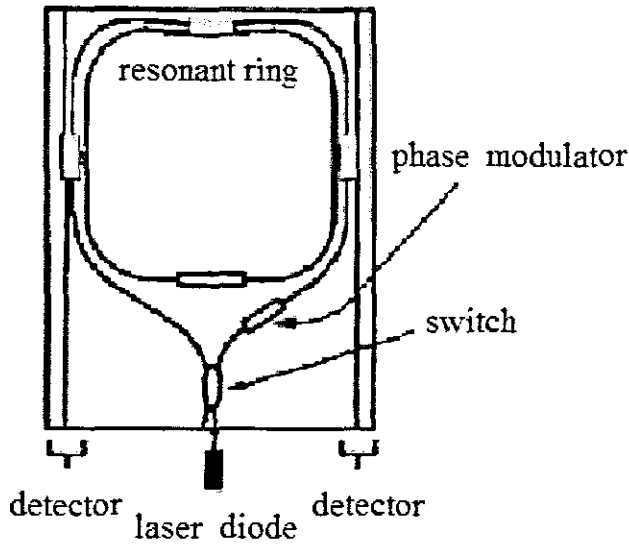
Figure 2.10: Scheme of fully integrated resonant ring gyro

This approach represents a solution for strongly reducing the backscattering induced noise, which is the most serious noise factor in optical passive resonator gyros. The phase modulator induces a binary phase shift keying modulation (BPSK) on the carrier, putting the backscattered light wave and the counter propagating signal out of the gyro bandwidth. However, it doesn't seem appropriate for space applications. In fact, it has been proposed for substituting FOGs for car navigation, robotics and similar applications.

2.3.4 Integrated Optic Ring Laser Gyro

An example of integrated optic ring laser gyro is reported in figure 2.11. The operating principle is again the frequency sensitivity due to Sagnac effect (Suzuki, Takiguchi, Hotate, 2000).
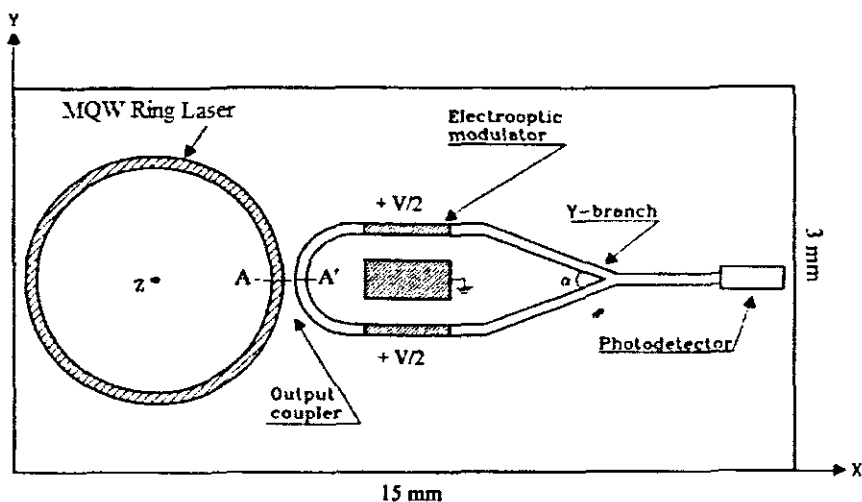
Figure 2.11: Scheme of Integrated Optic Ring Laser Gyro

The ring and the circular coupler are multi-quantum well (MQW) structures in GaAs/GaAlAs. The beams generated inside the ring laser are coupled out by the coupler, pass through the two waveguides and are combined at the Y junction. An electro-optic modulator is used to induce a phase modulation mainly for two reasons: to erase any initial offset and to identify the direction of rotation through fast Fourier transform of the photocurrent. Therefore, neither effects of birefringence and coupling between the two polarizations, nor polarization noise can be observed. The overall dimensions of the chip are 15 *mm* x 3 *mm*, ring radius is 1.5 *mm* and ring width is 0.3*mm*.

The avantages of this approach are integration of different optical functions on a single chip of very small dimensions, reduction in size and mass, absence of any matching technique between the optical beam frequencies and the cavity resonant frequencies, high polarization selectivity, negligible curvature losses because of the strong optical field confinement due to the presence of the MQWs structure, high quality factor, good sensitivity and relatively low quantum limit. Quantum limit is an intrinsic noise due to laser operation; in particular it is due to the spontaneous emission. It enlarges the beam line width increasing the measurement uncertainty and, then, reducing the sensitivity of the sensor. This kind of noise is related also to the sidewall roughness which is responsible for some backscattering effect inside the ring. It decreases when the effective ring radius increases and the optical losses of the cavity decrease. Disadvantages for the integrated optic ring laser gyro are lock-in and possible mode competition, that is an effect due to the variation of the gain in the active medium for which bidirectional of ring laser is lost. Main performances are quality factor of 2.24×10^6, resolution of 3.5×10^{-6} °/s and power consumption of 1 *W*.

2.3.5 Solid Micro-optical-electromechanical Systems (MOEMS) gyros

Optical MEMS sensors have been under development since several years. The aim is to increase the accuracy of micro-inertial sensors for highly precise navigation. It is quite difficult to design a micro-optical gyroscope because their small dimensions prevent them having a path large enough to detect low rotation rates. Design techniques for MOEMS devices can be found in (Gilbert J. R., 1996).

An interferometric MOEMS gyroscope (MIG) has been proposed by Air Force Institute of Technology (AFIT), as in figure 2.12. In this open loop device, the basic concept of the interferometric fiber optic gyroscope is integrated with MEMS. The MEMS mirrors are placed on a silicon substrate to create a spiral path for the light from the outside, where the laser is placed, to the center of the die, where the interference pattern is detected. The mirrors are arranged in such a way to increase the path length of the device with respect to a standard

Sagnac interferometer. The propagation is in free -space and the laser beam only interact with mirrors on the corners of the spiral path to keep the losses low (Stringer, 2000).
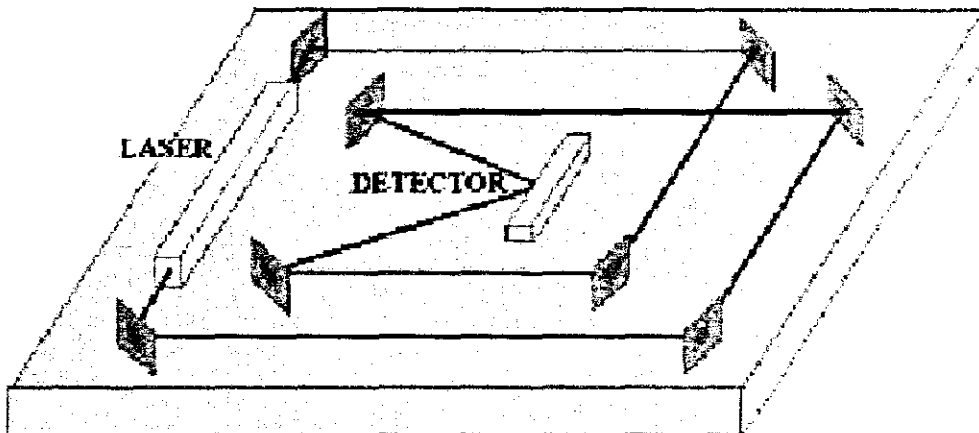
Figure 2.12: Scheme of MIG approach

The difference of the AFIT-MIG with respect to the standard Sagnac interferometer is that the previous one is not a circular but a spiral design. Its operation is based only on the total path length and not on the geometry of the path. Each part of the path is considered and the related time difference is determined. The sum of the different results is independent of the path geometry and it is converted to a phase difference.

The fundamental limit of detection associated with such a kind of device is due to photon shot noise, which is an uncertainty in the current generated at the detector, corresponding to the intensity of the interfering beams. This intensity is a function of the phase difference due to the rotation. The fundamental limit of detection is a measure of the minimum change in the detectable rotation rate. When the noise level is too high the interferometer will not be able to sense any rotation rate.

The detection limit is function of the path length of the interferometer: for a nine-leg interferometer the parameter is $0.0118rad/sec$ or $0.6761°/sec$. As the number of the optical legs increases, the detection limit decreases: it is reduces by a factor of almost 2 when the optical legs are doubled. This parameter value is useful for both military and civilian applications. Furthermore, the detection limit is also function of the quality of laser and detector used, and then high quality detector must be used to determine small rotation rate. For the above considerations small devices have difficulty achieving reasonable performance. Then, it should be used in civilian and military applications.

2.4 Micro-Electro-Mechanical-System (MEMS) gyros

Micro gyroscope is a device to detect rotation speed of objects using in navigation system or balanceable control as inertial sensors. The whole size of gyroscope system is under $10^{-1}m$ including micro sensor, modu- and demodulation transformer circuits, power supply interface, and output signal interface etc. sections. The basic theory used is similar with macro gyroscopes like capacitance, electrostatic, vibration, and thermal etc., the micro world has particular property. The MEMS fabrication technology is only way to make applications micromation suitable for micro projects such as micro robots, and vehicles etc. (Suzuki, Takiguchi, Hotate, 2000).

The micromachined gyroscopes use vibrating mechanical elements to sense rotation. They have no rotating parts that require bearings. They can be easily miniaturized and batch fabricated using micromachining techniques. The vibratory gyroscopes are based on the transfer of energy between two vibration modes of a structure caused by Coriolis acceleration, named after the French scientist and engineer G. G. de Coriolis (1792–1843), which is an apparent acceleration that arises in a rotating reference frame and is proportional to the rate of rotation. To understand the Coriolis Effect, set up a particle traveling in space with a velocity vector v. An observer sitting on the X-axis of the coordinate system, shown in figure 2.13, is watching this particle. If the coordinate system along with the observer starts rotating around the -axis with an angular velocity Ω, the observer thinks that the particle is changing its trajectory toward the X-axis with an acceleration equal to $2mv \times \Omega$. Although no real force has been exerted on the particle, to an observer, attached to the rotating reference frame an apparent force has resulted that is directly proportional to the rate of rotation. This effect is the basic operating principle underlying all micro vibratory structure gyroscopes (Tang, Gutierrez, Wilcox, Stell, Vorperian, Calvet, Li, Charkaborty, Bartman, Kaiser, 1996).
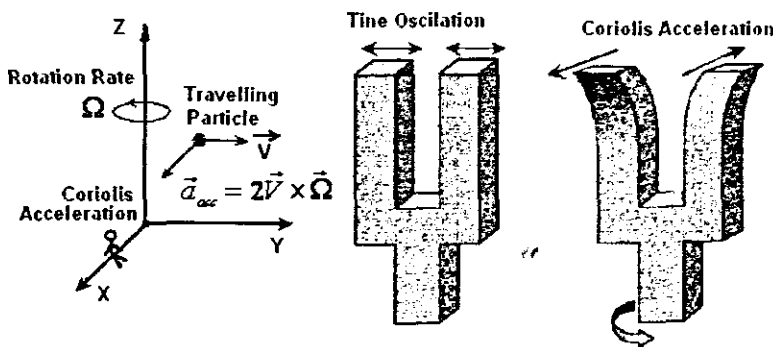
Figure 2.13: Tuning Fork Coriolis Force illustration

MEMS gyroscopes are fabricated by using the micromachining techniques in silicon or piezoelectric materials. In those gyroscopes a resonant primary excited mode contributes,

together with Coriolis acceleration produced by the rotation, to a secondary resonant mode which gives the measure of the rotation. The operating principle of vibrating gyros is the same for the different kinds of device. In particular, those gyros can be modeled by a two free directions mass-spring system as shown in figure 2.14.
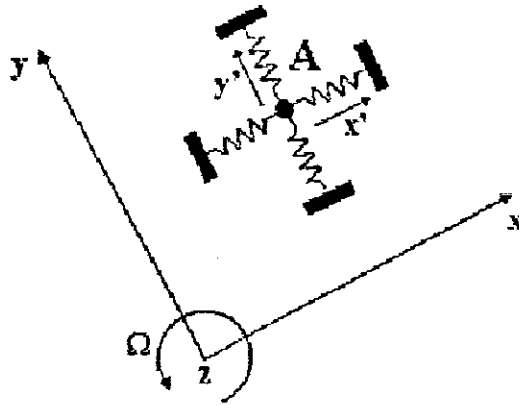
Figure 2-14: Mass-spring system—vibrating MEMS gyroscope operating principle

The elementary sensing unit is represented by a particle *A* and the spring represents the elasticity of the particle supporting structure. The particle has two degrees of freedom; at any time instant its movement is defined by the displacements x' along x-axis e y' along y-axis. A rotation of the plane *xy*, which is the reference frame, around an orthogonal z-axis is characterized by an angular rate. To measure it, a vibration of the particle along x-axis must be first induced; the vibration amplitude has to be constant. This oscillation is indicated as the primary motion of the gyroscope or drive mode. The vibration is produced by a feedback control system, which excites the particle at its resonant frequency while maintaining the vibration amplitude at a set value (Tang, Gutierrez, Wilcox, Stell, Vorperian, Calvet, Li, Charkaborty, Bartman, Kaiser, 1997).

When the gyroscope rotates, the particle experiences a Coriolis force, F_c, which has an amplitude proportional to the applied rotation rate . and its direction is, in the rotation frame, perpendicular to the primary motion direction:

$$F_c = 2m(\vec{\Omega} \times \vec{v})$$

(2.11)

where *m* is the vibrating mass and *v* is the velocity in the direction of the primary motion.

The Coriolis force will induce a particle vibration along the y-axis, indicated as the secondary motion of the gyroscope or sense mode. A measurement of its amplitude allows

estimating the angular velocity of the reference frame. The Coriolis acceleration is proportional to the primary motion, thus, the amplitude and the frequency of the drive oscillation have to be as large as possible. At the same time, it has to be ensured that the frequency and the amplitude remain constant; the amplitude control is accomplished by an automatic gain control loop while frequency stability is obtained by a phase locked loop.

The angular rate of the frame can be also measured by means of a closed-loop control over the secondary motion. The measurement is used to generate a control force able to annul the motion along y-axis; the control force magnitude represents the measure of the rotation rate.

2.4.1 MEMS Gyro Configurations

A large number of vibrating gyroscopes has been proposed whose configurations are rather complicated. They can be broadly classified with reference to the structure as follows: a) vibrating beams like prismatic, triangular; b) tuning forks including single, dual, multi-tine; c) vibrating shells like hemispherical, ring, cylinder; d) vibrating plates like linear disk, angular disk, linear plate.

Vibrating shells with hemispherical and cylinder configurations are macro-sized devices while vibrating beam, tuning fork, ring and plate gyroscopes are micro-sized devices manufactured from silicon or quartz.

An example of a simple oscillator is reported in figure 2.15. The sensing element is an equilateral prism, a flexural vibration is induced by piezoelectric or electrostatic elements placed at opposite sites of the prism. A periodic voltage applied to a piezoelectric actuator placed on the bottom face (A) of the beam induces a vibration along x-axis; this is the primary motion of the gyro.
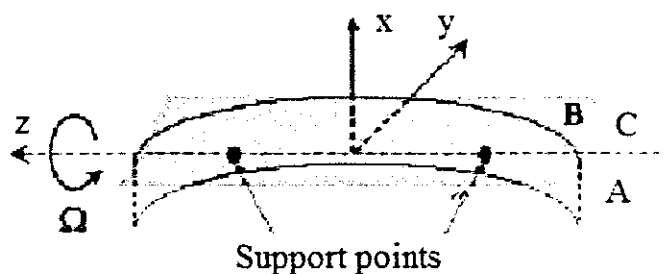
Figure 2-15: Beam gyroscope structure

When the device is rotated about the longitudinal axis z, Coriolis forces produce a secondary motion, which is a vibration along y-axis. Both primary and secondary vibration,

are detected by sensors placed on the two other faces (B and C) of the prism. The primary motion is sensed by summing the voltages from the two elements while the voltage contributions due to the secondary motion are opposite in phase, thus a difference is taken as measure of the angular rate. In this configuration the secondary motion is uncontrolled and its response could be sensitive to errors in cross-sectional structure, due to fabrication process, and to variable damping forces arising from the material and/or the adhesive bond (Ayazi, Najafi, 2001).

The basic structure of a tuning fork vibratory gyroscope in double configuration is illustrated in figure 2.16.
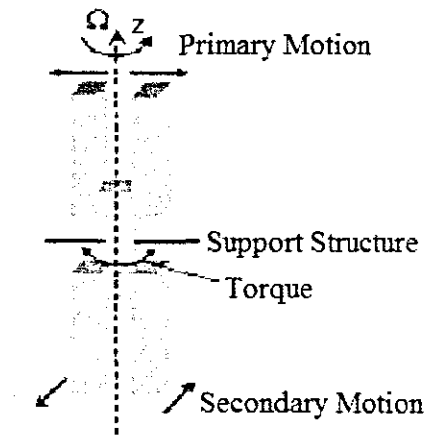
Figure 2.16: Basic structure of a tuning fork vibratory gyroscope in double configuration

The tuning fork consists of two tines that are connected together via a central block attached to a supporting structure. The two upper tines are subjected to a vibration of fixed amplitude in the plane of the device. This represents the primary motion of the gyroscope. The tines vibrate in antiphase condition so that no force results on the supporting structure from the primary motion. The actuation mechanisms used to induce primary vibration can be electrostatic, piezoresistive or piezoelectric; actuators are placed on the sides of the two tines. When the device is rotated about an axis parallel to the centr al axis of the fork, the primary motion generates two opposite Coriolis forces that will be able to torque the central block. In turn, the two -bottom tines experience a vibration, one opposite to the other, that is perpendicular to the direction of the primary vibration.

To detect the Coriolis-induced vibration (secondary motion), capacitive, piezoresistive or piezoelectric detection mechanisms can be used. The voltage detected by the sensors is taken as a measure of the applied rotation rate. The main adva ntages of a tuning fork are the stable centre of gravity and the compensation of all forces and moments of inertia in the chip (Geiger, Folkmer, Merz, Sandmaier, Lang, 1998).

Since the turning fork theory has simple structures, easy understanding, suitable for MEMS fabrication processes, this operation principle is widely applied in MEMS gyro systems. The SEM picture of MEMS dual mass vibration structure shows in figure 2.17 (Przekwas, Turowski, Furmanczyk, Heike, and Pryputniewicz, 2001).
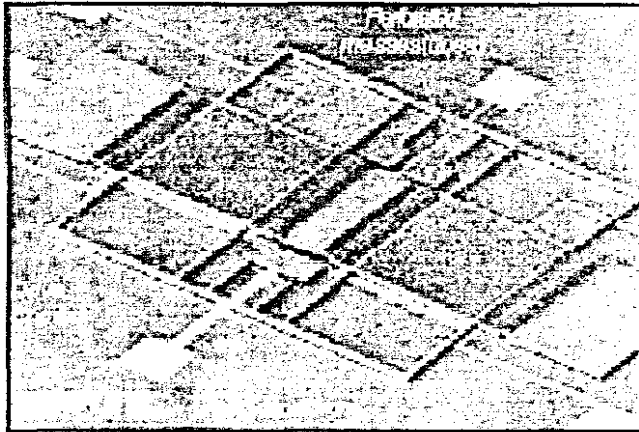
Figure 2.17: SEM view of Draper's single-crystal silicon-on-glass tuning-fork gyroscope

A shell resonator gyroscope is based on the concept that the nodes on the circumference of a vibrating cylinder ring do not stay fixed with respect to the cylinder itself when it is rotated around its central axis, but they move by a quantity proportional to the turn, as sketched in figure 2.18. This is due to the Coriolis coupling between the two vibration modes that change as cos2 . primary and sen2 . secondary around the circumference.
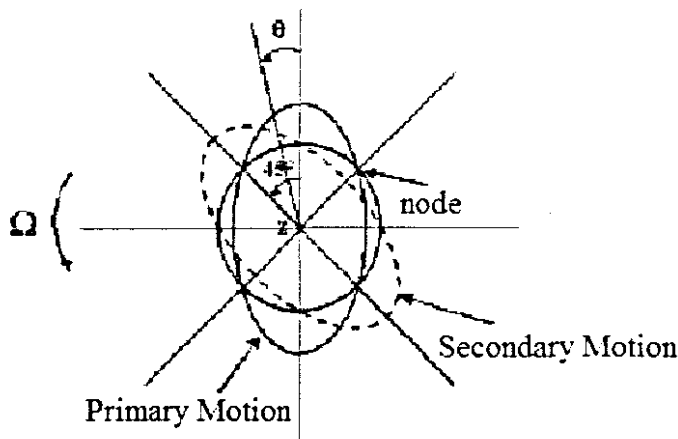
Figure 2.18: Cylinder Gyroscope Operating Principle

A certain number of electrodes are located around the circumference with the aim to excite and detect both the primary and secondary vibration modes. As an example, in figure 2.19 is illustrated a structure using eight electrodes: the pairs (1,5) and (3,7) control the primary mode while (4,8) and (2,6) detect the secondary mode. If there is no rotation the electrodes

(4,8) and (2,6) check the position of nodes and there is no output. When the cylinder rotates the nodes move due to the secondary mode and the electrodes (4,8) give an output voltage.
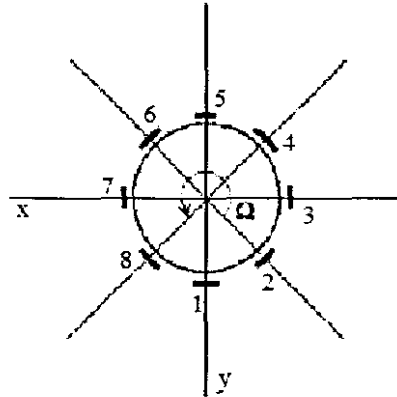
Figure 2.19: Vibrating Cylinder Gyroscope Structure Using Eight Electrodes

The value of the output signal is used as feedback signal to the electrodes (2,6) which apply the electrical voltages to control the node position; when the output from electrodes (4,8) is zero, the voltage applied to the electrodes (2,6) is assumed as measure of the rate (Hopkin, 1997).

An example of vibratory plate's gyroscope is illustrated in figure 2.20.
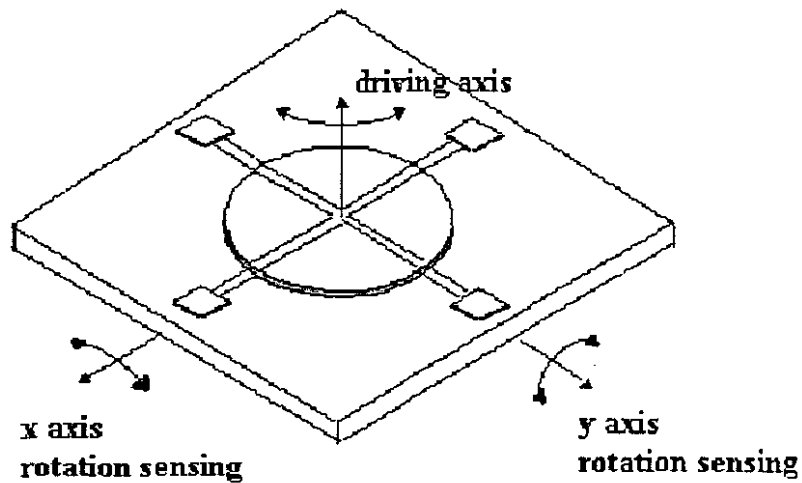
Figure 2.20: Vibrating Angular Disk Gyro Structure

It is based on an angular resonance of a rigid polysilicon rotor suspended by four torsional springs anchored to the substrate. The inertial rotor is driven at angular resonance about the z-axis perpendicular to the substrate using electrostatic comb drive. A rotation rate around the x-axis induces a Coriolis angular oscillation around the y-axis and likewise a rotation rate around the y-axis induces a Coriolis angular oscillation around the x-axis. This Coriolis oscillation is usually measured using the change in capacitance between the rotor and four "quarter circle" electrodes beneath the inertial rotor. Dual axes operation can be achieved by

using a different voltage modulation frequency for each pair of diametrically placed electrodes. In this way, a rotation of the rotor in the sense axis of these electrodes generates a voltage on an integrator electrically connected to the rotor. Separate demodulation circuitry for each sense axis provides two voltage outputs proportional to angular rate inputs about respective axes (Lutz, Golderer, Gerstenmeier, Marek, Maihofer, Mahler, Munzel and Bischof, 1997).

Micromachined gyroscopes had experienced a large development because their batch processing is highly compatible with silicon IC fabrication technology. Both bulk etching of single crystal silicon and polysilicon surface micro-machining put some conditions on the geometrical structure of the device. The configuration has also to guarantee dynamic balance, decoupling and tuning of primary and secondary motions. Several devices both in silicon and piezoelectric material have been reported; they differ in structure, control and sensing. Some examples are here reported.

A bulk-micromachined, silicon MEMS vibratory gyroscope for space applications, such as altitude and maneuver control, inertial navigation system and instrumentation, has been reported. The gyroscope has a scale factor of 24mVs°, a bias stability of 70°/h and an angle random walk of 6.3h°. A surface-micromachined x-axis vibratory gyroscope was proposed in recent years. The sensor element is an inner wheel while the outer rectangular structure is the secondary oscillator; the device is driven by comb actuators. The gyroscope realizes the decoupling of driving and sensing mechanisms. The main performance are: resolution of 0.005°/s, angle random walk of 0.27h°, bandwidth of 50Hz, sensitivity of 10mV/(°/s). A vibrating ring gyroscope, fabricated through the high aspect ratio combined poly and single-crystal MEMS technology, has been fabricated. The operating principle is the same one described for vibrating cylinder gyroscope. The gyroscope demonstrated a resolution of 0.5°/s in a 25Hz bandwidth limited by the electronic noise and a zero bias drift less than 10°/s over the temperature range -40 to 85°C. By using a high aspect–ratio fabrication process a new tactical-grade device with a projected random walk as small as 0.05°h, an open-loop sensitivity of 200μV/°/s in a dynamic range of ±250°/s was also proposed. A micromachined single-crystalline silicon ring gyroscope with resolution of 0.005°/s, bandwidth of 70Hz and noise floor less than 0.5°/s in 65 Hz bandwidth has béen also reported. Main applications are terrestrial navigation and GPS dead-reckoning. An example of high performance vibrating shell gyro, which has found applications in spacecraft inertial reference units (IRUs), and in commercial aviation is the hemispherical resonator gyro (HRG) The gyroscope has shown a bias of 1°/hr, a random walk of 0.01°/hr and a scale factor ranging in 50-100ppm and could be applied in space INS for future missions. A commercial device in quartz by Litton is also available claiming a bias stability of 0.003°/hr (Putty, Najafi, 1994).

A vibrating quartz gyro in double tuning fork configuration is reported. The same technology is used for the gyro used in an Inertial Measurement Unit also in production. For this device a resolution less than 0.002°/s in a bandwidth of 60Hz and temperature range of 40 to 80°C is reported. The full range is ±100°/s and the output noise is 0.01°sHz. This gyroscope finds application in automotive, commercial aircraft, helicopter, marine systems, tactical missiles, and military aircraft. Further possible applications are onboard of spacecraft for antenna stabilization, flight event initiation, and instrumentation, maneuvering system, spin monitoring, stability and control (Core, Tsang, and Sherman, 1993).

As it was already explained, vibratory gyroscopes can work in open or closed loop mode to measure the angular velocity. If there is a change in the rotation rate, the amplitude of the sense mode doesn't change instantaneously but it required some time to reach the steady state. With matched sense and drive resonant modes, the time response, approximately equal to $2Q/\omega$, where Q is the mechanical quality factor, limits the bandwidth of the sensor to a few hertz. The bandwidth of gyroscope operating in an open-loop mode can be increased with a slight mismatch in the sense and drive mode resonant frequencies but, at the same time, this reduces the sensitivity. In the closed-loop-operating mode, the amplitude of sense mode is continuously monitored and set to zero; this means that the bandwidth and the dynamic range of the sensor can be greater than the corresponding open-loop values even with matched resonant modes. The bandwidth is then limited by the readout and control electronics and can be increased to values approaching the resonant frequency of the structure.

For a gyroscope rotating around z-axis and driven in the x direction, sensitivity can be expressed by:

$$\Delta y = 2\Omega \frac{F_e}{m\omega_x} \frac{1}{\sqrt{\left(\frac{\omega_y}{Q_y}\right)^2 \omega_x^2 + (\omega_x^2 - \omega_y^2)^2}} \tag{2.12}$$

where Δy is the displacement due to the Coriolis acceleration, Fe is the driving force, m the inertial mass, Q_x, Q_y, ω_x and ω_y the mechanical quality factor and the resonant frequency in the driving and the sensing mode, respectively.

The gyroscope resolution depends on different parameters. In open loop mode with matched sense and drive resonant modes, the resolution can be improved by reducing the noise of the readout circuit, increasing the Coriolis-induced capacitance change of the device, lowering the resonant frequency, increasing the mechanical quality factor and

minimizing the parasitic capacitances. Even if a lower resonant frequency of the structure can improve the sensitivity, it must be greater than the environmental noise (>2kHz) to get better signal. Stronger Coriolis forces will be obtained by increasing the amplitude of vibration in the drive mode. If the proof mass oscillates in vacuum, very high quality factor can be obtained. Q can be strongly increased by significantly reducing energy losses and it can be got if the resonant structure operates in vacuum. This requires hermetically sealed, robust vacuum-packaging techniques, such us those using silicon or glass wafers bonded to the sensor substrate.

Furthermore, if the resonant frequencies of drive and sense modes are matched, Q amplifies the coupling and the resolution is then increased. The difficulty is to design the device in a way such as the two resonance frequencies are perfectly matched (better than 1Hz) over the temperature range and other environmental factors. The tolerances in the fabrication process are very high to control; thus normally an active tuning is used.

An important performance parameter for a vibratory gyroscope is its zero rate output (ZRO) (or zero bias). Imperfections in the geometry of the vibrating mechanical structure, in the electrodes that control the sense and drive modes or in the electrical coupling between these electrodes, asymmetric damping of the structure can produce an output signal even in the absence of rotation. This error, called the quadrature error, can be sometime orders of magnitude larger than Coriolis signal, and, of course, it may cause errors in sensing the rotation rate. ZRO can be significantly reduced by electrically and mechanically decoupling the sense and drive modes and by reducing the fabrication process errors. Moreover, high-quality materials with low internal damping will also reduces the ZRO and, in any case, any residual zero bias error should then be further reduced electronically.

A high-performance gyroscope should have an accurate scale factor, with small temperature sensitivity, on a wide dynamic range, about 140dB. To obtain good results a particular attention has to be paid to the materials, which form the structure. Using several materials in the same structure can cause changes of scale factor with the temperature; best performance can be obtained in all-silicon devices. Temperature changes can induce variation of the resonant frequency and this can, in turn, affect the scale factor; some compensation in temperature of the scale factor could be required. Another concern about a vibrating mechanical element is the long-term drift and fatigues problem, then the reliability of the device. Low-noise electronics for readout, processing and control is necessary for operation both in open and closed loop mode. Monolithic integration of the sensor and the readout electronics reduces the parasitic effects and improves the resolution of the sensor.

From the preview categories of the gyroscope systems, two majority different methods involved, which are Sagnac Effect for all optical type gyroscope systems and Coriolis Effect for all MEMS vibration structures type gyroscope systems, have been introduced. The main obstacles of two current theories are large size, heavy weight, and high cost for optical gyroscopes; the low sensitivity and small measurement range for MEMS vibratory gyroscopes. Currently, it is important to improve the performance of the existing micro gyroscopes by MEMS technology and develop the new type micro gyroscope systems, which could be hybrid system coming from combination optical interferometer and MEMS vibratory gyroscope system (Norgia, Donati, 2001).

2.5 Future Trends and Conclusions

The current major obstacle to a larger use of inertial navigation system (INS) is the system stability and high cost. High performance sensors are required to improve INS technology, together with advances in computer technology (memory and throughput), power quality, and electronics.

The main issue for active ring resonator gyros is the reduction of the lock-in effect that requires design and technology efforts such as the reduction of backscattering centers inside the active structure, together with a strong reduction of size for integrated solution. Good perspectives appear for performance of passive ring resonator gyros: the use of silicon technology will allow reducing optical losses, then quantum limit, and radius, then size. For high performance space applications, reduction of power, size and weight, by improving the integration of optical functions external to the fiber loop, and drift stability, by using closed-loop configurations with integrated phase modulation block are required to IFOGs.

Continuous improvement of the performance is required for MEMS gyros. This means a particular care in material uniformity, mixed micromachining fabrication processes on silicon and deep etching techniques allowing high quality factor of the structures, robust vacuum packaging techniques and tuning in frequency to compensate sensor drifts and long-term effects. Low-noise and low-drift interface electronic circuitry is also required. A strong integration effort will allow implementing devices for inertial platforms, fabricating multiaxis devices on a single chip together with accelerometers and electronics. Further issues are cost and reliability.

At near term, MEMS and improved fiber optic technology are expected to replace RLGs and mechanical devices while RLGs are superior over IFOGs when high scale factor stability

is required. Mechanical gyros and accelerometers are still expected to be used in guidance systems. IFOGs and MEMS/MOEMS are used for guiding re-entry bodies.

At far term, MEMS and integrated optics gyros will dominate the low and medium performance range due to orders of magnitude in performance improvement, design improvement and higher level of integration. Integrated optics gyros are expected to be used when navigation grade is required since MEMS show some restrictions. Moreover, integrated optics gyros would be no "*g*" sensitive devices. IFOGs should become dominant for strategic application. However, the optical gyroscope applications are limited by heavy weight and huge size because of the long fiber optical light paths. There is lack on MEMS fabrication processes of the micro fiber optical. So the new measurement approach or novel sensing structures need to find for micro gyroscopes, which is main purpose of this doctoral research. In this thesis, the novel micro gyroscope system would be proposed based on the operating principles and successful experiments of the MEMS gyroscopes and optical gyroscopes (Armenise, Ciminelli, De Leonardis, Diana, Passaro, Peluso, 2001).

In next chapter 3, the optical sensing technology will be introduced, which is highest interesting sensing research areas and the optical interferometer will act main role in the novel micro gyroscope system.

CHAPTER THREE
INTRODUCTION TO FIBRE OPTIC SENSORS RELEVANT TO GYROSCOPE DEVELOPMENT

In last chapter, the various types of gyroscopes have been introduced including mechanical wheels, Sagnac Effect gyro, and MEMS gyro. It is clear found the gyroscope devices develop ward to micro scale to fit in micro applications. The MEMS gyro system has extremely small size, but the performances need evaluation. Similarly, the optical gyro systems show perfect capability for angular rate sensing, but the devices are not in micro scales.

The optical sensing technology has been proved and used for the highest performance sensing devices, especially for micro displacement measurement like SEM (Scanning Electro Microscope) etc. It was thought that combine the optical sensing methods MEMS gyro system could achieve the best volume-performance ratio.

In this chapter optical sensing technologies are introduced to give basic background and understanding of optical displacement measurements, which could be used to improve current micro gyroscope systems.

3.1 Phase-Modulated Optical Sensors: Interferometeric Fiber Optic Sensors

Phase-modulated optical fiber sensors are usually associated with interferometers because the optical phase of light wave or the phase difference between two light waves is usually detected by means of interferometric techniques. They usually employ coherent light sources and can precisely detect the phase shift caused by the environment parameters of interest. There are mainly four configurations of interferometric optical fiber sensors: the Michelson, the Mach-Zehnder, the Fabry-Perot, and the Sagnac.

One of the areas of greatest interest has been in the development of high performance interferometeric fiber optic sensors. Substantial efforts have been undertaken on Sagnac interferometers, ring resonators, Mach-Zehnder, Michelson interferometers, and Fabry-Perot Interferometer as well as dual mode, polarimetric, grating and etalon based interferometers. In this section, the Sagnac, Mach-Zehnder, Michelson interferometers and Fabry-Perot Interferometer are briefly reviewed.

3.1.1 The Sagnac Interferometer

The Sagnac effect is the relative phase shift between two beams of light that have traveled an identical path in opposite direction in a rotating frame. The explanation of the Sagnac effect is simple for the inertial frame of reference. The motions of the mirrors during the light transit time between mirrors causes the clockwise and counter-clockwise waves to be reflected at different points of space, which leads to an optical path difference. Modern fiber-optic gyroscopes (Sagnac interferometers) used for navigation are based on this effect. They allow highly accurate measurements of rotation rates down to about $0.1°$ per hour. The schematic setup of a Sagnac interferometer is shown in figure 3-1. Light is decomposed into two beams by a 50:50 beam splitter, with one traveling clockwise (CW) and the other counter-clockwise (CCW) around a polarization-maintaining single-mode glass-fiber loop. The two beams interfere after passage through the loop, and the interference signal is measured with a photodiode. If only reciprocal effects are involved in the experiment, then the two beams interfere constructively (relative phase shift $\Delta\phi = 0$). If $\Delta\phi \neq 0$, then non-reciprocal effects occur, one of them being the Sagnac effect that results from rotation of the fiber loop during the measurement. The Sagnac effect is a relativistic effect but can be understood with a simple picture (see Fig. 3.1): Let us assume that a fiber coil (N windings with radius R) is rotated clockwise with a angular velocity and that light is injected into the loop at time t=0. At $t \approx \dfrac{2\pi R N}{c}$, the CW and CCW beams meet again at the starting point. However, due to the rotation of the loop, they have traveled different path lengths (Lefevre, 1993).
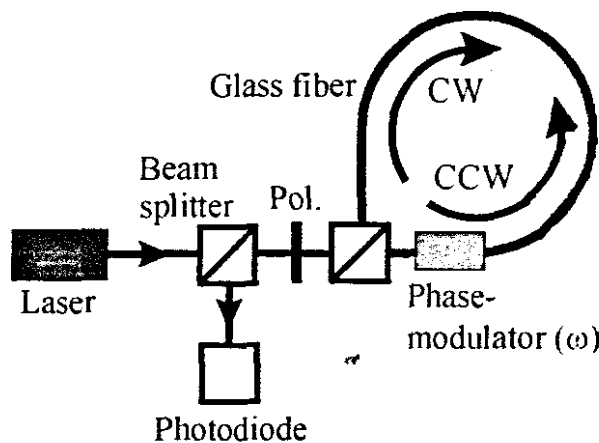
(a)
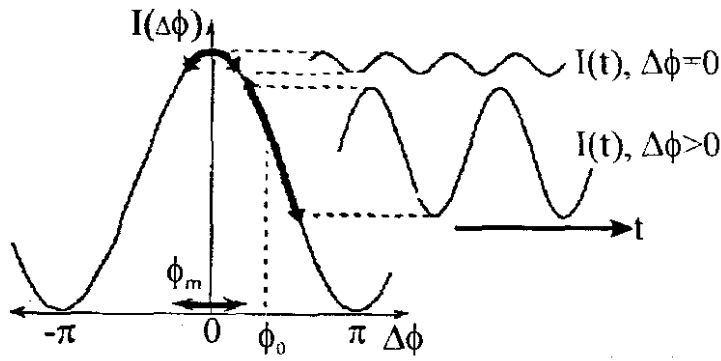
(b)

Figure 3.1: (a) Schematic setup of a Sagnac interferometer and its modification for magneto-optical measurements in transmission (Faraday Effect) or reflection (Kerr effect), respectively. (b) Intensity versus relative phase shift between CW and CCW beams, $\Delta\phi$ and time-dependent signals for phase modulation
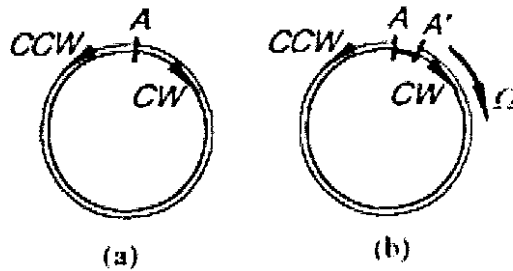
Figure 3.2: The Sagnac effect Principle Diagram

The figure 3.2 on the right indicates what happens if the loop itself is rotating during this procedure. Supposing that radius of fiber round is R, and light emitting and detector sensors are fixed in 'A' point. The system is rotating with Ω in the clockwise direction relatively inertia space. When clockwise direction light (CW) and the counter-clockwise direction light (CCW) are emitted in opposite direction around, the photo sensor also rotates from 'A' to 'A'. So the two light paths are different length. The clockwise direction light pursues 'A' after back, which crosses the distance more than $2\pi R$. While the counter-clockwise direction light goes face to 'A', which crosses the distance less than $2\pi R$. The difference between the travel times causes the difference light distance (Burns, 1994).

Assume light transmitting in vacuum, which velocity is c. The paths of clockwise and counter-clockwise light are L_{CW}, L_{CCW}, spending time is t_{CW}, t_{CCW} individual.

48

$$C = C_{cw} = C_{ccw} \tag{3.1}$$

$$L_{cw} = 2\pi R + R\Omega t_{cw} = C_{cw} t_{cw} \tag{3.2}$$

$$L_{ccw} = 2\pi R - R\Omega t_{ccw} = C_{ccw} t_{ccw} \qquad \ldots\ldots\ldots\ldots \tag{3.3}$$

From equation (3.1), Δt is expressed,

$$
\begin{aligned}
\Delta t = t_{cw} - t_{ccw} &= 2\pi R \frac{2\pi\Omega - (C_{cw} - C_{ccw})}{C_{cw} \cdot C_{ccw}} \\
&= 2\pi R \frac{2\pi R\Omega}{C^2} = 4A\Omega\!\Big/\!C^2
\end{aligned}
\tag{3.4}
$$

Where A is area of fiber coil round.

Accounting, it is only approximately and simple evolvement above result in the equation (3.4). The strict evolvement should be applied in broad theory of relativity. The light transmitted in fiber optical, its speed is relation with refractive index of medium.

So, clockwise and counter-clockwise light is:

$$C_{cw} = \frac{\dfrac{c}{n} + R\Omega}{1 + \dfrac{\dfrac{c}{n} \cdot R\Omega}{c^2}} = \frac{\dfrac{c}{n} + R\Omega}{1 + \dfrac{R\Omega}{cn}} \tag{3.5}$$

$$C_{ccw} = \frac{\dfrac{c}{n} - R\Omega}{1 - \dfrac{\dfrac{c}{n} \cdot R\Omega}{c^2}} = \frac{\dfrac{c}{n} - R\Omega}{1 - \dfrac{R\Omega}{cn}} \tag{3.6}$$

where n is refractive index of medium. From equation (3.4), (3.5-6), the Δt is given by

$$\Delta t = t_{cw} - t_{ccw} = 2\pi R \frac{2\pi\Omega - (C_{cw} - C_{ccw})}{C_{cw} \cdot C_{ccw}} \approx 2\pi R \frac{2R\Omega - 2R\Omega(1 - \frac{1}{n^2})}{\frac{c^2}{n^2}}$$

$$= 2\pi R \frac{2\pi R\Omega}{C^2} = 4A\Omega/C^2 \tag{3.7}$$

The equation (3.7) is same as equation (3.4) in the vacuum. Corresponding phase difference is:

$$\Delta\phi = 2\pi\Delta t c/\lambda = 8\pi A\Omega/\lambda c \tag{3.8}$$

The difference in path length can be expressed as:

$$\Delta L = 2R\Omega t = \frac{4\pi R^2 N}{c}\Omega \tag{3.9}$$

and the corresponding phase difference between the two beams is:

$$\Delta\phi = \frac{8\pi^2 R^2 N}{\lambda c}\Omega \tag{3.10}$$

It is interesting to note that although the above calculation is over-simplified (e.g., the speed of light in vacuum, c, was assumed instead of that in the glass fiber) it yields the correct result. Exact relativistic calculations show that the phase shift is indeed independent of the material of the wave guide and the above equations apply.

The interferometer output intensity is given by,

$$I = I_0(\frac{1}{2}e^{\frac{\Delta\phi}{2}} + \frac{1}{2}e^{-\frac{\Delta\phi}{2}})^2 = I_0\cos^2\Delta\phi = \frac{1}{2}I_0(1 + \cos\Delta\phi) \tag{3.11}$$
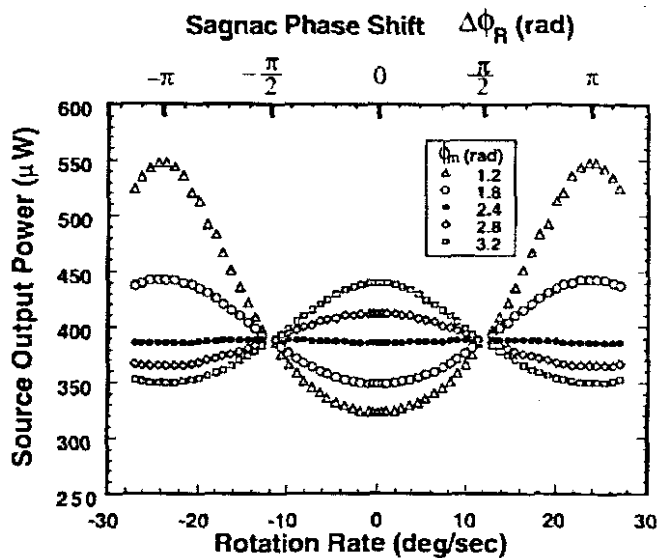
Figure 3.3: Source output power versus rotation rate for various modulation amplitude

Sagnac effect is the basic principle for all kinds of optic gyroscopes. The fiber optic gyroscope is solid state in that it has no mechanical moving parts and does not require mechanical dithering, as most ring laser gyros do. The long light path required in optic gyroscopes is essential lack. Currently, there are not good proposals about manufacture micro fiber optical method.

In the fiber optic gyroscope, the Sagnac effect execute the converter, which transform the angular rate of objects to phase shift changing, then interferometer read-out system can give the precision results about the phase shifts responding to power measurements as shown in figure 3.3. Finally, substituting the phase shift changing is back to angular velocity. The principle of Sagnac effect is directly linking the angular rate with the phase shift. The long interference light path can not be avoided and ignored by the sensitivity required (Smith, 1989).

3.1.2 Mach-Zehnder Interferometer

Interferometers are perhaps even more widely used in integrated optical circuits, in the form of a Mach-Zehnder interferometer, in which light interferes between two branches of a waveguide that are (typically) externally modulated to vary their relative phase. This interferometer's configuration consists of two beam splitters and two completely reflective mirrors. The source beam is split and the two resulting waves travel down separate paths. A slight tilt of one of the beam splitters will result in a path difference and a change in the interference pattern. The Mach-Zehnder interferometer can be very difficult to align, however

51

this sensitivity adds to its diverse number of applications. The Mach-Zehnder interferometer can be the basis of a wide variety of devices, from RF modulators to sensors to optical switches.

The Mach-Zehnder configuration (Figure 3.4) is an intrinsic sensor based on the interference between a sensing and a reference wave. The two beam interferometer uses a laser diode as the source of coherent light which is coupled into a single mode fiber. The light is then split equally into two fibers by a 3 dB coupler. One leg of the Mach-Zehnder interferometer is the sensing leg while the other is the reference. The reference fiber is kept protected from the desired perturbation to be measured and light passes through this leg normally. The sensing fiber is used to monitor the perturbation. Two complementary outputs are available for signal processing (Dandridge, 1991).
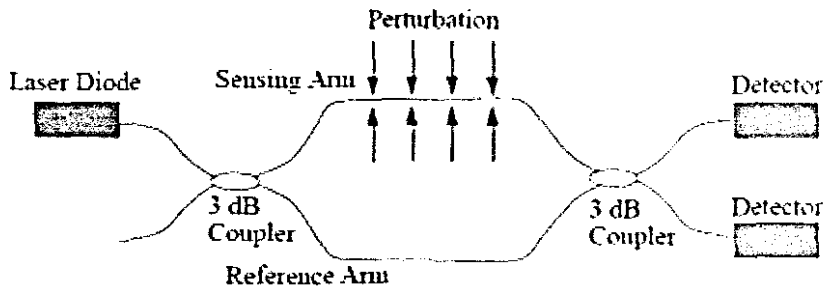
Figure 3.4: Mach-Zehnder Interferometer

The electric fields of the two light waves can be expressed as

$$E_r = E_0 e^{i\omega_0 t} \text{ and } E_2 = E_0 e^{i(\omega_0 t + \Delta\phi)} \tag{3.12}$$

where E_r is the reference wave, E_s is the sensing wave, and $\Delta\phi$ is the phase difference induced by the sensing fiber. At the photodetector, the intensity is given by

$$I_{out} = \langle E_r^2 \rangle + \langle E_s^2 \rangle + 2\langle E_r E_s \rangle \tag{3.13}$$

where $\langle \ \rangle$ represents the time integration performed by the photodetector. This Equation reduces to

$$I_{out} = I_0 (1 + \cos \Delta\phi) \tag{3.14}$$

where $I_0 \propto E_0^2$ and we have assumed the ideal conditions of equal splitting ratios, no coherence or polarization effects, and no losses.

The information is contained in the phase difference between the two waves. The phase corresponding to a length of fiber L is given by

$$\phi = kn_e L \tag{3.15}$$

where $k = 2\pi / \lambda$ is the propogation constant in air, λ is the laser diode emitting wavelength, and n_e is the fiber's effective refractive index. If the desired measurand is X, then the change in ϕ may be represented by

$$\Delta\phi = kL\frac{dn_1}{dX}\Delta X + kn_1\frac{dL}{dX}\Delta X \tag{3.16}$$

If the coefficients $\dfrac{dn_1}{dX}$ and $\dfrac{dL}{dX}$ for the sensing fiber are known, ΔX can be found from the output signal, expressed by Equation (3-16).

In this configuration, quantities such as strain, force, pressure, and temperature can be measured directly. Other quantities such as magnetic field, acoustic pressure, electric field, and current can be measured indirectly by attaching the sensing fiber to materials that respond to these parameters.

The output of the sensor, Equation (3.14), is sinusoidal and is shown in figure 3.5. The signal goes through one period for every 2π shifts in $\Delta\phi$. This period is referred to as one fringe. The sensor has maximum sensitivity at the quadrature (Q) point.
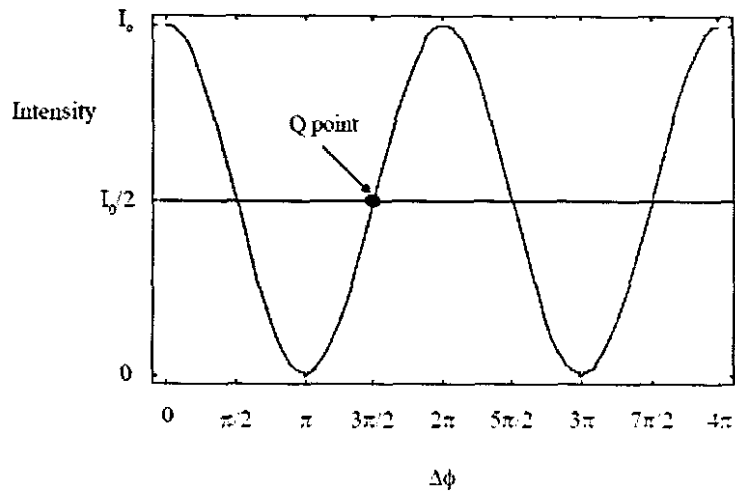
Figure 3.5: Mach-Zehnder Intensity Output

Figure 3.5 illustrates a number of difficulties for this sensing scheme:

a) The signal must be maintained around the Q point in order to avoid loss of sensitivity.

b) If the sign of $\Delta\phi$ changes at a maximum or minimum of the fringe, there is no way of knowing this occurred. Therefore, the sensor also experiences phase ambiguity under these conditions.

c) Because the signal is composed of the phase difference between the sensing and reference arms, no absolute information is available. Upon powering up the system, the initial condition of X, the measurand, cannot be deduced from the signal. The system can only track ΔX.

d) Any wavelength instability in the source will cause a change in the phase because of the k term in Equation (3.16).

These difficulties are characteristics of all interferometric type sensing schemes. Various signal demodulation methods have been developed to overcome some of the these drawbacks of the sensor including active and passive homodyne, differentiate cross multiplication, synthetic heterodyne, and true heterodyne (Wilson and Hawkes, 1989).

3.1.3 Michelson Interferometers

A very common example of an interferometer is the Michelson or Michelson-Morley type. Here the basic building blocks are a monochromatic source emitting light or matter waves, a

detector, two mirrors and one semitransparent mirror often called beam splitter. These are put together as shown in the figure 3.6, and the interference pattern shows in figure 3.7.
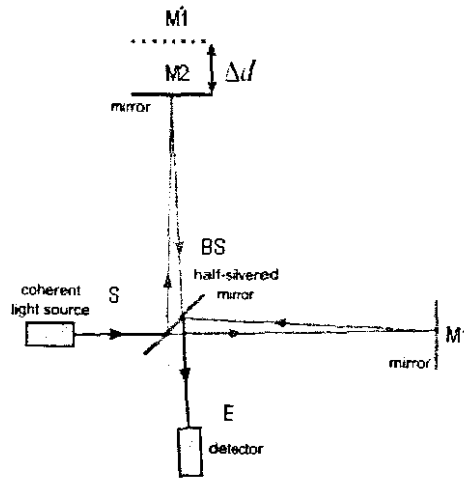
Figure 3.6: Michelson interferometer Typical Configuration
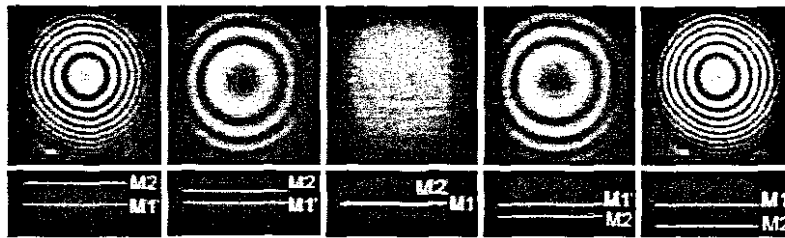
Figure 3.7: Output Intensity Relating with the different Path Length

There are two paths from the (light) source to the detector. One reflects off the semi-transparent mirror, goes to the top mirror and then reflects back, goes through the semi-transparent mirror, to the detector. The other first goes through the semi-transparent mirror, to the mirror on the right, reflects back to the semi-transparent mirror, then reflects from the semi-transparent mirror into the detector (Kersey, 1991).

If these two paths differ by a whole number (including 0) of wavelengths, there is constructive interference and a strong signal at the detector. If they differ by a whole number and half wavelengths (e.g., 0.5, 1.5, 2.5 ...) there is destructive interference and a weak signal. The output intensity shows in figure 7 with different path length. This might appear at first sight to violate conservation of energy. However energy is conserved, because there is a re-distribution of energy at the detector in which the energy at the destructive sites is re-distributed to the constructive sites. The effect of the interference is to alter the share of the reflected light which heads for the detector and the remainder which heads back in the direction of the source (Bock, Urbanczyk, Wojcik, Beaulieu, 1995).

In the basic Michelson interferometer (Figure 3-6) the light from a source, S, is divided by a 50% beam splitter oriented at 45 degrees to the beam. The transmitted beam travels to mirror M1 where it is back reflected to BS. 50% of the returning beam is deflected by 90 degrees at BS and it then strikes the screen, E (the other 50% is transmitted back towards the laser and is of no further interest here). The reflected beam travels to mirror M2 where it is reflected. Again, 50% of it then passes straight through BS and reaches the screen (the remaining 50% is reflected towards the laser and is again of no further interest here). The two beams that are directed towards the screen, E, interfere to produce fringes on the screen.

Suppose that mirror M1 is moveable. The optical path difference is $2\Delta d$ between the rays reflected from M1' and M2. A point on the screen E will be bright if $2\Delta d = n\lambda$, and dark if $2\Delta d = (n + \frac{1}{2})\lambda$. If the two mirrors are precisely parallel, then the whole illuminated area of the screen will be uniformly lit (Bhatia, 1993).

$$I_{out} = I_1 + I_2 + 2\sqrt{I_1 I_2} \cos(\frac{4\pi\Delta d}{\lambda})$$ (3.17)

Here I_{out} is the output intensity of the interferometer. I_1 and I_2 are the intensity reflected from M1 and M2.

From the intensity changing rule, which is the every time Δd changing $\frac{\lambda}{4}$, the intensity changing once from bright to dark, if the bright or dark appears N times during the M1 moving. The M1 moving distance can be calculated by,

$$D = N\frac{\lambda}{4}$$ (3.18)

The interferometer was used in the famous Michelson-Morley experiment that provided evidence for special relativity. In Michelson's day, the interference pattern was obtained by using a gas discharge lamp, a filter, and a thin slot or pinhole. In one version of the Michelson-Morley experiment, they even ran the interferometer off starlight. Starlight is temporally incoherent light, but since for small instruments it can be considered as a point source of light it is spatially coherent and will produce an interference pattern. The Michelson interferometer finds use not only in these experiments but also for other purposes.

3.1.4 Fabry-Perot Interferometer

Fabry-Perot Interferometer (FPI) interferometer makes use of multiple reflections between two closely spaced partially silvered surfaces. Part of the light is transmitted each time the light reaches the second surface, resulting in multiple offset beams which can interfere with each other. The large number of interfering rays produces an interferometer with extremely high resolution, somewhat like the multiple slits of a diffraction grating increase its resolution.

A Fabry-Perot (FP) interferometer contains a pair of partial mirrors. The multi-path reflected lights in the FP cavity interfere with one another. FP sensors can work at either transmissive mode or reflective mode, as shown in Figure 3.8. When the reflections at mirrors are high, a FP interferometer usually works in transmissive mode as shown in Figure 3.8(a), in which the FP cavity functions as an optical filter. When the reflections at mirrors are low, a FP interferometer usually works in reflection mode as shown in 3.8(b), in which the FP interferometer can be regarded as a two-beam interferometer with all the multi-path reflections neglected (Santos, Leite, and Jackson, 1992).
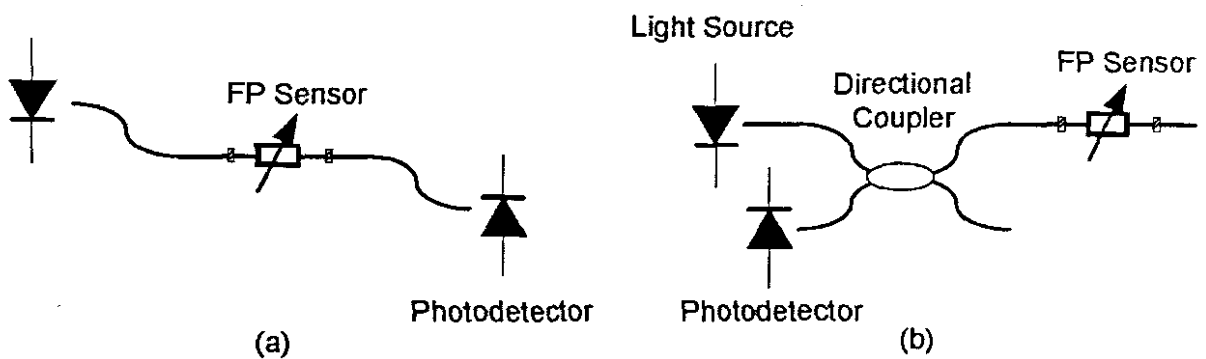
Figure 3.8: Fabry-Perot Sensor (a) Tran missive mode. (b) Reflective Mode

There are two main categories of fiber Fabry-Perot (FP) interferometric sensors, namely intrinsic FP interferometers (IFPI) and extrinsic FP interferometers (EFPI) respectively. Basic structures of these two kinds of FP interferometers are shown in figure 3.9(a) and figure 3.9(b), respectively.

An IFPI sensor contains two internal partial reflection mirrors. The fiber between the reflectors serves as both a sensing element and a light waveguide. A typical IFPI sensor is shown in Figure 3.9(a). An EFPI sensor contains a lead-in fiber with a partial mirror at the end-face, a cavity of air or other transparent medium and a reflector on the other end which may also be a piece of fiber. A typical EFPI sensor is shown is Figure 3.9(b). IFPI sensors usually have lower power loss than EFPI sensors and are more preferred in dense multiplexing applications.
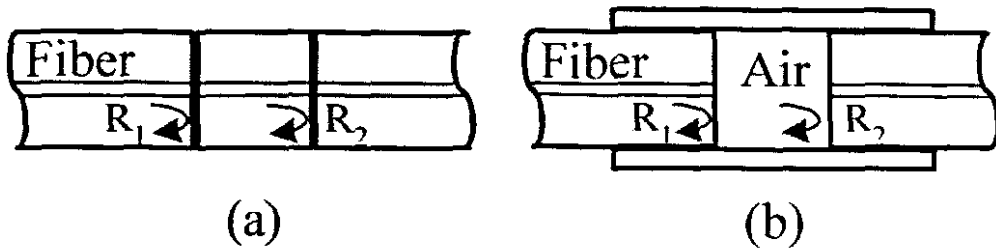
Figure 3.9: Fabry-Perot interferometric sensors. (a) IFPI sensor. (b) EFPI sensor

FP sensors have some advantages over other fiber sensors for multiplexed sensor networks. One significant advantageous feature of FP sensor is that it can be configured as an in-line sensor and can be multiplexed along a single fiber for quasi-distributed temperature and strain sensing. Unlike the multiplexing of Mach-Zehnder and Michelson interferometers, which need many optical splitters and combiners, the multiplexing of FP sensors is relatively easer. One can arrange a large number of FP sensors along a single fiber without extra optical components if the power loss at each sensor can be controlled to a low level (Murphy, Gunther, Vengsarkar, and Claus, 1991).

A typical EFPI sensor configuration is shown in figure 3.10. The light from a laser source propagates along an input/output single mode fiber to the Fabry-Perot cavity that is formed by the input/output and the target fibers. A fraction of this incident light, approximately 4%, is reflected at the output endface of the input/output fiber back into the fiber. The light transmitted out of the input/output fiber projects onto the fiber endface of the target fiber. The reflected light from the target fiber is partially recoupled into the input/output fiber. The interference between the two reflections produces interfering fringes as the air-gap is changed.
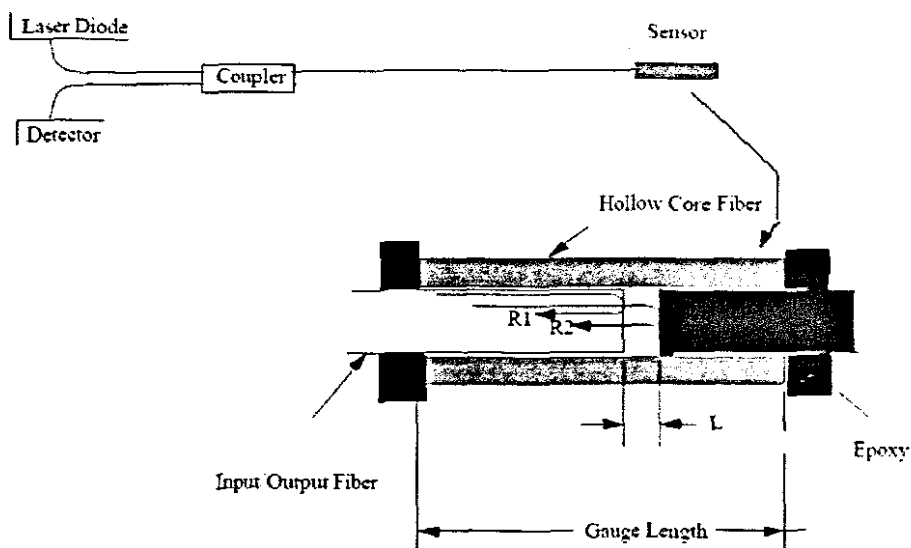
Figure 3.10: Typical FPI sensor structure

The optical wave fields of the two reflections could be represented in terms of its complex amplitude $U_i(x,z,t)$ given by

$$U_i(x,z,t) = A_i \exp(j\phi_i), \quad i = 1,2 \tag{3.19}$$

where the variable A_i is a function of the transverse coordinate x and traveled distance z, and the subscripts $i = 1,2$ stand for the reference and sensing reflections, respectively. Assuming that the reference reflection $A_1 = A$, then the sensing reflection coefficient A_2 can be approximated by the simplified relation

$$A_2 = A\left[\frac{ta}{a + 2s\tan[\sin^{-1}(NA)]}\right] \tag{3.20}$$

Where a is the fiber core radius, t is the transmission coefficient of the air-glass interface (0.98), s is the separation between the reflectors, and NA is the numerical aperture of the single mode fiber given as $NA = (n_1^2 - n_2^2)^{1/2}$, and n_1 and n_2 are the refractive indices of the core and the cladding, respectively. The intensity detected at the photodiode is given as

$$I = |U_1 + U_2|^2 = A_1^2 + A_2^2 + 2A_1A_2\cos(\phi_1 - \phi_2) \tag{3.21}$$

which can be expanded as

$$I = A^2\left[1 + \frac{2ta}{a + 2s\tan[\sin^{-1}(NA)]}\cos(\frac{4\pi s}{\lambda}) + (\frac{ta}{a + 2s\tan[\sin^{-1}(NA)]})^2\right] \tag{3.22}$$

Assumed that $\phi_1 = 0$ and $\phi_2 = 2s(\frac{2\pi}{\lambda})$, and λ is the wavelength in free space. Equation (3.19) indicates that changes in the separation distance between the surfaces of the fibers aligned in the support tube produce a sinusoidal modulation of the output signal.

A typical output of the EFPI sensor is shown in figure 3.11. A phase change of 360 degrees in the sensing reflection corresponds to one fringe period. At a wavelength of 1.3μm, the change in gap for one fringe period is 0.65 μm. The drop in detector intensity is due to the decrease in coupled power from the sensing reflection as it travels farther away from the single-mode input/output fiber (Yu, Kim, Deng, Xiao, and Wang, 2003).
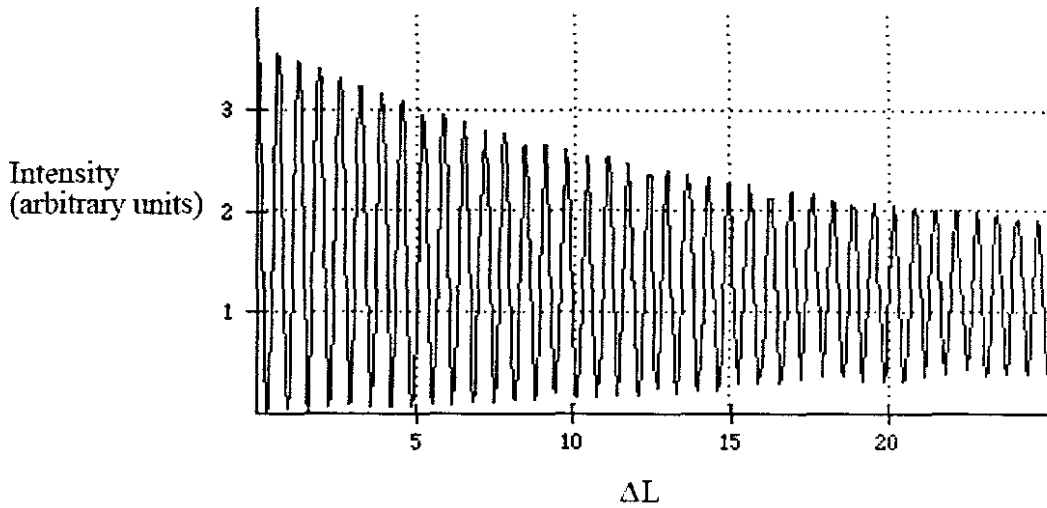
Figure 3.11: EFPI output for 25 μm change in gap

The EFPI, because it is an interferometric sensor, suffers from the same limitations as mentioned for the Mach-Zehnder configuration. Because it is an extrinsic sensor, the methods used to overcome these limitations are different. The current methods employed are quadrature phase shifted operation, dual wavelength method, and white light interferometry.

3.2 Wavelength-Modulated Fiber Optical Sensors

Wavelength-modulated optical fiber sensors change the spectrum of the light being transmitted, reflected or emitted. Such sensors include blackbody radiation, fluorescence, phosphorescence and fiber Bragg grating (FBG) sensors.

FBG sensors, whose reflection and transmission spectrum are dependent on temperature and strain, are truly wavelength-modulated sensors. The diagram of a FBG is illustrated in figure 3.12(a). A Bragg grating with periodic refractive index variation can be formed by UV irradiation. Different techniques, some of which include pointwise, interferometric, and phasemask-based writing methods, have been reported for the fabrication of FBGs (Morey, Meltz and Glenn, 1989). A FBG is a narrow band reflector. The characteristic reflection spectrum of a FBG is shown in figure 3.12(b).

The central wavelength in the reflection spectrum of a FBG, known as Bragg wavelength, is given by

$$\lambda_B = 2n_e\Lambda \qquad (3.23)$$

where n_e is the effective refractive of the fiber and Λ is the period of the gratings. For a Bragg wavelength of $1.5\mu m$, Λ is selected to be $0.5\mu m$.
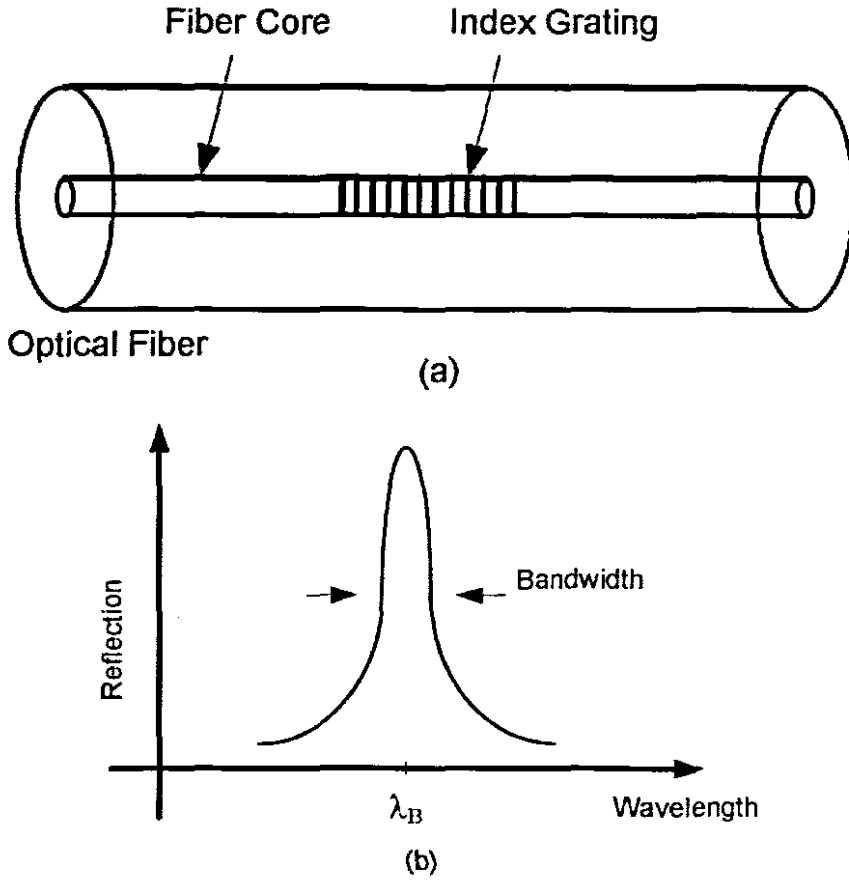
Figure 3.12: Fiber Bragg gratings. (a) Structure. (b) Reflection spectrum

FBGs can be used for temperature and strain sensing. The central wavelength of an FBG is affected by the changes of the refractive index and the periodic spacing between gratings, which are dependent on the environmental temperature and strain. Therefore, temperature and strain perturbations of a FBG sensor can be determined by monitoring the shift of the Bragg wavelength.

The shift of λ_B due to temperature change ΔT can be given as

$$\Delta\lambda_B = 2(\Lambda\frac{\partial n_e}{\partial T} + n_e\frac{\partial \Lambda}{\partial T})\Delta T = \lambda_B(\alpha + \sigma)\Delta T \tag{3.24}$$

Where $\alpha = \frac{1}{\Lambda}\frac{\partial \Lambda}{\partial T}$ is the thermal expansion coefficient and $\sigma = \frac{1}{n_e}\frac{\partial n_e}{\partial T}$ is the thermo-optic coefficient of the fiber.

61

The shift of λ_B due to strain ε_z perturbation can be given by

$$\Delta\lambda_B = \lambda_B(1-p_e)\varepsilon_z \qquad (3.25)$$

where ε_z is the axial strain and p_e is the effective strain-optic constant. For a typical optical fiber, $p_e = 0.22$.

FBG sensors have several advantages including low power loss, high sensitivity, and large scale multiplexing capability. Quasi-distributed temperature and strain sensing with FBG sensors have been reported with different multiplexing schemes. Multiple FBG sensors are usually arranged in a serial array (Ball, Meltz and Morey, 1995). The most common multiplexing schemes include TDM, WDM, FDM and their combinations.

In a TDM scheme, the locations of FBG sensors are determined by the time delay of the reflected light pulse. The reflected light from each sensor is measured by a variety of wavelength-measurement technique including interferometric systems, scanning wavelength filters, and edge filters. FBG sensors in a TDM scheme can either have different central wavelengths or have nominally the same central wavelength with low reflectivity. The interference and crosstalk between sensors have been a drawback for a TDM sensor array.

In a WDM scheme, FBG sensors are fabricated with different central wavelengths. When illuminated by a broadband light source, different FBGs will reflect the light at different wavelengths. One can either use a tunable optical filter to select the light from individual sensor and a frequency discriminator to detect the wavelength change in time domain or use an optical spectrometer to detect the wavelength shift in spectral domain. Because each FBG has to occupy a certain bandwidth for wavelength shift, the multiplexing capacity of a WDM scheme is usually limited due to the available wavelength range. The fabrication of FBG sensors with different central wavelengths requires multiple phase masks or interferometric setups and is difficult for mass production (Othonos, 1997).

Froggatt et. al. demonstrated a FDM scheme for FBG sensors with nominally equal Bragg wavelength. The system utilized a FMCW technique to modulate the frequency of a coherent light source. The locations of FBG sensors are determined by the beating frequencies between the reflections of FBG sensors and a reference air gap reflector. The spectrum of each FBG was obtained by inverse Fourier transforming the frequency band associated with each sensor. Hybrid multiplexing schemes, which may take advantages of different multiplexing schemes, can be used to increase the multiplexing capacity of FBG sensors. One example is a WDM/TDM combined multiplexing scheme given by Davis et al (Cranch and Nash, 2001).

3.3 Polarization-Modulated Sensors

Polarization-modulated optical fiber sensors are the sensors in which the polarization state of light is changed due to the external perturbation such as electric field, magnetic field etc. One of the polarization-modulated sensors is optical current sensor based on magneto optic Faraday Effect, which will rotate the polarization plane. An optical fiber coil in a number of turns has been used as current or voltage sensing element (Ning, Wang, Palmer, Grattan, and Jackson, 1995). Some other materials with larger magneto-optic constants, such as bulk-glass, yttrium iron garnet etc., have also been utilized in current sensors. Another type of polarization-induced sensors is related to the anisotropic properties of crystal-like materials. Light traveling in crystals with orthogonal polarizations will have different propagation speeds and change its polarization states. Optical temperature and electric field sensors based on thermal-optic and Kerr effects have been reported, in which the environmental perturbation changed the refractive indices of crystals and the polarization states of the light.

Polarization-modulated sensors usually use a polarimetric technique to detect the optical phase difference between orthogonal polarizations, which is similar to the interferometric technique for phase-modulated sensors. Some researchers regard polarization-modulated sensors as phase-modulated sensors because of their similarities in the phase-detection scheme. The multiplexing of polarization-modulated sensors is rarely reported due to the complexity of the polarimetric detection, which may require polarizer, wave plate and other optical components. A FDM multiplexed current sensor array, which contains multiple polarization-modulated fiber lasers, was given by Yong *et al* (Bohnert, Gabus, Nehring, and Brandle, 2002)

3.4 Multiplexing and Distributed Sensing

Many multiplexing schemes for optical fiber sensors, some of which include time, frequency, wavelength, coherence, polarization, and spatial-division multiplexing schemes, have been reported. Together with the different multiplexing topologies discussed below, there are many different multiplexing configurations for different sensors (Dandridge, 1991). We will discuss common sensor topologies including serial, star, and ladder, and different multiplexing schemes including time-division-multiplexing (TDM), frequency-division-multiplexing (FDM), wavelength-division-multiplexing (WDM) and coherence-multiplexing (CM), especially for interferometric sensors (Dandridge, Tveten, Kersey, Yurek, 1987). (Details see Appendix A)

3.5 Optical Sensor Applications

Fiber optic sensors are being developed and used in two major ways. The first is as a direct replacement for existing sensors where the fiber sensor offers significantly improved performance, reliability, safety and/or cost advantages to the end user. The second area is the development and deployment of fiber optic sensors in new market areas.

For the case of direct replacement, the inherent value of the fiber sensor, to the customer, has to be sufficiently high to displace older technology. Because this often involves replacing technology the customer is familiar with, the improvements must be substantial.

The most obvious example of a fiber optic sensor succeeding in this arena is the fiber optic gyro, which is displacing both mechanical and ring laser gyros for medium accuracy devices. As this technology matures it can be expected that the fiber gyro will dominate large segments of this market (Sirkis, 1994).

Significant development efforts are underway in the United States in the area of fly-by-light where conventional electronic sensor technology are targeted to be replaced by equivalent fiber optic sensor technology that offers sensors with relative immunity to electromagnetic interference, significant weight savings and safety improvements.

In manufacturing, fiber sensors are being developed to support process control. Oftentimes the selling points for these sensors are improvements in environmental ruggedness and safety, especially in areas where electrical discharges could be hazardous.

One other area where fiber optic sensors are being mass-produced is the field of medicine, where they are being used to measure blood gas parameters and dosage levels. Because these sensors are completely passive they pose no electrical shock threat to the patient and their inherent safety has lead to a relatively rapid introduction.

The automotive industry, construction industry and other traditional users of sensors remain relatively untouched by fiber sensors, mainly because of cost considerations. This can be expected to change as the improvements in optoelectronics and fiber optic communications continue to expand along with the continuing emergence of new fiber optic sensors.

New market areas present opportunities where equivalent sensors do not exist. New sensors, once developed, will most likely have a large impact in these areas. A prime

example of this is in the area of fiber optic smart structures. Fiber optic sensors are being embedded into or attached to materials (1) during the manufacturing process to enhance process control systems, (2) to augment nondestructive evaluation once parts have been made, (3) to form health and damage assessment systems once parts have been assembled into structures and (4) to enhance control systems.

Fiber optic sensors can be embedded in a panel and multiplexed to minimize the number of leads. The signals from the panel are fed back to an optical/electronic processor for decoding. The information is formatted and transmitted to a control system which could be augmenting performance or assessing health. The control system would then act, via a fiber optic link, to modify the structure in response to the environmental effect (Claus and Udd, 1991).

Interesting areas for health and damage assessment systems are on large structures such as buildings, bridges, dams, aircraft and spacecraft. In order to support these types of structures it will be necessary to have very large numbers of sensors that are rapidly reconfigurable and redundant. It will also be absolutely necessary to demonstrate the value and cost effectiveness of these systems to the end users.

3.6 Summary

This chapter discusses the background of optical fiber sensors of phase shift modulation. Two categories of distributed sensing systems, intrinsic distributed sensing and multiplexed point sensor networks are introduced, which is really important technology for designing three axes MOEMS gyroscopes system. Three MEMS vibration structures could share the same light interferometer read-out system, which are unbeatable advantages for micro devices. The researcher about optical multiplexing technology will be further work in multi-axes gyroscope system. The signal of a sensor in a sensor network can be modulated in intensity, wavelength, phase, or state of polarization. In-line fiber sensors, including FP interferometers and FBGs, are preferred in quasi-distributed temperature and sensing sensing.

The optical sensing background review helps to understand the advantages of the optical measurements techniques and measurement concepts, which is necessary preparative for designing MOEMS gyroscope chip.

CHAPTER FOUR
MOEMS GYROSCOPE OPERATING THEORY AND MODELING DESIGN

Based on the concepts of gyroscope systems and optical sensors introduction of the last two chapters, a MOEMS gyroscope system is proposed in this chapter. This gyroscope design is new and as far as was ascertained, have never been designed before. The design includes a discussion of operating principles, a mathematical model to describe and quantify the behaviour of the proposed sensor. The components of the optical interferometer devices are also introduced.

4.1 Introduction

In this chapter, two major theories used in gyroscope technology are introduced, which are Sagnac effect for all optical gyroscope systems and Coriolis effect for MEMS vibration gyroscope systems. Both techniques have most advantages at the different aspects. The novel Micro opto-electro-mechanical system (MOEMS) gyroscope presented in this chapter is the intersection of optical gyroscopes and mechanical gyroscopes. This MOEMS gyroscope system is different from the the mechanical interferometric gyroscope (MIG) which was a hybrid opto-mechanical gyroscope with injection-interferometer readout mentioned in chapter 3 (Norgia Donati, 2001). The MOEMS gyroscope proposed here consist of a MEMS vibration structure based on Coriolis force theory and an optical readout system based on optical interferometry based in the silicon microstructure. The MOEMS gyroscope could be the next generation navigation system for civil and military applications. The operation principle and features compared with optical gyroscopes and mechanical gyroscopes to that of the MOEMS device will be introduced. The MEMS fabrication processes and performances simulation will be discussed in chapter 5 and chapter 6.

The Sagnac effect is one of light interference theory and only method directly relating with angular measurement sensor, which describes the relation between the rotation velocity and the output intensity of the Sagnac effect interferometer by two opposition direction beams traveling long distance fiber optical. And all optical gyroscope systems are based on Sagnac effect theory. Through deep studying about the Sagnac effect and one most useful application fiber optical gyroscope (FOG) based on this theory, which is a rotation-rate sensor often configured to provide angular-output by using digital electronics to do the mathematical integration. It senses rotation rate about its sensing or input axis by forming an interference pattern between two nearly coherent lightbeams generated by an internal light source and beamsplitter. The physical rotation rate causes a very small proportionate phase

shift of the interference pattern due to the Sagnac effect. The key obsolete disadvantage using Sagnac effect applications are high cost of long fiber optical or waveguide for increasing sensitivity and complex manufacturing processes.

Another useful method for angular rate sensor is Coriolis Effect, which describes the relation between rotation velocity and Coriolis force under electronic and mechanical actuator. With MEMS fabrication technology development, the Coriolis force system has been successfully made in micro size to fit in any macro and micro applications as navigation guide or stability control. The performance of the Coriolis effect MEMS gyroscope technology such as sensitivity, temperature bias, responding time, power consumption, and measurement range can not perform well like optical gyroscopes due to the electron readout system like capacitive, piezoelectricity, piezoresistance. But the size is small enough not to be.

The current initiative is focused on containing total ownership costs, especially maintenance costs, without any relaxation of performance, reliability, or maintainability requirements and associated inertial navigation system, developing new micro size and high performances gyroscope system, the novel MOEMS gyroscope has been proposed in this dissertation. It consists of two parts about a MEMS resonator structure to sense the inertial Coriolis force and an optical readout performed by a laser diode that acts as an injection interferometer. The laser beams impinges the resonating structure and the end face of waveguide; the retro-reflection is injected back into the waveguide and this generates two rays interference. The vibration distance created by angular rate makes the light path difference of the interferometer. Therefore, the output intensity of the interferometer is proportion with angular rate.

4.2 MOEMS Gyroscope Theory and Modelling Introduction

The system designed here is a combination of Sagnac & Coriolis methods, which takes advantages from both sides of the optical and mechanical techniques available. As far as output processing is concerned there are many digital signal process methods which can be used for deriving an electronic output. The optical gyro systems based on Sagnac effect have essential shortcoming on the size, which is the long light path for interfering creating due to sensitivity requiring based on Sagnac effect. At this stage, the micro or nano-level fiber optical products are still challenge for the manufacturing. On the other hand, the interferometric readout measurement systems are the best micro distance sensor systems available.

The MOEMS gyroscope is consist of two parts, which are MEMS vibratory structure, and the interferometric micro distance readout system. Firstly, the input rotation velocity is transformed to linear movements based on Coriolis force theory at specifically direction by MEMS vibratory structure. Then, the interferometeric micro displacement readout system will give the precision distance result to represent the rotation velocity. The Coriolis force is proportion with rotation velocity, shown in equation (4.1). The reason to choose the Coriolis acceleration theory is smaller volume and lighter weight by MEMS fabrication technology. With MEMS technology development, the variable micro sensors and actuators are be designed and fabricated based on conventional electron and mechanical principles and theories.

$$\vec{a}_c = 2 \cdot \vec{v} \times \vec{\Omega} \tag{4.1}$$

Here $\vec{\Omega}$ is rotation rate of the inertial reference, $\vec{v}$ is the linear velocity, and the Coriolis force $\vec{F}_c$.

There are many successful micro vibratory structures developed for MEMS gyroscope system based on Coriolis force theory, which use the electro-mechanical methods about capacitor, piezoelectricity, resistance bridge etc. to sensor the displacement created by rotation velocity.

The interferometer is consisting of light source, fiber optical, coupler and photo-detector. One reflected face is fixed at the end of fiber optical beam, shows in figure 4.1. Another reflected face is mounted on MEMS vibratory structure (Lee and Taylor, 1992).
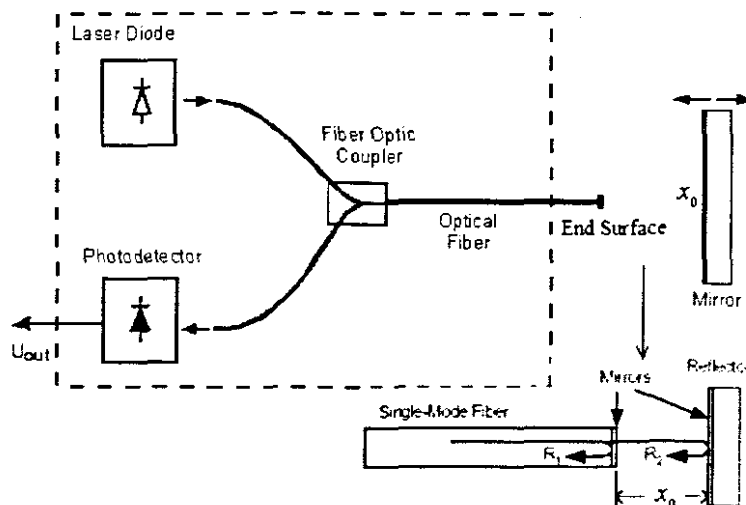
Figure 4.1 Fibers Optical Readout Configuration

4.2.1 Vibratory Part of MOEMS Gyroscope

All micromachined vibratory rate gyroscopes operate under the same dynamic principles. A structural mass is forced into oscillation in one principle structural mode, designated the "drive" mode. The presence of rotation induced Coriolis force couples the drive mode into an orthogonal structural mode, designated the "sense" mode. The amount of magnitude of vibration induced in the sense mode is proportional to the rotation rate of the device. As an illustration, consider a structural mass attached to a frame free to move in inertial space (i, j) (Figure 4.2).
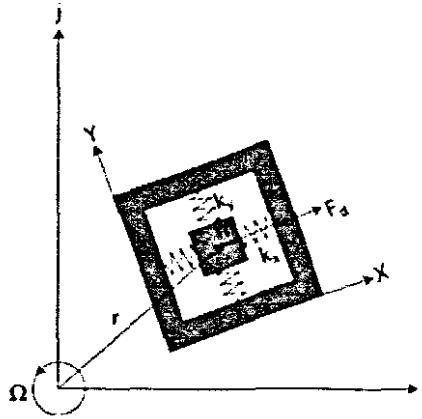
Figure 4.2: Non-ideal Gyroscope Model

In the coordinate frame of the moving device (X, Y), the equations of motion, assuming the operating frequency is much greater than the rotation rate ($\Omega^2 << \sqrt{\dfrac{k_x}{m}}, \sqrt{\dfrac{k_y}{m}}$), are

$$m\ddot{x} + k_x x - 2m\Omega\dot{y} = F_d(t) \tag{4.2}$$

$$m\ddot{y} + k_y y - 2m\Omega\dot{x} = F_c(t) \tag{4.3}$$

where m is the lumped mass of the system, k_x and k_y are the x and y stiffness values, respectively, and Ω is an input angular rate. To achieve highest sensitivity, the stiffnesses between x and y are typically designed to be the same ($k_x = k_y = k$) and in this case, the system is driven at its resonant frequency using a harmonic excitation force F_d

($F_d = F_0 \sin\omega_n t$, $\omega_n = \sqrt{\dfrac{k_x}{m}} = \sqrt{\dfrac{k_y}{m}}$). The measured sense Coriolis acceleration a_c is proportional to the input angular velocity,

$$\vec{a}_c \approx \Omega X_0 \omega_n \cos\omega_n t \tag{4.4}$$

69

where X_0 is the magnitude of vibration in the x direction. Utilizing these principles, several classifications of rate gyroscope have been devised.

For compendia analysis, the two dimension spring model sets up like figure 4.3 to show the Coriolis force operation principles. The rotation rate is putted into from z-axis; the model is called z-axis rotation rate vibratory structure (Maenaka and Shiozawa,1994).
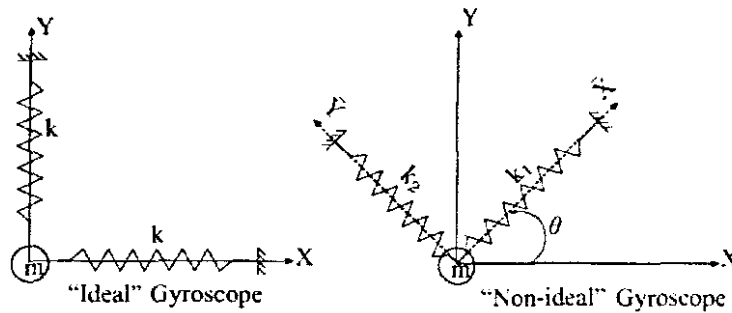
Figure 4.3: Structural imperfections shift the orientation of the principal axes, i.e., $\bar{X}$ and $\bar{Y}$ axes, relative to the measurement/excitation directions, i.e., X and Y axes, in a nonideal gyroscope. Note that the two principal stiffness values k_2 and k_1 are different in a nonideal gyroscope

In an "ideal" gyroscope, the principal stiffnesses are equal, and the principal coordinates coincide with the measurement (X–Y) coordinates, i.e., the drive and sense axes (see Fig. 4.4). In the presence of structural imperfections, the two principal stiffness values do not match. Hence, there is an angular mismatch between the principal axes and the measuring coordinate system. This "non-ideal" behavior results in a frequency mismatch between the drive and the sense resonant frequencies and undesired coupling of the modes leading to errors in the sense output. Two types of errors are caused by the non-diagonal-stiffness and damping matrices. While the non-diagonal-stiffness matrix causes quadrature error, i.e., error signal in quadrature with the measured Coriolis force, the nondiagonal damping leads to errors in phase with the measured Coriolis force. System identification is the first stage of any corrective procedure to compensate for the above errors.

70
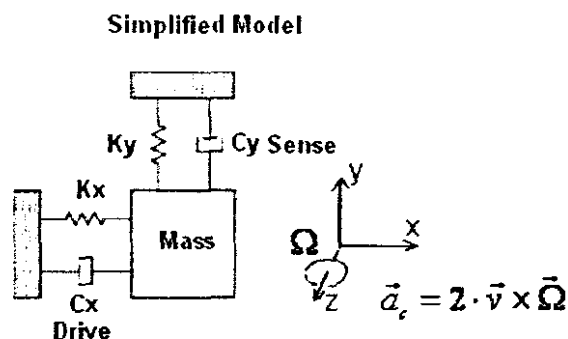
A Coriolis acceleration is generated by a oscillating proof mass in a rotating reference frame. The proof mass is oscillated along the x-axis (the driven mode), supply the velocity $\vec{v}$, the reference frame rotates around the z-axis, and the Coriolis force is detected as deflections along the y-axis (the sense mode).

$$\vec{F}_c = 2m(\vec{v} \times \vec{\Omega}) \tag{4.5}$$

This equation shows that orthogonal lateral-axis vibration and acceleration sensing are required to detect the z-axis rotation (Fujishima, Nakamura and Fujimoto, 1991).

For operation supplied the linear velocity $\vec{v}$, the mass is driven vibration in the x-direction with amplitude A_d a driving frequency ω_d.

$$x = A_d \sin \omega_d t \tag{4.6}$$

So the velocity in x-axis is given by:

$$\vec{v} = \dot{x} = A_d \omega_d \cos \omega_d t \tag{4.7}$$

Rotation input about the z-axis generates Coriolis acceleration in-plane along the y-axis. Lateral displacement of the proof mass due to Coriolis acceleration in response to a rotation signal. Notice that the Coriolis acceleration is an amplitude-modulated signal where the carrier frequency is the oscillation frequency and the rotation rate modulates the amplitude. The resulting Coriolis acceleration is a dual sideband signal centered on the oscillation frequency. The Y-axis accelerations are proportional to velocity, the equation is given by:

$$\vec{F}_c = 2m\dot{x}\Omega \tag{4.8}$$

$$\ddot{y}_{Coriolis} = 2\Omega A_d \omega_d \cos \omega_d t \tag{4.9}$$

As a point of reference, for a Coriolis model with an oscillation amplitude, $A_d = 1mm$, driven oscillation frequency, $\omega_d = 20kHz$, and an input rotation rate, $\Omega = 1\deg/\sec$, the Coriolis acceleration has a magnitude of 0.45milliG's. From above discussed, the rotation rate measurement is transformed the Coriolis acceleration measurement. And the Coriolis

acceleration measurement will be transformed to measure the mass the displacement driven by Coriolis acceleration at y-axis.

Differential equation for the mass movement in the y-direction is given by

$$m\ddot{y} + c_y\dot{y} + k_y y = 2mA_d\omega_d\Omega\sin(\omega_d t + \frac{\pi}{2})$$ (4.10)

The steady state solution is given by

$$y = A_y\sin(\omega_d t + \frac{\pi}{2} - \varphi) = A_y\cos(\omega_d t - \varphi)$$ (4.11)

There, amplitude at y-direction is given by

(4.12)

$$A_y = \frac{2A_d\omega_d\Omega}{\omega_y^2\sqrt{(1-\frac{\omega_d^2}{\omega_y^2})^2 + 4\zeta_y^2\frac{\omega_d^2}{\omega_y^2}}}$$

This is maxima displacement created by rotation velocity. The value is proportion with rotation velocity.

In equation (4.11), the phase is given

$$\varphi = \tan^{-1}\frac{2\zeta_y\omega_d\omega_y}{\omega_y^2 - \omega_d^2}$$ (4.13)

where $\zeta_y = \frac{c_y}{2m\omega_y}$ (4.14)

where Q_y is the quality factor at the sensing mode given by

$$Q_y = \frac{1}{2\zeta_y}$$ (4.15)

If the driven frequency is equal to y-axis nature frequency, $\omega_d = \omega_y$, the mass amplitude becomes at resonance condition, the amplitude can be reduced to:

$$A_y = \frac{2A_d\Omega Q_y}{\omega_y} = \frac{2A_d Q_y}{\omega_y}\Omega \qquad\qquad (4.16)$$

$$\varphi = \tan^{-1}\infty = 90^0 = \frac{\pi}{2} \qquad\qquad (4.17)$$

In the ideal frequency matched, the oscillation equation driven by Coriolis force at y-axis is given by:

$$y = \frac{2A_d Q_y}{\omega_y}\Omega\sin(\omega_d t) \qquad\qquad (4.18)$$

From above perform mathematical calculations, the results of the relative between the angular rate, Coriolis acceleration and oscillation in y-axis are clear, which shows the y-axis amplitude is proportion with the z-axis angular rate, and the x-axis driver oscillation redound to amplifier the amplitude of the y-axis. In the micro size, the nature frequency of oscillation beams is very high, and very light. It is the advantage for driving the mass at the x-axis under low power consumption, and achieves the high sensitivity (White and Heppler, 1995).

The angular rate measurements are converted to measure the y-axis amplitude, the relationship shows in figure 4.5. The rotation acceleration $\dot{\Omega}(t)$, which means the variety rate of rotation velocity, is far less than the driven frequency ω_d. That means the amplitude can be filtered by high frequency filter gate.
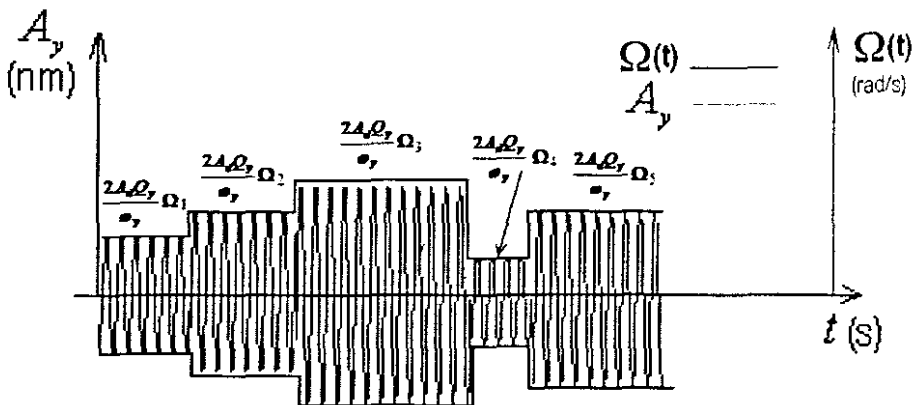
Figure 4.5: Oscillating Coriolis Displacements Creating by Variable Rotation Velocity

There are many methods to measure these especial micro displacements like bridge resistances, bridge capacitances, piezoelectricity and optical interferometry methods etc. Currently, the optical interferometer is the most precise displacement measurement method.

In next section, the operation principle of micro optical interferometer readout is introduced for rotation rate measurement.

4.2.2 Fiber Optical Interferometer Readout System for MOEM Gyroscope

Optical fiber sensors are excellent candidates for monitoring environmental parameters because of their numerous advantages over conventional sensors. Some of the advantages include light weight, small size, high sensitivity, immunity to electromagnetic interference, and potential for large-scale multiplexing. The widespread use of optical fiber communication devices by the telecommunication industry has resulted in mass production of associated optical and electrical components that are also used in optical fiber sensor systems. Therefore, economies of scale have produced substantial reductions in optical fiber sensor cost.

Many optical fiber sensors have found numerous applications in industry, some of which include fiber optic gyroscopes for automotive navigation systems, strain sensors for smart structures, and a variety of fiber optic sensors for manufacturing and process control. Fiber optic sensors have also been used to monitor a large number of environmental parameters such as position, vibration, temperature, acoustic waves, chemicals, current, and electric field (Ecke, Pfeifer, Schauer and Willsch, 1999).

Optical fiber sensors can be broadly classified as either intrinsic or extrinsic, and more specifically classified by their operating principles. Information in each type sensor can be conveyed by polarization, phase, frequency, wavelength, and intensity modulation, or a combination of the above.

If all sensing mechanisms take place within the fiber itself, the sensor is classified as intrinsic. In this type sensor, the fiber functions as both a transmission medium and sensing element. An external parameter induces a change in the light guiding properties of the fiber which is detected and demodulated to produce measured information. In extrinsic sensors, the fiber plays no role in the sensing mechanism and only serves to bring the light to and from an external medium where it is modulated. The external medium can range from special optical crystals to air (Doi, Iwasaki, Shionoya and Okamoto, 1997).

Optical fiber sensors can be further classified by their operating principle. If the sensor is based on the interference between light waves, it is referred to as interferometric. Interferometric sensors are classified by their geometry; Fabry-Perot, Mach-Zehnder, Michelson, and Sagnac. Other sensors are based on the loss of light from the fiber or coupled to the fiber and are referred to as intensity based sensors.

The optical micro displacement measurement sensor part is used for the MOEMS gyroscope system. The optical interferometer readout system has been proofed with the high sensitivity, high precision, high integration, and low cost etc. characteristics comparing with the other electronic approaches. All the measurement sensors are designed integration with the optical readout system. Interference is one of useful readout system, which is a complex wave phenomenon, and observed in other frequency wave areas, like the mechanical wave, sound wave, light wave, electric wave etc. In the optical technology, the interference will be happened under those situations, no matter the sensor is a Michelson, a Mach-Zehnder, a Sagnac or a Fabry-Perot interferometer: 1) frequency of two beams must be same; 2) the vibration of two beams must be same direction; 3) phasic or phase shift of two beams must be holed constant. Those interferometry techniques have been introduced in previous section.

From the discussed above, the rule about Intensity variation is found, which is described the relation between the output intensity and the light path length difference. Every $\frac{\lambda}{2}$ path length displacement of two light rays changing is bringing on once changing of the intensity from max. to min. The intensity interval symmetrical distributing phenomenon of the light interference is foundation for high-precision deformation measuring systems and micro displacement sensors because of light wavelength ($10^{-6}m$). The use of optical fibers and micro optical chips allows making the interferometers extremely compact and economic.

In this dissertation, the micro fiber optic interferometer will be proposed to match with MEMS vibratory structure. Whatever is the size, response frequency and sensitivity, the micro fiber optical interferometer is more superior to electronic measurement sensors. The fiber optical interferometer has simplest configuration and smallest size including the super-luminescent diode laser (SLDL), PIN photo-detector, erbium-doped fiber amplifier (EDFA), one 1x2 EDFA coupler and the partially reflecting surface at the end of fiber optical, shows in below figure 4.6. When the light travels through the one arm and the coupler to the end of fiber optical, the part of light energy is reflected back to fiber optical going through the coupler and the second arm to the photo-detector converted to the current. That is called the first light beam. The rest light energy goes out the fiber optical and arrives the external reflected surface, which is movement surface and measured surface as well. The light is fully reflected back to fiber optical, goes through the same path as the first beam light at the photo-detector being converted to the current as well. That is called the second light beam. Those two light beams are consisting of the interferometer and produce the interference at the photo-detector. Because two light beams come from the same light source, the frequency

is same, the initialization phase shift is stability, and the path length difference is the twice of the distance between the end of fiber optical and external reflected surface. All the interference conditions are satisfied. In this simple structure processes, the output intensity is presenting the distance, which the sensitivity can achieve sub-angstrom level, between the end of fiber optical and the external reflected surface (Ooki, Arimoto, Shionoya, Matsuura and Iwasaki, 1993).
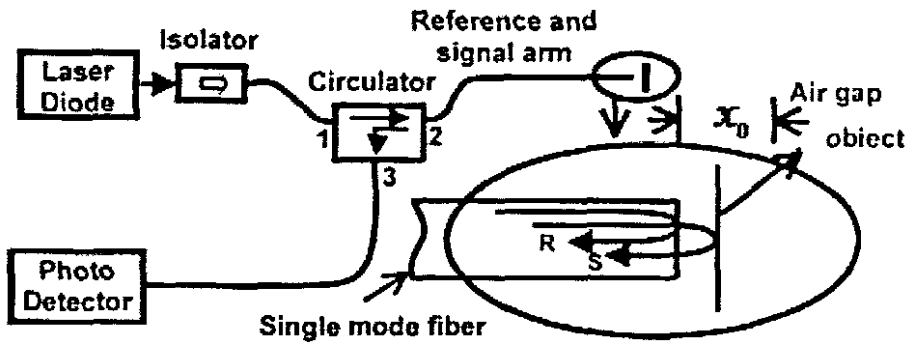
Figure 4.6: Diagram of Micro Fiber Optical Interferometer

Normally, the end surface of fiber optical is fixed, and the external surface is mounted on the movement static mass or deformable surface. The environments parameters, which are the survey parameters, will affect the external surface, which means the movement or deformable surface will be modulated by the special environment changing. The physical changing of the external surface will change the physical distance between the external surface and the end fiber optical, break and modulation the output interference intensity, since the light wavelength is micro-meter, the distance measurement sensitivity is ability to nano-level. This is the basic interferometer principle for distance measurement.

Let us discuss equations how integrate the interferometry with MEMS Coriolis force vibratory structure to sense the rotation rate.
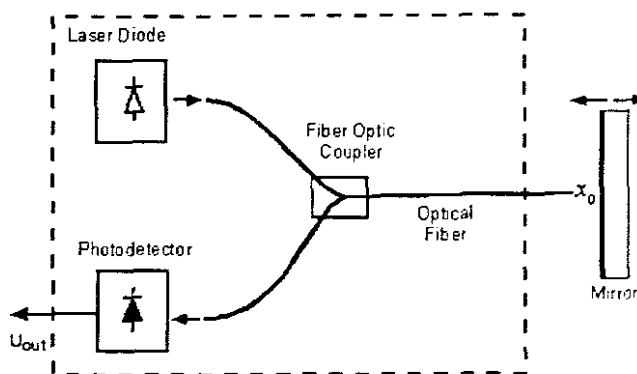
Figure 4.7: Configuration of Fiber Optical Interferometer

In practical experiment, figure 4.7 shows the configuration of the modified fiber optical interferometer. The radiation of the laser diode is coupled into the fiber and propagates through the coupler to fiber. Then, one part of radiation is reflected from the end face of the fiber and other part of radiation is flashed into the air, reflected from the mirror and returned back into the fiber. The optical beam reflected from the end face of the fiber interferes with the beam reflected from the mirror. As a result the intensity of the optical radiation at photodetector is periodically changed depending on the distance x_0 between the fibers and mirrors as follows. The reflected light from the air–object interface at the far end of the air gap is partially coupled back into the fiber (sensing reflection) and it interferes with the Fresnel reflection from the glass–air interface at the fiber end (reference reflection). Although multiple reflections occur within the air gap, the effect of subsequent reflections to the primary ones is found to be negligible. In contrast to a conventional Michelson interferometer, only one of the two arms is employed in the present case and a circulator replaces the coupler. The circulator routes the input optical wave from Port 1 to Port 2. The reflected interfering waves that are coupled back to Port 2 are routed to Port 3 without being partially coupled back into Port 1. In essence, the configuration resembles a Fizeau interferometer, but it is a fiber-based version with low finesse due to the low reflectance of the fiber–air interface, the low coherence length of the semiconductor laser used, and the diverging cone nature of the emitted light beam from the fiber end. Ideally, the circulator should not couple any light wave back to the laser cavity, to ensure the stability of the light source. However, in practice, there is always a tiny amount of light feedback. In order to further prevent back-reflection-induced relative intensity noise (RIN), an isolator is placed immediately after the laser source. The air gap distance establishes the optical phase difference between the reference reflection and the sensing reflection, which in turn determines the power of light monitored at Port 3 of the circulator.

According to the interference theory, the detected optical power at the output of the sensor can be represented by:

$$I_0 = I_r + I_s + 2\sqrt{I_r I_s}\,\cos(\Delta\varphi + \varphi_0) \tag{4.19}$$

where I_r and I_s are the optical powers of the reference light wave and sensing light wave respectively, and $\Delta\varphi$ is the optical phase difference between these two waves. φ_0 is the difference of two light initialization phase shift, which is equal to $\varphi_0 = \varphi_r - \varphi_s$. $\Delta\varphi$ is proportional to the air gap distance x, and can be expressed by:

$$\Delta\varphi = \frac{4\pi n_0}{\lambda} x \tag{4.20}$$

Here, n_0, the refractive index of the air is gap, and λ is the wavelength of the light source.

From the figure 4.7, the initialization path-length difference is given by $\Delta L = 2x_0$. The phase shift between two light beams is given by:

$$\Delta\varphi = \frac{2\pi}{\lambda} \Delta L = \frac{4\pi n_0}{\lambda} x_0 \tag{4.21}$$

Assuming that the laser input optical power into the fiber is I_i, the power of the reference light I_r can be calculated using Fresnel law, which approximately yields:

$$I_r = (\frac{n_1 - n_0}{n_1 + n_0})^2 I_i \approx 4\% I_i \tag{4.22}$$

where $n_1 \approx 1.46$ is the fiber core refractive index.
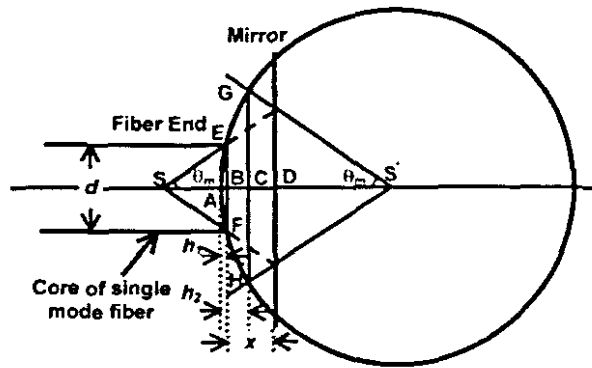
Figure 4.8: Simplified Schematic Diagrams for Derivation of I_s

To obtain the expression for the sensing light wave power I_s, which is a function of the air gap distance x, the numerical aperture of the fiber, and object reflectance etc., we consider the simplified case in which the single mode fiber is perpendicular to the object surface and I_s is only a function of x. We assume that the light wave emanating from the fiber end can be regarded as a point source S in free space and is emitted within the acceptance cone of angle θ_m, as shown in figure 4.8. The reflected light m from the object is then equivalent to that from a point source S', where S' is the mirror image of S (therefore $SD = DS'$). Taking

the reflectance of the object as ideally unity, the power of the reflected light from source S' is thus 96% I_i. A spherical surface centered at S' can be drawn across the fiber end such that the radius of the sphere is $r = S'E = S'F = S'G = S'H = S'A$. Let S_{AEF} and S_{AGH} represent the areas of the spherical cap *AEF* and *AGH* of height h_1 and h_2, respectively. Considering the 4% loss of optical power at the air–fiber end interface each time the light exits and re-enters the fiber, and the proportionality relationship between optical power passing through the two spherical caps, the ratio of I_s over I_i is thus,

$$\frac{I_s}{I_i} = 96\% \times 96\% \frac{S_{AEF}}{S_{AGH}} \tag{4.23}$$

Mathematically:

$$\frac{S_{AEF}}{S_{AGH}} = \frac{2\pi r h_1}{2\pi r h_2} = \frac{h_1}{h_2} \tag{4.24}$$

Assuming that x is the air gap distance to be measured and d is the diameter of the sensing fiber core, as can be seen in figure 4.8,

$$h_1 = AS' - BS' = \sqrt{(2x + 0.5d / \tan\theta_m)^2 + (0.5d)^2} - (2x + 0.5d / \tan\theta_m) \tag{4.25}$$

$$h_2 = AS' - CS' = AS'(1 - \cos\theta_m)$$
$$= \sqrt{(2x + 0.5d / \tan\theta_m)^2 + (0.5d)^2}(1 - \cos\theta_m) \tag{4.26}$$

Substituting equation (4.21) to (4.26) into (4.19), the output intensity ratio is given by:

$$\begin{aligned}
\frac{I_o}{I_i} = {} & 4\% + 92\%(1 - \frac{2x + 0.5d / \tan\theta_m}{\sqrt{(2x + 0.5d / \tan\theta_m)^2 + (0.5d)^2}})/(1 - \cos\theta_m) \\
& + 0.384[\cos(\frac{4\pi n_0 x}{\lambda})] \times \sqrt{(1 - \frac{2x + 0.5d / \tan\theta_m}{\sqrt{(2x + 0.5d / \tan\theta_m)^2 + (0.5d)^2}})/(1 - \cos\theta_m)}
\end{aligned} \tag{4.27}$$

In our case, a laser diode with an emitting wavelength of 1.55 um is used as the light source, and the single mode fiber has a numerical aperture of 0.1 and a diameter of 9 um. By substituting these values into Eq.(4.27), the output signal can be plotted as a function of x and the result is shown in figure 4.9. It can be seen that the sensor output is a raised cosine

79

with a period of $\dfrac{\lambda}{2}$ and there is a downward trend as the gap distance increases. This trend can be easily understood from the fact that the light coupled back to the fiber is less when the object moves away (Liang, Monteiro, Monteiro and Lu, 1991).
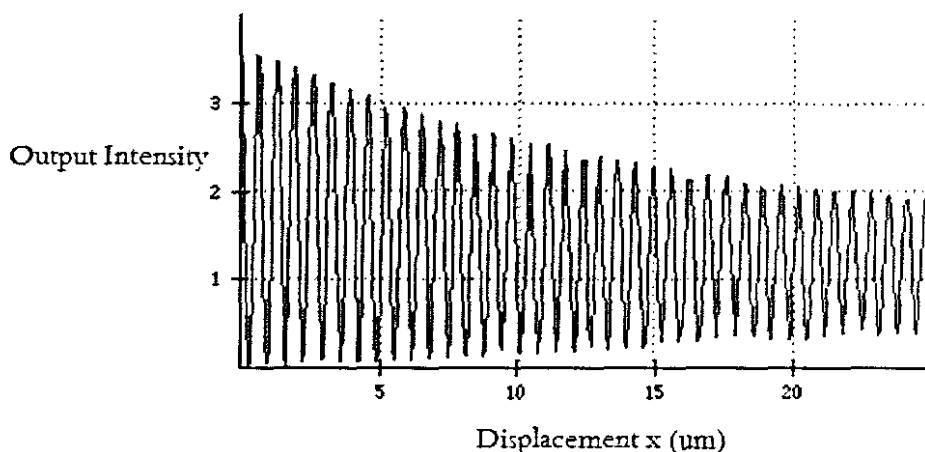
Figure 4.9: Simulation Result of Relation between Sensor Intensity Output I_0/I_i and Air Gap Distance x

The fiber optical interferometry distance readout system can be applied for any distance measurement sensor systems. Before the interferometer is used in any applications, the performances of the distance measurement would be tested.

4.2.3 Vibratory Effecting on Interferometry Intensity Output

Now, we shall consider the interferometric signal appearing as a result of the reflection of the light from the vibrating surface resonator. In technique definition, the vibration movement is shuttle moving with some reciprocities frequency. In one quarter movement from the original point to the ultimate point, the movement feature is same as the linear movement. The oscillation coming from the out environments could be any vibratory source like sound wave, heat wave, earthquake wave etc. depending on the monitor requirements. In this dissertation, the rotation rate is required the parameter. But like mention above, the rotation rate will not directly affect the output intensity of the fiber optical interferometer. The Coriolis Effect is the link between the output intensity and the rotation rate, which is transforming the inertial rotation rate to the one axis oscillation, and then the interferometer will measure the amplitude about this oscillation and get the corresponding rotation rate.

When the external surface resonator oscillates proportion with rotation rate, the phase difference of interfering rays is varied as follows. The principle diagram shows in figure 4.10,

which is describing the affection oscillation input to output intensity of the micro fiber optical interferometer.
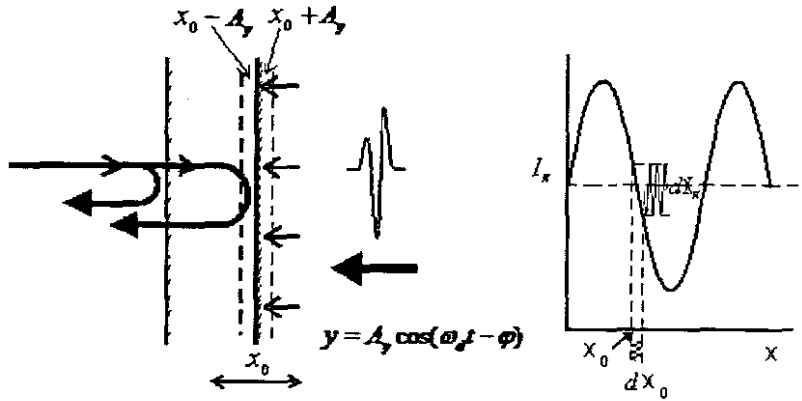
Figure 4.10: Effecting Oscillation Input to Output Intensity

During the rotation rate and Coriolis effecting, the oscillation happened in y-axis is:

$$y = A_y \cos(\omega_d t - \varphi) \tag{4.28}$$

The path-length difference is given by:

$$\Delta L = 2[x_0 + y] \tag{4.29}$$

x_0 is the setting position, also the half interferometer cavity length. The length of cavity and the initialization movement surface setting position is conform to demodulation methods, and discussed later.

If the driven angular frequency is match with the sensing angular frequency, $\omega_d = \omega_y$, the amplitude and phase shift become:

$$A_y = \frac{2 A_d Q_y}{\omega_y} \Omega \tag{4.30}$$

$$y = \frac{2 A_d Q_y}{\omega_y} \Omega \sin(\omega_d t) \tag{4.31}$$

So the phase shift is given by:

$$\Delta \varphi = \frac{4\pi}{\lambda} [x_0 + \frac{2A_d Q_y}{\omega_y} \Omega \sin(\omega_d t)] \qquad (4.32)$$

Form figure 4-10, the movement surface is vibrating between $(0, 2A_y)$, x_0 be the original movement surface setting point. The interferometer cavity length must be more than $|2A_y|$. While the amplitude, $|A_y|$, is determined by input rotation rate ($A_y = \frac{2A_d Q_y}{\omega_y} \Omega$), another parameters are determined by MEMS structure design. So different the measurement range has the different cavity length; different the sensitivity and responding time requirements have the different MEMS structure frequency (Smith, Bao, 1996).

The interference intensity output related with phase shift is given by:

$$I_0 = I_r + I_s + 2\sqrt{I_r I_s} \cos[\frac{4\pi}{\lambda} x_0 + \frac{8\pi A_d Q_y}{\lambda \omega_y} \Omega \sin(\omega_d t)] \qquad (4.33)$$

The I_r is the intensity of the partial reflected surface, I_s is the intensity of full reflected surface. Assuming the reflective index of partial reflected surface is β, at the ideal situation $I_r = \beta I_i$, and then $I_s = (1 - \beta) I_i$.

$$I_0 = \beta I_i + (1 - \beta) I_0 + 2\sqrt{\beta(1 - \beta) I_i^2} \cos[\frac{4\pi}{\lambda} x_0 + \frac{8\pi A_d Q_y}{\lambda \omega_y} \Omega \sin(\omega_d t)]$$

$$= I_i + 2I_i \sqrt{\beta(1 - \beta)} \cos[\frac{4\pi}{\lambda} x_0 + \frac{8\pi A_d Q_y}{\lambda \omega_y} \Omega \sin(\omega_d t)] \qquad (4.34)$$

The output intensity is changing with the variable rotation rate; the equation can be reduced to:

$$I_0 \cong \cos[\frac{4\pi}{\lambda} x_0 + \frac{8\pi A_d Q_y}{\lambda \omega_y} \Omega \sin(\omega_d t)] \qquad (4.35)$$

$$I_0 \cong \cos[\frac{8\pi A_d Q_y}{\lambda \omega_y} (\frac{x_0 \omega_y}{A_d Q_y} + \Omega \sin \omega_d t)] \qquad (4.36)$$

Let $\alpha = \dfrac{8\pi A_d Q_y}{\lambda \omega_y}$, $\beta = \dfrac{x_0 \omega_y}{A_d Q_y}$, there are the design parameters according to design datasheet. The equation (4-35) can be reduced to:

$$I_0 \cong \cos[\alpha(\beta + \Omega \sin \omega_d t)] \tag{4.37}$$

Derivative I_0 is given by:

$$\dot{I}_0 = -\sin[\alpha(\beta + \Omega \sin \omega_d t)]\alpha \Omega \omega_d \cos \omega_d \tag{4.38}$$

Due to equation $\cos^2 x + \sin^2 x = 1$

$$(\dfrac{-\dot{I}_0}{\alpha \Omega \omega_d \cos \omega_d})^2 = \sin^2[\alpha(\beta + \Omega \sin \omega_d t)] \tag{4.39}$$

$$(I_0)^2 \cong \cos^2[\alpha(\beta + \Omega \sin \omega_d t)] \tag{4.40}$$

So $(\dfrac{-\dot{I}_0}{\alpha \Omega \omega_d \cos \omega_d})^2 + (I_0)^2 = 1$

$$(\dot{I}_0)^2 + \alpha^2 \Omega^2 \omega_d^2 \cos^2(\omega_d t) I_0^2 = \alpha^2 \Omega^2 \omega_d^2 \cos^2(\omega_d t) \tag{4.41}$$

From above equation evolvement, the rotation rate can be described by output intensity like:

$$\Omega^2 = \dfrac{1}{\alpha^2 \omega_d^2 \cos^2(\omega_d t)} \dfrac{\dot{I}_0^2}{1 - I_0^2} \tag{4.42}$$

$$\Omega = \dfrac{1}{\alpha \omega_d \cos(\omega_d t)} \dfrac{\dot{I}_0}{\sqrt{1 - I_0^2}} \tag{4.43}$$

$$\Omega \approx \dfrac{1}{\alpha \omega_d \cos(\omega_d t)} \dot{I}_0 (1 + I_0) \tag{4.44}$$

Another mathematic processed for output intensity equation (4.35) shows below:

$$I_0 \cong \cos[\frac{4\pi}{\lambda}x_0 + \frac{8\pi A_d Q_y}{\lambda \omega_y} \Omega \sin(\omega_d t)] \tag{4.45}$$

Here, $\varphi_0' = \frac{4\pi}{\lambda}x_0$ is initialization phase shift of the movement surface setting point, which is equivalent to non-rotation rate phase shift, $\Omega = 0$. The output intensity of initialization movement surface setting point is located at middle of I_{max} and I_{min}, there is linear scope, the precision region for small rotation rate measurement, and easier for demodulation method, the setting point shows in figure 4.11.
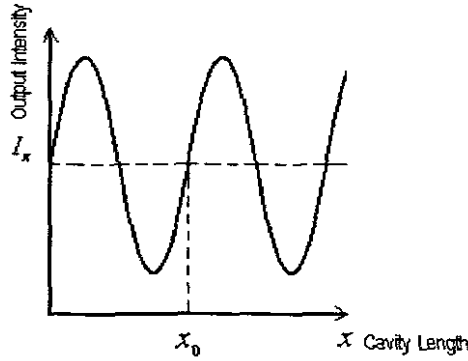
Figure 4.11: Initialization Position of the Vibratory Reflected Surface

The setting point is accord with rule shown below:

Let $x_0 = \frac{k\lambda}{2}$,

$$\Delta\varphi = \frac{4\pi}{\lambda}x_0 = 2k\pi \quad (k = 0,\pm1,\pm2,...) \tag{4.46}$$

$$I_{max} = (\sqrt{I_r} + \sqrt{I_s})^2 \tag{4.47}$$

Let $x_0 = \frac{\lambda}{4}(2k+1)$,

$$\Delta\varphi = \frac{4\pi}{\lambda}x_0 = (2k+1)\pi \quad (k = 0,\pm1,\pm2,...) \tag{4.48}$$

$$I_{min} = (\sqrt{I_r} - \sqrt{I_s})^2 \tag{4.49}$$

From the above equation discussion, the setting point x_0 must be set at half cycle output intensity, and half of the cavity length.

$$x_0 = \frac{\lambda}{4}(2k + \frac{1}{2}), \ (k = 0, \pm 1, \pm 2, \ldots)$$

(4.50)

The equation (4.35) describes the relation about the interferometer output intensity and rotation rate. Expanding I_0 by cosine triangular function and using the Bessel functions, the alternating components of the intensity modulation would be found. Cosine triangular function $\cos(\alpha + \beta) = \cos\alpha\cos\beta - \sin\alpha\sin\beta$.

$$I_0 \cong \cos\frac{4\pi}{\lambda}x_0\cos[\frac{8\pi A_d Q_y}{\lambda\omega_y}\Omega\sin(\omega_d t)] - \sin\frac{4\pi}{\lambda}x_0\sin[\frac{8\pi A_d Q_y}{\lambda\omega_y}\Omega\sin(\omega_d t)]$$

(4.51)

The Bessel function is given by:

$$\sin(x\sin\theta) = 2\sum_{n=1}^{\infty}J_{2n-1}(x)\sin[(2n-1)\theta]$$

(4.52)

$$\cos(x\sin\theta) = J_0(x) + 2\sum_{n=1}^{\infty}J_{2n}(x)\cos2n\theta$$

(4.53)

$$I_0 = \cos\frac{4\pi x_0}{\lambda}[J_0(\varphi_m) + 2J_2(\varphi_m)\cos(2\omega_d t) + 2J_4(\varphi_m)\cos(4\omega_d t) + \cdots]$$
$$- \sin\frac{4\pi x_0}{\lambda}[2J_1(\varphi_m)\sin(\omega_d t) + 2J_3(\varphi_m)\sin(3\omega_d t) + \cdots]$$

(4.54)

Here $\varphi_m = \frac{8\pi A_d Q_y}{\lambda\omega_y}\Omega$

$$I_0 = \cos\frac{4\pi x_0}{\lambda}J_0(\varphi_m) - 2\sin\frac{4\pi x_0}{\lambda}J_1(\varphi_m)\sin(\omega_d t) + 2\cos\frac{4\pi x_0}{\lambda}J_2(\varphi_m)\cos(2\omega_d t)$$
$$- 2\sin\frac{4\pi x_0}{\lambda}J_3(\varphi_m)\sin(3\omega_d t) + 2\cos\frac{4\pi x_0}{\lambda}J_4(\varphi_m)\cos(4\omega_d t) + \cdots$$

(4.55)

According to the setting point rule Equ.(4-49) mentioning above, the $\cos\dfrac{4\pi x_0}{\lambda} = 0$,

$\sin\dfrac{4\pi x_0}{\lambda} = -1$ is given. The intensity output equation can be reduced to:

$$I_0 = \sin[\frac{8\pi}{\lambda}\frac{A_d Q_y}{\omega_y}\Omega\sin(\omega_d t)]$$

(4.56)

$$I_0 = 2J_1(\varphi_m)\sin(\omega_d t) + 2J_3(\varphi_m)\sin(3\omega_d t) + ...$$

(4.57)

Here, $\varphi_m = \dfrac{8\pi A_d Q_y}{\lambda\omega_y}\Omega \ll 1$, so $J_1(\varphi_m) = \dfrac{\varphi_m}{2} = \dfrac{4\pi A_d Q_y}{\lambda\omega_y}\Omega$. Holding the first grade Bessel

function

$$I_0 = \frac{8\pi A_d Q_y}{\lambda\omega_y}\Omega\sin(\omega_d t)$$

(4.58)

I_0 is the output intensity and readout, demodulated by close-loop circuit. φ_m is the constant parameter due to the design and materials. Then, the relation between the rotation rate and output intensity shows in equation (4.58),

$$\Omega \approx \frac{I_0\lambda\omega_y}{8\pi A_d Q_y\sin(\omega_d t)} = \frac{I_0}{\varphi_m\sin(\omega_d t)}$$

(4.59)

The equation shows above that is the linearization format about the relation between the interferometer intensity output and rotation rate. These whole operation principles are using the Coriolis Effect as the intermedia to transform the rotation rate to one axis oscillation movement, and then applied the optical interferometry to readout the amplitude of that axis oscillation. The sensitivity, measurement range, bandwidth, responding time, power consume etc. performances are much better than electronic measurement sensors due to the light features. The other prior feature is about size. The MOEMS gyroscope can be fabricated by MEMS technology: the vibration part is already made by MEMS technology; the simulation discussion will be introduced in chapter 6. The optical interferometer parts are all standardization devices, like VCSEL, optical chip (Y-branch coupler), PIN etc. The size all matches with vibration structure. And the micro and optical parts can be separation encapsulation, which bring many advantages to the later assembly and maintenance.

The relative parameters of the angular motion can be calculated by integrating equation (4.58). This results in the equation below which indicates angular displacement, θ which is useful for navigation systems directly.

The angular movement is the integral of angular rate:

$$\Delta\theta = \int \Omega dt = \varphi_m \int_{t1}^{t2} \frac{I_0}{\sin(\omega_d t)} dt = [\varphi_m \frac{1}{\omega_d} \ln\left|\tan(\frac{\omega_d t}{2})\right| + C] \int_{t1}^{t2} I_0 dt \qquad (4.60)$$

From equation (4.59), the operator of navigation would indicate the angular movement variation value $\Delta\theta = \theta_{t2} - \theta_{t1}$, which feedback signal would emendate the application during the steering.

Therefore for any intensity readout the angular movement value can be calculated as $\Delta\theta$ due to the reference frame, by means of a simple digital signal processor circuit attached to the optical readout of the MOEMS device.

If equation (4.59) is differentiated, the rotation acceleration is obtained shown in equation (4.61).

$$\ddot{\theta} = \frac{d\Omega}{dt} = \varphi_m \frac{\dot{I}_0 \sin(\omega_d t) - I_0 \omega_d \cos(\omega_d t)}{\sin^2(\omega_d t)} \qquad (4.61)$$

This is another useful output signal to control the system's stability. From equation (4.61), the signal is fast attenuation signal as the expectation.

4.3 MOEMS Vibration Gyroscope Compare with Optical Gyroscope Based on Sagnac Effect

The Sagnac effect is the relative phase shift between two beams of light that have traveled an identical path in opposite direction in a rotating frame. The explanation of the Sagnac effect is simple for the inertial frame of reference. The motions of the mirrors during the light transit time between mirrors causes the clockwise and counter-clockwise waves to be reflected at different points of space, which leads to an optical path difference. Modern fiber-optic gyroscopes used for navigation are based on this effect. They allow highly accurate measurements of rotation rates down to about 0.1° per hour. The schematic setup of a

Sagnac interferometer is shown in figure 14. Light is decomposed into two beams by a 50:50 beam splitter, with one traveling CW and the other CCW around a polarization-maintaining single-mode glass-fiber loop. The two beams interfere after passage through the loop, and the interference signal is measured with a photodiode. If only reciprocal effects are involved in the experiment, then the two beams interfere constructively relative phase shift $\Delta\phi \neq 0$. If $\Delta\phi \neq 0$, then non-reciprocal effects occur, one of them being the Sagnac effect that results from rotation of the fiber loop during the measurement.

The corresponding phase difference between the two beams is:

$$\Delta\phi_{Sagnac} = \frac{8\pi A}{c\lambda}\Omega \quad (A = \pi R^2) \tag{4.62}$$

where, A is area of ring fiber round.

It is interesting to note that although the above calculation is over-simplified (e.g., the speed of light in vacuum, $c = 3\times10^8 m/s$, was assumed instead of that in the glass fiber) it yields the correct result. Exact relativistic calculations show that the phase shift is indeed independent of the material of the wave guide and the above equations apply.

Since the Sagnac effect was discovered, this theory is applied to manufacture the whole optical gyroscope such as laser gyroscope, ring gyroscope, and fiber optical gyroscope etc. The fiber optical gyroscope systems are hasty developed due to many advantages like no movement parts inside, high precision output, long consumption etc.

Another hand, the Sagnac effect method is based on two light beams path-length different created by rotation speed. The long distance light path is required because of the light speed. So the disadvantages of Sagnac effect gyroscope system are large size and weight, complex fabrication processes due to long fiber optical or optical integrated chip.

At mention above, in MOEMS gyroscope the light phase shift created by rotation velocity is described like:

$$\Delta\phi_{MOEMS\_Gyro} = \frac{4\pi}{\lambda}x_0 + \frac{4\pi}{\lambda}\frac{2x_{max}Q_y}{\omega_y}\Omega\sin(\omega_d t) \tag{4.63}$$

Because $\frac{4\pi}{\lambda}x_0$ is constant number, which is defined by initialization interferometer cavity length.

$$\Delta\phi_{MOEMS\_Gyro} - \frac{4\pi}{\lambda}x_0 = \frac{8\pi}{\lambda}\frac{x_{max}Q_y}{\omega_y}\Omega\sin(\omega_d t) \qquad (4.64)$$

Assuming, at the same input rotation velocity for each gyroscope system, two phase shift ratio are

$$\frac{\Delta\phi_{MOEMS\_Gyro} - \frac{4\pi}{\lambda}x_0}{\Delta\phi_{Sagnac}} = \frac{8\pi}{\lambda}\frac{x_{max}Q_y}{\omega_y}\Omega\sin(\omega_d t)/\frac{8\pi A}{c\lambda}\Omega \qquad (4.65)$$

$$\left|\Delta\phi_{MOEMS\_Gyro}\right| = \left|(\frac{x_{max}Q_y}{\omega_y}\frac{c}{A})\Delta\phi_{Sagnac}\right| + \frac{4\pi}{\lambda}x_0 \qquad (4.66)$$

Here $\frac{x_{max}Q_y}{\omega_y}\frac{c}{A} \geq 1$, which means the sensitivity of MOEMS gyroscope system is higher than optical gyroscope using Sagnac effect method. So the MOEMS gyroscope design is satisfied to civilization and military user.

4.4 Experimental Results of Fiber Optical Interferometry Read-out System

In our experiment, the sensing probe was held on a multi-axis translation stage; a polished wafer was used as the object and was mounted on a nano-positioner. The nano-positioner incorporates active error compensation, capacitive displacement sensor and DAC interface, and thus it can be controlled to establish position measurement with a resolution of 1 nm. The probe was aligned perpendicular to the wafer and separated from it with a very small air gap. The probe and the nano-positioner were mounted on a base plate and put in an environmental chamber on top of a vibration isolation table to isolate external variation that can influence the stability of the displacement set-up.

4.4.1 Sensitivity

The sensitivity of the sensor in response to the cavity length change is obtained by the derivative I_0.

$$S(x) = \frac{dI_0}{I_i \cdot dx} = 8\pi n \cdot \int_{\lambda-BW/2}^{\lambda+BW/2} \frac{I_0}{I_i} dx$$

$$= 8\pi n \cdot \int_{\lambda-BW/2}^{\lambda+BW/2} \{1 + 2\sqrt{\beta(1-\beta)} \cos[\frac{4\pi}{\lambda} x_0 + \frac{8\pi A_d Q_y}{\lambda \omega_y} \Omega \sin(\omega_d t)]\} dx$$

(4.67)

where n is the refractive index of the medium in the fiber optical interferometer cavity. Eq. (4-67) can be used to calculate the sensitivity and Eq. (4.35) can be used to calculate the signal amplitude of an fiber optical interferometer sensor with any mirror combination and at any physical cavity length x, provided that the distribution function of the light source is known. Figure 4.12 shows an example of the intensity and the sensitivity as a function of the cavity length x for a fiber optical interferometer sensor with 30% reflective films, zero angular misalignment, and at 1300 nm wavelength.
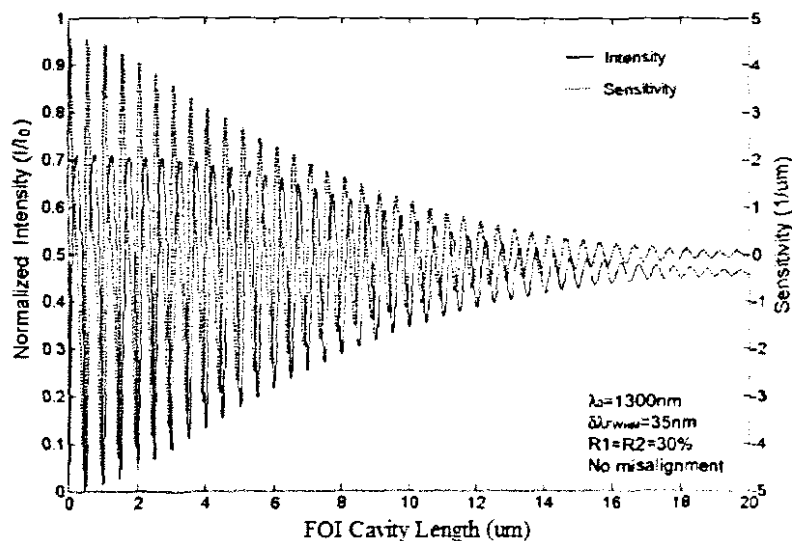
Figure 4.12: Interference Fringes and Sensitivity as a Function of Optical Path Length of a Typical Low-Finesse FOI Sensor

Sometime it is of more interest to know the maximum sensitivity of an FOI sensor designed for dynamic measurements of weak perturbations, such as acoustic waves and dynamic pressure (Xu, Geiger, and Dakin, 1995). For a low-finesse FOI, the maximum sensitivity usually occurs at the quadrature points of the transfer function when an LED or a SLED is used, which are

$$x_{min(S)} = \frac{(2m+1/2)\lambda}{4n}, \text{ for the sensitivity valleys}$$

(4.68)

$$x_{max(S)} = \frac{(2m+3/2)\lambda}{4n}, \text{ for the sensitivity peaks}$$

(4.69)

where m=0, 1, 2, ..., is the interference fringe order number, and $I_{min(S)}$ and $I_{max(S)}$ are the cavity lengths corresponding to the sensitivity peaks and valleys, respectively.

Many researchers have proved this in the past. However, this conclusion is valid only for a low-finesse and a narrow source bandwidth. For example, the maximum sensitivity point in the transfer function will move to shorter cavity length as the finesse increases and to longer cavity length as the source bandwidth increases. These short and long shifts can not easily be observed directly from Eq. (4.66). For the sake of convenience, the positions of these maximum sensitivity points are called as "quasi-quadrature points" or "quasi-Q points".

4.4.2 Fringe Contrast

The fringe contrast C of a fiber optical interferometer (FOI) is defined as

$$C = [I_{max} - I_{min}]/[I_{max} + I_{min}]$$ (4.70)

where I_{min} and I_{max} are the fringe intensities at a peak and the valley next to the peak of the interference fringes, and x_P and x_V are the corresponding cavity lengths, respectively (Wolthius, Mitchell, Saaski, Hartl, and Afromowitz, 1991).

The peaks and valleys of the fringes occur at dI/dx = S(x)=0. By letting S(x)=0 in Eq. (4.67), the positions of the peaks and valleys may be computed. However, an analytical solution cannot be directly obtained from Eq. (4.67). When a narrow bandwidth Gaussian-type light source is used, which means $\delta\lambda \ll \lambda$, the fringe valleys and peaks occur at

$$x_{min} = \frac{2m\lambda}{4n}, \text{ for the valleys}$$ (4.71)

$$x_{max} = \frac{(2m+1)\lambda}{4n}, \text{ for the peaks}$$ (4.72)

However, this approximation becomes invalid when the source bandwidth is comparable with the wavelength. Numerical analysis has to be used to locate the peaks and valleys more accurately as shown in figure 4.13.
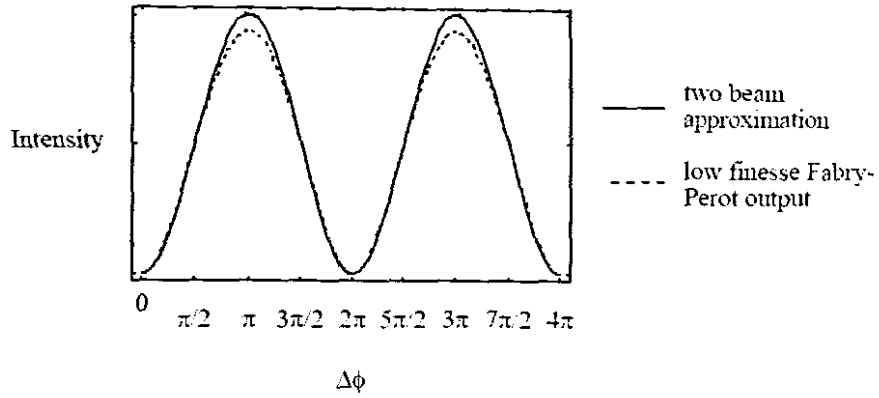
Figure 4.13: Low finesse FOI output and two beam approximation

4.4.3 Dynamic Range

The dynamic range of an FOI sensor with linear operation is defined as the maximal magnitude of the measurand without significant distortion. Obviously, the maximal magnitude of the measurand is absolutely determined by the allowed maximal cavity length change. Here, for the sake of continuity, we define the dynamic range as the maximum cavity length change Δx, in which the variation of the sensitivity $S(x)$ is within 3-dB from its peak, a common number used to define the response flatness of a sensor or a system, thus

$$\Delta S = \left| [S(x) - S(x_{\min}, x_{\max})] / S(x_{\min}, x_{\max}) \right| \le 50\% \tag{4.73}$$

$$\Delta x = 2 \times \left| x - x_{\min,\max} \right| \tag{4.74}$$

Other linearity bounds may be used for the definition of a linear region and dynamic range depending on the specific applications. In order to convert the dynamic range Δx into that of the measurand, an equation relating the cavity length change and the measurand is required, that means the results are different for different sensor configurations (Cox and Jones, 1983).

4.4.4 Sensor Stability

An experiment on our sensor's long-term stability was also conducted when the wafer was fixed. In this experiment, both the output of the sensor and temperature inside the sensor-containing chamber were monitored as a function of time, and data were collected at a sampling rate of 1 data/s for 24 hrs. The result is shown in figure 4.14. It can be seen that the sensor output drifts with time, the drift is strongly correlated with the chamber temperature and it is recoverable when the temperature recovers. This can be explained by the fact that the air gap was established with mechanical fixtures which expand/contract in dimension

92

when the temperature changes. The output change of our sensor is thus to a certain extent the response to the displacement change induced by temperature (Arya, Vries, Murphy, Wang, and Claus, 1995).
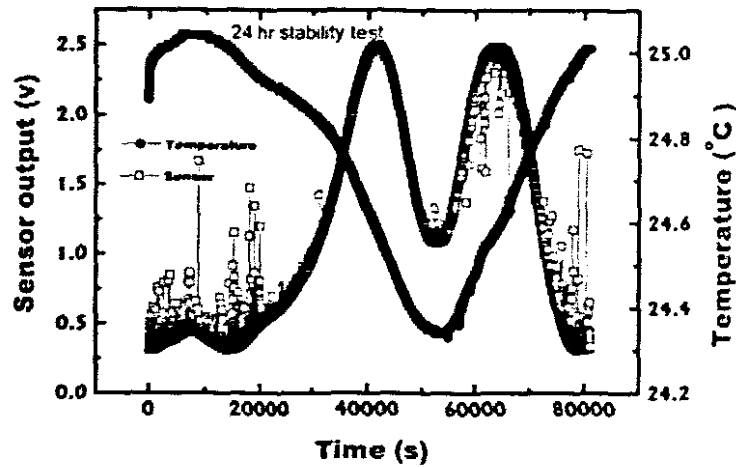
Figure 4.14: Sensor Stability Test Result

The fringe pattern of the fiber optical interferometer is simulated by Matlab about the relation between the output intensity of interferometer and the various parameters of the fiber optical cavity, as shown in figure 4.15. The wavelength of light source, the reflected of two surfaces and parameters of the fiber or waveguides can be adjusted in this program and the whole program is attached in appendix B.
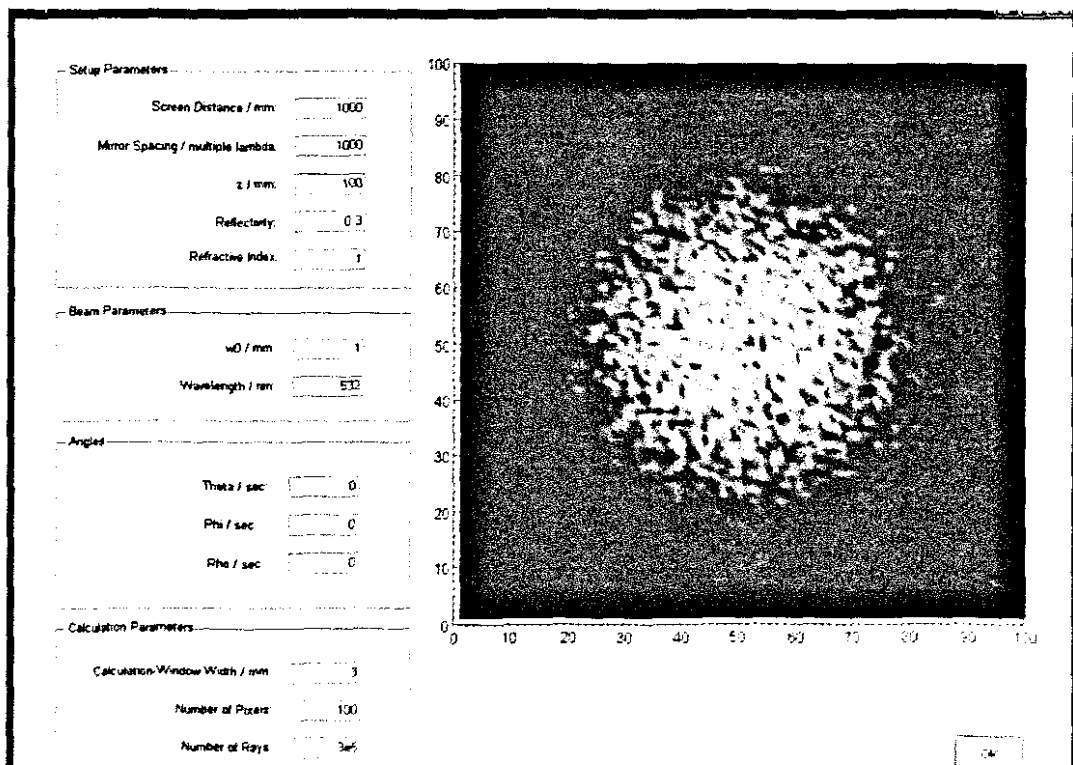
Figure 4.15: Simulation of Output Intensity of Fiber Optical Interferometer

93

4.5 Rotation Direction Factorial of MOEMS Gyroscope System

The rotation rate $\vec{\Omega}$ direction is determined by two parameters, which are the direction of driving velocity in x-axis, the movement direction of static mass in y-axis as shown in figure 4.16.

$$\vec{\Omega} = \vec{v} \times \vec{a} \qquad\qquad (4.75)$$
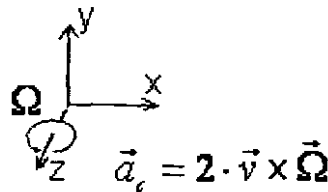
Figure 4.16: Ideal Model of Coriolis Force Theory

The driven velocity direction is determined by phase shift of input *AC* voltage, assuming the right direction is positive. If the rotation direction is anticlockwise and the driven velocity in positive of x-axis as shown in figure 4.16, the static mass would move up in positive direction of y-axis. Opposite this processes, the mass moving direction is determined by the output intensity changing, which means the value of output current changing can present the mass movement direction. So the mass movement direction and driven velocity direction could determine the rotation rate direction. The directions are defined in table 4.1. The rotation rate determined method described in table 4.2.

Table 4.1: The Direction Definitions

Mass Movement Direction $\vec{M}$	Driven Velocity Direction $\vec{v}$	Rotation Rate Direction $\vec{\Omega}$
Up +	Right +	counter-clockwise +
Down -	Left -	Clockwise -

Table 4.2: The Rotation Rate Direction Determination

Driven Velocity Direction $\vec{v}$	Mass Movement Direction $\vec{M}$	Rotation Rate Direction $\vec{\Omega}$
+	+	+
+	-	-
-	+	-
-	-	+

From table 4.2, we find the rotation direction is the XOR function results between driven direction and mass movement direction. The phase signal of driven voltage and the phase shift signal of the output intensity put into the XOR gate as the two inputs, then the positive and negative of the output signal can determine the rotation direction, as shown in figure 4.17.
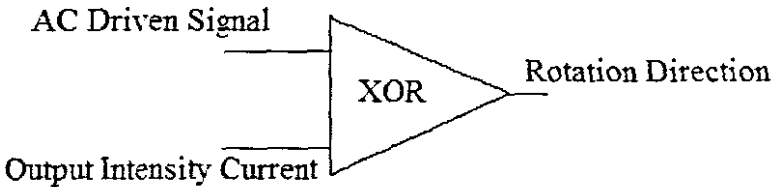
Figure 4.17: Rotation Direction Indication Circuit

4.6 Summary

In chapter 4, the MOEMS operation principles and mathematical model evaluation is introduced and discussed. The reason to integrate the optical interferometer readout with MEMS two grades vibration damping structure using to response the Coriolis force is considering both micro size and high performances. Small size, low power consumption and low cost are always expected in the sensors; the high performances are most important features for the sensors. But normally, the size and performance are contradictory factor when the sensor is design. Either Small size with low performances or big size with high performances is useless to fit into application in the practice.

The current problems about gyroscope applications are the size and performance issues. The fiber optical gyroscope (FOG) has the high performances but heavy volume and big size, which are determined by Sagnac effect and current manufacture technique of fiber optical and other active optical devices. The MEMS gyroscope based on Coriolis effect development with MEMS fabrication technology has extreme micro size, simple structure and low cost; just the rotation rate measurement performances are not satisfied with the critical applications like military user due to the electrical and mechanical measurement methods.

This chapter is firstly introduced the basic characteristic of light, emphases described the light interferometric methods and structures. Based on the MEMS vibration gyroscopes introduction in chapter 3 and optical interferometer techniques, the MOEMS vibration gyroscope is proposed about operation principles and mathematics model including the micro vibration part based on Coriolis force theory and micro fiber optical interferometer displacement readout system based on light interference. Finally, there is giving the performances comparison between the MOEMS vibration gyroscope system and optical gyroscope system based on Sagnac effect, which illuminate the MOEMS vibration gyroscope can absolute achieve the performances of optical gyroscopes based Sagnac effect and be integrated on one chip. In next chapter 5, the solid model and further performances simulation will be discussed.

CHAPTER FIVE

MOEMS GYROSCOPE DESIGN, MODELING, AND PERFORMANCE SIMULATION

In this chapter, the MOEMS gyroscope structure design, modeling and performances simulation would be introduced and discussed including the signal perturbation form both mechanical and optical sides. There are many micro structures possible for the mechanical part (MEMS vibratory part). The few typical vibratory structures are proposed according to Coriolis force theory. The fiber optical interferometer has not many variable structures. The optic-electronic converter circuits and the noise analyzing have been presented here.

5.1 Introductuion

Micromachined sensors measure angular velocity by utilizing the Coriolis effect, a direct consequence of a body's motion in a rotating frame of reference. In a fixed frame of reference, assume that a mass oscillates with velocity v_y (in the Y direction). If the frame of reference begins to rotate at a rate Ω_x about the X-axis, this mass is then subject to a Coriolis force and a corresponding acceleration equal to $2\Omega_x \, v_y$. The Coriolis acceleration, a_z, is perpendicular to the plane containing the velocity (oscillation) and the rotation vector. The Coriolis Effect may thus be thought of as an energy transfer process from a primary mode (Y) of oscillation into a secondary mode (Z) that can be measured. It is this excitation of the secondary resonance mode that forms the basis of detection using the Coriolis Effect. Highly symmetrical elements such as rings, cylinders, or disks use the resonant frequency, which is degenerate. There are two distinct modes of resonance sharing the same oscillation frequency. The resonant frequency degeneracy causes the primary mode (excitation signal) to be in phase-quadrature with the secondary mode (sense signal), thus maximizing coupling between the two modes and improving accuracy and sensitivity.

5.2 Design, Modeling Micro Vibration Parts of MOEMS Gyroscopes

Modeling the specific issues of gyroscopes at the micro-scale is important to understand theoretical operation and to optimize structural design or even steer the development of new fabrication technology. Since micro vibration part of MOEMS gyroscopes involve multiple physical domains like electronics, mechanics, electrostatics, dynamics and thermodynamics, complete static and dynamic analysis are very difficult. A practical way to do this is to derive simplified models for mechanical components and then use commercially available visual

simulators like Matlab and Coventorware, which are software to do analysis, calculation and signal processes.

Covenorware is a library of parameterized mechanical component models equipped with electrical properties. The library is composed of beams, plate masses, anchors, electrostatic comb drives, and electrostatic gaps etc. A micro vibratory part of MOEMS gyroscope can be formed by ARCHITECT Saber interconnecting these components. The schematic of the micro vibrato structure can be then loaded into the Analyzer modules simulator to perform both electrical and mechanical simulations. Imperfection sources can be included in the component models to evaluate manufacturability. Therefore the multi-domain simulation of the whole micro vibration system can be used to achieve optimal designs and gain understanding of special issues existing in MEMS fabrication technology.

Form chapter 4 discussions, the operation of vibratory part o MOEMS gyroscopes is based on Coriolis acceleration which is proportional to the velocity $\vec{v}$ of the vibrating structure and the external rotation rate $\bar{\Omega}$, but three parameters are in different axis. They are consisted of two gradation vibration system, which means the primary vibrating motion is the drive mode and the secondary motion due to the Coriolis force is the sense mode. The vibrating structure may be in the form of a vibrating beam or gimbal. The vibratory equation group is given by:

$$m_x \frac{du_x^2}{dt^2} + c_x \frac{du_x}{dt} + k_x u_x = F_{\text{electrostatics}} = F_e \sin(\omega_d t) \tag{5.1}$$

$$F_{coriolis} = -2m_x \cdot \bar{\Omega} \times \vec{v}_x \tag{5.2}$$

$$m_y \frac{du_y^2}{dt^2} + c_y \frac{du_y}{dt} + k_y u_y = F_{coriolis} \tag{5.3}$$

Here, m_x, m_y are respective mass of the driven and sense directions. c_x, c_y are respective damping of the driven and sense directions. k_x, k_y are respective elasticity index of the driven and sense directions. u_x, u_y are respective displacement of the driven and sense directions. $F_{\text{electrostatics}}$, $F_{coriolis}$ are respective driving force of the driven and sense directions. Those two typical damping vibration systems are linked by input rotation rate Ω based on Coriolis force theory (Mochida, Tamura, Ohwada, 1999).

First, let us build model for actuator driven, which is the necessary requirement in Coriolis force theory. Micro comb-driven structures are common used to provide electrostatic force as the actuator, drive the mass vibration. The configuration shows as figure 5.1.
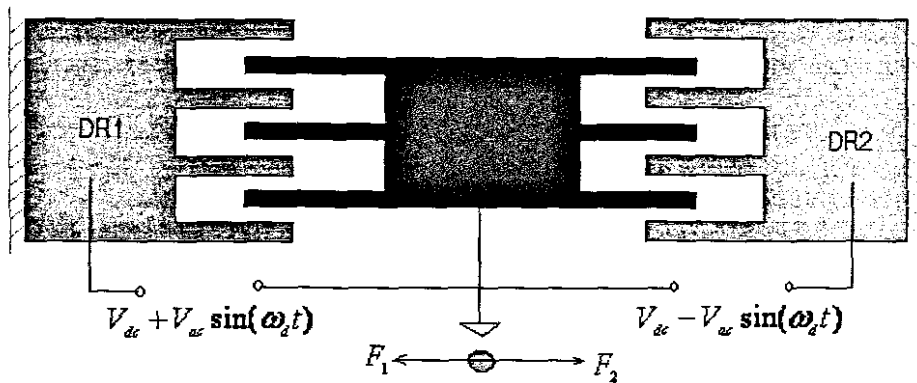
Figure 5.1: Vibratory Structure Electrostatics Driven Configuration

Let the tooth number of comb-driven be *N*, the intersection area between fixed tooth and moveable tooth is *A*, the distance of two teeth is *d*. The voltage applied for both *DR1* and *DR2* is $V_{dc} + V_{ac} \sin(\omega_d t)$ and $V_{dc} - V_{ac} \sin(\omega_d t)$. Here V_{dc} is offset DC voltage to avoid movement tooth lock-in with the fixed tooth. The V_{ac} AC voltage deicides the mass vibration frequency. The electrostatic force of both *DR1* and *DR2* is given by:

$$F_1 = \frac{1}{4} N\varepsilon \frac{A}{d \cdot x} [V_{dc} + V_{ac} \sin(\omega_d t)]^2 \tag{5.4}$$

$$F_2 = \frac{1}{4} N\varepsilon \frac{A}{d \cdot x} [V_{dc} - V_{ac} \sin(\omega_d t)]^2 \tag{5.5}$$

The competitive electrostatic force is given by:

$$
\begin{aligned}
F_{electrostaic} &= F_1 - F_2 \\
&= \frac{1}{4} N\varepsilon \frac{A}{d \cdot x} [V_{dc} + V_{ac} \sin(\omega_d t)]^2 - \frac{1}{4} N\varepsilon \frac{A}{d \cdot x} [V_{dc} - V_{ac} \sin(\omega_d t)]^2
\end{aligned}
\tag{5.6}
$$

$$F_{electrostaic} = F_1 - F_2 = N\varepsilon \frac{b}{d} V_{dc} V_{ac} \sin(\omega_d t) \tag{5.7}$$

Here, $\varepsilon = 8.854 af / um$, *b* is the length of tooth. V_{dc} is direct current voltage; V_{ac} is amplitude of the alternating current voltage; ω_d is driven frequency.

Let $F_{electrostaic} = N\varepsilon \dfrac{b}{d}V_{dc}V_{ac}\sin(\omega_d t) = F_e \sin(\omega_d t)$, and substitute into equation (5.1),

$$m_x \frac{du_x^2}{dt^2} + c_x \frac{du_x}{dt} + k_x u_x = F_{electrostatics} = F_e \sin(\omega_d t) \tag{5.8}$$

$$\frac{m_x}{k_x}\frac{du_x^2}{dt^2} + \frac{c_x}{k_x}\frac{du_x}{dt} + u_x = \frac{F_e \sin(\omega_d t)}{k_x} \tag{5.9}$$

Let $c_x = \dfrac{\sqrt{k_x m_x}}{Q_x} = 2\xi_x \sqrt{k_x m_x}$, $\omega_x = \sqrt{\dfrac{k_x}{m_x}}$

The transform function is given by,

$$\frac{1}{\omega_d^2}\cdot s^2 \cdot Y(s) + 2\xi_x \frac{1}{\omega_x}\cdot s \cdot Y(s) + Y(s) = \frac{F_e}{k_x}X(s) \tag{5.10}$$

$$\frac{Y(s)}{X(s)} = \frac{\dfrac{F_e}{k_x}}{\dfrac{s^2}{\omega_d^2} + \dfrac{2\xi_x s}{\omega_x} + 1} \tag{5.11}$$

The displacement solution is given by,

$$u_x = u_{max}\sin(\omega_d t - \alpha) \tag{5.12}$$

Here, the vibration amplitude is given by

$$u_{max} = \frac{F_e}{k_x}\frac{1}{\sqrt{(1-(\frac{\omega_d}{\omega_x})^2)^2 + (\frac{2\xi_x \omega_d}{\omega_x})^2}} \tag{5.13}$$

The vibration phase is given by,

$$\alpha = \arctan(\frac{\dfrac{2\xi_x \omega_d}{\omega_x}}{1-(\dfrac{\omega_d}{\omega_x})^2}) \tag{5.14}$$

The driven vibration movement equation made by comb-driven is given by,

$$u_x = \frac{F_e}{k_x} \frac{1}{2\xi_x \sqrt{1 + (\frac{1}{\tan\alpha})^2}} \cdot \sin(\omega_d t - \alpha) \qquad (5.15)$$

Adjusting the phase shift of AC power source, let the alternating current driving signal be like $V_{ac}\sin(\omega_d t + \alpha)$, the driven displacement equation can be reduced to

$$u_x = \frac{F_e}{k_x} \frac{1}{2\xi_x \sqrt{1 + (\frac{1}{\tan\alpha})^2}} \cdot \sin(\omega_d t) \qquad (5.16)$$

The velocity of driven axis is derivative of vibration displacement, then

$$\vec{v}_x = \frac{F_e}{k_x} \frac{\omega_d}{2\xi_x \sqrt{1 + (\frac{1}{\tan\alpha})^2}} \cdot \cos(\omega_d t) \qquad (5.17)$$

From driven velocity equation, the driven vibratory velocity is direct proportion with electrostatics F_e and driven frequency ω_d, and inverse proportion with the elastic index k_x of driven axis.

Based on Coriolis force theory, there are variable frequency input rotation rate $\Omega(t) = R\cos(\omega_R t)(\text{deg}/ s)$, vertical with the driven axis. Here, the R is amplitude of input rotation rate, the ω_R is the frequency of the rotation rate. Then the Coriolis force is given by

$$F_{coriolis} = 2m_x \cdot \vec{\Omega} \cdot \vec{v}_x = 2m_x \cdot \frac{\pi}{180} R\cos(\omega_R t)\frac{F_e}{k_x} \frac{\omega_d}{2\xi_x \sqrt{1 + (\frac{1}{\tan\alpha})^2}} \cdot \cos(\omega_d t)$$

$$= \frac{\pi R m_x F_e \omega_d}{360\xi_x k_x \sqrt{1 + (\frac{1}{\tan\alpha})^2}} [\cos(\omega_d + \omega_R)t + \cos(\omega_d - \omega_R)t] \qquad (5.18)$$

At sense axis, there is the vibration damp system as well, so the vibration equation is given by

$$m_y \frac{du_y^2}{dt^2} + c_y \frac{du_y}{dt} + k_y u_y = F_{coriolis} \qquad (5.19)$$

101

The sense displacement solution is given by

$$u_y = y_+ \cos[(\omega_d + \omega_R)t - \phi_+] + y_- \cos[(\omega_d - \omega_R)t - \phi_-] \tag{5.20}$$

In the above equation, both positive and negative of amplitude and phase are given by

$$y_+ = \frac{\pi R m_x F_e \omega_d}{360 \xi_x k_x k_y \sqrt{1 + (\frac{1}{\tan \alpha})^2}} \cdot \frac{1}{\sqrt{[1 - (\frac{\omega_d + \omega_R}{\omega_y})^2]^2 + (\frac{1}{Q_y} \frac{\omega_d + \omega_R}{\omega_y})^2}} \tag{5.21}$$

$$y_- = \frac{\pi R m_x F_e \omega_d}{360 \xi_x k_x k_y \sqrt{1 + (\frac{1}{\tan \alpha})^2}} \cdot \frac{1}{\sqrt{[1 - (\frac{\omega_d - \omega_R}{\omega_y})^2]^2 + (\frac{1}{Q_y} \frac{\omega_d - \omega_R}{\omega_y})^2}} \tag{5.22}$$

$$\phi_+ = \arctan \frac{\frac{1}{Q_y} \frac{\omega_d + \omega_R}{\omega_y}}{1 - (\frac{\omega_d + \omega_R}{\omega_y})^2} \tag{5.23}$$

$$\phi_- = \arctan \frac{\frac{1}{Q_y} \frac{\omega_d - \omega_R}{\omega_y}}{1 - (\frac{\omega_d - \omega_R}{\omega_y})^2} \tag{5.24}$$

Because $\omega_R \ll \omega_d$, so $y_+ \approx y_-$, $\phi_+ \approx \phi_-$, then the amplitude and phase of the sense axis is reduced to

$$y_+ \approx y_- \approx y_0 = \frac{\pi R m_x F_e \omega_d}{360 \xi_x k_x k_y \sqrt{1 + (\frac{1}{\tan \alpha})^2}} \cdot \frac{1}{\sqrt{[1 - (\frac{\omega_d}{\omega_y})^2]^2 + (\frac{1}{Q_y} \frac{\omega_d}{\omega_y})^2}} \tag{5.25}$$

$$\phi_+ \approx \phi_- \approx \phi_0 = \arctan \frac{\frac{1}{Q_y} \frac{\omega_d}{\omega_y}}{1 - (\frac{\omega_d}{\omega_y})^2} \tag{5.26}$$

Finally, the sense vibration equation described by Coriolis force is given by,

$$u_y = 2y_0 \cos(\omega_d t - \phi_0) \tag{5.27}$$

The Coriolis force vibration equation shows the displacement of sense axis is direct proportion with m, and electrostatics F_e, and inverse proportion with the elastic index k of both driven axis and sense axis (Soderkvist, 1994).

When the driven frequency is equal to nature frequency of driven axis, $\omega_d = \omega_x$, the phase shift of driven axis vibration is $\alpha = 90^0$. Further, if driven axis nature frequency is equal to sense axis nature frequency, $\omega_x = \omega_y$, then the vibration amplitude of sense axis is reduces to

$$y_0 = \frac{\pi R m_x F_e \omega_d Q_x Q_y}{180 k_x k_y} \tag{5.28}$$

The amplitude of the input rotation rate is coming out from equation (5.28),

$$R = \frac{180 k_x k_y y_0}{\pi m_y F_e \omega_d Q_x Q_y} \text{ (deg/s)} \tag{5.29}$$

According to the above two gradation vibration system discussion, the mathematics model is designed, shown in figure 5.2.
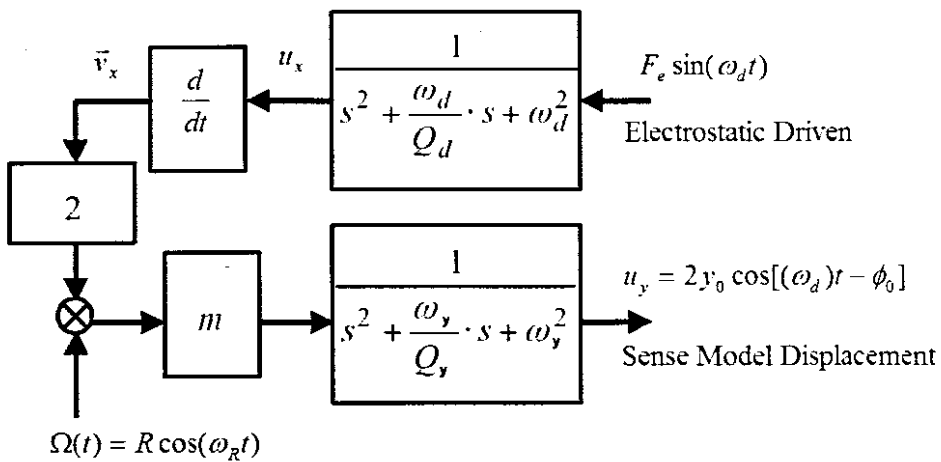
Figure 5.2: Coriolis Effect Vibration Model of the Transducer

The Coriolis acceleration is an amplitude modulated signal with the carrier at the drive frequency ω_d. In response to a sinusoidal rotation rate signal with amplitude R, the Coriolis acceleration in a single sideband is given by $\frac{1}{\sqrt{2}}\frac{m_x}{m_y}u_{max}\omega_d R$, where u_{max} is the amplitude of the vertical vibration. Large drive amplitude and higher drive frequency helps to increase the Coriolis acceleration. However, it becomes difficult to achieve a large amplitude motion at high frequency with 5V actuation at atmospheric pressure. In this gyroscope, $\frac{m_x}{m_y}=0.6$, $\omega_d = \omega_y = 32\pi kHz$ and $u_{max} \approx 200nm$. 1°/sec rotation about the Z-axis corresponds to 15.4µg ($g = 9.8m/s^2$) lateral Coriolis acceleration along the Y-axis (Lemkin and Boser, 1999).

In terms of sense, the transducer response to certain Coriolis acceleration is a function of sense resonant frequency ω_y as well as quality factor Q_y, and Qs if operating near sense resonance. Lower sense resonant frequency is desirable to improve the acceleration sensitivity at the cost of shock resistance. The transducer sensitivity is also affected by Brownian motion noise from the mechanical structure.

5.3 Signal Static Mass MEMS vibratory Structure Model in CoventorWare

For designing the micro vibratory structure, there are rules and functions to follow, which is discussed in last section. Firstly, the micro vibratory structure must vibrate in 2-dimention, the driven axis and the sense axis. The first vibration axis is driving axis, which is actuated by electrostatics force from the outside alternating current source and keeping vibration during power on. The second vibration axis is sense axis, vibrated during input rotation rate due to the Coriolis Effect. As the discussion above section, the signal mass micro vibration structure will be introduced and show the performances simulation.

The Z-plane Coriolis response vibration structure in this section uses a perforated rectangular plate mass suspended by four two-segment flexures, two comb drives, and three electrodes. The micro vibration structure is designed to resonate in its fundamental mode parallel to the substrate plane (Y direction) and is excited via two comb drives as shown in figure 5.3. If the vibration structure is subjected to an external angular velocity about the X-axis, the velocity of the mass in the Y direction results in a Coriolis force acting on the mass in the vertical Z direction of the substrate. Because the perforated mass and the rectangular electrodes include a parallel plate capacitor, the resulting oscillatory motion is electrically sensed in this direction, which enables determination of the inertially induced Z-

displacement, and hence rotation of the vibration structure about the X-axis (MEMS Design and Analysis Tutorials)
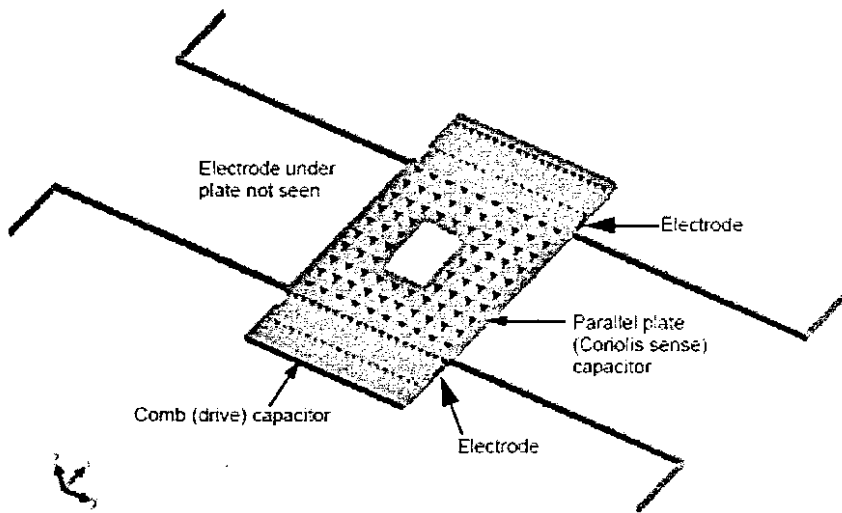
Figure 5.3: Micro Single Mass Vibration Structure with Straight Beams

The Coriolis acceleration, a_z, is perpendicular to the plane containing the velocity (oscillation) and the rotation vector. The Coriolis Effect may thus be thought of as an energy transfer process from a primary mode (Y) of oscillation into a secondary mode (Z) that can be measured. It is this excitation of the secondary resonance mode that forms the basis of detection using the Coriolis Effect. Highly symmetrical elements such as rings, cylinders, or disks use the resonant frequency, which is degenerate. There are two distinct modes of resonance sharing the same oscillation frequency. The resonant frequency degeneracy causes the primary mode (excitation signal) to be in phase-quadrature with the secondary mode (sense signal), thus maximizing coupling between the two modes and improving accuracy and sensitivity.

The micro vibration structure schematic, dimensions, and other geometrical properties, along with mechanical and electrical properties are designed by CoventorWare, and shown in figure 5.4. The properties are listed in table 5.1.
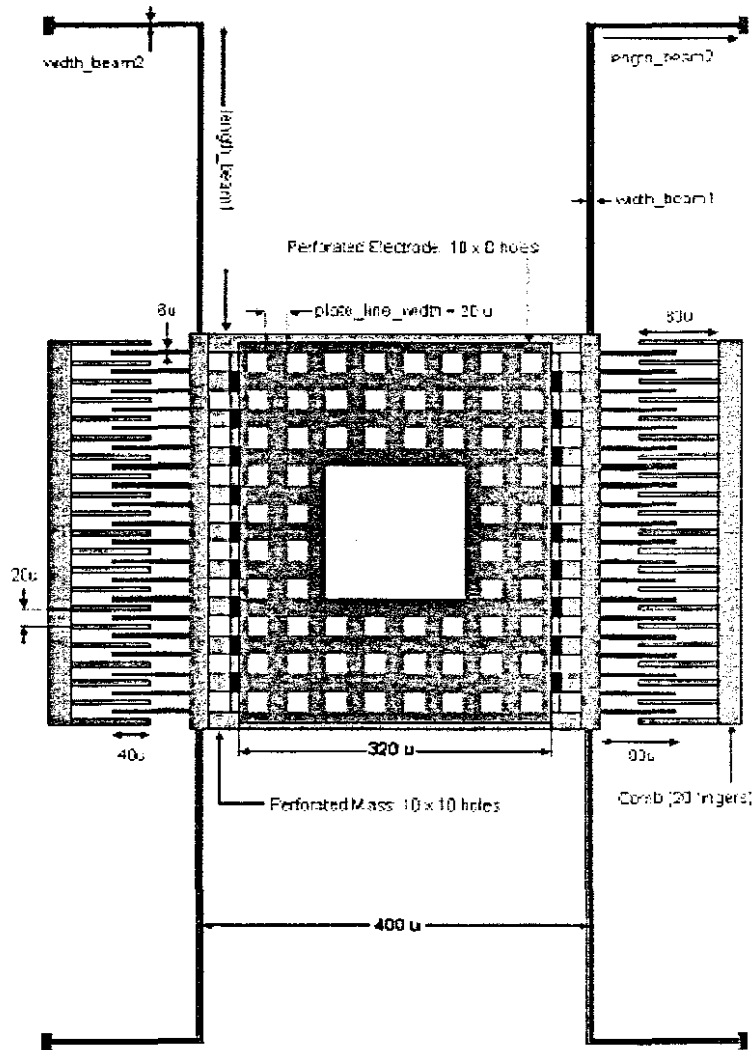
Figure 5.4: Micro Coriolis Response vibration Structure Dimensions

Layer thickness information is automatically extracted from the process file, and Young's modulus, Poisson's ratio, and density information is automatically extracted from the Material Properties Database file by CoventorWare, shown as in table 5.2.

Table 5.1: Micro Vibration Structure Properties

Properties	Variable Name	Value
Dimensions		
length of vertical beam suspensions	length_beam1	650u
length of horizontal beam suspensions	length_beam2	160u
width of vertical beam suspensions	width_beam1	8u
width of horizontal beam suspensions	width_beam2	8u
distance between perforation holes	plate_line_width	20u
plate size in X direction	plate_size_x	400u
plate size in Y direction	plate_size_y	400u
number of plate holes in X direction	plate_num_holes_x	10
number of plate holes in Y direction	plate_num_holes_y	10
length of comb fingers	finger_length	80u
width of comb fingers	finger_width	6u
distance of finger center lines	finger_pitch	20u
overlap of comb fingers	Finger_overlap	40u
number of fingers	finger_num	20
lateral offset of fingers	finger_lateral_offset	0
finger anchor width	finger_anchor_width	24u

Table 5.2: Material properties for Vibration Structure

Property	SILICON (substrate)	POLYSILICON (electrodes and proof mass)	Units
Elastic constants - E	1.69e05	1.6e05	MPa
Elastic constants - nu	3.0e-01	2.2e-01	
Density	2.5e-15	2.23e-15	kg/μm^3
Stress (x,y,z)	0	0	MPa
TCE	2.5e-06	4.7e-06	1/K
Thermal Conductivity	1.48e08	1.48e08	pW/μm $\cdot$ K
Specific Heat	7.12e14	1.0e14	pJ/kgK

5.3.1 Place and Connect Parametric Component Symbols in CoventorWare

In this sequence, you will place the parametric components used to build the vibration structure. Before beginning, consider how the symmetry of the design can be used to make

placing components and assigning their variables easier. Each component may require many parameter settings that include complex equations, negative signs, underscores, etc. These parameter definitions must be entered correctly to obtain correct results. By placing a component, entering its parameters, and then copying and pasting any additional components needed, you will usually only have to make changes in component orientation, and will not have to re-enter all the parameters. Figure 5.5 shows the schematic that will be created by the CoventorWare library.
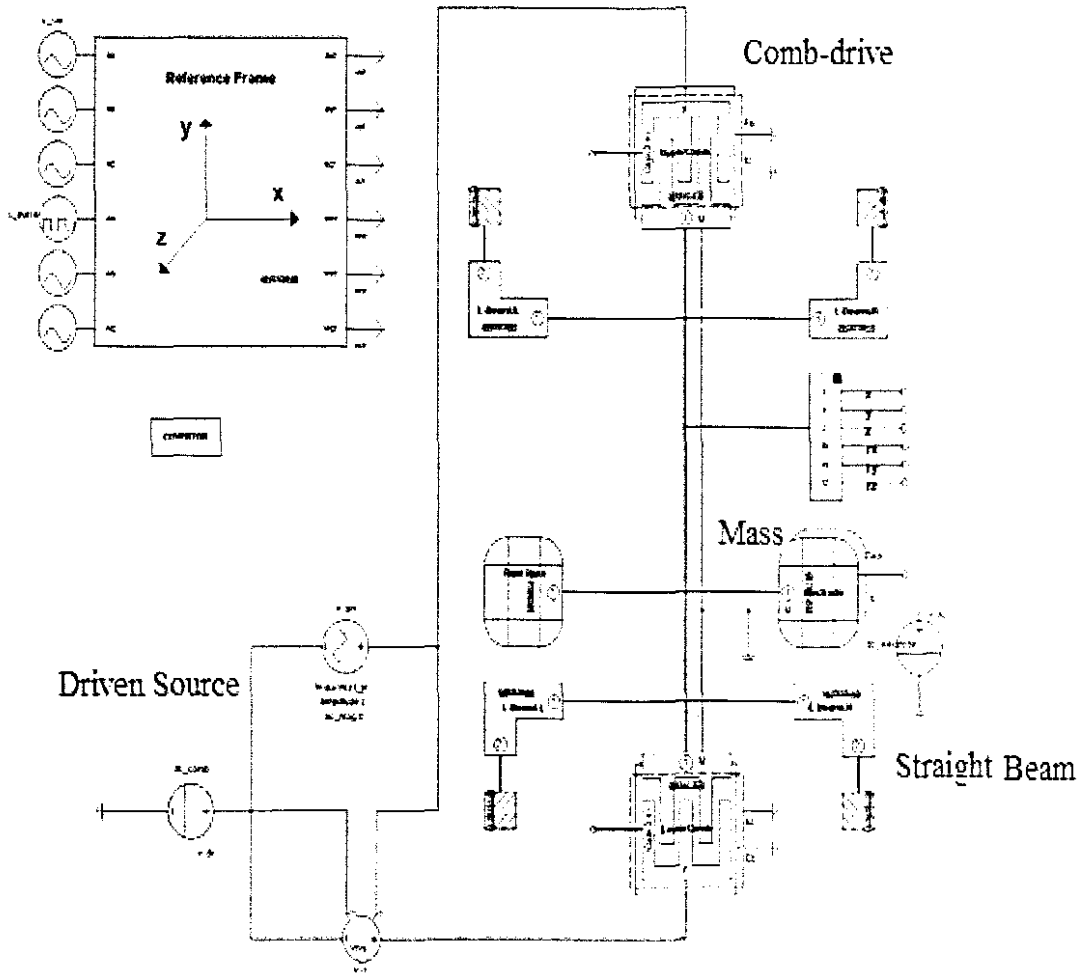
Figure 5.5: Micro Vibration Structure Schematic

The vibration structure consists of beams, a perforated rectangular plate mass, three rectangular electrodes, and two comb-drives. Beams are considered as purely mechanical components and are described in this system model using the parametric *EM* library component *beam*. The inertial behavior of the central plate of the gyroscope is captured in the parametric EM library component *rigid_plate*. A capacitor is formed by the perforated plate and the electrode. This capacitor is electrostatically represented by the *electrode* library component. Combs (whose mass is incorporated in the *rigid_plate*) are described in this system model using the *straight_comb* to represent the electrostatics. (See Appendix C)

During schematic creation, many parameters have been entered in the Properties window for each component. These parameters must be carefully selected and entered in order to maintain consistency. After all parameters are putted into components properties windows. The 2-dimension and 3-dimension model will be abstracted from the components with the parameters. There are shown as figure 5.6 and figure 5.7.
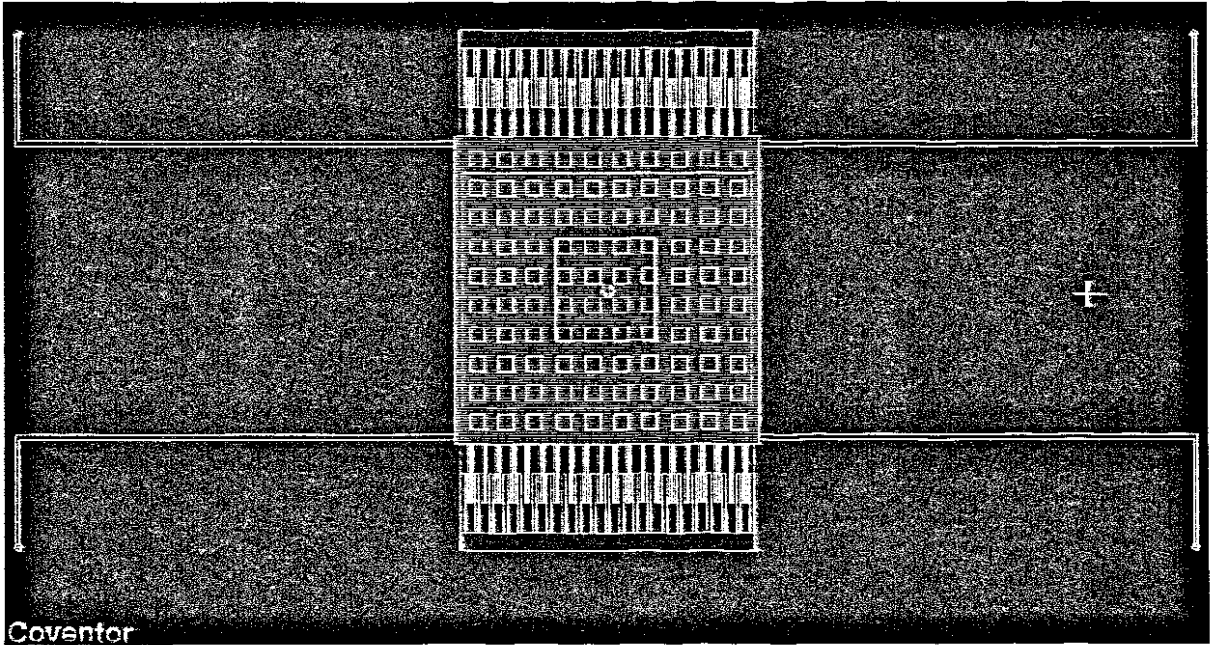
Figure 5.6: Two Dimensions View of Vibratory Structure
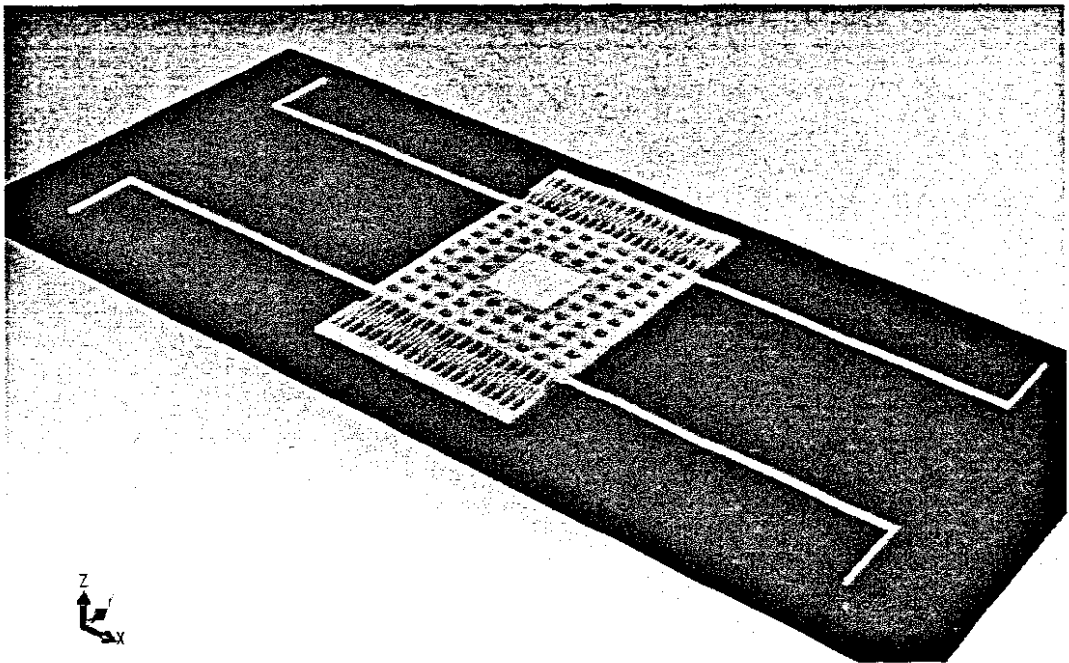
Figure 5.7: Three Dimensions View of Vibratory Structure

109

5.3.2 Vibratory Structure Architect Analysis Due to CoventorWare

Architect can simulate the mechanical behavior of the vibration structure in CoventorWare package. The simulation results can then be used to optimize the performance of the devices and redesign the structures.

5.3.2.1 Pull-in Voltage

In this analysis, the voltage of the electrode is increased from 0 to 5V. Perform a DC Transfer analysis on the z wire. Increase the voltage from 0 to 5 volts in steps of 0.25. As seen in the Pull-in voltage in figure 5.8, the mass pulls in at around 3.25 volts. The pull-in voltage can intuitionistic tell us the elasticity statue of the beams. Here the electric field is to present the elasticity index of beams. This character design depends on the outside DC power supply.
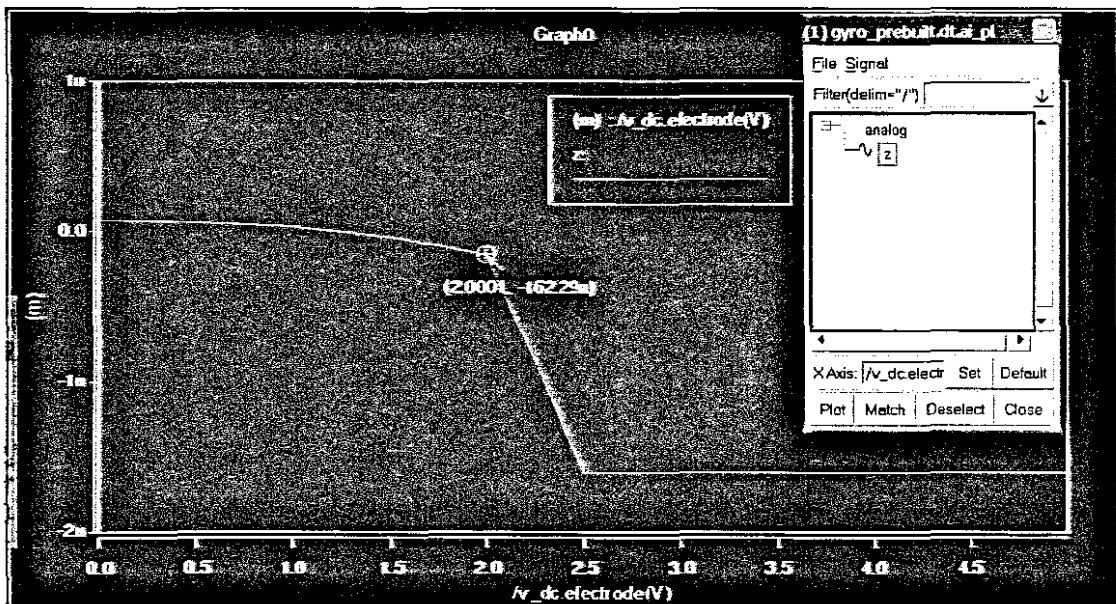
Figure 5.8: Plot Pull-in Voltage for Single Mass Structure

5.3.2.2 Impact of Driving Bias Voltage on Levitation

Run a DC transfer on the v_dc.v_dc_comb with an increasing bias voltage from -25 to 25 volts. Display results for the z signal as shown in figure 5.9.

Notice the symmetry in the plot. Levitation force is caused by vertical asymmetry due to the presence of the ground plate. On the bottom side field lines leave the stator fingers and go into the ground. On the top side the field lines leaving the stator fingers are forced to end at the movable finger top side, resulting in a net force upwards. This voltage is the DC part of

the comb-drive actuator voltage. Due to the gravity for the comb-drive, this electric field force supplies the levitation force beside of the beams support. Adjusting the driving bias voltage can change the gap distance between the comb-drive and the substrate. The result shows in the figure 5.9.
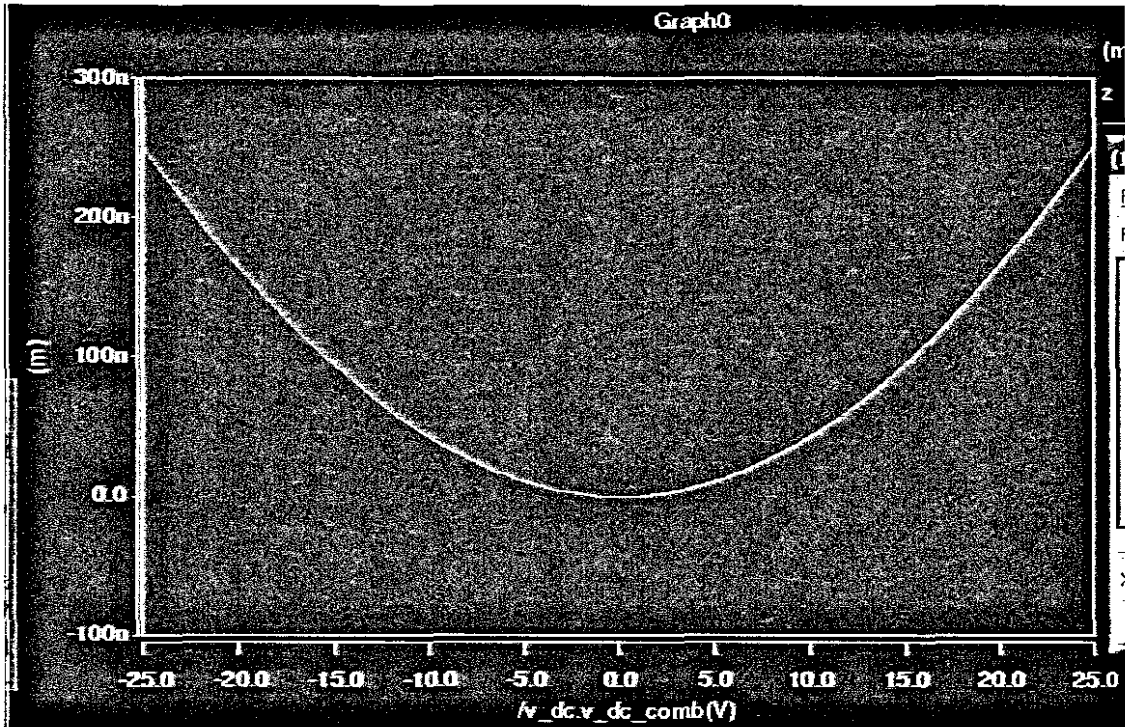
Figure 5.9: Evaluation Due to Bias Voltage

5.3.2.3 Resonance Frequencies (Natural Frequencies)

For Coriolis effect application, the match nature frequencies of the sense and drive vibration axis is important for the sensitivity and responding time etc. performances. Measurement nature frequencies of the structure are the pivotal factor to designer.

Perform an analysis of the device as all small AC signal sources are varied from 1 kHz to 50 kHz. List the signals for x, y, and z translations show as figure 5.10.
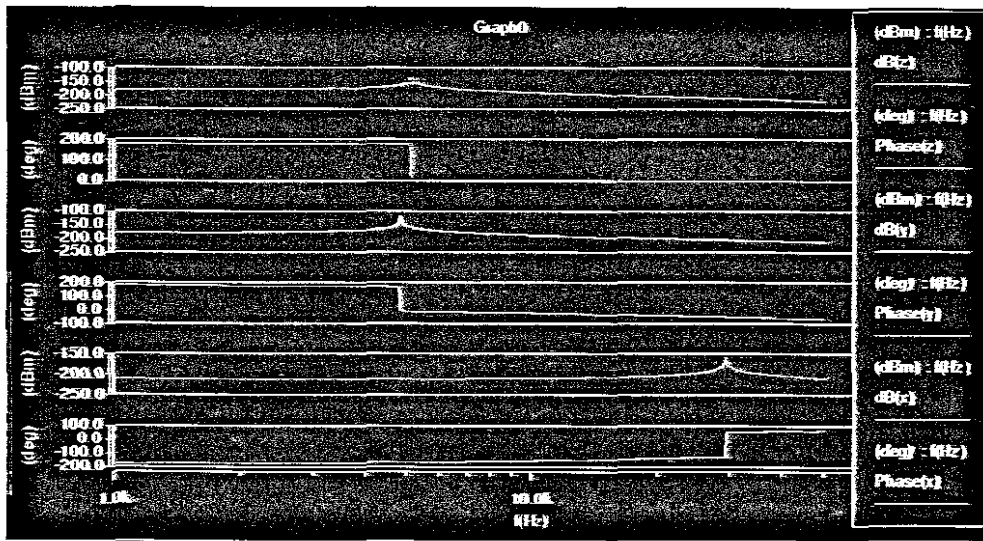
(a) List of Three Axis Resonance Frequencies
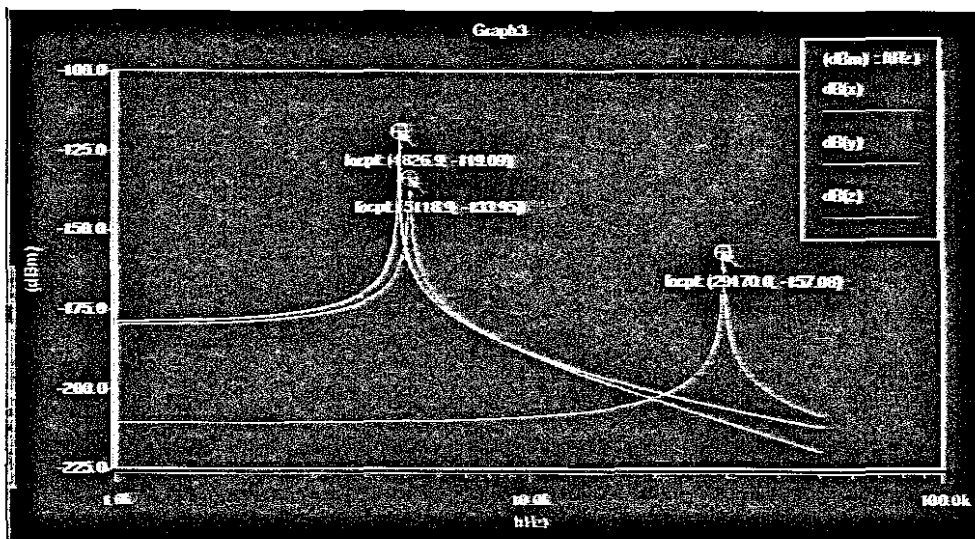
(b) Three Axis Resonance Frequencies Plot Together

Figure 5.10: Small Signal AC Analysis for Resonance Frequencies of Three Axes

5.3.2.4 Resonance Frequencies: Impact of Length_Beam1 Parameter

In this step vary the parameter *length_beam1*, which is the longer beam, vibratory mode, and main frequency control beam. The investigation is the impact on resonant frequencie from changing length of beam1. Those results help designer to modify and optimize the nature frequency of the y-axis, which can match the driven frequency from alternating current signal. The beam1 is main portion to supply the damping and effects on the frequency of y-axis.

Perform a vary analysis using looping commands to vary the length of beam1 in the outer loop while performing a small signal AC analysis in the inner loop. For the small signal analysis, use a frequency range from 1k to 50 k for 1000 points. Vary the beam length from 300u to 700u in increments of 5 (see Figure 5.11).

112
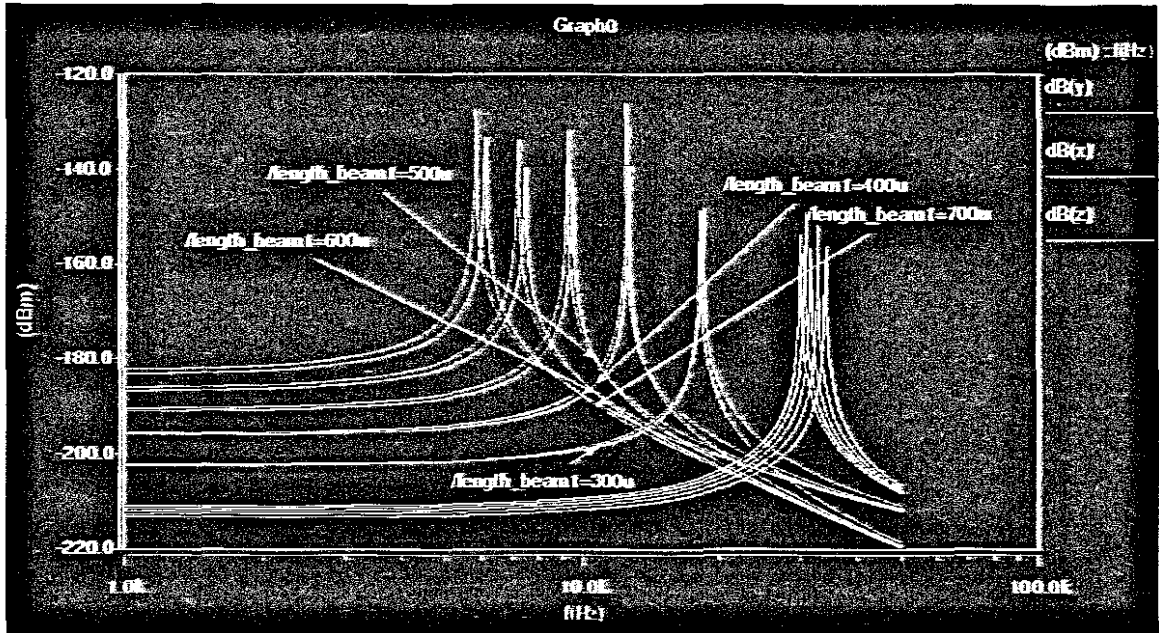
Figure 5.11: Resonance Frequencies for Varying Beam Lengths

When the lengths of horizontal beams increase, *y* and *z* mode resonance frequencies decrease while the *x* mode frequency remains almost the same.

The relative position of the *y* and *z* mode resonant frequencies change and the resonance matching occurs around *length_beam1* = 400μm.

For good cross talk performance, the *x* mode resonant frequency should be as far as possible from the *y* and *z* mode resonant frequencies, but these last two frequencies should not be too low.

5.3.2.5 The Beam and Mass Load Force Analysis

First of all, we must simplify this structure. For several conditions are satisfied, the whole vibration plate can be divided into two symmetrical parts, shown as figure 5.12. (Conditions: 1.the medium is regarded as vacuum, 2. the material is well-proportioned, 3. the boundary condition of two sides are same, 4. the whole structure is symmetrical) For each part, it receives F/2 force, viz. ma/2 (Seidel, Reidel, Kolbeck, Muck, Kupke, and Koniger, 1990).
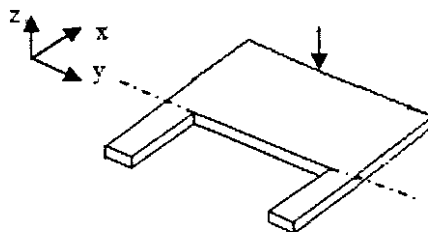
Figure 5.12: Half Size of Vibration Structure

113

Next, we will concentrate upon one beam because key quantity that affects the change of capacitance is displacement of top plate. And the displacement of top plate is namely the displacement of the free end of beams for the concentrative mass will not bend. Now just see one beam and analyze it, shown as figure 5.13.
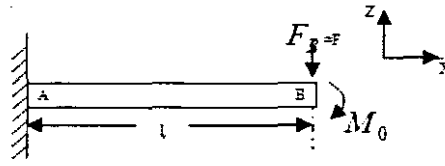
Figure 5.13: Statues of Force and Bending Moment Act on the Beam

M_0 is an assumptive bending moment. The real bending moment is M .

$$M = M_0 - \frac{1}{4}Fx \qquad (5.30)$$

Under the action on the beam, finally the beam's deformation is shown below
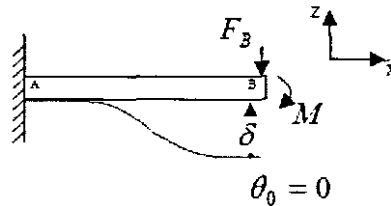
Figure 5.14: Beam Deformation Model

The rotation angle of the end, which connects with concentrative mass, is still zero when the displacement goes up to max, shown as figure 5.14. δ is the maximal displacement.

In terms of the particularity of this structure (two sides fixed), we use the theorem of energy—*Castigliano's Theorem* to require the max displacement of the beam in succession.

The denotation of strain energy is U.

$$U = \int_0^l \frac{M^2}{2EI_z}dx \qquad (5.31)$$

I_z is the moment of inertia to the axis Z.

$$I_z = \frac{bh^3}{12} \tag{5.32}$$

Apply $\theta_0 = 0$ to require bending moment

$$\begin{aligned}\theta_0 &= \frac{\partial U}{\partial M_0} \\ &= \int_0^l \frac{M}{EI_z} \frac{\partial M}{\partial M_0} dx \\ &= \frac{1}{EI_z} \int_0^l (M_0 - \frac{1}{4}Fx)dx = 0\end{aligned} \tag{5.33}$$

By solving this equation, the real bending moment is given by:

$$M_0 = \frac{1}{8}Fl \tag{5.34}$$

$$M = \frac{1}{8}Fl - \frac{1}{4}Fx = \frac{1}{4}F(\frac{l}{2} - x) \tag{5.35}$$

So the max displacement is given by:

$$\begin{aligned}\delta &= \frac{\partial U}{\partial F_B} \int_0^l \frac{M}{EI_z} \frac{\partial M}{\partial F_B} dx \\ &= \frac{F}{4EI_z} \int_0^l \left(\frac{l}{2} - x\right)^2 dx \\ &= \frac{Fl^3}{48EI_z}\end{aligned} \tag{5.36}$$

5.3.2.6 Gyroscope Thermo-mechanical Noise

The governing differential equation for the sensing mode is given by

$$m\ddot{y} + c\dot{y} + ky = F_C \tag{5.37}$$

Where F_C is Coriolis Force as Ω input.

The fluctuating force due to thermal noise for a system with a bandwidth Δf is given by

$$F_N = \sqrt{4k_B Tc\Delta f}\,(N) \tag{5.38}$$

The thermal noise equivalent rate signal can be found by equating the fluctuating force due to thermal noise to the coriolis force

$$2m\Omega_n \omega_d A_d = \sqrt{4k_B Tc\Delta f} \tag{5.39}$$

Substituting $c = \dfrac{m\omega_y}{Q_y}$, using $\varsigma_y = \dfrac{c}{2m\omega_y}$ and $Q_y = \dfrac{1}{2\varsigma_y}$

$$\Omega_n = \sqrt{\frac{k_B T\omega_y \Delta f}{m\omega_d^2 A_d^2 Q_y}}\,(rad/\sec) \tag{5.40}$$

According to the above equation, the thermo-mechanical noise equivalent angular rate could be reduced by using a large mass m, high driving frequency ω_d, large driving amplitude A_d, small bandwidth Δf and high Q (vaccum could be used to obtain high Q (Gabrielson, 1993).

Let us look at an example, suppose that the parameters of a vibration structure are: A_d=10um, m=1.2x10⁻⁹ Kg, f_d =1000Hz, Δf=100Hz and Q_y =1000, working at the room temperature (T=300K). The thermo-Mechanical noise equivalent rate signal is given $\Omega_n = 7.4 \times 10^{-4}\,rad/\sec = 0.004^0/\sec$.

5.3.2.7 Sensitivity and Monte Carlo Analysis

Sensitivity analysis is an alternate and very effective method for studying the impact of design parameters on a given performance measure such as resonance frequency, DC point displacement, transient amplitude, etc. With sensitivity analysis, the sensitivity to a parameter is calculated by a measurement-based perturbation method. A specified parameter p is perturbed from its nominal value, and the effect on a specified performance measure F for the design is determined as shown $sensitivity = \dfrac{\delta F}{\delta p}$.

To provide meaningful comparisons, the results are usually normalized: $sensitivity = (\Delta F / F)/(\Delta p / p)$, $\Delta F = sensitivity \cdot F \cdot (\Delta p / p)$.

116

Where *p* the nominal value of the perturbed parameter; Δp the amount by which the parameter is perturbed; *F* the nominal value of the performance measure; ΔF the amount by which the performance measure changes in response to the parameter perturbation.

Using the following process to execute the sensitivity analysis:

1. Increase the parameter value by the value defined in the Perturbation field.
2. Run the specified analyses.
3. Calculate the specified measurements.
4. Repeat steps 1-3 for each parameter in the Parameter List field.
5. Repeat steps 2 and 3 using the nominal parameter values.
6. Calculate the sensitivity based on the difference between the nominal and perturbed parameter values according to the equation for sensitivity given above.

In this section, we will investigate the sensitivity of the resonance frequency of the gyroscope's driving mode (*y*) to the following design parameters: *width_beam1*, *width_beam2*, *length_beam1*, and *length_beam2*, as well as the Young's Modulus and the height of the *poly* layer. Verify the results that appear in the report window (Figure 5.15).

```
------------------------------------------------------------------------
                        Sensitivity Report Options
------------------------------------------------------------------------

        Minimum sensitivity magnitude to report:      0
        Report sorted by:                             Value
        Sensitivity normalization:                    Normalized
        Normalization threshold:                      100E-15


------------------------------------------------------------------------
            Sensitivity of X at Maximum of MAG(y) in pfile ac
------------------------------------------------------------------------

                        Nominal Value = 6.4333k

                Part        Parameter      Nominal
    Instance    Type        Name           Value      Sensitivity   Bar-chart

    -           -           width_beam1    7u            1.41        ---------
    -           -           length_beam1   650u         -1.39        ---------
    -           -           poly_layer->elastic  160g    0.702       ----
    -           -           width_beam2    5u            0          .
    -           -           poly_layer->h  10u           0          .
    -           -           length_beam2   150u          0          .
```

Figure 5.15: MEMS Vibration Structure Sensitivity Report

The resonance frequency of the driving mode is most sensitive to the design parameter *length_beam1*. A sensitivity of -1.4 means that a 1% perturbation of the horizontal beam length results in a 1.4*1%= 1.4% decrease in the investigated resonance frequency. In absolute terms, increasing the horizontal beam length from 600μm to 606μm results in a decrease of the resonance frequency of 1.4%*Nominal Value*6μm/600μm=100.6Hz.

It is important to keep in perspective the absolute changes in parameters. A 1% change in the horizontal beam length *length_beam1* is 6µm, whereas a 1% change in horizontal beam width is 0.07µm. Due to inaccuracies in fabrication process, the designer would most likely expect changes in the beam width larger than 0.07µm and changes in the horizontal beam length of much less than 6µm. For this reason, it is worthwhile to scale the sensitivities shown above to a common absolute perturbation. We could then identify those dimensions whose changes push one or more of the key performance measures outside the desirable performance regime.

Let's assume that fabrication-induced deviations of the in-plane dimensions are up to 0.2um. Let's further assume that the acceptable driving frequency range is to within 150Hz from the nominal value (7.1869 kHz). Then, for instance, the absolute change in the driving frequency for a 0.2um change in *length_beam1* would be 0.2um/6um*100.6Hz = 3.35Hz, which is well within the acceptable range. Table 5.3 shows changes in the driving frequency due to 0.2um (absolute) perturbations of the all the in-plane design variables for this sensitivity analysis.

Table 5.3: Driving Frequency Change Due to Parameter Variations

Variable name	Nominal Value in µm	Expected change in µm	Perturbation (%)	Sensitivity	ΔF in Hz
length_beam1	650	0.2	0.0333	-1.4	-3.35
width_beam1	7	0.2	2.8571	1.05	215.61
width_beam2	5	0.2	4.0	0.351	100.9
length_beam2	160	0.2	0.1333	-0.351	-1.34

It is obvious that the width of the horizontal beams causes a problem. A change of 0.2 µm in *width_beam1* results in a change of 215.61Hz in the driving frequency, which is outside the acceptable design regime (defined as +/-150Hz of the nominal value). Thus, the sensitivity analysis has immediately given us an indication that the current design suffers from sensitivity to changes in the width of the horizontal beams which will most likely lead to yield problems during mass production of the current design.

In the next step we will use the statistical Monte Carlo analysis function to investigate the yield impact of the assumed parameter changes in more detail. Monte Carlo analysis uses component tolerances and statistical distributions to randomly vary system parameters during successive simulations. Trends in the data reveal the influence of particular

parameters on performance; you can then identify where to change tolerances to improve yield and reduce cost.

Run a Monte Carlo analysis on the resonance frequency in the Y direction with 500 sample points. The measure block will automatically record the resonance frequencies of all 500 Monte Carlo runs in the output plot file *measure_out*. Then *measure_out* serves as the input to the pfhistogram block, which converts the statistical data into a histogram plot file called *histogram_out*. Display the analysis results in CosmosScope as shown in figure 5.16.
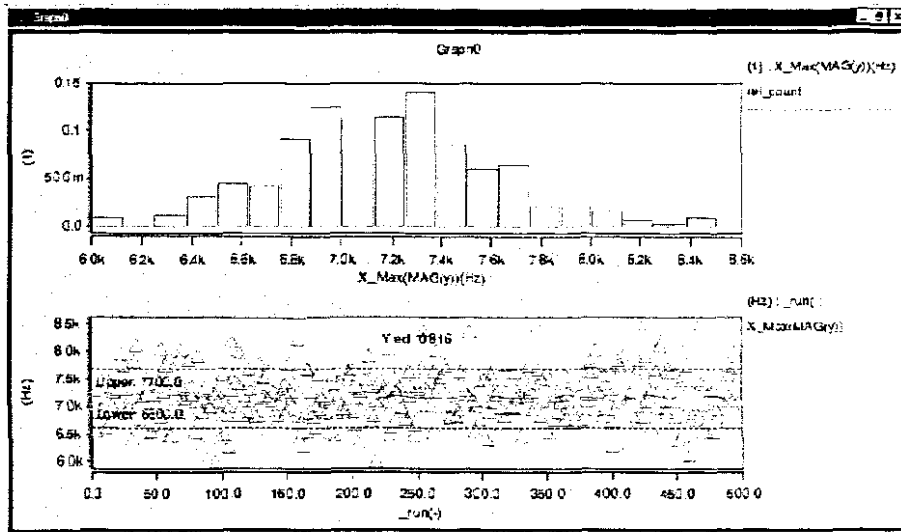
Figure 5.16: Results of the Monte Carlo Analysis

The appearance of the graphs in Figure 5.16 will vary from run to run due to the statistical nature of the Monte Carlo analysis. Needless to say, the accuracy of statistical analysis depends strongly on the number of sample points taken. The bigger the number of runs included in the Monte Carlo analysis, the more accurate and reproducible the results.

The histogram on the top of Figure 5.16 shows the relative distribution of the resonance frequency of the vibration structure's driving mode. The graph highlights the statistical probability of certain frequencies. The graph on the bottom shows the measured frequency points for each of the 500 sample points of the Monte Carlo run. The results of the yield analysis indicate that 81.6% of the device samples will have a driving frequency within the required limit of the nominal value +/-500Hz.

The reliability of a statistical analysis depends largely on the in-depth knowledge of the fabrication technology being used. The realistic yield analysis usually requires a much larger number of variable parameters and sample points than shown in the previous example. Depending on the access to certain fabrication tolerances, the Monte Carlo analysis function

can be a powerful tool to help optimize the manufacturability of a MEMS design by giving valuable insight into the sources of manufacturing performance variation. Results of Monte Carlo analysis can also serve as valuable inputs for the optimization of MEMS fabrication processes.

5.3.2.8 Transient Analysis

Transient analysis simulates the response of a device to any time-varying input. In this section, transient analysis will be used to analyze the response time as well as the detection amplitude of the vibration structure. While transient analysis is the most powerful analysis technique for understanding device performance, it is also the most computationally time consuming.

The vibration structure schematic has two sources of time-varying input: the sinusoidal voltage applied to the combs to keep the mass oscillating in the Y-direction, and the pulse source representing the changing angular velocity of the sensor and its substrate about the x-axis. For this tutorial, the sinusoidal driving signal will have amplitude of 2 volts as specified earlier and a frequency equal to its natural frequency. The angular velocity input will be a *hat* profile (specified earlier in the settings) of the pulse source connected to the w_x terminal of the reference frame. This angular velocity turns on at 5 *ms*, takes 6 *ms* to rise to 1 *rad/s*, remains on for 15 *ms*, and then takes 6 *ms* to return to 0.

The DC voltage offset (*dc_comb*) of 13.4 volts is the voltage at which the desired stroke of the comb drive (+/-10μm) is achieved for a sinusoidal voltage of amplitude 2 volts applied at its resonance frequency. This optimal voltage was determined by running a vary loop of Small Signal AC analyses varying the global variable *dc_comb* to determine the value that gives a resonant peak of amplitude 10um. The interested reader is encouraged to confirm these results. Note that by default, CosmosScope plots the AC analyses in dB. This can be changed to amplitude by double-clicking on the desired signal in its legend and modifying the appropriate attribute.

The result of the simulation should be similar to the plot shown in figure 5.17. The oscillation in Y after 1 *ms* is only 100 *nm*, which is far from its expected steady state value of 10 *µm*. Because the angular velocity that will be sensed lasts only 15 *ms*, most of the simulation time would be spent achieving the steady state oscillation.
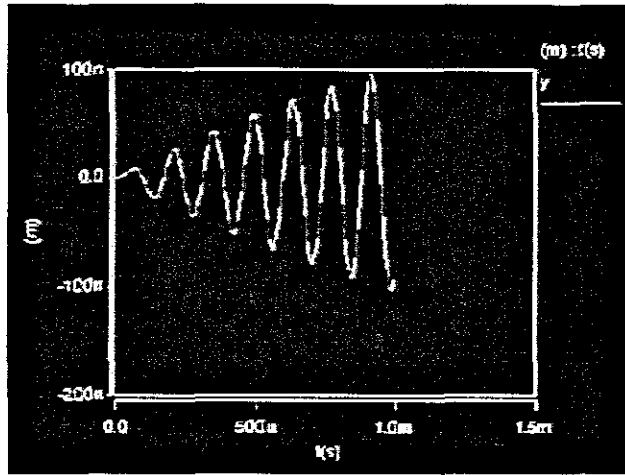
Figure 5.17: Transient Simulation from Quiet State

To avoid the initial start-up transient, we wish to start the simulation from the steady state rather than from the quiet DC state. The steady state can be computed directly by solving the governing system of equations in the frequency domain via a small signal AC analysis. The values of all the voltages and positions that result from the AC analysis can then be used as the starting point for a subsequent transient analysis.

Plot the detection, driving and sensing signals. Compare them with the results shown in figure 5.18. Notice that the detection signal starts to rise at about 0.005s, synchronous with the sensing signal. Further notice that the detection signal starts decreasing to a minimum at the same time the sensing signal does. The general behavior of the detection signal is similar to the sensing signal in terms of delay, rise time, width, and fall time.
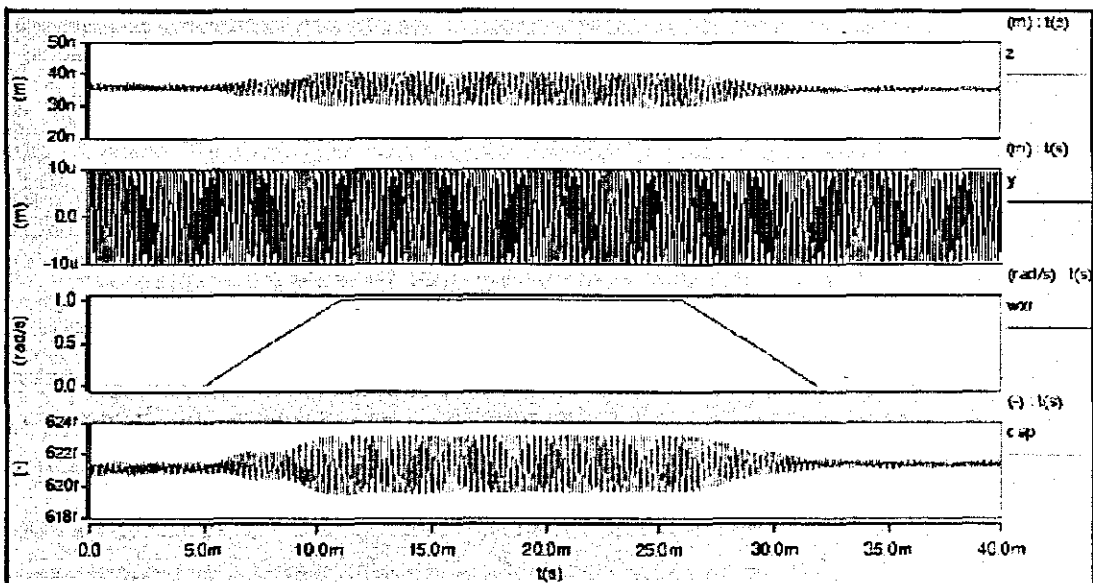
Figure 5.18: Transient Analysis (length_beam2=150*um*)

121

The amplitude of the driving motion (y) is slowly declining over time. This may be surprising because the in-plane mode was excited at its resonance frequency. The reason for this behavior is called numerical damping, which is an intrinsic property of numerical transient solvers. The amount of numerical damping imposed on the system depends on the transient solver settings *Truncation Error*, *Truncation Error Norm*, and *Integration Method*. Of the two Saber transient solvers, the Trap solver imposes less numerical damping and is therefore recommended for resonant sensor structures such as resonators and gyroscopes. The *Truncation Error*, specified in the Calibration tab, defines the maximum allowable error at each time step of the transient simulation. The smaller the truncation error, the more accurate the simulation. However, the smaller the truncation error, the smaller the time step, and thus the longer the simulation time. The cost of a highly accurate simulation with little numerical damping is a dramatic increase of the simulation time.

5.3.2.9 Matching Resonance Frequencies for Driving and Detection Mode

A second transient run shall reveal the design trade-off of matching resonance frequencies for the driving and the detection mode.
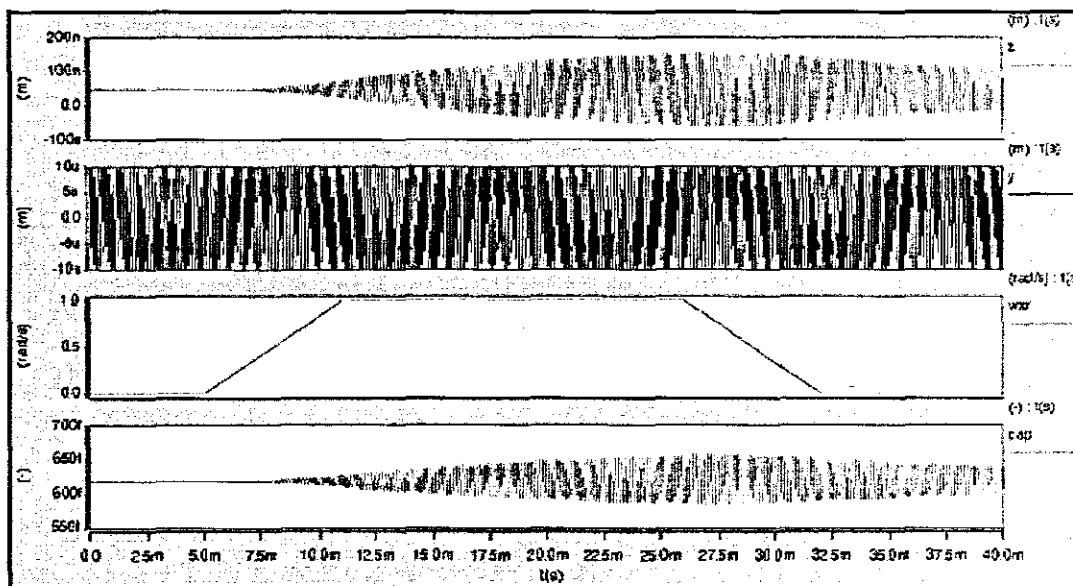
Figure 5.19: Transient Analysis (length_beam2=282um)

Verify the results shown in figure 5.19. Observe that the detection signal starts to rise at about 0.0075s, which is delayed by 0.0025s from the sensing signal. Note that the detection signal persists long after the sensing signal has decreased to zero. The maximum displacement amplitude response to the electrode capacitance is 40*f*, which is more than 10 times than in the previous simulation run with *length_beam2* = 150*um*.

A design with a match between the Y and Z resonant frequencies guarantees a maximum output signal. However, the dynamic behavior is comparably slow compared to designs with mismatching frequencies. The right distance between the detection and driving frequency is a trade-off between output signal amplitude and response dynamic and therefore, one of the most important design criteria of vibratory structure. The objective is to have a detection signal that mimics the general behavior of the sensing signal with a significant optical read output system.

5.3.2 Finite Element Method (FEM) Analysis and Simulation

The section presents system vibration model results with FEM analysis results for each models resonance frequencies. The nature frequencies of main vibration models must be far more than other unexpected vibration models. Name parts of the vibration as shown in figure 5.20. The mesh diagram shows in figure 5.21.
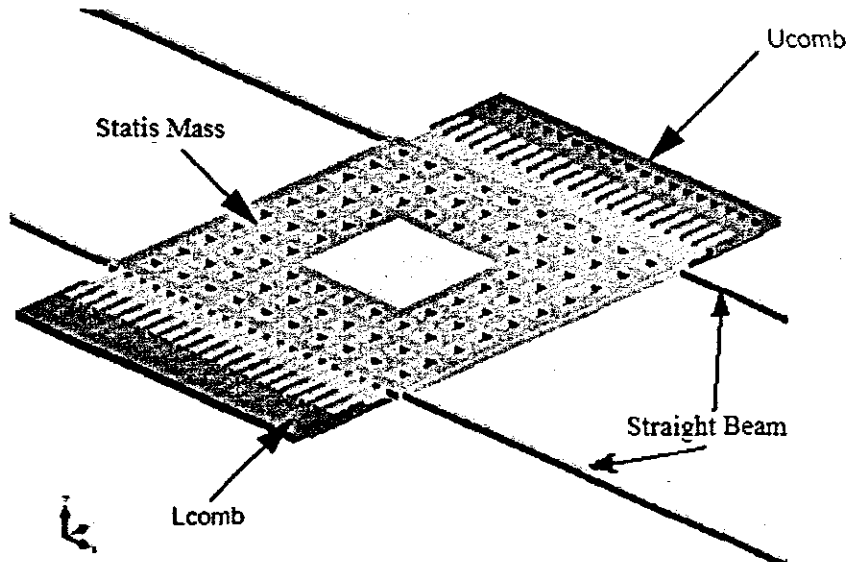
Figure 5.20: Micro Vibration Part Assignments
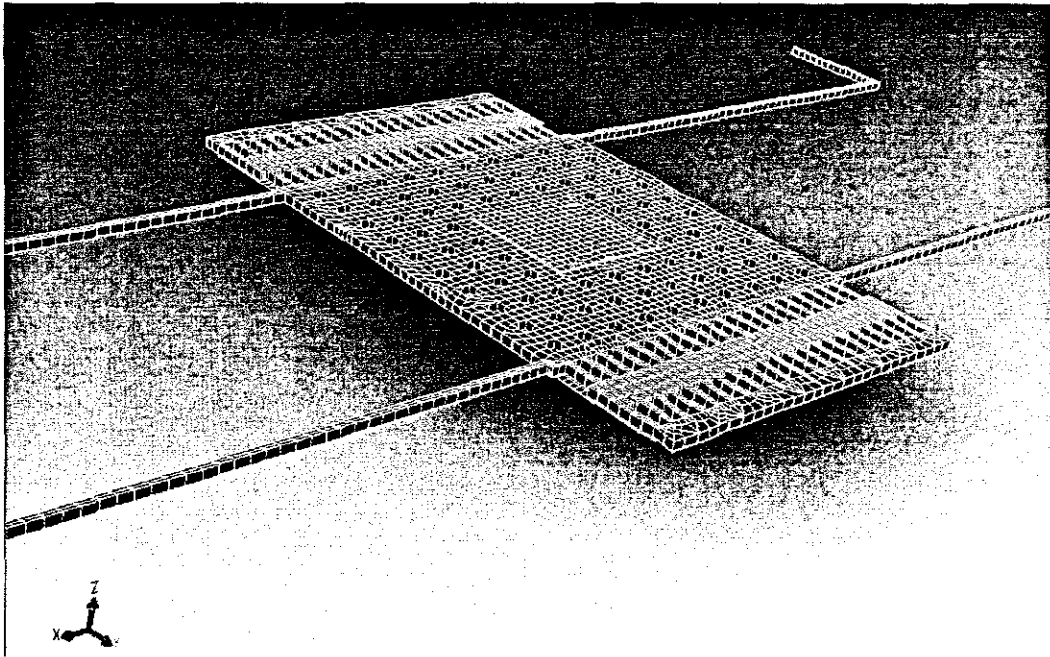
Figure 5.21: Manhattan Mesh after Partitioning

5.3.2.1 Vibration Modal Analysis

In this next procedure, modal analysis is performed on the vibration structure. *MemMech* solves an eigenvalue problem to find the natural frequencies and mode shapes of the structure. We will view the modal results and compare them to those of the system model.

The results for the six modes (see Figure 5.22) are viewed by choosing the Mode Domain table from the results window. The figure 5.23 shows the virtual dynamic model for three main vibration models. The former two vibration models are the useful model for the angular measurement. The frequencies of former two vibration models must more than other four vibration models, and then the model error can be reduced.

modeDomain			
	Frequency	Generalized Mass	Damping
1	1.41943E04	5.330366E-09	0
2	2.372236E04	5.235481E-09	0
3	3.471248E04	5.460092E-09	0
4	4.089248E04	9.707958E-10	0
5	5.090506E04	1.960702E-09	0
6	7.404934E04	1.389208E-09	0

OK

Figure 5.22: Vibration Structure Modal Domain Results
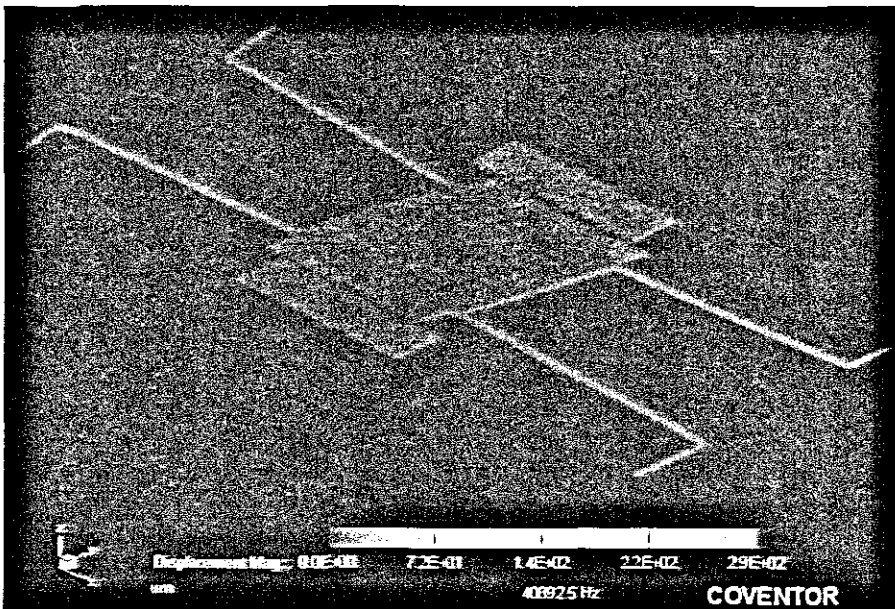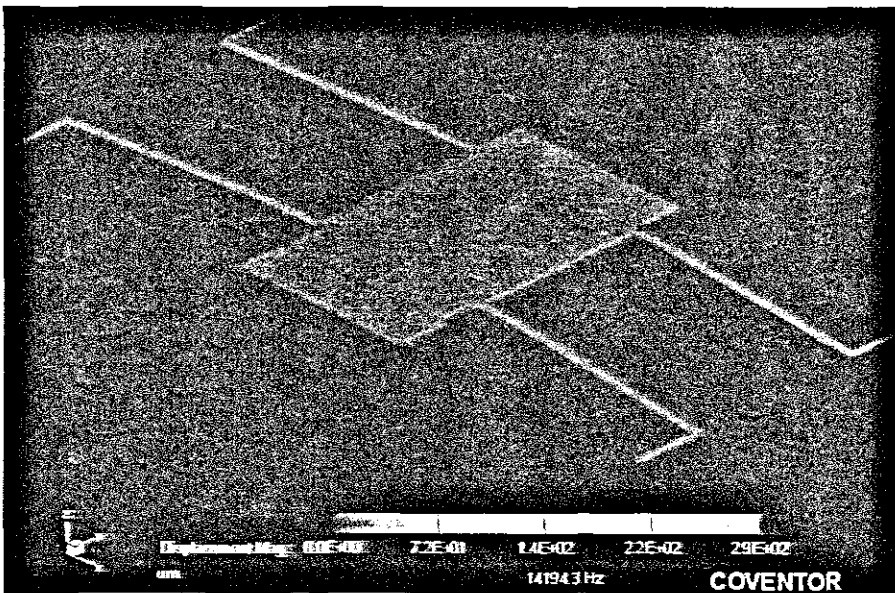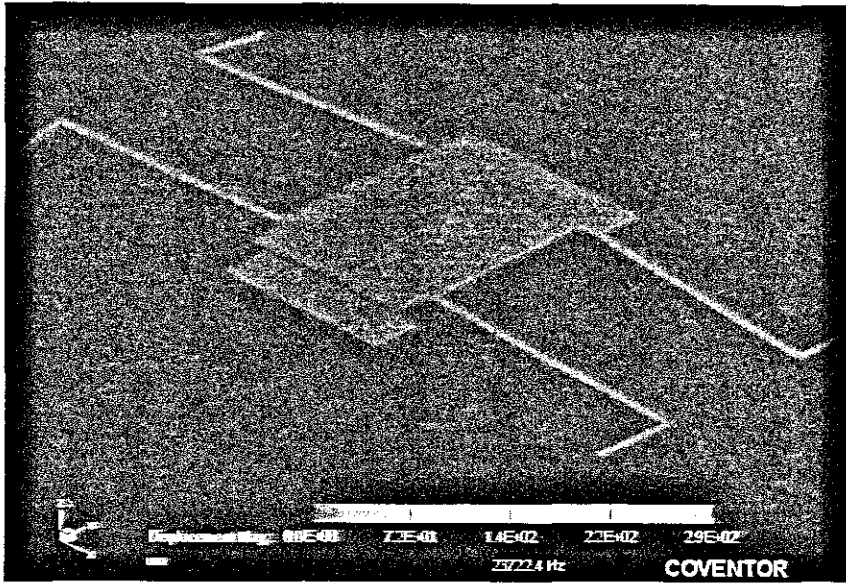
Figure 5.23: Former Three Vibration Models Domain

5.4 MEMS Package and Vibration structure Thermomechanical Analysis

A very important part of the MEMS design cycle is incorporating the device into an appropriate package, which is never simple and may require several design iterations. The conditions of stress, temperature, and other effects experienced by the package during operation can severely influence the performance of the device. Also, in most cases there is an order of magnitude difference in the model definitions for the device and package that makes efficient modeling difficult.

The section studies the effects of the ambient temperature of a package on the performance of a packaged sensor. The package model is based on a design from the Kyocera Standard Package Library, which was developed for CoventorWare with joint collaboration with Kyocera. This library facilitates the selection process by providing ready-made package models, which can in turn be used to analyze the effects of the packages on MEMS devices using MemPackage. The Standard Package Library also provides the layout and process files for the models so that users can modify a design to best fit their device. The package used in this section is a Surface Mount Device (SMD) that is a modified version of Kyocera's SMD_KD_V99902_A model.

This section performs a thermo-mechanical analysis on a package component, based on a heat flux imposed from the device mounted in the package. The results are used to analyze the resultant stresses on the device, illustrating how power dissipated from the device can cause package curvature, which is transferred back to the device as stresses. The package model is shown in figure 5.24. Table 5.4 shows the material properties for package.
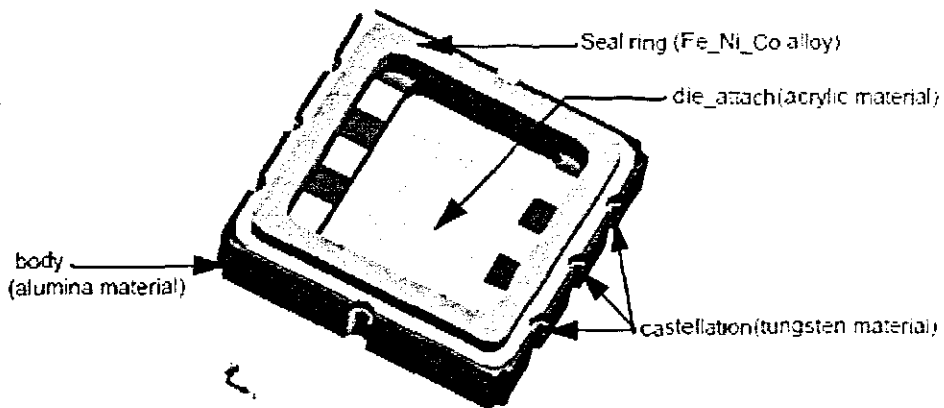
View of pins on bottom of model
(tungsten material)
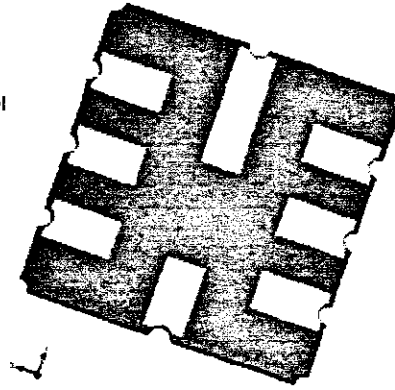
Figure 5.24: Package Model with Part Names

Table 5.4: Material Properties for Package

Property	alumina parts	die_attach metal parts	pins, castellations, metal parts	Units
	Alumina_A440	Acrylic	Tungsten_Kyocera	
Elastic constants - E	3.1e05	3.00e03	3.45e05	MPa
Elastic constants - nu	2.4e-01	3.9e-01	3.0e-01	
Density	3.6e-15	1.0e-15	1.65e-15	kg/μm^3
TCE.	7.1e-06 1	1e-05	4.6e-06	1/K
Thermal Conductivity	1.4e07	1.4e-01	1.67e08	pW/μm·K
Specific Heat	7.7e14		1.34e14	pJ/kgK
Electrical Conductivity			1.84e13	pS/μm
Dielectric	9.8e00	3.5e00		

Setting the mesher properties in the Analyzer function of CoventorWare for FEM analysis, and then generate the mesh shown the meshing view as figure 5.25.
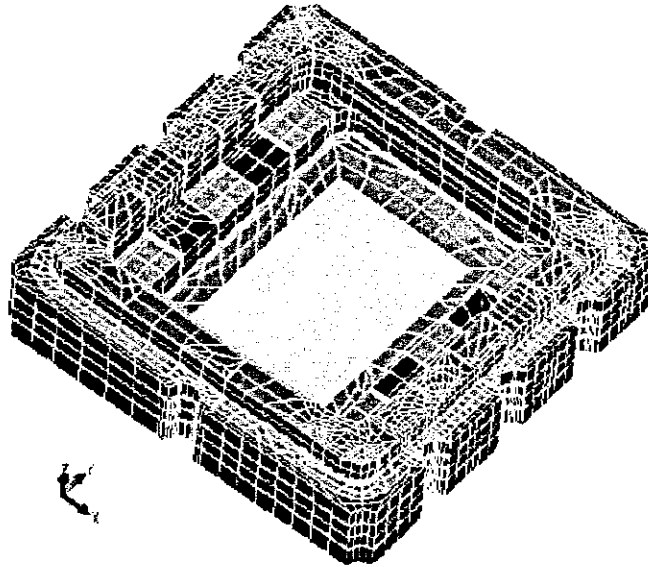
Figure 5.25: Meshing Packages for FEM Analysis

View the 3-D stress results in the Visualizer window generated by CoventorWare, as shown in figure 5.26.

Figure 5.26: Package Stress Results

The stress color map shows stress in the pins area. However, the area of concern is on and around the surface where the device is mounted. With temperature changes, the Visualizer window will show curvature in the package those results in a stress on the package and vibration structures, shown as figure 5.27 and 5.28.

223K
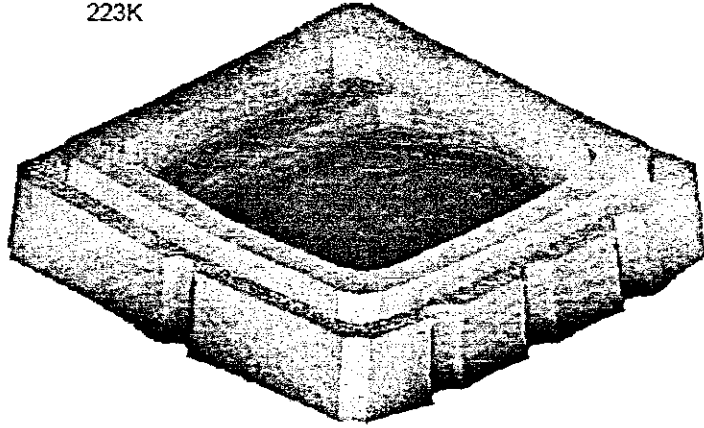
423K
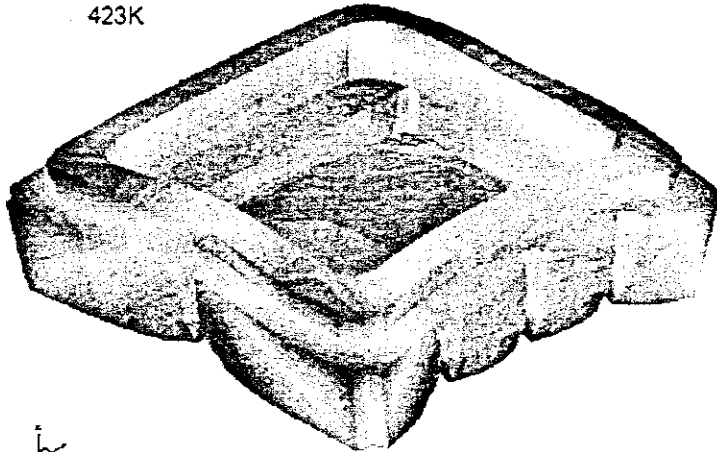
Figure 5.27: Package Results of Curvature Deformed by Temperature

223 K

129

453K
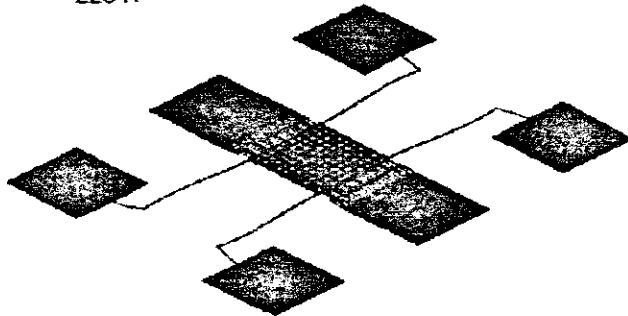
Displacement Mag : 8.7E-02   4.7E-01   0.5E-01
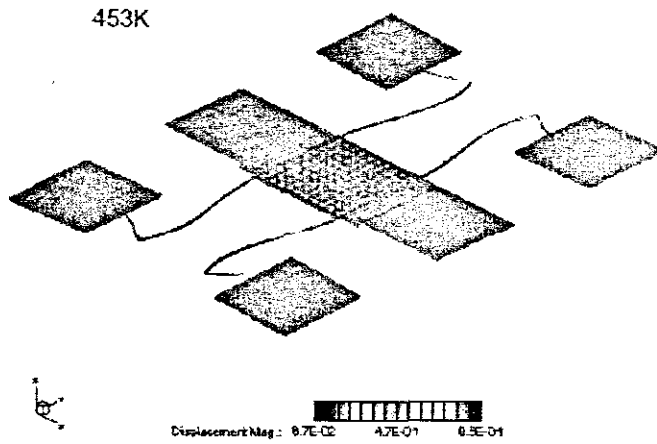
Figure 5.28: Displacement Magnitude Results of Vibration structure

Figure 5.27 and 5.28 show the displacement results at 223K and 423K. At 223 K, the package shell contracts; and at 423K, it expands.

This is accomplished by specifying mating surfaces (patches) for the two components, which are vibration chip to convert the rotation rate to the vibration movement, shown as figure 5.29, and the package contains the vibration chip to provide the physics protection and circuit interface. See Figure 5.30.
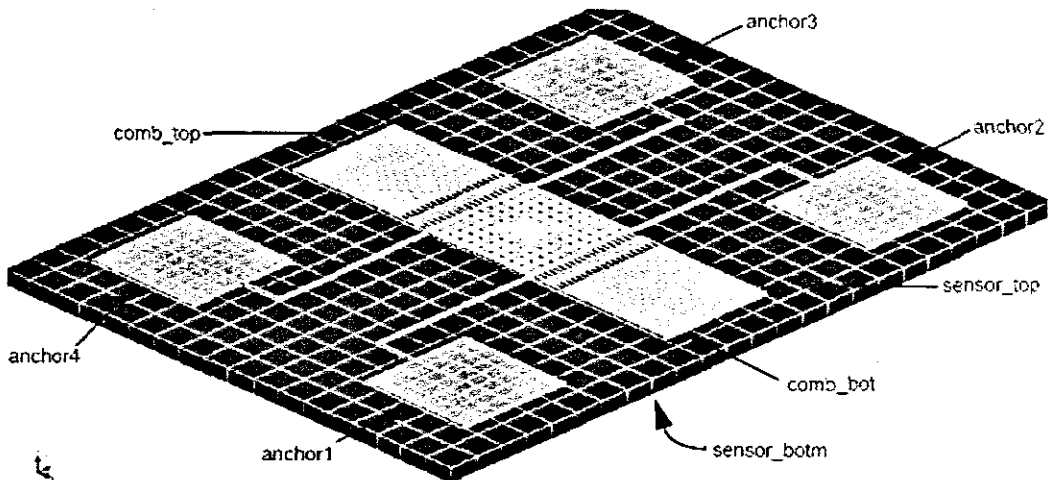
Figure 5.29: Rotation Rate Sensor Patch by Coriolis Force Theory
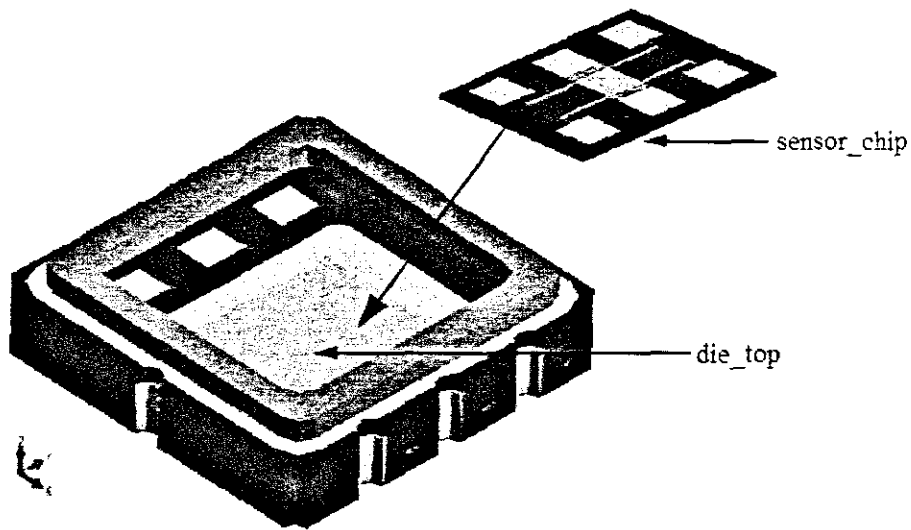
Figure 5.30: Connecting the Sensor Chip to the Package

The bottom of the sensor substrate (sensor chip) is connected to the package mounting area (die top) using attachment materials.

5.5 MEMS Dual-Mass Vibratory Structure Design

In last section 5.2, the design and mechanical simulations of single mass vibration structure is introduced. It is design fundamental, which is strictly designed according to the Coriolis force theory. The vibration structure is satisfied to convert the rotation motion to sense axis oscillation motion. The structure can be further optimal to achieve higher sensitivity, stability, and thermo-noise etc. The performances can be improved by changing shapes of support beams, layer materials, and mass size etc. Those remodels are not transnatured.

The dual-mass vibration structure has been proposed in many capacitor MEMS inertial sensors system. The symmetrical structure has two proof masses spring system, which is not only double the weight, but also compensate the errors coming from the detector circuits, shown as figure 5.31 (Seshia A., 1999).

131
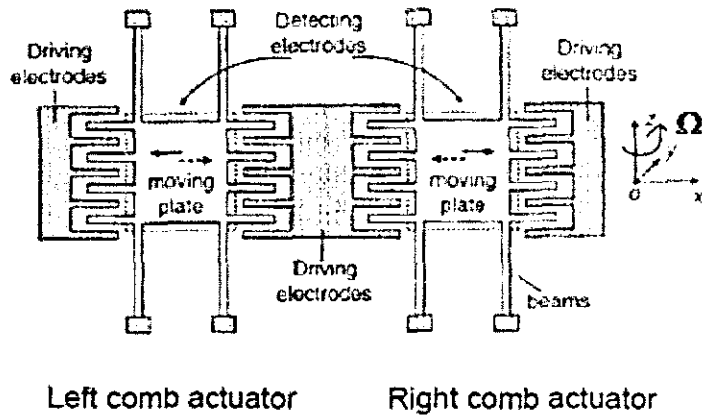
Figure 5.31: Dual Mass Vibration Structure with Straight Beams

The operation of the two micro masses designs is very similar with the single mass vibration structure. Figure 5.33 illustrates operation of the dual proof mass tuning fork micro vibratory structure shown in Fig. 5.32. As illustrated in Fig. 5.33, the two proof masses are driven in anti-phase by the electrostatic comb-drives. Each proof mass is actuated by two sets of comb-drives: one outside and one inside, operating one at a time. The outside comb-drives are at the extreme ends of the dual mass, at the extreme left and right edges of the configuration shown in Figs 5.32, and 5.33. The inside comb-drives are between the two proof masses. The comb-drives produce electrostatic forces and therefore can only pull the masses; they can not push (Hanson, Marinis, Furlong, and Pryputniewicz, 2001).
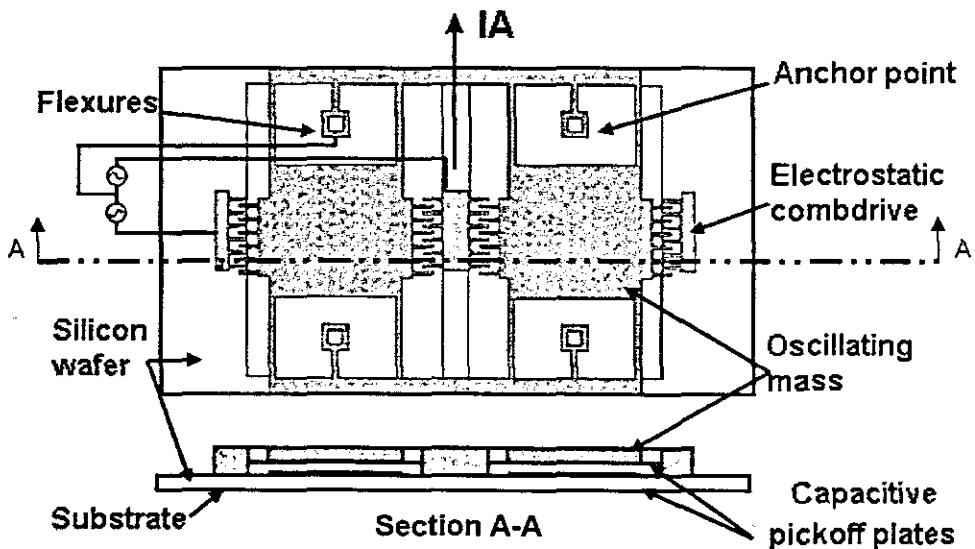
Figure 5.32: Dual Mass Micromachined Tuning Fork Micro Vibration Structure

132
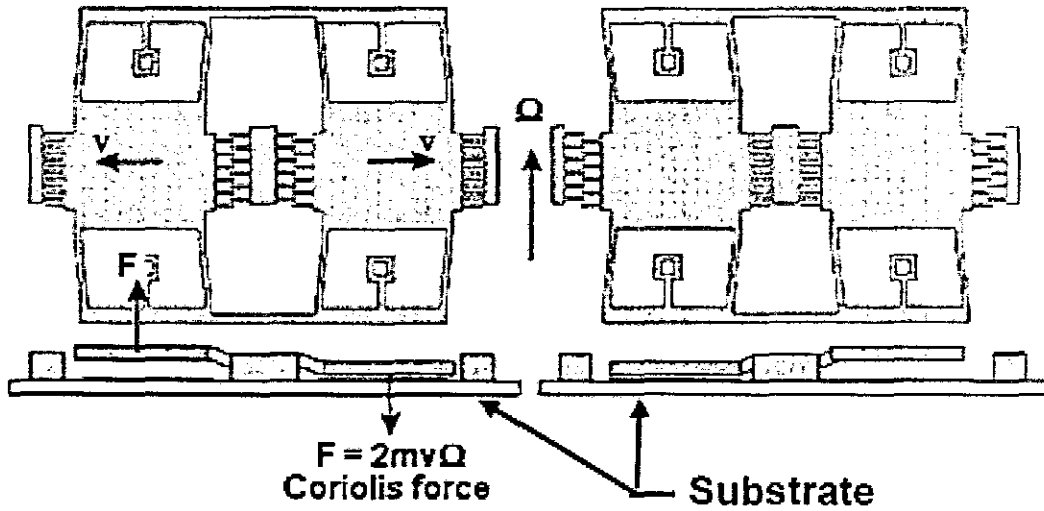
Figure 5.33: Schematic of the Operation of a Dual Mass Vibration Structure

Therefore, an actuation cycle consists of four parts. During part-1, when the actuation voltage is applied, the outside comb-drives pull the proof masses toward themselves while simultaneously the flexures supporting the proof masses deform storing elastic energy.

During part-2 of the actuation cycle, when the voltage on the outside comb-drives is reduced, the flexures straighten and bring the proof masses to their original, neutral, positions. At this point, actuation voltage is applied to the inside comb-drives and the proof masses are pulled toward the inside while the flexures deform away from their equilibrium positions; this is part-3 of the actuation cycle. During part-4, when the actuation voltage is reduced again, the flexures return the proof masses to their neutral positions.

Typically, the 4-part actuation cycle is repeated a few thousand times per second. This vibration produces the in-plane velocity, $\bar{v}$, necessary to define Coriolis acceleration described by Eq. (5.41). If the vibrating proof masses are subjected to an angular velocity, $\bar{\Omega}$, Fig. 5.33, around the central axis of the two proof masses, then, using Eq. (5.41), the Coriolis force is defined as

$$F_c = m \cdot Coriolis\_Acceleration = 2m(\Omega \times V) \tag{5.41}$$

where F_c is the Coriolis force, and m is the mass of each of the vibrating masses. The Coriolis force will cause one of the proof masses to raise out-of-plane away from the substrate while the other proof mass drop down toward the substrate. The movement shows as figure 5.34.
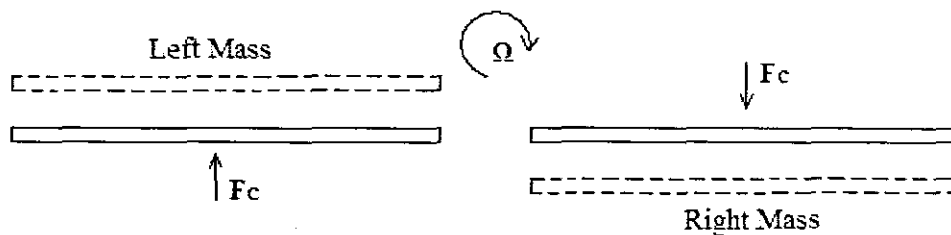
Figure 5.34: Movement Diagram of Dual Mass by Coriolis Force Theory

In the dual-mass vibration structure, the vibration principles are similar with the signal mass vibration structure like the Coriolis force theory, comb-driver actuators, and the movement behaviors etc. The difference is just integrating the two signal mass vibration structures, and each vibration structure works same as the signal mass vibration structure. The advantages are incarnated about detector readout stage, which means that the displacement results of readout from each vibration structure are same but opposite directions. The two results can be compared each other and do some triangular transform calculation, which will reduce the noise effecting from power source and environment like thermo-noise etc and help to identify the direction rotation rate from the phase shift between the two vibratory mass. The dual-mass vibration structure has been used in practical applications because of better performances about sensitivity, bandwidth, precision etc. The high symmetrical structure is not only propitious to performance simulation, but also easy to fabrication by MEMS technology.

The optical readout systems are concerned more and more because of the photoemission. The light has all characters of wave like amplitude, phase, frequency etc. and all wave theories like diffraction, interference etc. The parameters, which is used to describe the light, are easily affected by the out side force, environments etc. The optical sensors have been widely used in many applications, especially for the micro displacement measurement. In chapter 4, the optical interferometric measurement principles have been introduced. Next section, the fiber optical interferometer and displacement readout system will be presented and discussed the performances.

5.6 Model Design and Components Introduction of Fiber Optical Displacement Readout System

In the last section, the micro vibration structures have been introduced. Through the vibratory model simulation, the main vibratory model is satisfied the design requirements and Coriolis Effect operation principles. The rotation rate measurement is transformed to one known direction vibration movements by two grades damping spring system. The amplitude of vibration is proportion with of the input rotation rate, and the vibratory frequency, which is

determined by the actuator frequency and nature frequency of structure dimensions, is not containing of the information of rotation rate. Although the amplitude created by rotation rate is very small at micron level, the optical readout system is working proved at nano-level. The optical interferometer can provide the enough sensitivity to tiny angular velocity measurement. The fiber optical interferometer is normal and mature displacement measurement device. Whatever the size and precision etc., the fiber optical interferometer can match and satisfy the MEMS devices.

In this work, Corning SMF-28 single-mode fibers with a CTE of $5.6 \times 10^{-7} um / um /^{0} C$ and Pyrex tubes with a CTE of $32.5 \times 10^{-7} um / um /^{0} C$, an L.D. of 1550 um and a P.D. of 1550um were used. For fiber optical interferometer, a one-meter-long SMF-28 fiber was first cleaved, then the cleaved-end was inserted into a 20mm long Pyrex tube from one end, and finally the fiber and the tube were fusion-bonded together. All the bonding processes were completed on a bonding stage and the optical devices are integrated on board with a simple setup shown in Fig. 5.35.
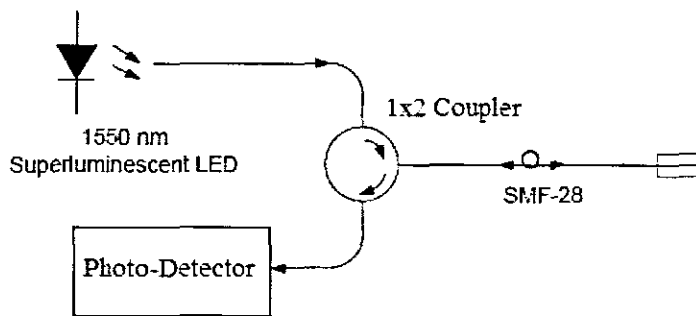
Figure 5.35: Fibers Optical Interferometer without External Movement Surface

The size of interferometer head shows as the figure 5.36. Through the advanced MEMS optical fabrication processes, all optical devices can be integrated on one optical chip including light emitting, optical coupler, waveguides, photo detector and half reflected surface, which is one important reflected surface in the fiber optical interferometer. This fixed half reflected surface and the external movement surface, which is normal mounted on moveable measurement devices, are providing two coherence light beams for interferometer. The output intensity exactly presents the displacement between the movement surface and fixed surface. The output quantum of interference light can be converted to voltage or current by photo-detector for measurement (Cibula, Donlagic, Stropnik, 2002).
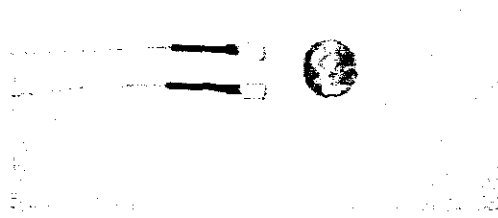
Figure 5.36: Photographs of two fiber optical interferometer head without external surface

Figure 5.37 shows the general configuration of a fiber optical interferometer measurement system. It consists of a broadband light source, a circulator, a sensing interferometer, a tunable optical filter (TOF), receiving electronics, a computer and optical fibers (SMF) to connect all the optical parts (Deng, 2004).
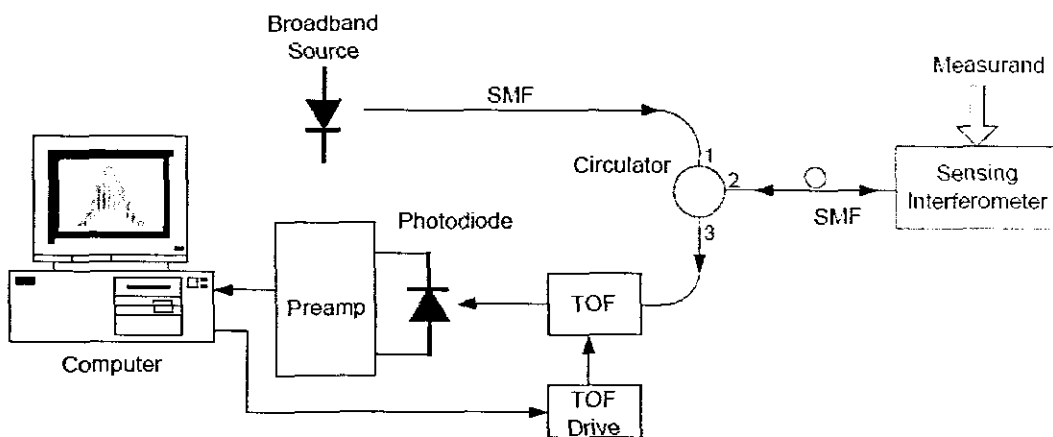
Figure 5.37: General configuration of a fiber optical interferometer measurement system

5.6.1 Photo-Electron Demodulation Methods Introduction

The interferometer measurement system may operate either in a scan mode demodulation (or spectrum acquisition mode) or a fringe-tracking mode demodulation (or linear operation mode). The optical path difference (OPD) is modulated by vibration created by rotation rate in the MOEMS gyroscope system.

The basic idea of the demodulation of an interferometric sensor is to accurately recover the optical path difference with minimum uncertainty, no matter the sensor is a Michelson, a Mach-Zehnder, a Sagnac or a Fabry-Perot interferometer. In any interferometric sensor, the OPD can be generally expressed as nL, where n is the refractive index of the medium comprising the interferometer, and L is the physical path length difference between the path of the sensing light beam and that of the reference light beam (L is length of a round-trip in the case of a reflective Fabry-Perot sensor). Any measurand change can be represented by the OPD change of the transducer. The recovery of OPD starts from the measurement of the

136

phase angle, ϕ. For an interferometric sensor interrogated with a monochromatic source of wavelength λ, ϕ is given by

$$\phi = 2\pi \cdot OPD / \lambda = 2\pi nL / \lambda \qquad (5.42)$$

A perturbation of a measurand causes a change in the length L, or the refractive index n, or both, resulting in a phase shift defined by the following equation

$$\phi + \Delta\phi = \frac{2\pi}{\lambda} \cdot OPD + \frac{2\pi}{\lambda} \cdot \Delta(OPD) = \frac{2\pi}{\lambda} nL + \frac{2\pi}{\lambda}(n \cdot \Delta L + L \cdot \Delta n) \qquad (5.43)$$

Unfortunately, the phase angle and the shift cannot be measured directly by any instruments. Therefore, the demodulation is somehow related to the detection of the intensity or the intensity distribution of the optical power received by a detector. Of course, it is much more sensitive than the intensity-based detection (Egorov, Mamaev, Polyantsev, 1995).

In the cases of two-beam interference, which is the case for all interferometers mentioned before except a Fabry-Perot interferometer, the optical intensity arrives at the photodiode is

$$I_{out} = (I_1 + I_2)/2 + \sqrt{I_1 I_2} \cos\phi \qquad (5.44)$$

5.6.1.1 Scan Mode Demodulation

In a scan mode, the wavelength of output interference light is changing with the optical path difference (*OPD*).

$$\Delta(OPD)/OPD = \Delta\lambda / \lambda \qquad (5.45)$$

where $\Delta\lambda$ is the shift of the fringe peak from the original wavelength λ.

The scan mode technique is based on the detection the output spectrum of the sensing interferometer. The spectrum of the signal from the sensor is usually obtained by means of a spectrometer with a CCD or a photo-detector array, shown in figure 5.38. This technique eliminates the need of any moving parts or reference interferometer, and provides a combination of the high sensitivity of an interferometric sensor with absolute accuracy and reliability of spectrum encoding. It can also provide non-incremental absolute measurements of the OPD and correspondingly the external physical measurand. Scan mode fiber optical

interferometer has been widely used, in the past 10 years, in the detection of static or quasi-static parameters, such as micro-displacement, temperature, pressure, and strain. Recently, *Scan mode fiber optical interferometer also becomes a powerful tool in biomedical sensing* and imaging.
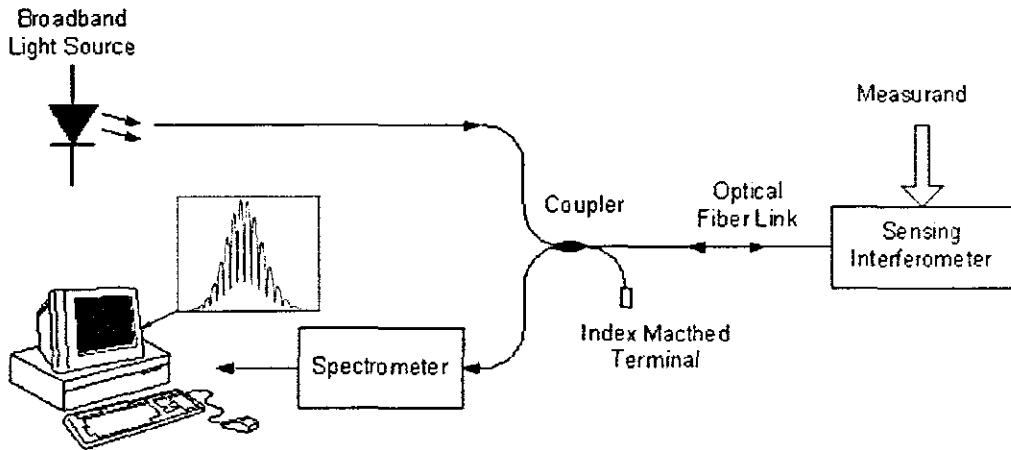
Figure 5.38: The principle diagram of a fiber optical interferometer sensing system

Once the output spectrum of a fiber optical interferometer sensor has been obtained, *OPD* may be recovered by using fringe counting (Agrawal, 1997).

Two major issues of the current spectral domain techniques are the slow response, which limits them to the measurement of static or quasi-static signals, such as temperature, displacement, strain and pressure, and the requirements of expensive spectrum processing components, such as diffraction gratings and detector arrays, especially those operating in the 1.0~1.7μm band.

5.6.1.2 Fringe-Tracking Mode Demodulation

When very small OPD changes or dynamic perturbations are to be measured, linear or quadrature operation has to be considered for the highest sensitivity and largest signal bandwidth provided by the linear region. A linear region is defined as a small region on one side of an interference fringe near the point where sensitivity is the maximum, as illustrated by figure 5.39. Compared with other sensor demodulation techniques, sensors operating in the linear region have the advantages of linear transfer function, ultra-high frequency response, and no fringe direction ambiguity, simple signal-processing and highest sensitivity at the Q-point. They are, therefore, suitable for the detection of small variations, such as acoustic wave, ultrasound, vibration, magnetic field, partial discharge, and pressure and *temperature etc.*
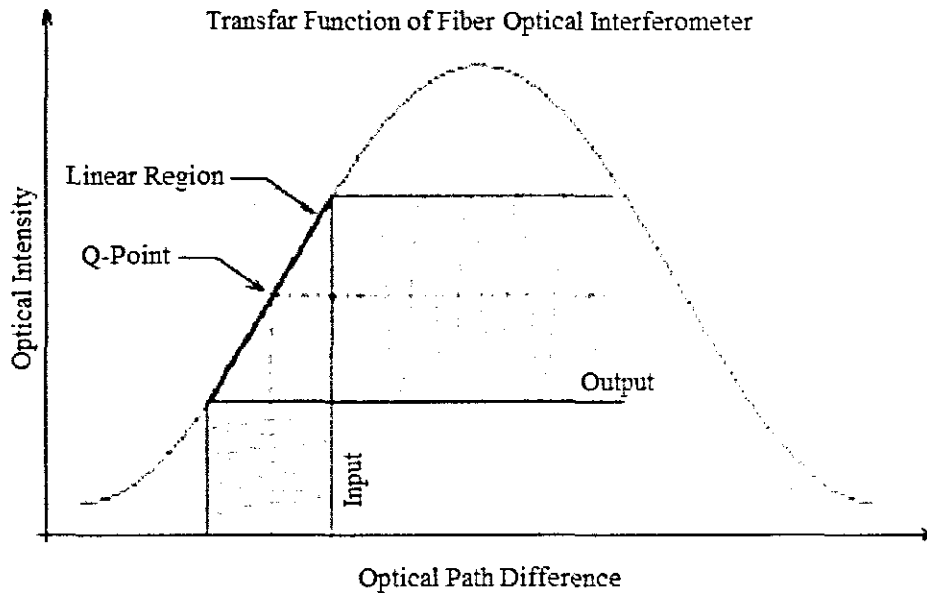
Figure 5.39: Liner Region of an Interferometric Sensor

However, confining the operation to the linear region places difficult manufacturing constraints on the sensor head by requiring the initial cavity length to be positioned at the Q-point or sometimes one end of a linear region of the transfer function (Ward, 2002). They also suffer from signal fading caused by random environment fluctuations, such as temperature changes, which may drive the sensors out of the linear region.

Therefore, poor control of the operation point has been one of the major factors that limit the practical application of interferometric optical sensors. In the absence of an efficient operating-point stabilization method, a "trial and fail" strategy was used during the sensor fabrication to select sensors that had an operating-point close to its quadrature point in a specific system. Apparently, the yield is extremely low considering the nanometer accuracy required for the quadrature point control and the operation of the sensor may still suffer from environment drifts unless it is made really insensitive to any environmental disturbance. To solve this problem, various schemes have been demonstrated in the past, such as using a bias, homodyne or heterodyne demodulation, and quadrature-shifted demodulation. Each of these techniques will be reviewed briefly below.

a) Using a Bias

A straightforward way to adjust the operating-point is to apply a bias on the sensing interferometer. In the demonstration of acoustic wave detection using a fiber-optic Fabry-Perot interferometer (FFPI) by Yoshino *et al*, an acoustic wave bias was applied to the FFPI which was controlled by a servo system to maintain the operating-point against the temperature-induced phase shift. In another experiment for partial discharge detection with a

diaphragm-based Fabry-Perot sensor by Yu *et al*, static water pressure was used to manually adjust the operating point for the compensation of fabrication errors and temperature-induced phase shift. Unfortunately, Q-point stabilization using a bias is a very application specific approach and not a universal solution for all applications. It is also not an efficient approach because of the complexity (Green and Cable, 1982).

b) Homodyne and Heterodyne Detection

One or two phase shifters generated by stretching sections of fibers wound on piezoelectric transducers have been widely used in the demodulation of fiber optical interferometers with high accuracy. A generalized form of this configuration is shown in figure 5.40. Depending on the type of the detection system used, either the phase shifter A controlled by a feedback circuit to maintain the interferometer at its quadrature point, or the phase shifter B driven by a piezoelectric element with an oscillator, or both can be used. The detection systems of this kind can categorized, according to their configuration, into five classes: passive homodyne (HOM), homodyne with dc phase tacking (PTDC), homodyne with ac phase tacking (PTAC), true heterodyne (HET), and synthetic heterodyne (SHET). A complete review of these schemes can be found in reference (Gerges, Farahi, Newson, Jones, Jackson, 1988).
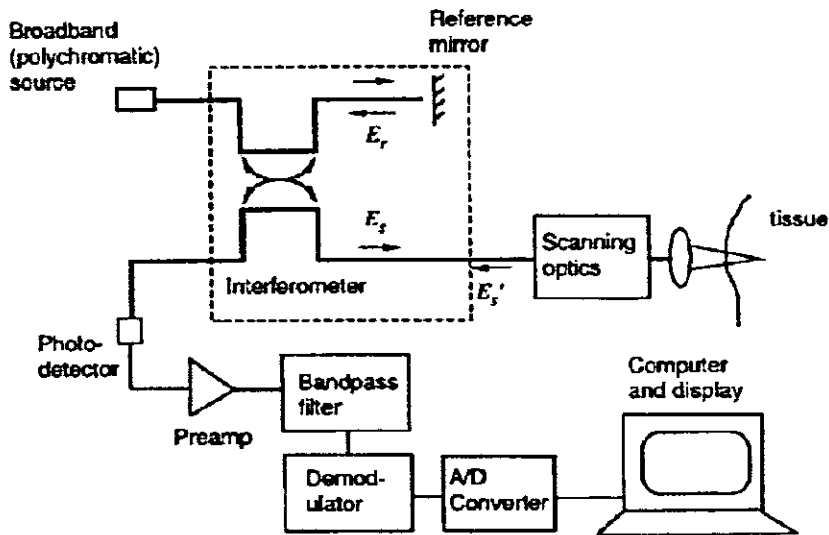
Figure 5.40: Generalized homodyne and heterodyne detection system for a fiber optical interferometer

In order to achieve the high level of performance, homodyne and heterodyne require relatively large size of phase modulators, which increase the sensor size and decrease reliability, and fast reset circuitry, which adds additional noise.

c) Quadrature-shifted demodulation

140

Quadrature-shifted demodulation is another important linear demodulation scheme, in which two or three interferometric sensor outputs with a $\pi/2$ phase shift one from the other are used to recover the measurand without signal fading or direction-ambiguity. Quadrature-shifted outputs can be obtained by using a passive quadrature demodulator (PQD) which is an output coupler matrix comprising of four fiber-optic directional couplers with precisely controlled path-lengths between them, two phased-shifted sensors, a two-wavelength passive quadrature demodulator, or a three-wavelength digital phase demodulation system (Lo and Chuang, 2001).

d) Advantages of Fiber optical Interferometer

- Retains all the advantages of conventional mirrors interferometer.
- It is a universally effective method for most interferometric sensors, including Mach-Zehnder, Michelson, Sagnac, F-P, and even FBG sensors.

- Can readily be tailored for both static and dynamic signals.

- May significantly improve the sensors' sensitivity and fringe visibility.

- Is compatible with most available signal-processing approaches, such as fringe counting, fringe tracking, spectral processing, quadrature point stabilization, and systems using a tunable source.

- May drastically reduce the cost of each sensor system to a fraction of current system cost, provided a low cost optical integration chip for environment monitor.

The fiber optical interferometer model consists of a single-mode fiber with a dielectric mirror of reflectance $R1$ formed on the end-face of the fiber, a "cavity" filled with air, water, polymer, or any other transparent material, and a reflector with a mirror of reflectance $R2$ on its front surface. The distance between the two mirrors is l, defined as the physical cavity length of the fiber optical interferometer, shown as the figure 5.41. The reflector can be formed by the end-face of any flat surface including a diaphragm or a short piece of fiber. This model is a simplified representation of the extrinsic Fabry-Perot interferometric (EFPI), the in-line fiber etalon (ILFE), the diaphragm-based Fabry-Perot interferometer (DFPI), or the MEMS-based Fabry-Perot interferometer, the thin film interferometer, and all other etalon type devices (Arya, de Vries, Murphy, Wang, and Claus, 1995).
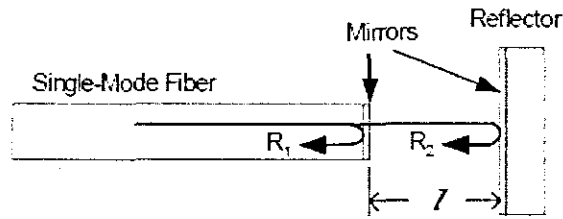
Figure 5.41: Fiber Optical Interferometer Head Models

5.6.2 Low Noise Analog Optical Receiver

Analog optical receivers are one of the most critical components which partially determine the sensitivity, the resolution and the measurement range of a fiber-optic sensing system.

In almost every area of measurement, the ultimate limit to the detect ability of weak signals is set by noise - the unwanted signals that obscure the desired signal. In an optical receiver, the signal-to-noise ratio is defined as

$$SNR = \frac{average\_signal\_power}{noise\_power} = \frac{i_p^2}{i_n^2} \tag{5.46}$$

where $i_p = Dp_{in}$ is the photocurrent generated by the incident optical power p_{in} on a photodiode, D is the responsivity of the photodiode, and i_n is the total equivalent input noise current of the receiver. The resolution of a sensing system is reached when $SNR=1$, or $i_p = i_n$.
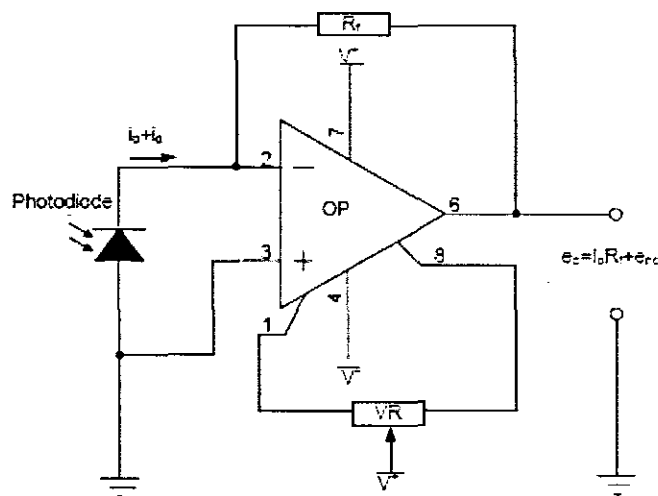
Figure 5.42: Schematics of a basic transimpedance amplifier

The most widely used preamplifier is a transimpedance amplifier, or called current-to-voltage converter, as shown in figure 5.42. The preamplifier appears extremely simple, but its noise performance is much more complex. Particularly, when a transimpedance amplifier is used for fiber optic sensing, high gain (large feedback resistance R_f) is generally required for very low level of optical signals. Also photodiodes typically exhibit large shunt capacitance that rolls off the diode impedance. This combination produces noise gain peaking at higher frequencies and a complex response to the op amp's input noise voltage. In addition, the high R_f resistance increases the significances of the resistor's noise and the noise of the amplifier input current (Sirkis et al., 1995).

Figure 5.43 shows the noise model of the basic transimpedance amplifier, where R_D, C_D are the resistance and capacitance of the photodiode, C_{ia}, i_{ni}, e_{ni} are the input capacitance, noise current and noise voltage of the OP amp., and e_{nR}, C_S are the noise voltage and stray capacitance of R_f, respectively.
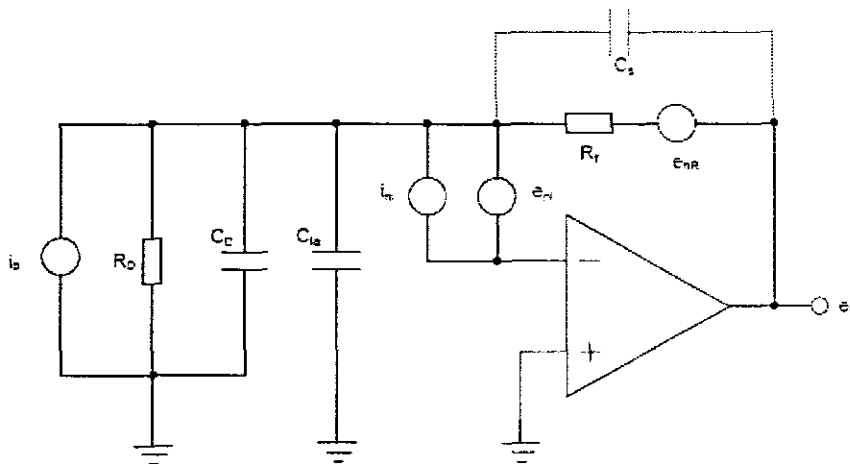
Figure 5.43: Noise Analysis Model of the Basic Transimpedance Amplifier

5.6.3 Noise Analysis and Noise Sources

In general, the sources of noise can be classified into two types, intrinsic noise and external noise. The intrinsic noise is the noise generated by the electronic circuits itself, including detector noise, thermal noise and amplifier noise, while the external noise is induced or coupled into the circuits through various mechanisms, such as electromagnetic interference (EMI), power supply, light source, and reflection due to unmatched load. This section introduces the mechanism behind each noise source.

5.6.3.1 Intrinsic Noise

a) Detector noise

Detector noise is also called shot noise. It is generated by random fluctuations of current (both dark current and photocurrent) flowing through the photodiode (Bertone and Webb). The shot noise current can be expressed as

$$i_{n(D)} = \sqrt{2q(i_d + i_p)\Delta f} \tag{5.47}$$

where q –electron charge (1.6×10^{-19} coulombs); i_d –dark current, leakage current generated by bias voltage applied to the photodiode; i_p –photocurrent generated by the incident optical power; Δf –effective noise bandwidth of the receiver, determined by R_f and the shunt capacitance.

b) Thermal noise

Thermal noise is caused by random thermal motion of electrons in the shunt or feedback resistor R_f. The random thermal motion of electronics manifests as a fluctuation current even in the absence of an applied voltage. The equivalent input thermal noise can be written as

$$i_{n(T)} = \sqrt{\frac{4k_B T \Delta f}{R_f}} \tag{5.48}$$

where k_B is the Boltzmann's constant ($1.38 \times 10^{-23} J \cdot K^{-1}$), T is the temperature in Kelvin, and R_f is the feedback or shunt resistance, which is also a function of temperature for Silicon, InGaAs and Ge PIN photodiodes. As temperature decreases, the shunt/feedback resistance increases, and thus the thermal noise decreases. However, the increase of the resistance is limited by the signal bandwidth and gain requirements.

c) Amplifier noise

The amplifier noise depends on the type of OP amp. used and is also a function of the frequency f. The amplifier noise current is given by (Franco, 1998)

$$i_{n(A)} = \sqrt{\langle i_{ni} \rangle^2 + \langle e_{ni} \omega C_T \rangle^2} \tag{5.49}$$

where i_{ni}–amplifier input noise current; e_{ni}–amplifier input noise voltage; $\omega = 2\pi f$; C_T – total input capacitance seen by the amplifier.

The total intrinsic current noise:

$$i_{n(\text{int rinsic})} = \sqrt{\left\langle i_{n(D)} \right\rangle^2 + \left\langle i_{n(T)} \right\rangle^2 + \left\langle i_{n(A)} \right\rangle^2} \qquad (5.50)$$

5.6.3.2 External Noise

External noise sources impose a background noise floor that requires attention to amplifier's environment rather than the amplifier itself and the peripheral components. This background noise typically results from the light source, and the parasitic noise coupling of external electrostatic and magnetic sources. These sources can dominate the noise performance, overriding any effort to further reduce the direct noise effects of the amplifier.

a) Electromagnetic Interference (EMI) noise

Electric field coupling, such as from the power line, supplies noise through mutual capacitances that exist between any two objects. AC voltage difference between the two objects drives these mutual capacitances, coupling noise currents from one to the other. Figure 5.44 illustrates an example of electrostatic noise coupling. Electrostatic noise source V_e represents any AC voltage source that creates an electric field in the vicinity of the amplifier. This source couples noise current i_{ne} through the mutual capacitances C_M to the amplifier's two inputs. The amplifier amplifies not only the photocurrent i_P, but also the noise current i_{ne} .
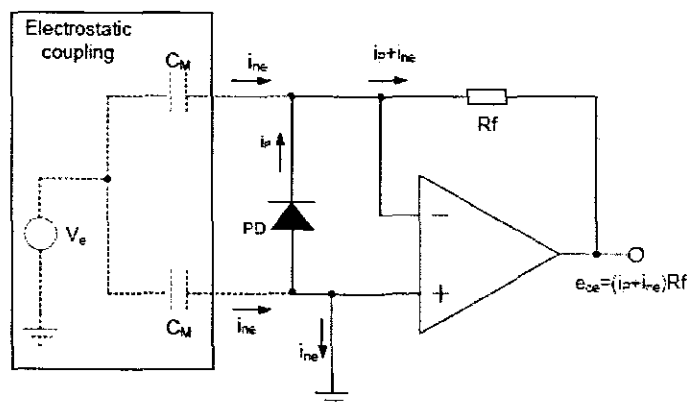
Figure 5.44: Electrostatic Noise Coupling Through Mutual Capacitances

Magnetic noise coupling and radio-frequency interference (RFI) introduce circuit noise through a mutual inductance. In this type of EMI coupling, the interference source acts like the primary of a transformer, and the loops in the preamplifier resemble secondary windings. Figure 5.45 illustrates the loops exist in a basic transimpedance amplifier which may result in noise coupling. The preamplifier forms three magnetic receptor loops through the circuit connections of the photodiode, the feedback, and the load (Beard and Mills, 1996).
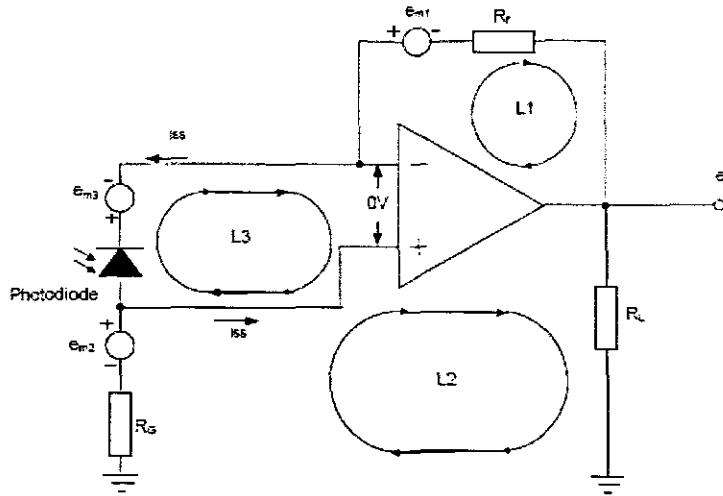
Figure 5.45: Magnetic and RFI Noise Coupling Through a Mutual Inductance

b) Power supply

Noise on the power supply lines of the op-pamp (OP) couples to the amplifier's output with a magnitude controlled by the supply line impedance, the amplifier's power supply rejection ratio (PSRR), and the circuit's noise gain. In most cases, the supply-line impedance has the highest contribution to the noise coupling. Figure 5.46 shows the mechanism how power noise can propagate to the amplifier output. Ideally, $V_P = V+$ and $V_N = V-$. But due to the existence of the line inductance L_P, the actual voltages applied to the OP react with the signal current i_S,

$$V_p = V^+ - i_S Z_L \qquad (5.51)$$

$$V_N = V^- + i_S Z_L \qquad (5.52)$$

where $Z_L = L_P s$ is the resistance of the power-supply lines, producing a voltage error across the photodiode as

$$e_{erroe} = 2i_S Z_L / PSRR \qquad\qquad (5\text{-}53)$$
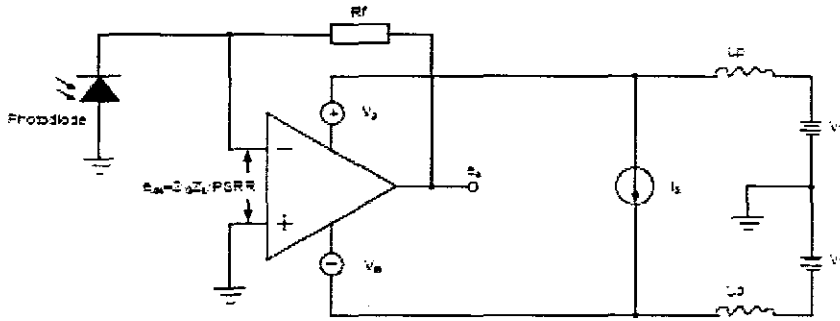
Figure 5.46: Noise coupling from power-supply

c) Light noise

Noise, such as EMI and power-supply noise, can also couple into the light source through the SLED driver. Random environmental temperature change may also cause the output power fluctuation and wavelength drift. Fig. 5.47 shows the noise performance of an optical receiver (with 87 *kHz* low pass filter) with and without a constant optical power input, respectively. The receiver had a total noise V_{rms} of 553V in the absence of any optical power input, and a total noise V_{rms} of 752V when a constant input power of 2.5W was applied. Since the shot noise was negligible at this low level optical power, the increase of the noise level was attributed to the SLED driver.
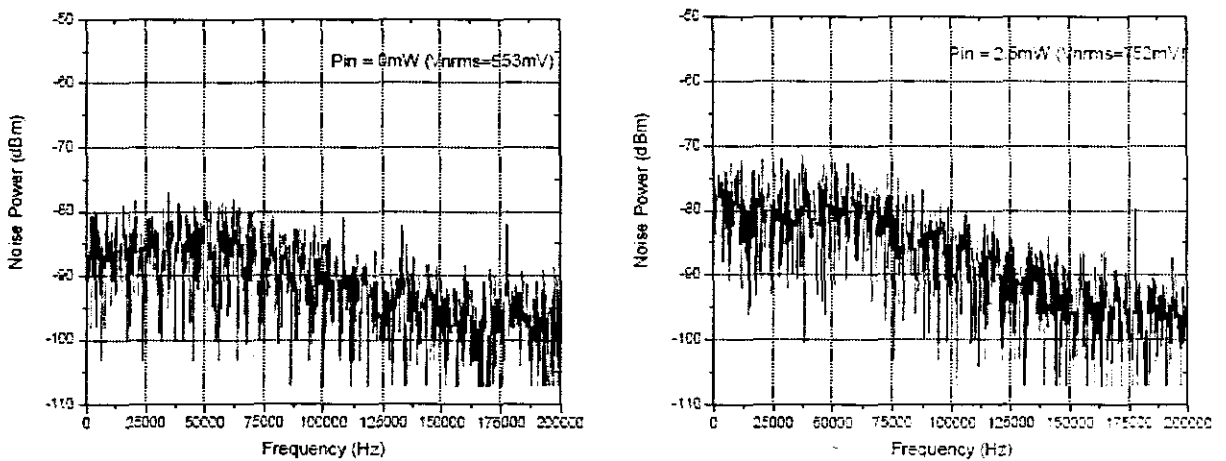
Figure 5.47: Noise from the Light Source (a) without Optical Input (b) with 2.5μW Optical Input

d) Reflection

Reflection may happen if there is any mismatch between the output resistance of the amplifier and its load. This reflection may directly add onto the total output noise, or cause an oscillation in the amplifier circuits. Reflection increases with the increase of signal frequency.

5.6.4 Noise Reduction Strategies

In order to achieve the best resolution or highest SNR in a fiber optical interferometer interrogation system, a variety of noise reduction strategies have been exploited in the design and construction of the sensing systems. This section describes each method briefly (Gunther, Wang, Fogg, Murphy, and Claus, 1992).

a) Trace layout

Noise can be reduced by carefully placing the traces during the PCB design. There are several general rules which can be used for the optimization of the trace layout:

- Minimizing the areas of the circuit's loops minimizes the mutual inductances that couple magnetic noise. Careful component layout achieves this by placing the amplifier's components, especially the photodiode, close to the OP amp.
- By matching loop areas and distances from a noise source, the amplifier's Common Mode Rejection Ratio (CMRR) rejects the resulting equal noise coupling effects.
- Reducing the length of power-supply line can reduce the mutual inductance of the traces.
- Avoid unnecessary ground loops.

b) Low-pass filter

In order to remove or reduce the out of band noise, a second-order low pass filter was used after the preamp to limit the noise bandwidth to that of the signal. Figure 5.48(a) is the schematics of a second-order low pass filter.
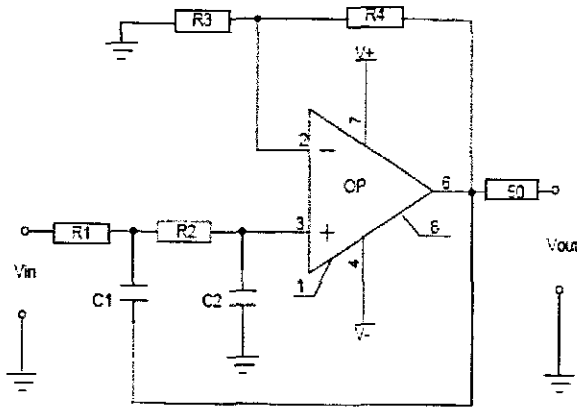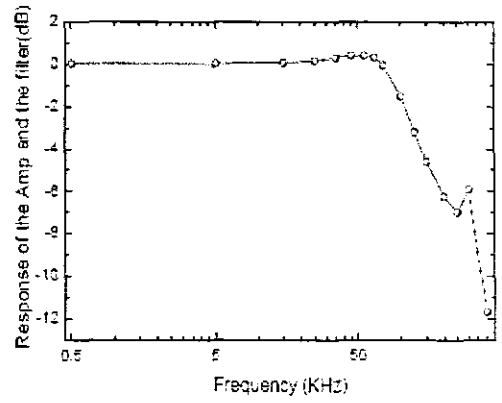
(a)   (b)

Figure 5.48: Noise reduction using a low pass filter (a) a second order low pass filter; (b) frequency response of the preamp with the low pass filter

By selecting $R_1=R_2=R$, $C_1=C_2=C$, and $R_3=R_4$, the gain and the cutoff frequency of the filter can be calculated by

$$g = 1 + R_4 / R_3 = 2 \tag{5.54}$$

$$f = \frac{1}{2\pi\sqrt{R_1 C_1 R_2 C_2}} = \frac{1}{2\pi RC} \tag{5.55}$$

Choosing R and C, a cutoff frequency about 87kHz for engine pressure measurements was easily realized. Figure 5.48 (b) is the experimental frequency response of the preamp and the low pass filter. The noise performances of the optical receiver for fiber optical interferometer sensors before and after the filter are given in figure 5.49. The total noise was reduced to half while a gain of 2 was added. Apparently, an equivalent noise reduction of 12dB was readily obtained.
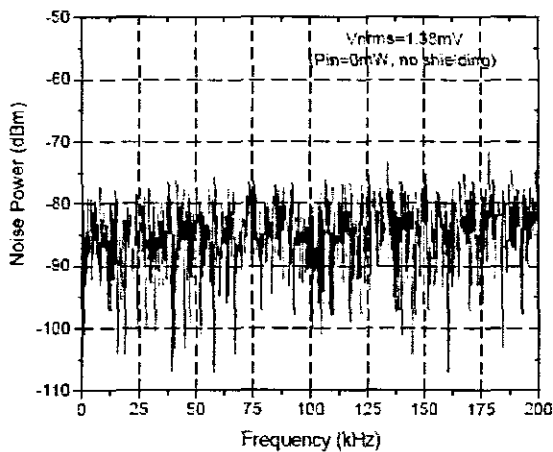
(a)   (b)
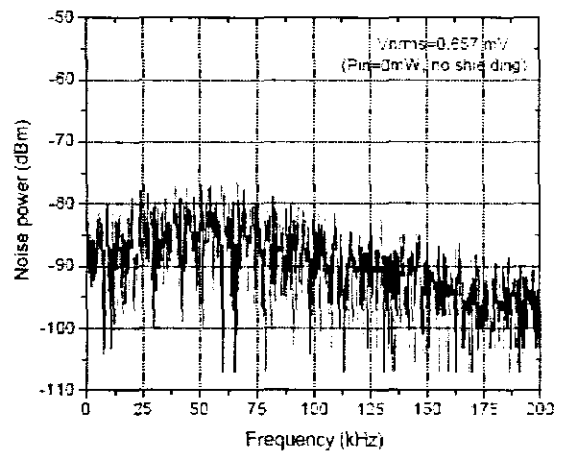
c) Power-supply isolation

The light source and the optical receiver may be the two most noise sensitive components in a sensor system. Therefore a linear power supply was used for low noise circuits, including the optical receivers and the SLED driver, while a switching power-supply was used for high current parts and any digital parts in the system, as shown in figure 5.50.
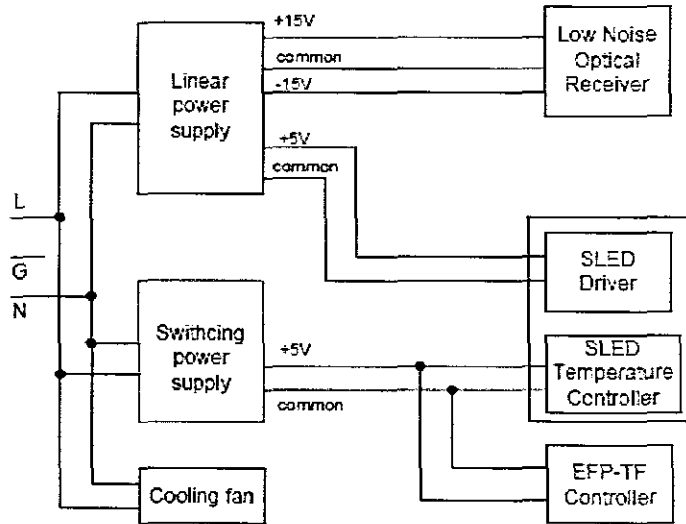
Figure 5.50: Light Source Power-Supply Isolation

d) Power-supply filtering

Since the linear power-supply is shared by the optical receivers, the SLED driver, and other circuits, the isolation of the preamplifier from others provides further protection from noise coupling through the power-supply lines. In this work, a power-supply filtering was applied using two voltage-regulator ICs, LM7812 and LM7912, as shown in figure 5.51 (a), with the tested noise performances before (Point A) and after the filter (Point B) given in Figure 5.51 (b) and (c), respectively.

At Point A, the power-supply showed noise peaks at the 60Hz and its harmonic frequencies. Although the total noise power level was reduced less than 2dB at Point B, the noise amplitudes were remarkably attenuated at all major peaks.

150
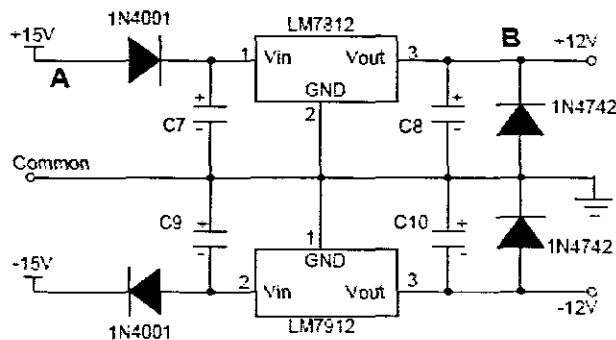
(a)
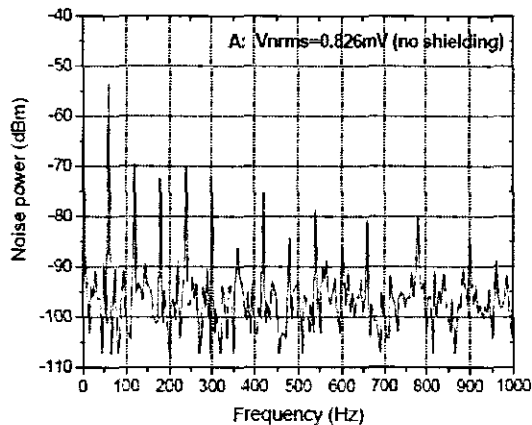
(b)
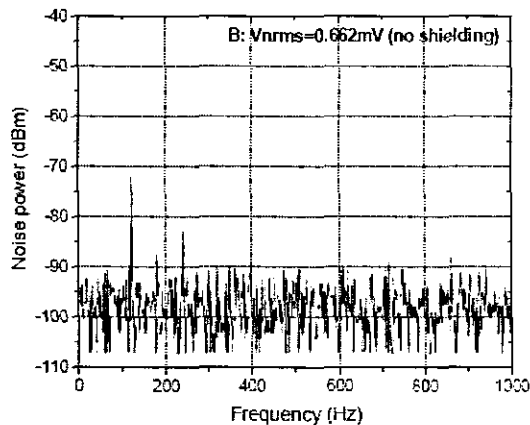
(c)

Figure 5.51: Power-supply filtering. (a) Circuits; (b) Noise spectrum at Point *A*; (c) Noise spectrum at Point *B*

e) Decoupling

Another effective way to reduce noise from the power-supply lines is decoupling by placing a bypass capacitor C_B between the component's power-supply pin and the ground pin. Fundamentally, adding the bypass capacitor shunts the line impedances to reduce the supply line voltage drops produced by i_S. From another perspective, the capacitors serve as local reservoirs for the immediate supply of high frequency current demands. With the bypass capacitor, the error voltage in Eq. (5.69) is reduced due to the decrease of the Z_L

$$Z_L = \frac{L_P s}{1 + L_P C_B s^2}$$

(5.56)

f) Shielding, Grounding and Cabling

Physically shielding the amplifier from an EMI source offers the best protection for noise coupling. Making the shield with a material of high electrical conductivity and enough

151

thickness ensures that the coupled currents produce little voltage drop across the shield. To be effective, the shield's ground must be earth ground. The shield should be connected to the system ground to minimize the effects of the parasitic capacitance induced.

5.6.5 Optical Receiver Circuits for the Micro Fiber Optical Interferometer Readout System

An InGaAs PIN (FD80FC) from Fermionics Opto-Technology was chosen as the photodiode. The FD80FC has an active area of $80\mu m$, a dark current of $0.04nA$, a capacitance of $0.68pF$, and a responsivity of $0.84A/W$. the FC receptacle package makes it easy to be integrated into a preamplifier case (Franco, 1998).

Figure 5.52 is the schematics of the narrowband channel in the optical receiver for the fiber optical interferometer displacement readout system. OP37 was selected as the OP-amp. because of its large gain bandwidth product ($63MHz$), relatively low current noise ($0.4pA/Hz^{1/2}$ @ 1 kHz) and voltage noise ($3nV/Hz^{1/2}$ @ 1 kHz), excellent Common Mode Rejection Ratio (CMRR) $126dB$, low drift (0.2 $\mu V/^{o}C$), low input offset voltage (10 μV). Potentiometer VR_1 was used for offset adjustment, while VR_2 for gain adjustment. The frequency response of the receiver is given in figure 5.53.
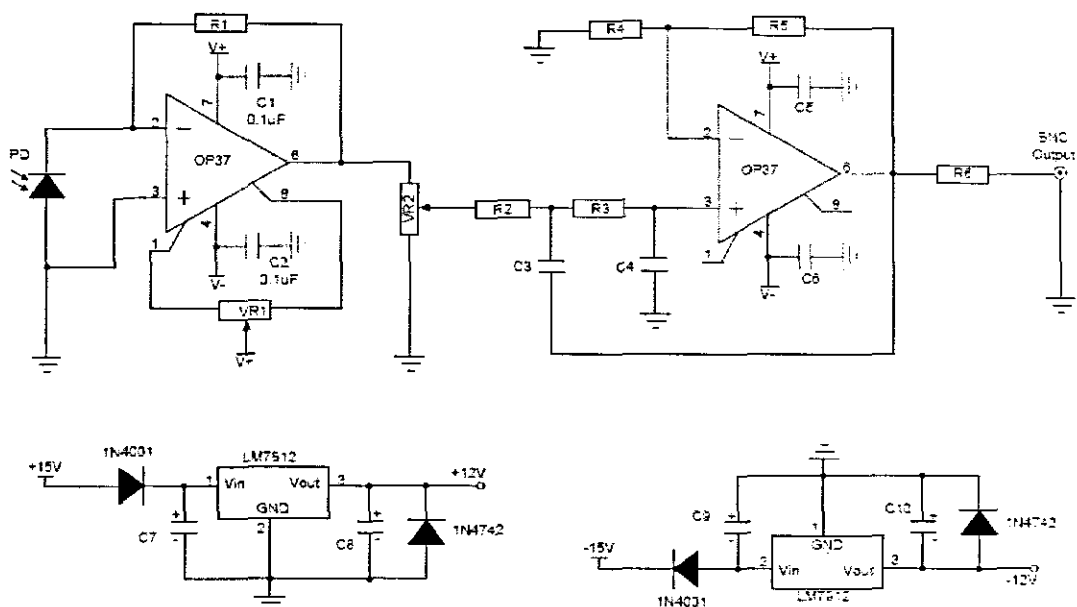
Figure 5.52: Schematics of the Optical Receiver for the Fiber Optical Interferometer System
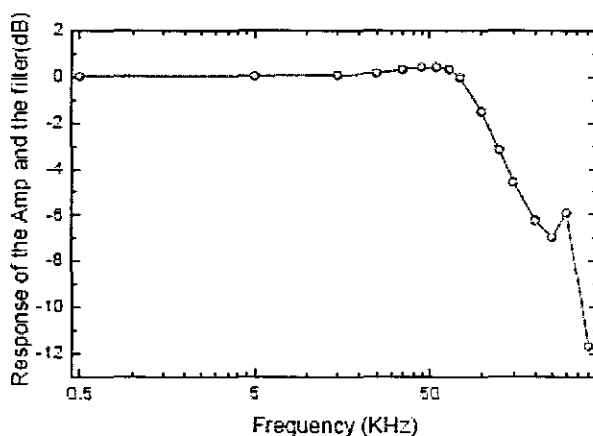
Figure 5.53: Frequency Response of the Preamp with the Low Pass Filter (LPF)

In addition to noise performance, the gain linearity of the optical receiver is also a very important parameter. Figure 5.54 shows the relationship between the optical input power and the receiver output voltage when the gain was set to the maximum. A maximum gain of 1.8×10^6 and a linearity of R=0.99998 were obtained.
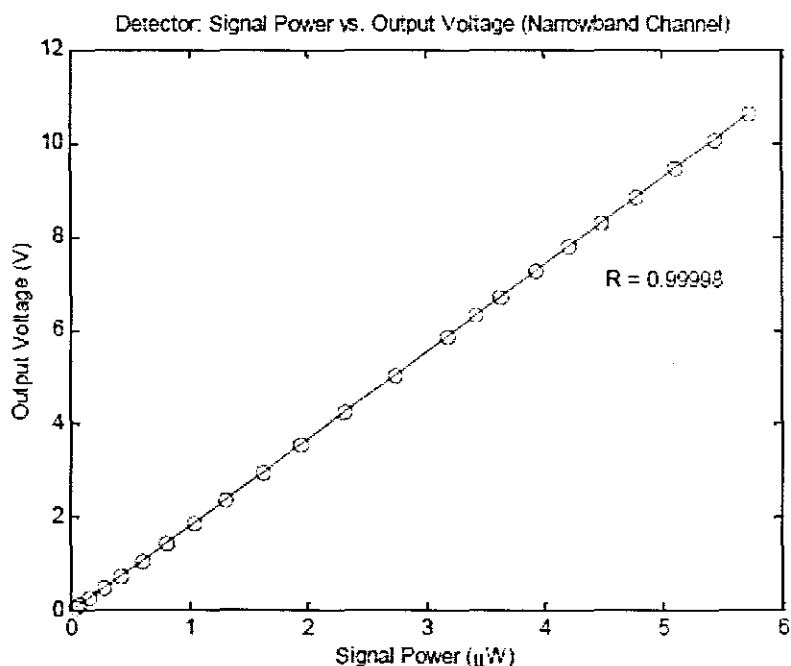
Figure 5.54: Gain Linearity

5.6.6 Instrumentation of the Micro Fiber Optical Interferometer Readout System

A 1550 nm fiber optical interferometer displacement readout system is built using the developed EFP-TF. The layout schematic of the system is shown in figure 5.55.

153
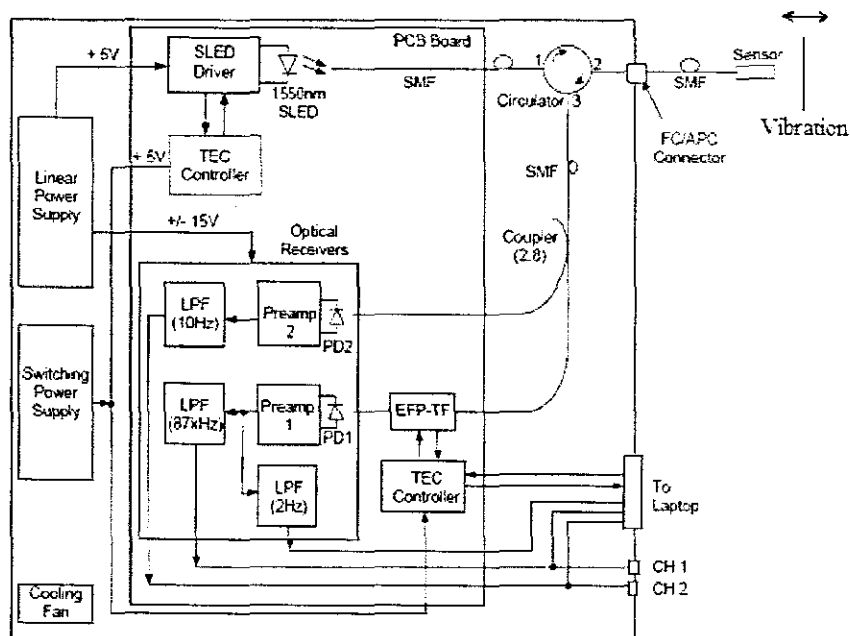
Figure 5.55: Layout Schematic of the Fiber Optical Interferometer Readout Interrogation System

The system is generally composed of a linear power-supply, a switching power supply, a 1550nm SLED and its driver and temperature controller, a 1550nm wideband circulator, a 2:8 optical coupler, optical power split ratio 20:80, an tunable filter (TF) and its temperature controller, thermoelectric cooling (TEC) , two channel low noise optical receiver, a cooling fan, a laptop computer with a data acquisition card and Labview programs for TF control and low frequency signal recording, and a two channel digital oscilloscope for high frequency signal above 10 kHz monitoring. Two receiver channels, including a narrowband channel and a broadband channel were built into the system for the purpose of self-calibration as described in Reference. The broadband channel responds only to source power fluctuations, fiber bending and other factors common to both the broadband channel and the narrowband channel, but not to the measurand signal due to the low coherence length of the broadband light source. When the narrowband signal is divided by the broadband output, any common-mode fluctuations can be removed from the former one. For this reason, the bandwidth of the broadband optical receiver was designed to be very low for best SNR, but high enough for most fluctuations. The signal bandwidth of the narrowband channel is determined by the frequency response requirement of the perturbation to be measured. For static or quasi-static measurements, such as temperature and strain, a bandwidth from DC to a few Hz is usually sufficient. For dynamic signals, such as vibration and pressure fluctuations, a bandwidth from DC up to hundreds of kHz may be required. In acoustic applications, such as hydrophone and P.D. detection, a band-pass filter can be used to remove both low frequency and high frequency noises.

A 1550 nm SLED from *Exalos ESL*1505 with 2.5mW Power in single model fiber (SMF) at 180 *mA* maximum operating current and 60 nm bandwidth was selected as the light source due to its both large bandwidth and good output power. The high output power eases the power budget and increases the SNR in a sensing system. The large bandwidth is also important because it takes advantage of the large tuning range of the tunable filter (TF) and provides a large dynamic range for both the signal amplitude and the compensateable drifts. Figure 5.56 shows the output spectrum of the SLED at the maximum operating current.
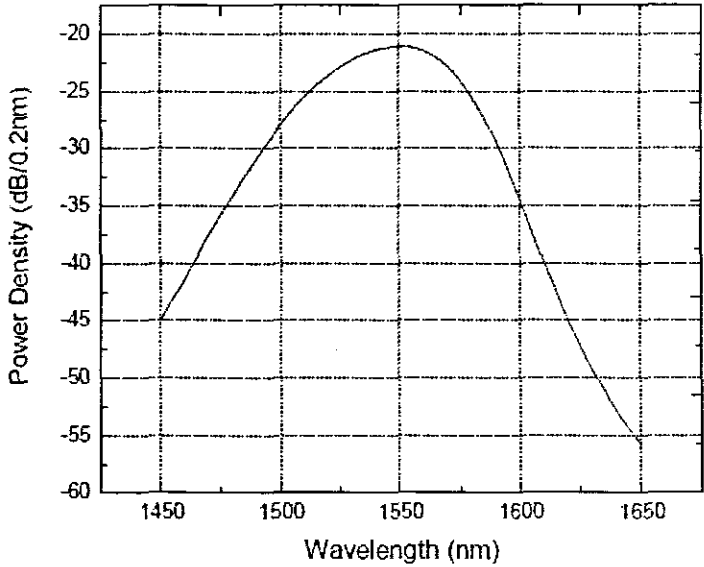
Figure 5.56: Output Spectrum of the SLED at 180*mA* and 20^{0}C

Since the SLED's output power and spectrum are temperature dependent, temperature control is very necessary to reduce the temperature effects. Also because of the high output power of the SLED, temperature control is very important to protect the SLED from being damaged.

5.7 Summary

This chapter investigated the various MEMS solid vibration structure model including single static mass, dual static mass with straight beams and folded beams, which are proved to suitable for Coriolis force theory; and the fiber optical interferometer displacement readout system, which are successfully used in many MEMS sensors for displacement measurement and spectrum analysis like micro scan electro scope, acceleration meter, velocity meter etc.

In this chapter, the performances of micro vibration structures are researched and simulated by using CoventorWare, Matlab, Labview etc. software. The simulation results can be used for the further optimal design and fabrication processes design. Researching the

components of the fiber optical interferometer, which show the major noise from the optical interferometer readout system including light source, photo-detector receiver, amplifier, filters circuits etc. The basic optical interferometer displacement readout system design is given including optical components and circuits. The researchers can change the components, portion circuits, and various modulation and demodulation methods according to the measurement requirements and sensor design expectation.

Based on all performances simulation from both mechanical and optical readout system parts, the combination of MEMS sensor and optical sensors, which solve out the interface of mechanical components and optical components, is feasibility and reasonable solution for high precision, micro size, and tough environments. Through the series and transfer functions, the rotation movements are changed to one axis disciplinary vibration movement, and then the high precision optical readout systems are instead of the conversional electronic methods to measure the simple movement. The optical measurement systems comparing with electronic measurement methods have lots of advantages about the simple structure, few components, measurement stability, high precision, fast response time, low cost, adaptive distribution network, and small volume etc. Anyway the optical sensors, optical measurement methods will replace most conventional electronic measurement methods with the decreasing cost of optical components.

The integrated MOEMS gyroscope system design is finally given in this chapter. Although there are many aspects, which need further research and improvement, this novel MOEMS gyroscope system is presented the new approach for rotation rate sensors. Hoping more researchers is interesting in developing angular sensors, and provides more novelty production.

CHAPTER SIX

MEMS FABRICATION TECHNOLOGY AND MOEMS GYROSCOPE CHIP FABRICATION PROCESSES

In this chapter, the MEMS fabrication technology is introduced to enhance the background of MEMS technology, and prepare for the fabrication processes of the MOEMS gyroscope chip. The first prototype of the MOEMS gyroscope chip would be based on single static mass with four straight beams. The fiber optical interferometer is embedded into the substrate of the MEMS vibration structure. The demodulation circuits and interface port will be located on PCB. The micro gyroscope chip and peripheral circuits will be separately packaged.

6.1 Historical Development of MEMS Technology

The field of microelectronics began in 1948 when the first transistor was invented. This first transistor was a point-contact transistor, which became obsolete in the 1950s following the development of the bipolar junction transistor (BJT). The first modern day junction field-effect transistor (JFET) was proposed by Shockley (1952). These two types of electronic devices are at the heart of all microelectronic components, but it was the development of integrated circuits (ICs) in 1958 that spawned today's computer industry.

IC technology has developed rapidly during the past 40 years; an overview of the current bipolar and field-effect processes can be found in Chapter 4. The continual improvement in silicon processing has resulted in a decreasing device size; currently, the minimum feature size is about 200 nm. The resultant increase in the number of transistors contained within a single IC follows what is commonly referred to as *Moore's law*. Figure 6.1 shows that in just 30 years the number of transistors in an IC has risen from about 100 in 1970 to 100 million in 2000. This is equivalent to a doubling of the number per chip every 18 months (Clemens, 1997).

6.2 Basic MEMS Fabrication Processes Methods

The earliest methods used to manufacture silicon structures such as MEMS devices made use of lithography and etch technology. Chemical etching removes an unwanted section from the silicon structure. When chemical etching and etch-stopping techniques, such as a masking film, are used together inventively, complex structures can be produced. In 1982 when Howe made his micro beams, he used the now common technique of etching an underlying sacrificial layer. The sacrificial layer has an increased level of phosphorus to enhance the etch rate in hydrofluoric acid (Sniegowski, 1996). Current methods for the fabrication of MEMS devices include: surface micromachining, bulk micromachining, as well

as lithography. Most MEMS devices available currently are produced using either bulk or surface micromachining techniques.

MEMS promises to revolutionize nearly every product category by bringing together silicon-based microelectronics with micromachining technology, making possible the realization of complete systems-on-a-chip. MEMS is an enabling technology allowing the development of smart products, augmenting the computational ability of microelectronics with the perception and control capabilities of microsensors and microactuators and expanding the space of possible designs and applications.

Microelectronic integrated circuits can be thought of as the "brains" of a system and MEMS augments this decision-making capability with "eyes" and "arms", to allow microsystems to sense and control the environment. Sensors gather information from the environment through measuring mechanical, thermal, biological, chemical, optical, and magnetic phenomena. The electronics then process the information derived from the sensors and through some decision making capability direct the actuators to respond by moving, positioning, regulating, pumping, and filtering, thereby controlling the environment for some desired outcome or purpose. Because MEMS devices are manufactured using batch fabrication techniques similar to those used for integrated circuits, unprecedented levels of functionality, reliability, and sophistication can be placed on a small silicon chip at a relatively low cost.   This chapter intends to give holistic introduction about MEMS fabrications processes, capability and potential. Through this chapter, the supernatural faculty and interesting for the MEMS study would be enkindled. The MEMS technologies are huge and wide knowledge involved electrical, mechanical, optic, chemical and material etc. The introduction of MEMS technology just is assembly statement in this chapter. Based on the solid model, math model and current MEMS fabrication methods, the micro vibration structure fabrication processes are proposed (Howe R.T., 1988).

MEMS devices are extremely small, for example, MEMS has made possible electrically-driven motors smaller than the diameter of a human hair right. But MEMS is not primarily about size. MEMS is also not about making things out of silicon, even though silicon possesses excellent materials properties, which make it an attractive choice for many high-performance mechanical applications; for example, the strength-to-weight ratio for silicon is higher than many other engineering materials which allows very high-bandwidth mechanical devices to be realized.

Instead, the deep insight of MEMS is as a new manufacturing technology, a way of making complex electromechanical systems using batch fabrication techniques similar to those used for integrated circuits, and uniting these electromechanical elements together with electronics.

Advantages of MEMS are, firstly, MEMS and Nanotechnology are extremely diverse technologies that could significantly affect every category of commercial and military product. MEMS are already used for tasks ranging from in-dwelling blood pressure monitoring to active suspension systems for automobiles. The nature of MEMS and its diversity of useful applications make it potentially a far more pervasive technology than even integrated circuit microchips.

Second, MEMS blurs the distinction between complex mechanical systems and integrated circuit electronics. Historically, sensors and actuators are the most costly and unreliable part of a macroscale sensor-actuator-electronics system. MEMS allows these complex electromechanical systems to be manufactured using batch fabrication techniques, decreasing the cost and increasing the reliability of the sensors and actuators to equal those of integrated circuits. Yet, even though the performance of MEMS devices is expected to be superior to macroscale components and systems, the price is predicted to be much lower.

This section is intended for people new to micro-electro-mechanical systems (MEMS) technology. It gives a brief overview of the technology and some of the methods used to create microstructures. The section is not intended as a comprehensive, all inclusive, description which is pointless anyway as the technology continues to develop. It is merely a short introduction to the basic fundamentals of the technology.

MEMS technology is based on a number of tools and methodologies, which are used to form small structures with dimensions in the micrometer scale (one millionth of a meter). Significant parts of the technology have been adopted from integrated circuit (IC) technology. For instance, almost all devices are built on wafers of silicon, like ICs. The structures are realized in thin films of materials, like ICs. They are patterned using photolithographic methods, like ICs. There is however several processes that are not derived from IC technology, and as the technology continues to grow the gap with IC technology also grow.

There are three basic building blocks in MEMS technology, which are the ability to deposit thin films of material on a substrate, to apply a patterned mask on top of the films by photolithograpic imaging, and to etch the films selectively to the mask. A MEMS process is usually a structured sequence of these operations to form actual devices. Please follow the links below to read more about deposition, lithography and etching which are three major processes for manufacture to MEMS applications (Klaassen, Petersen etc., 1995).

6.2.1 MEMS Deposition Processes: Surface Micromachining

The first example of surface micromachining for an electromechanical purpose occurred in 1967 when Nathanson made an underetched metal cantilever beam for a resonant gate

transistor. By the 1970's plans were being developed for a metal magnetically actuated microengine; however, there were fatigue problems with metals, and due to the fatigue problem metals are rarely used as structural members in micromachining. The present state of the micromachining method was introduced in the 1980's by Howe and Muller where polysilicon was introduced as the primary material for the structural layers.

Surface micromachining (SMM) builds structures by patterning thin multiple layers deposited on a substrate. This produces finished product using batch fabrication where no assembly is required. SMM is usually based on low pressure chemical vapor deposition (LPCVD) of the structural, e.g., polysilicon, sacrificial, e.g., silicon dioxide, and photoresistive layers onto the substrate. These layers are then patterned using dry etching to make in-plane features, and wet etching removes the sacrificial layers used to support the structures during deposition.

The surface micromachining technology makes thin micromechanical devices on the surface of a silicon wafer. Large numbers of devices can be inexpensively made, and this technology integrates well with electronics. On the surface of a silicon wafer, thin layers of structural and sacrificial material are deposited and patterned. At the end of the processing the sacrificial material is removed, and completely assembled micro mechanical devices remain.

One of the basic building blocks in MEMS processing is the ability to deposit thin films of material. In this text we assume a thin film to have a thickness anywhere between a few nanometer to about 100 micrometer. The film can subsequently be locally etched using processes described in the Lithography and Etching sections.

MEMS deposition technology can be classified in two groups:

a) Depositions that happen because of a chemical reaction:

- Chemical Vapor Deposition (CVD)
- Electrodeposition
- Epitaxy
- Thermal oxidation

These processes exploit the creation of solid materials directly from chemical reactions in gas and/or liquid compositions or with the substrate material. The solid material is usually not the only product formed by the reaction. Byproducts can include gases, liquids and even other solids.

160

b) Depositions that happen because of a physical reaction:

- Physical Vapor Deposition (PVD)
- Casting

Common for all these processes are that the material deposited is physically moved on to the substrate. In other words, there is no chemical reaction which forms the material on the substrate. This is not completely correct for casting processes, though it is more convenient to think of them that way.

6.2.2 MEMS Etching Processes: Bulk Micromachining

The first appearance of using chemicals to etch a substrate protected otherwise by a mask was in the fifteenth century when acid and wax was used to etch and decorate armor; by the 1600's chemical etching for the decoration of armor and weapons was common practice. In 1822 photosensitive masks were introduced as lithography by Niépce and increased the tolerances of the etching to a new level. Bulk micromanufacturing, or micromachining, as it is known today, was developed from technology that was first used in the 1960s for microelectronic applications, but this technology was improved upon and in the 1970s was being implemented to produce three-dimensional microstructures. Bulk micromachining (BMM) is used for the production of microsensors and accelerometers; this technique removes material from a substrate, usually silicon, silicon carbide, gallium arsenide, or quartz, using a type of etching, either dry or wet, to produce desired three-dimensional structures, .typically for MEMS applications out of silicon. Figure 6.1 illustrates an example of a wet bulk micromachining process (Bhardwaj, Ashraf, and McQuarrie, 1997).

Deposit photoresist

Open contacts

Silicon wafer

↓ ↓ ↓ ↓ ↓ ↓ ↓ ↓ UV light

━━━━━━━━━━━━━━ mask

Deposit aluminum

Develop resist

Pattern aluminum

↓ ↓ ↓ ↓ ↓ ↓ ↓ ↓ Implant boron

Pattern black oxide

Anneal and oxidation

Silicon etch
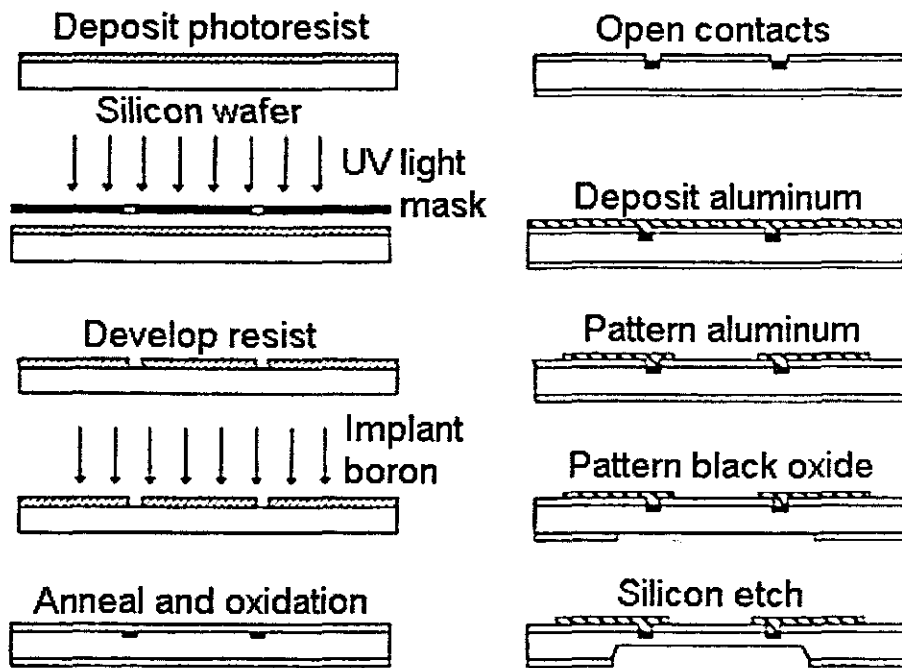
Figure 6.1: Steps in the bulk micromachining process

Bulk micromachining can also be done using dry etchants; however, wet chemical etching is traditionally faster, than dry etching processes, having rates of about 1 µm/minute and allows the operator to select specific materials to etch preferentially. Wet etchants that are used for isotropic etching, where the rate of material removal is the same in all crystallographic directions, are usually acids: Piranha (4:1, H2O2:H4SO4), buffered HF (5:1, NH4F:conc.HF), and HNA (HF/HNO3/ CH3COOH). Anisotropic etchants, which etch in one crystallographic direction faster than in the other directions, are used for machining of microcomponents; there are many different types of chemicals that are used as anisotropic etchants: alkaline aqueous solutions such as KOH, NaOH, LiOH, CsOH, NH4OH, quaternary ammonium hydroxides, and alkaline organics like ethylenediamine, chlorine (trimethyl-2-hydroxyethyl ammonium hydroxide), and hydrazine with pyrocathechol or pyrazine.

Bulk Micromachining makes micromechanical devices by etching deeply into the silicon wafer. There are several ways to etch the silicon wafer. Anisotropic etching uses etchants like KOH that etch different crystallographic directions at different rates. Certain crystallographic planes etch extremely slowly, and are called stop planes. Anisotropic etching usually produces Vee grooves, pyramids, and channels into the surface of the silicon wafer. Isotropic etching etches all directions in the silicon wafer with nearly the same rate, and produces rounded depressions on the surface of the wafer that usually resemble hemispheres and cylinders. Deep Reactive Ion Etching, RIE or DRIE, uses plasma to etch straight walled structures on the wafer that resemble the mesa hills in the American south west.

In order to form a functional MEMS structure on a substrate, it is necessary to etch the thin films previously deposited and/or the substrate itself. In general, there are two classes of etching processes:

a) Wet etching where the material is dissolved when immersed in a chemical solution
b) Dry etching where the material is sputtered or dissolved using reactive ions or a vapor phase etchant

6.2.3 Lithography

Today LIGA (in German, Lithographie, Galvanoformung, Abformung) is researched in many laboratories around the world. The technology has reinvigorated attempts at developing alternative micromolds for the large-scale production of precise micromachines. Mold inserts, depending on the dimensions of the microparts, the accuracy requirements and the fabrication costs are realized by e-beam writing, deep UV resists excimer laser ablation, electrodischarge machining, laser cutting and X-ray lithography as involved in the LIGA technique (Guckel H., Christenson T. R., Skrobis, Denton, Choi, Lovell, Lee, Bajikar, and Chapman, 1990).

LIGA is a process that was developed in the early 1980s by W. Ehrfeld at the West German IMT in Karlsruhe. LIGA was one of the first major techniques to allow on-demand manufacturing of high-aspect-ratio structures in other words, very skinny and tall, compared to traditional photolithographic techniques, with lateral dimensions below one micrometre. This capability is important in the fabrication of MEMS devices. Because of the high-energy of X-rays needed, the source must be synchrotron light.

While photolithography has been used extensively in integrated circuit manufacture for almost 50 years, nanostructured stamp lithography techniques to pattern silicon and other device-relevant materials have recently been improved enough to offer a realistic alternative to purely radiation-based patterning and formation methods.

Whereas LIGA greatly assisted research in micromachining and MEMS, leading elements of nanotechnology will likely take advantage of the various new forms of nano-contact printing.

Products with these features can be made by the LIGA process:

* Any lateral geometry of structures.
* Structural height above 1 mm.
* Smallest lateral dimensions down to 0.2 µm.

163

- Aspect ratios of free-standing individual structures and details, respectively, above 50 and 500, respectively.
- Surface quality in the submicron range with roughnesses, Ra, of 30 nm.
- Various materials: Polymers: PMMA, POM, PSU, PEEK, PVDF, PC, LCP, PA, PE. Metals: Nickel, copper, gold, NiFe, NiP. Ceramics: PZT, PMNT, Al2O3, ZrO2; alloys.

A Brief Description outline of the LIGA-Process: Microcomponents can be manufactured not only by silicon technologies, but also by the LIGA process developed at the Forschungszentrum Karlsruhe. The LIGA process has the advantage of allowing microcomponents to be manufactured in almost any lateral geometry and structure height out of polymers, metals, and ceramics, thus covering the range of "non-silicon" materials. The LIGA process comprises the steps of X-ray deep lithography, electroforming, and molding.

In X-ray deep lithography, a polymer layer (resist) sensitive to X-radiation is exposed to X-radiation by the shadow produced by X-ray mask, which transfers to the resist an exact image of the absorber structures on the mask. The exposed areas are dissolved selectively by wet chemical methods. In most cases, the resist is made of polymethylmethacrylate (PMMA, plexiglass). The very high energy and parallel nature of X-rays, compared to optical and UV lithography, allows very high structures with almost vertical and very smooth sidewalls to be produced.

When these polymer structures are produced on a metal starting layer, the structural areas exposed after the developing process can be filled up with various metals by electrodeposition, such as nickel, gold, copper or alloys (electroforming). Once the metal has built up, the remaining PMMA is removed, and only metal microstructures remain in place. If the metal is allowed to grow clearly beyond the resist, a continuous, stable metal plate is obtained which carries the microstructures and can serve as a tool for molding.

Mass production of polymer microcomponents makes use of molding, hot embossing or injection molding. These replication techniques allow very many microcomponents to be produced with one mold insert in parallel and largely automatically. When producing large numbers of metal microcomponents, the molded polymer components are used as lost molds for the deposition of metals (electrodeposition). The brief LIGA processes show in figure 6.2.
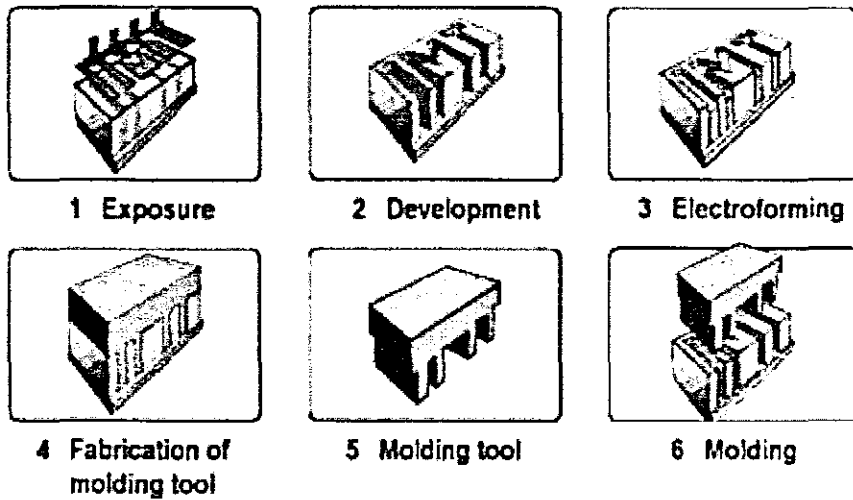
Figure 6.2: LIGA Processes

Advantages of LIGA processes are described below:

a. High accuracy: Resist structure of a reflection grating, 0.25 μm step height, 125μm structural height.

b. Any lateral shape: Separation nozzle as an example of arbitrary lateral shaping.

c. High aspect ratio: Bar structure 400 μm high, with parallel sidewalls.

6.2.4 MEMS Wafer Bonding

There are a number of different methods available for bonding micromachined silicon wafers together, or to other substrates, to form larger more complex devices.

A method of bonding silicon to glass that appears to be gaining in popularity is anodic bonding (electrostatic bonding). The silicon wafer and glass substrate are brought together and heated to a high temperature. A large electric field is applied across the join, which causes an extremely strong bond to form between the two materials. Figure 6.3 shows a glass plate bonded over a channel etched into a silicon wafer (RIE), forming a pipe through which fluid can flow.
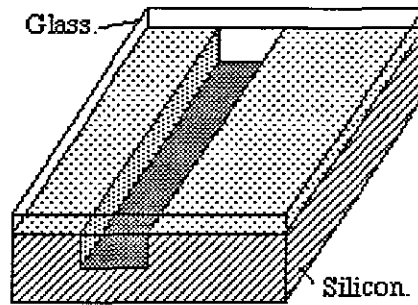
Figure 6.3: the example of bonding Silicon and Glass

It is also possible to bond silicon wafers directly together using gentle pressure, under water (direct silicon bonding).

Other bonding methods include using an adhesive layer, such as a glass, or photoresist. Whilst anodic bonding and direct silicon bonding form very strong joins they suffer from some disadvantages, including the requirement that the surfaces to be joined are very flat and clean.

Wafer bonding techniques can potentially be combined with some of the basic micromachined structures to form the valves, pumps, etc, of a microfluid handling system.

6.3 MEMS Materials

MEMS technology can be implemented using a number of different materials and manufacturing techniques; the choice of which will depend on the device being created and the market sector in which it has to operate.

a) Silicon

Silicon is the material used to create almost all integrated circuits used in consumer electronics in the modern world. The economies of scale, ready availability of highly accurate processing and ability to incorporate electronic functionality make silicon attractive for a wide variety of MEMS applications. Silicon also has significant advantages engenderred through its material properties. In single crystal form, silicon is an almost perfect Hookean material, meaning that when it is flexed there is virtually no hysteresis and hence almost no energy dissipation. As well as making for highly repeatable motion, this also makes silicon very reliable as it suffers very little fatigue and can have service lifetimes in the range of billions to trillions of cycles without breaking. The basic techniques for producing all silicon based

MEMS devices are deposition of material layers, patterning of these layers by lithography and then etching to produce the required shapes.

b) Polymers

Even though the electronics industry provides an economy of scale for the silicon industry, crystaline silicon is still a complex and relatively expensive material to produce. Polymers on the other hand can be produced in huge volumes, with a great variety of material characteristics. MEMS devices can be made from polymers by processes such as injection moulding, embossing or stereolithography and are especially well suited to microfluidic applications such as disposable blood testing cartridges.

c) Metals

Metals can also be used to create MEMS elements. While metals do not have some of the advantages displayed by silicon in terms of mechanical properties, when used within their limitations, metals can exhibit very high degrees of reliability. Metals can be deposited by electroplating, evaporation, and sputtering processes. Commonly used metals include Gold, Nickel, Aluminum, Chromium, Titanium, Tungsten, platinum, and silver.

6.4 MOEMS Gyroscope Model Fabrication Design

The MOEMS gyroscope is consisted by micro vibration structure and fiber optical interferometer readout system. The micro vibration structure can be fabricated by MEMS fabrication technology. In chapter 5, the micro vibration structure model of MOEMS gyroscope has been introduced and simulated by CoventorWare. The single mass and dual mass structures with the straight beams and folded beams have been discussed. Here, the fabrication processes of the single mass with the straight beams are presented as example.

- Choose the 200um thickness Silicon wafer as substrate, and washing.
- Using LPCVD technique to grow the Si_3N_4.
- Using LIGA technique to etch the Si_3N_4 layer to creating isolation.
- Deposition sacrifice PSG layer.
- Deposition N-type polysilicon layer.
- Sputtering Au layer on the polysilicon layer.
- Using LIGA technology to etch Au layer as full reflected surface, which is one reflected surface of fiber optical interferometeric cavity.
- Using LIGA technology to etch the patterns of liberative holes, mass, straight beams and comb-driver.

- Sputtering metal pole for comb-driver.
- Release the sacrifice PSG layer.

The MEMS fabrication processes are shown in figure 6.4 to 6.8 individual. The top view of the single mass of micro vibration structure shows in figure 6.9, which presents the shapes and positions of each layer and electrodes for comb-driver.
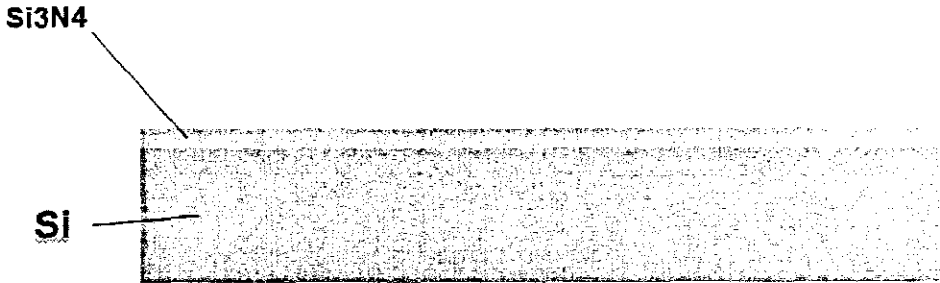
Figure 6.4: The Si$_3$N$_4$ Isolation Layer Deposit
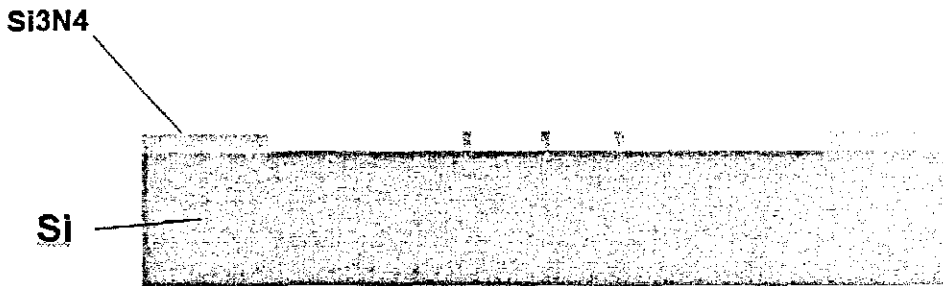
Figure 6.5: Etch the Stopping Pillar and Beam Anchor
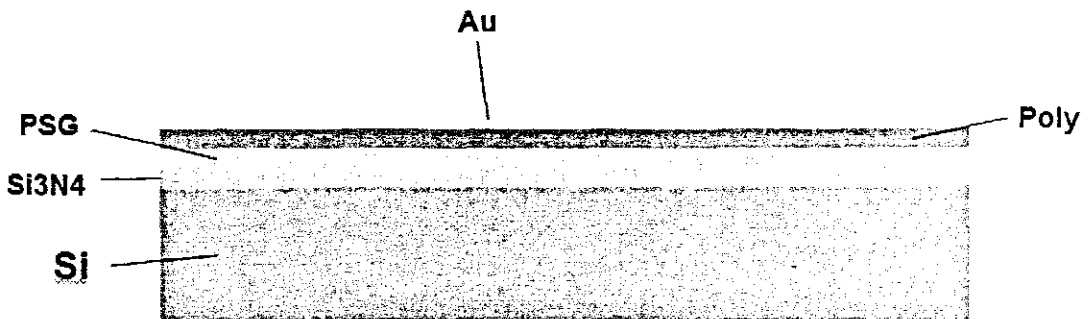
Figure 6.6: Deposit the Scarification, Static mass with Beams and Reflected Layers
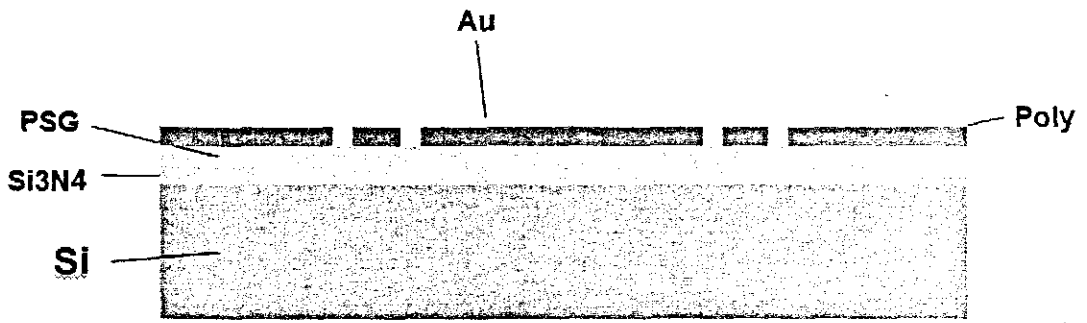
Figure 6.7: LIGA Etch the Mask Pattern for Mass, Beams, and Reflected Surface
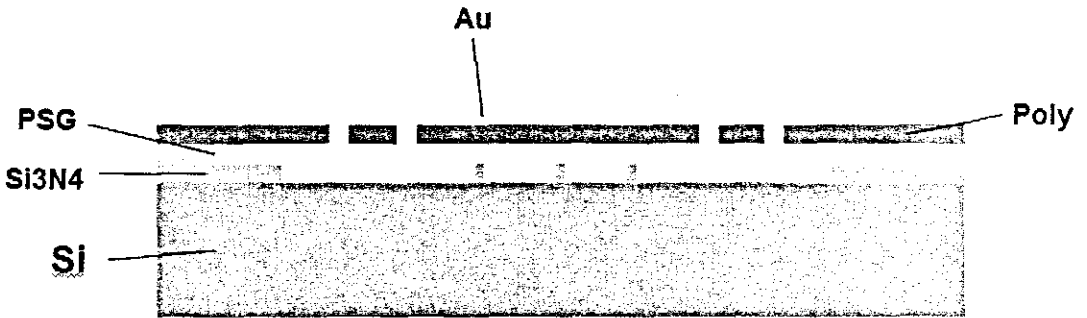
Figure 6.8: Release the Scarification Layer. Complete the Vibration Cavity
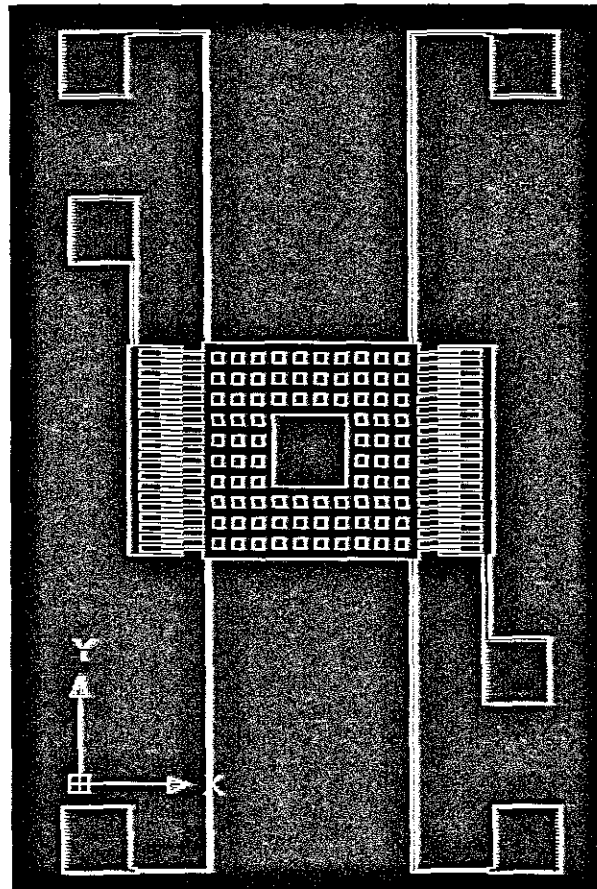
Figure 6.9: Top View of the MEMS Vibration Structure

6.5 Conclusion

In chapter 6, the MEMS fabrication technology is introduced about MEMS development history and important fabrication methods including etch technology, deposition technology and LIGA technology. Based on the introduction of MEMS fabrication processes, the single mass vibration structure fabrication processes are designed and described. However, the MEMS fabrication technology is not uniform standard. The different MEMS manufacture has different fabrication processes according to MEMS devices in the MEMS laboratories. The fabrication processes are presented above for the single mass vibration structure, which are the typical MEMS fabrication processes. The different researcher has different design practices, which means the sequences of MEMS fabrication processes and materials can be adjusted by MEMS fabrication engineers and clients. With the developing of MEMS devices and fabrication techniques, the manufacture precision and complex shapes can be fabricated.

CHAPTER SEVEN

CONCLUSIONS

The thesis was studied development and improvement of the micro rotation rate sensor, micro gyroscope based on MEMS fabrication technology. The micro silicon substrate vibration gyroscope with the micro fiber optical read-out system was designed to provide the micro size, high performance, and low cost characteristices.

7.1 Conclusion

Gyroscope is an important class of the motion sensor, used in motion or control. For a long time, the rotation rate measurement is a problem for navigation system used for any vehicles. The gyroscope systems have evolved from wheel spin to optical Sagnac gyroscopes and MEMS Corilolis gyroscopes. However, the cost, the volume and the performances of the gyroscope systems have been problematic to the user and manufacturer. The markets need a high performances and low cost, micro gyroscope system.

The research problems and motivations of the research are introduced in chapter one. The chapter covers the research scope, research methodology, and outline of the thesis. Through a literature review of the gyroscopes technology in chapter two and optical phase-shift sensing technology in chapter three, the novel MOEMS gyroscope system was proposed to achieve the best performance and size ratio and performance and cost ratio. The detailed description of the MOEMS gyroscope mathematical model and operation principles was explained in chapter four and compared the performances with the fiber optical gyroscopes based on Sagnac effect. The fiber optical interferometric readout system has been discussed and shown the sense ability. And then the solid micro model was programmed and simulated by Coventorware in chapter five. The the micro vibration structure was performed well according to Coriolis effect. The micro vibration structure is skillfully using the Coriolis force theory to convert the rotation motion to the one axis vibration motion. The vibration structure is suitably fabricated by MEMS fabrication technology, and very sensitive on the rotation rate. The fiber optical read-out system was designed to detect diaplacement of the static mass. The circuits design, sensitivity, and niose analysis were discussed in chapter five. The chapter six was proposed the MEMS fabrication processes of the typical single mass with the straight beams vibration structure step by step. The fabrication processes are all standard procedure, which are easy controlled and stabilitied on the finished products. The MEMS technology brings the new energy for the conventional manufactory industries, makes

subminiature the devices and various sensors with low cost and high performances. The fabrication processes can be different with different MEMS designer and according to the different MEMS devices.

This micro vibration structure with the optical read-out system is the original designs, which are skillful integration two high technologies in rotation sensing techniques, the Coriolis effect and light interferometry.

In this dissertation, the MOEMS gyroscope system was presented from the operation principles, mathematics model and solid model performaces simulation to the MEMS fabrication processes. The thesis study was followed the research problems, scope, and interrelated literature review. In the micro mechanical part, the Coriolis force was used to design the MEMS vibration structure to transform the rotation rate to the linear displacement. In the measurment part, the micro fiber optical interferometer was proposed to provide better precision instead of the capacitive sensing technique. It is the first time introduced the optical sensing technique to the MEMS gyroscope system. The interface of the optics and machine was successed presented in the thesis.

7.2 Recommendations for Future Work

Some possibilities for future research have been suggested throughout the previous chapters. In this section, some additional research directions that will lead to a better understanding of integrated micro gyroscope system. The model of MOEMS gyroscope will be further consummated and optimized about the size of vibration structure and the position of optical readout system. Addition, the multi-axis MOEMS gyroscope system is important researching objective based on optical multi-demodulation technology. The optical components and materials for fabricate vibration structure can be widely choose.

Based on the theory study and model simulation of the MOEMS gyroscope system, the prototype of the MOEMS gyroscope could be fabricated and tested in practical. The optical demodulation circuits and power supply circuits could be designed in many methods. The produces of MOEMS gyroscope system have long way to go.

This is not the research end for micro motion sensors like gyroscopes. For the good life, the research about micro sensors, MEMS fabrication and nano technology will go forever.

REFERENCES

Agrawal G. P., 1997, "Fiber-Optic Communication Systems", 2nd Edition, John Wiley &Sons Inc.

Andronova I. A., Malykin G. B., 2002, "Physical problems of fiber gyroscope based on the Sagnac effect", *Physics-Uspekhi,* vol. 45, no. 8, pp. 793-817.

Armenise M. N., Ciminelli C., De Leonardis F., Diana R., Passaro V., Peluso F., 2001, "Gyroscope technologies for space applications", Optoelectronics Laboratory, Bari.

Armenise M.N., Armenise M., Passaro V.M.N., De Leonardis F., 2000, "Integrate d optical angular velocity *sensor", European Patent EP 1219926, Politecnico di, Bari.*

Armenise M.N., Passaro V.M.N., De Leonardis F., Armenise M., 2001, "Modeling and Design of a Novel Miniaturized Integrated Optical Sensor for Gyroscope Applications", *Journal of Lightwave Technology,* vol. 19, no. 10, pp. 1476-1494.

Arya V., de Vries M. J., Murphy K. A., Wang A., and Claus R. O., 1995, "Exact analysis of the EFPI optical fiber sensor using Kirchhoff's diffraction formalism," *Optical Fiber Technology,* Vol 1, pp. 380–384.

Ayazi F., Najafi K., 2001, "A HARPSS Polysilicon Vibrating Ring Gyroscope", *IEEE J. of Microelectromechanical Sysem.,* vol. 10, no. 2, pp. 169-179.

Barbour N., Schmidt G., 2001, *"Inertial Sensor Technology Trends",* *IEEE Sensors Journal* vol. 1, no. 4, pp. 332-339.

Ball G. A., Meltz G. and Morey W. W., 1995, "Polarimetric Heterodyning Bragg-Grating Fiber Laser", *Optics Letters,* Vol. 18, pp. 1976.

Barbour N., Schmidt G., 2001, "Inertial Sensor Technology Trends", *IEEE Sensors Journal,*

vol. 1, no. 4, pp. 332-339.

Beard P. C. and Mills T. N., 1996, "Extrinsic optical-fiber ultrasound sensor using a thin polymer film as a low-finesse Fabry-Perot interferometer," *Applied Optics,* vol. 35, no.4, pp. 663-675.

Bergh R. A., Lefevre H. C., Shaw H. J., 1984, "An Overview of Fiber-Optic Gyroscopes", *Journal of Lightwave Technology,* vol. 2, no.2, pp. 91-107.

Bertone N. and Webb P., "Noise and Stability in PIN Detectors," [online], http://optoelectronics.perkinelmer.com/content/whitepapers/NoiseandStabilityPINDetectors.p df. [accessed 13 October 2006] [12 March 2006].

Bhatia V., 1993, "Signal Processing Techniques for Optical Fiber Sensors Using White Light Interferometry," *Master's Thesis,* Virginia Polytechnic Institute and State University, Blacksburg, VA.

Bhardwaj J., Ashraf H., and McQuarrie A., 1997, "Dry Silicon Etching for MEMS," *Proceedings of the Symposium on Microstructures and Microfabrication,* Spring Meeting of The Electrochemical Society, Montreal, Quebec, Canada.

Bock W.J., Urbanczyk W., Wojcik J., Beaulieu M., 1995, "White-light interferometric fiberoptic pressure sensor," *IEEE Transactions on Instrumentation and Measurement,* vol. 44, no. 3, pp. 694 – 697.

Bohnert K., Gabus P., Nehring J., and Brandle H., 2002, "Temperature and Vibration Insensitive Fiber-Optic Current Sensor," *Journal of Lightwave Technology,* vol. 20, no.2, pp.267-276.

Burns W. K., 1994, "Optical Fiber Rotation Sensing", *Academic Press,* San Diego.

Chan M. A., Collins S. D. and Smith R. L., 1994, "A micromachined pressure sensor with fiber-optic interferometric readout," *Sensors and Actuators A,* vol. 43, pp. 196-201.
Chow W. W., Gea-Banacloche J., Pedrotti L. M., Sanders V. E., Schleich W., Scully M. O., 1985, "The ring laser gyro", *Rev. of Modern Optics,* vol. 57, no.1, pp. 61-104.

Cibula E., Donlagic D., Stropnik C., 2002, "Miniature fiber optic pressure sensor for medical applications," *Sensors Proceedings of IEEE* June 2002, Vol. 1, pp. 711-714.

Clark W.A., Howe R.T., Horowitz R., 1996, "Surface micromachined Z-axis vibratory rate gyroscope", *Technical Digest Solid-State Sensor and Actuator Workshop,* Hilton Head Island, SC, USA; 3-6 June, pp.283-287.

Claus R.and Udd E., 1991, Editors, "Fiber Optic Smart Structures and Skins IV", Proceedings of SPIE, Vol. 1588.

Clemens J. T., 1997, "Silicon microelectronics technology", *Journal of interScience,* VLSI Research Department, Bell Labs, Murray Hill, New Jersey, November.

Core T. A., Tsang W. K., and Sherman S. J. 1993, "Fabrication technology for an integrated surface-micromachined sensor." *Solid State Technology.,* vol. 10, pp. 39-47

Cox E. R. and Jones B. E., 1983, "Fiber optic sensors based on Fabry–Perot interferometry," in *Proceedings of the First Inter-national Conference on optical Fiber Sensors optical* Society of America, Washington, D.C., pp. 122–126.

Cranch G. A. and Nash P. J., 2001, "Large-Scale Multiplexing of Interferometric Fiber-Optic Sensors Using TDM and DWDM," *Journal of Lightwave Technology,* vol. 19, no.5, pp. 687-698.

Culshaw B., 2004, Lightwave Technology "Optical fiber sensor technologies: opportunities and-perhaps-pitfalls", *Journal of Lightwave Technology,*Volume 22, Issue 1, Jan. 2004, pp. 39-50.

Dakin J. P., 1998, "Distributed optical fiber systems", *Optical Fiber Sensors: Systems and Applications,* vol. 2 , pp. 575-598.

Dandridge A., Tveten A., Kersey A., Yurek A., 1987, "Multiplexing of interferometric sensors using phase carrier techniques" *Journal of Lightwave Technology,* vol. 5, pp. 947.

Dandridge A., 1991, Fiber Optic Sensors Based on the Mach-Zehnder and Michelson Interferometers, in *Fiber Optic Sensors: An Introduction for Engineers and Scientists,* Edited by Eric Udd, Wiley, New York.

Deng J.D., 2004, "Development of Novel Optical Fiber Interferometric Sensors with High Sensitivity for Acoustic Emission Detection," Ph.D. Dissertation, *Virginia Polytechnic Institute and State University.*

Doi M., Iwasaki Y., Shionoya T. and Okamoto K., 1997, "High-resolution displacement measurement using mode interference in the optical waveguide", *IEEE Photonics Technology Letter,* vol. 9, no. 5, pp. 651-653.

Dollon M., Cros G., Sevellec A., Antoine P., Muller G., Willemenot E., Urgell A., Hardy G., Loret T., Faussot N., Cottreau Y., Gaiffe T., 2002, "A new family of IMU based on IFOG technology", *Process V ESA Conf. On Spacecraft Guidance, Navigation and Control,* Frascati, Italy, 22-25 Oct 2002, SP-516, pp. 41-45.

Dyott R. B., Bennett S.M., Allen D., Brunner J., 2002, "Development and Commercialization of Open Loop Fiber Gyros at KVH Industries", *IEEE Optical Fiber Sensors Conference,* 15th OFS 2002, pp. 19 -22.

Ecke W., Pfeifer P., Schauer J. and Willsch R., 1996, "Fiber optic displacement measuring system for high-temperature seismic sensor", *SPIE* 2839, pp. 290-301.

Egorov S. A., Mamaev A. N., Polyantsev A. S., 1995, "Spectrum signal processing in intrinsic interferometric sensors based on birefringent polarization-maintaining optical fibers," *Journal of Lightwave Technology,* vol. 13, no. 7, pp. 1231-36.

Fan L. S., Tai Y. C., and Muller R. S., 1998, "Integrated movable micromechanical structures for sensors and actuators", *IEEE Transactions on Electron Devices ED-35,* 724-730, June.

Franco S., 1998, "Design with Operational Amplifiers and Analog Integrated Circuits", 2nd Edition, McGraw-Hill Companies, Inc., Boston.

Fujishima S., Nakamura T. and Fujimoto K., 1991, "Piezoelectric vibratory gyroscope using flexural vibration of a triangular bar", In *Proceedings of the 45th Annual Symposium on Frequency Control 1991,* Los Angeles, CA, May 1991.

Gabrielson T. B., 1993, "Mechanical-thermal noise in micromachined acoustic and vibration sensors," *IEEE Trans. Electron Devices,* vol. 40, pp. 903–909, May.

Geen J.A., Sherman S.J., Chang J.F. and Lewis S.R., 2002, "Single-chip surface-micromachining integrated gyroscope with 50 deg/hour root Allan variance", *Digest of 2002 IEEE International Solid-State Circuits Conference,* San Francisco, CA, 3-7 Feb. 2002, pp.426-427.

Geiger W., Merz J., Fischer T., Folkmer B., Sandmaier H., and Lang W., 1999, "The silicon Angular Rate Sensor System MARS-RR", *Transducers'99,* Sendai, Japan, June 7-10, pp.1578-1581.

Geiger W., Folkmer B., Merz J., Sandmaier H., Lang W., 1998 "A new silicon rate gyroscope", *Proc. the 11th IEEE Micro Electro Mechanical Systems Workshop (MEMS'98),* Heidelberg, Germany, Feb 1998, pp. 615–620.

Gerges S., Farahi F., Newson T. P., Jones J. D. C., Jackson D. A., 1988, "Fibre-optic interferometric sensor utilising low coherence length sources: Resolution enhancement," *Electronics Letter,* vol. 24, no. 8, 472-474.

Gianchandani Y.B., 2000, etc., "A fabrication process for integrating polysilicon microstructure with post-processed CMOS circuits", *Journal of Micromechanical Microengineer,* pp.380-386.

Gilbert J. R., 1996, "Exploring design spaces for optical MEMS devices", *Advanced Applications of Lasers in Materials Processing, 1996/Broadband Optical Networks/Smart Pixels/Optical MEMS and Their Applications,* IEEE/LEOS Summer Top, 5-9 Aug., pp. 54-55.

Green E. L. and Cable P. G., 1982, "Passive Demodulation of Optical Interferometric Sensors," *IEEE Trans. On Microwave Theory and Techniques*, vol. 30, no. 10, pp. 1627-32.

Greiff P., Boxenhorn B., King T., and Niles L., 1991, Proc., "Silicon monolithic micromechanical gyroscope", *IEEE 1991 Int. Conf. on Solid State Sensors and Actuators*, San Francisco, June 24–27, pp. 966–968.

Guckel H., Christenson T. R., Skrobis K. J., Denton D. D., Choi B., Lovell E. G., Lee J. W., Bajikar S. S., and Chapman T. W., 1990, "Deep X-ray and UV Lithographies for Micromechanics," in *Technical Digest, 1990 IEEE Solid-State Sensor and Actuator Workshop,* Hilton Head, SC, June, pp. 118–122.

Gunther M. F., Wang A., Fogg B. R., Murphy K. A., and Claus R. O., 1992,"Fiber optic impact detection and location system embedded in a composite material," in *Fiber Optic Smart Structures and Skins V,* edited by R.O. Claus and R.S. Rogowski, Boston, SPIE 1798, pp. 262-269.

Gyroscope, [online] http://en.wikipedia.org/wiki/Gyroscope[12 August 2005].

Hanson D. S., Marinis T. F., Furlong C., and Pryputniewicz R. J., 2001, "Advances in optimization of MEMS inertial sensor packaging," *Processing International Congress on Experimental and Applied Mechanics in Emerging Technologies,* Portland, pp. 821-825.

Haus H., Tatz H., Smith W., 1985, "Frequency Locking of Modes in a Ring Laser", *IEEE Journal of Quantum Electronics,* vol. 21, no. 1, pp. 78-85.

Hopkin I., 1997, "Performance and design of a silicon micromachined gyro", *Processing sympathetic Gyro Technology,* Stuttgart, Germany, pp. 1.0-1.10.

Howe R.T., 1988, "Surface-Micromachining for Microsensors and Microactuators", *Journal of Vacamatic Science Technology,* vol. 6, pp.1809-1813.

Juneau T., Pisano A.P., Smith J.H., 1997, "Dual axis operation of a micromachined rate gyroscope", *Tranducers' 97,* Chicago, IL, USA; 16-19 June 1997, pp.883-886.

Kersey A. D., 1991, "Distributed and Multiplexed Fiber Optic Sensors", in *Fiber Optic Sensors: An Introduction for Engineers and Scientists,* edited by Eric Udd, Wiley, New York.

Klaassen E., Petersen K. etc., 1995, "Silicon Fusion Bonding and Deep Reactive Ion Etching: A new Technology for Microstructures", *Proceedings of the 8th International Conference on Solid-State Sensors and Actuators,* Transducers'95, pp.556.

Komachia M., Sonobe H., Oho S., Ohbu K., Yuhara T., Izuka H., 1996, Applied Optics *"Secondary-phase modulation method for open loop fiber optic gyroscopes",* vol. 35, no. 19, pp. 3719-3725, July.

Lee C. E. and Taylor H. F., 1992, "In-line Fiber Fabry Perot Interferometer with High Reflectance Internal Mirrors", *Journal of Lightwave Technology,* Vol. 10.

Lefevre H. C., Marten P., Morrise J., Simonpieti P., Vivenot P. and Arditty H. J., 1990, "High dynamic range fiber gyro with all digital signal processing", *Fiber Optic and Laser Sensors.*

Lefevre H., 1993, "The Fiber Optic Gyroscope", Artech House, Norwood.

Lemkin M. and Boser B. E., 1999, "A Three-Axis Micromachined Accelerometer with a CMOS Position-Sense Interface and Digital Offset-Trim Electronics", *IEEE Journal of Solid-State Circuits*, Vol.34, April, pp.456-68.

Liang D., Monteiro FL., Fraser Monteiro M.L. and Lu B., 1991, "Three-dimensional interferometric and fiber-optic displacement measuring probe", *SPIE Fiber Optical Sensors: Engineering Application,* vol. 11, pp. 90-97.

Lo Y.-L. and Chuang C.-H., 2001, "New synthetic-heterodyne demodulator for an optical fiber interferometer," *IEEE J. of Quantum Electron.,* vol. 37, no. 5, pp. 658-663.

Lutz M., Golderer W., Gerstenmeier J., Marek J., Maihofer B., Mahler S., Munzel H. and Bischof U. 1997, "A precision Yaw Rate Sensor in Silicon Micromachining." *Proc., IEEE 1997 Int. Conf. on Solid State Sensors and Actuators*, Chicago, 16-19June, pp. 847-850.

Madni A.M.; Wan L.A., 1998, Aerospace Conference "*Microelectromechanical systems (MEMS): an overview of currentstate-of-the-art*", Proceedings., IEEE Volume 1, Issue , 21-28 Mary, vol.1, pp. 421-427

Maenaka K. and Shiozawa T., 1994, A study of silicon angular rate sensors using anisotropic etching technology. *Sensors and Actuators A*, vol. 43 no. 3, pp. 72-77, May.

MEMS Design and Analysis Tutorials.pdf, http://www.coventor.com/, Volume 1

Mochida Y., Tamura M., Ohwada K., 1999, MEMS'99 "*A micromachined vibrating rate gyroscope with independent beams for the drive and detection modes*", Orlando, FL, USA; 17-21 January, pp.618-623.

Monovoukas C., Swiecki A.K., Maseeh F., 2000, "Integrated optical gyroscopes offering low cost, small size and vibration immunity", *Intellisense Corp. Report*, http://www.intellisense.com/contentfiles/devicetechnologypapers/IntegratedOpticalGyroscope soffering lowcostsmallsizeandvibrationimmunity.pdf [12 June 2006].

Morey W. W., Meltz G. and Glenn W. H., 1989, "Bragg-Grating Temperature and Strain Sensors", *Proceedings of Optical Fiber Sensors 89*, Springer-Verlag, Berlin, pp. 526.

Murphy K. A., Gunther M. F., Vengsarkar A. M., and Claus R. O., 1991, "Quadrature phase-shifted, extrinsic Fabry-Perot optical fiber sensors," *Optics Letters*, Vol.16, no. 4, pp.273-275, February.

Ning Y. N., Wang Z. P., Palmer A. W., Grattan K. T. V., and Jackson D. A., 1995, "Recent progress in optical current sensing techniques," *Review of Scientific Instruments,* vol. 66, no. 5, pp. 3097-3111.

Norgia M., Donati S., 2001, "Hybrid opto-mechanical gyroscope with injection-interferometer readout", *Electronics Letter,* vol. 37, no. 121, pp. 756-758, June.

Online http://www.ais.honeywell.com/dss/sgp/products/rlg-gg1305an.htm[12 January 2007].

Online http://www.ngnavsys.com/Html/LN-100LG/[12 January 2007].

Online http://www.aselsan.com.tr/mging/products/ln100.htm[12 January 2007].

Ooki H., Arimoto R., Shionoya T., Matsuura K. and Iwasaki J., 1993, "Laser scanning mode interference contrast microscope and its application to step height measurement", *Application Physics,* vol. 32, no.11, pp. 4998-5001

Othonos A., 1997, "Fiber Bragg gratings", *Review of Scientific Instruments,* vol. 68, no. 12, pp. 4309-4341.

Pryputniewicz R. J., 1999, "Integrated approach to teaching of design, analysis, and characterization of micromechatronics," Paper No. IMECE2000/DE-13, *American Society Of Mechanical Engineers,* New York.

Przekwas A. J., Turowski M., Furmanczyk M., Heike A., and Pryputniewicz R. J., 2001, "Multiphysics design and simulation environment for microelectromechanical systems," *Processing International Symposium on MEMS: Mechanics and Measurements,"* Portland, OR, pp. 84-89.

Putty M. W., Najafi K., 1994, "A micromachined vibrating ring gyroscope", *Technique Digital Solid-State Sensor and Actuator Workshop,* Hilton Head Island, SC, June, pp. 213–220.

Sanders S. J., Strandjord L. K., Mead D., 2002, , "Fiber optic gyro technology trends-a Honeywell perspective", *Optical Fiber Sensors Conference Technology., OFS 2002,* vol. 1, pp. 5-8.

Santos J.L., Leite A.P., and Jackson D.A., 1992, "Optical fiber sensing with a low-finesse Fabry-Perot cavity," *Applied Optics,* Vol. 31, No. 34, pp.7361-7366, December.

Seshia A., 1999, "Design and Modeling of a Dual Mass SOI-MEMS Gyroscope", Berkeley.

Seidel H., Reidel R., Kolbeck R., Muck G., Kupke W., and Koniger M., 1990, "Capacitive silicon accelerometer with highly symmetric design," *Sensors Actuators,* vol. A21/A23, pp. 312-315.

Shearwood C., Williams C. B., Mellor P. H., Yates R. B., Gibbs M. R. J., and Mattingley, A. D., 1995, "Levitation of a micromachined rotor for application in a rotating gyroscope" *Electronics Letter,* vol. 31, no. 21, 1845-1846

Sirkis J. S., 1994, Editor, "Smart Sensing, Processing and Instrumentation", Proceedings of SPIE, Vol. 2191.

Sirkis J. et al., 1995, "In-line fiber etalon (ILFE) fiber optic strain sensors," *Journal of Lightwave Technology,* vol. 13, no. 7, pp. 1256-63.

Sniegowski J., 1996, "Multi-level polysilicon surface micromachining technology", Applications and issues, *ASME International Mechanical Engineering Congress and Exposition.*

Smith D. A., Bao Z., 1996, "Technology and applications of the integrated acousto-optic filter," *Electrotechnical Conference,* MELECON '96., 8th Mediterranean , vol. 1, 100-107, 13-16 May.

Smith R. B., 1989, "Selected Papers on Fiber Optic Gyroscopes", *SPIE Milestone Series,* Vol. MS 8.

Soderkvist J., 1994, "Micromachined gyroscopes", *Sensors and Actuators A,* vol. 43, pp. 65-71.

Sparks D., Slaughter D., Beni R., Jordan L., Chia M., Rich D., Johsnon J., Vas T., 1998, "Chip-scale packaging of a gyroscope using wafer bonding", *Sensors and Materials* vol. 11, no. 4, pp. 197-207.

Steward V., Grabbe D. G., Furlong C., and Pryputniewicz R. J., 2003, "Characterization of MEMS gyroscopes" *Processing 30th Annual Symposium and Exhibition of IMAPS-NE*, Boxboro, MA, pp. 222-229.

Stringer J., 2000, "The Air Force Institute of Technology (AFIT) Micro Electro-Mechanical Systems (MEMS) Interferometric Gyroscope (MiG)", *Thesis presented to the Faculty of the Graduate School of Engineering and Management*, March.

Suzuki K., Takiguchi K., Hotate K., 2000, "Monolithically Integrated Resonator Microoptic Gyro on Silica Planar Lightwave Circuit", *Journal of Lightwave Technology*, vol. **18**, pp. 66-72.

Tanaka K., Mochida Y., Sugimoto S., Moriya K., Hasegawa T., Atsuchi K., Ohwada K., 1995, "*A micromachined vibrating gyroscope*", *Proceedings IEEE Micro Electro Mechanical Systems 1995*, Amsterdam, Netherlands; 29 Jan.-2 Feb. 1995, pp.278-281.

Tang T. K., Gutierrez R. C., Wilcox J. Z., Stell C., Vorperian V., Calvet R., Li W. J., Charkaborty I., Bartman R., Kaiser W. J., 1996, "Silicon bulk micromachined vibratory gyroscope", *Tech. Dig. Solid-State Sensor and Actuator Workshop*, Hilton Head Island, SC, pp. 288–293.

Tang T. K., Gutierrez R. C., Wilcox J. Z., Stell C., Vorperian V., Calvet R., Li W. J., Charkaborty I., Bartman R., Kaiser W. J:, 1997, "A packaged silicon MEMS vibratory gyroscope for microspacecraft", *Proc. IEEE Micro Electro Mechanical Systems Workshop (MEMS'97)*, pp. 500-505.

Wagner J.F., 1990, "The Machine of Bohnenberger", *the Institute of Navigation*.

Ward B., 2002, "Prototype Fiber-Optic Acoustic Partial Discharge Sensor-Lessons Learned Documentation and Field Test," EPRI Internal Report 1001768.

White M. W. D. and Heppler G. R., 1995, "Vibration modes and frequencies of Timoshenko beams with attached rigid bodies", *ASME Journal of Applied Mechanics*, vol. 62, March, pp. 193-199.

Wilson J. and Hawkes J. F., 1989, "*Optoelectronics*", Prentice Hall, NY.

Wolthius R. A., Mitchell G. L., Saaski E., Hartl J. C., and Afromowitz M. A., 1991, "Development of medical pressure and temperature sensors employing optical spectrum modulation," *IEEE Transactions on Biomedical Engineering*, vol. 38, pp. 974–981.

Xu M. G., Geiger H., and Dakin J. P., 1995, "Interrogation of fibre-optic interferometric sensors using acousto-optic tunable filter," *Electronics Letter*, vol. 31, no. 17, pp. 1487-88.

Yazdi N,. Ayazi F., and Najafi K., 1998, Micromachined Inertial Sensors," *Proceedings of the IEEE* , vol. 86, no. 8, pp. 1640-1659.

Yu B., Kim D. W., Deng J., Xiao H., and Wang A., 2003, "Fiber Fabry-Perot Sensors for Partial Discharge Detection in Power Transformers", *Applied Optics*, Vol.42, No. 16, pp. 3241-50.

APPENDIX A: Relevant Optical Sensing Technology

Intrinsic Distributed Optical Sensing

An intrinsic distributed sensing system allows the environmental parameters to be measured at any point along the length of the fiber with a certain spatial resolution. It is also called a fully distributed sensing system. Usually, communication grade fiber, which has no discontinuous points, can be used to measure the field over kilometers with a resolution interval from centimeters to meters. Common measurands include distributed temperature and strain along the fiber.

Many fully distributed sensing systems use time domain techniques, in which the position of the measurement point is located by the time of flight of a back-scattered or forward-scattered light pulse. A well-known optical time domain reflectometry (OTDR) techniques often used to measure the back scattering of the light pulse, which is modulated by the environmental parameter along the fiber. In these systems, a short pulse of light is launched into the fiber and a small portion of light is back scattered and detected. The spatial resolution depends on the width of the light pulse. The measurand can be determined by measuring the intensity or wavelength of the reflected light pulse. An alternative approach is the optical frequency domain reflectometry (OFDR) technique. It is essentially derived from the frequency modulated continuous wave (FMCW) technique used in radar systems. In an OFDR system, a continuous wave (CW) light source is frequency-modulated and launched into a fiber. The frequency modulation can be done either by varying the optical carrier itself or its modulation envelope, and thus OFDR technique can be classified as coherent FMCW and incoherent FMCW. In coherent FMCW, the reflected light from different locations will have different optical frequencies and beat with the reflection from a reference point. The position information can be retrieved from the frequencies of the beating signal. The measurands can be determined by the magnitude of the beating signal. Incoherent OFDR technique actually measures the transfer function of the segment of the optical fiber. Its Fourier transform (FT) will give the time-domain response of the system under test.

Based on the types of the scattered light, fully distributed can be classified into three main sub-classes, namely Rayleigh scattering, Raman scattering and Brillouin scattering. Usually, backscattering are detected in most OTDR and OFDR based measurement systems. Forward-scattering can also be used as in stimulated Raman scattering and Brillouin scattering based systems. Some other optical effect, such as evanescent wave and Kerr effect etc. can also be used for distributed sensing.

Traditional OTDRs and OFDRs usually detect the Rayleigh back scattered light of the fiber. Variations of OTDR and OFDR for Raman scattering and Brillouin scattering, known as RODTR, ROFDR and BOTDR, BOFDR have been developed. In some Brillouin scattering based system, configurations named Brillouin optical time domain analysis (BOTDA) and Brillouin optical frequency domain analysis (BOFDA) were used to measure distributed temperatures and strains.

a. Rayleigh Scattering

Rayleigh backscattering has been widely used in an OTDR or OFDR based system for fault location, loss measurement and distributed sensing. Rayleigh scattering is an elastic scattering process in which the scattered light has the same wavelength as the incident light. In a distributed sensing system, the intensity or the state of polarization of the back-scattered light is modulated by environmental parameters such as temperature and strain. Hartog introduced a distributed temperature measurement system based on the temperature dependent absorption of a liquid-core fiber. Rogers suggested polarization optical time reflectometry (POTDR) technique for distributed measurement of magnetic field, electric field, temperature and pressure by detecting the polarization state change during the round trip propagation of a light pulse. Froggatt et al. introduced a distributed strain measurement system using a FMCW-based system.

Rayleigh backscattering systems usually measure the intensity of the backscattered light. However, the intensity of the light is also influenced by the fluctuation of light source, the optical connections between optical components, and the fiber bending in the optical path. Thus Rayleigh scattering based systems usually have limited accuracy and their practical applications in distributed sensing are limited.

b. Raman Scattering

Raman scattering is a non-linear process in an optical fiber. Raman scattering generates two side lobes centered at the spectrum of incident light, known as Stokes and anti-Stokes scattered light. These two Raman side lobes can be used to detect temperature profiles along a communication-grade optical fiber. The ratio of Stokes and anti-Stokes Raman scattered light can provide an absolute indication of temperature around the fiber which is not related to the incident light intensity, the power attenuation and the material composition of fiber. One can use optical filters to select the Raman scattered light and eliminate the Rayleigh scattering and Brilluoin scattering. Both OTDR and OFDR based Raman scattering

181

distributed temperature measurement systems have been reported. Commercial Raman scattering based distributed temperature sensors (York Sensors, DTS) are available.

Compared with the Rayleigh back scattering in a fiber, the intensity of the Raman back scattering is low and thus causes a low signal to noise ratio (SNR) in a Raman scattering based system especially when a narrow pulse width is used for higher spatial resolution. The low SNR limits the measurement accuracy of the distributed temperature sensing. Therefore, a large number of averages (up to hundreds of samples) or a long time integration (up to tens of minutes) is usually needed in a Raman distributed temperature sensing system.

c. Brillouin Scattering

Distributed temperature and strain sensing based on Brillouin scattering in an optical fiber is a relatively new technique and has attracted considerable research interests in the past few years. Brillouin scattering is a non-linear scattering process caused by the refractive index variation arising from acoustic waves. The wavelength shift in Brillouin scattered light, which is characteristic of the acoustic velocity in silica fiber, is a function of both temperature and strain around the fiber, and thus can be used for both temperature and strain sensing.

Compared with the wavelength shift of Raman scattered light, which can be tens of nanometers, frequency shift of Brillouin scattered light is very small (11GHz). One can use an optical filter to select the Brillouin scattered light out or can use a heterodyne scheme to detect the beating frequency between the Brillouin scattering and the incident light. Both spontaneous and stimulated Brillouin scatterings have been used for distributed temperature and strain sensing along a communication-grade fiber. One advantageof Brillouin scattering based system is that distributed temperature and strain profiles canbe monitored simultaneously.

Spontaneous Brillouin scattering based systems usually use the BOTDR technique in which a light pulse was injected to the fiber and back scatter Brillouin light pulse was measured. Some stimulated Brillouin scattering based systems use Brillouin optical time domain analysis (BOTDA) and Brillouin optical frequency domain analysis (BOFDA) techniques in which Brillouin interaction between a pumping optical pulse and a counter-propagating continuous wave is used to generate stimulated Brillouin scattering. Commercial Brillouin scattering based distributed temperature and strain sensing systems (NeubrexNBX-6000) are available.

Topology

Topology means the method how multiple sensors in a sensor network are arranged. Various topologies including serial, star, ladder, tree, matrix and their combinations have been reported. One can detect either the light transmitted by or reflected from the sensors. Correspondingly, sensor networks can work at either transmissive mode or reflective mode.

- **Serial Topology**

In a serial topology, multiple sensors are arranged in series as electrical components in a serial circuit. The biggest advantage of a serial topology is that one can arrange multiple in-line fiber sensors, such as Fabry-Perot sensors and FBG sensors, along a single fiber and thus simplify the deployment of quasi-distributed sensing. Figure 1 shows a typical sensor array with a serial topology. The sensors to be multiplexed are required to have low reflectivity and low power loss for dense multiplexing. The drawbacks of a serial topology include: the interference and crosstalk between sensors that may limit the performance of the sensor system and the reliability problem that one malfunctioned sensor may corrupt the signal of the whole sensor array. Various types of fiber sensors, including microbend, Mach-Zehnder, Fabry-Perot, FBG etc, have been multiplexed in serial topologies.
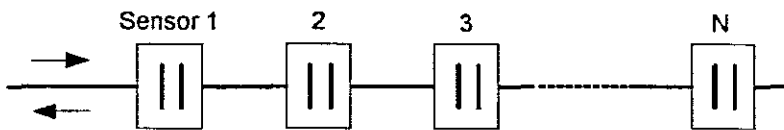
Figure 1 A sensor arrays with a serial topology.

- **Star Topology**

In a star topology, multiple sensors are independently connected to a single central point. A typical sensor network with a star topology is given in Figure 2. A 1 × N optical switch or optical splitter is used as the central unit. The biggest advantage of a star system is the independence between sensors that may lower the crosstalk and increase the reliability. However, the deployment for a large number of sensors may be difficult because of the splitting of optical power and embedding of multiple fibers into the structures.
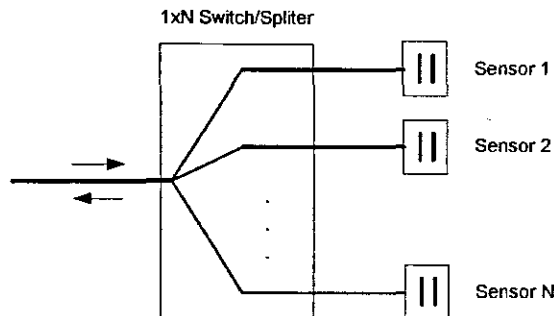
Figure 2 A sensor arrays with a star topology.

- **Ladder Topology**

In a ladder topology, multiple sensors are arranged in parallel. Figure 3 shows a typical sensor network with a ladder topology. Multiple light beam splitters and combiner are use to guide light to different sensors. Although the ladder topology also has the advantage of independence between sensors, the usage of multiple splitters and combiners increase the system complexity.
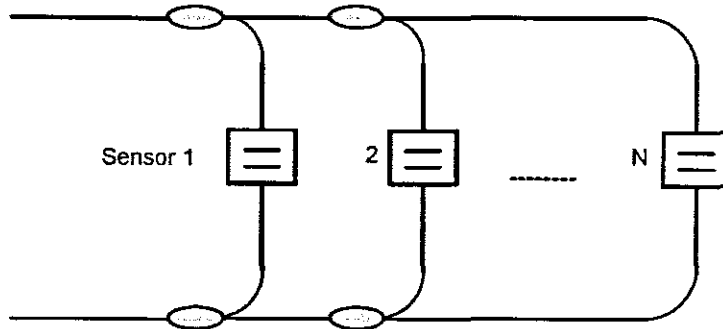
Figure 3 A sensor networks with a ladder topology

- **Hybrid Topology**

One may use a hybrid topology that contains different fundamental topologies. Figure 4 shows a sensor network with a mixed star/serial topology. The basic structure is a star topology. In each branch of the star network, multiple sensors are arranged in a serial topology. One can use this kind of hybrid topology to multiplex a large number of sensors and to balance the sensor performance and the reliability in properly designed networks.
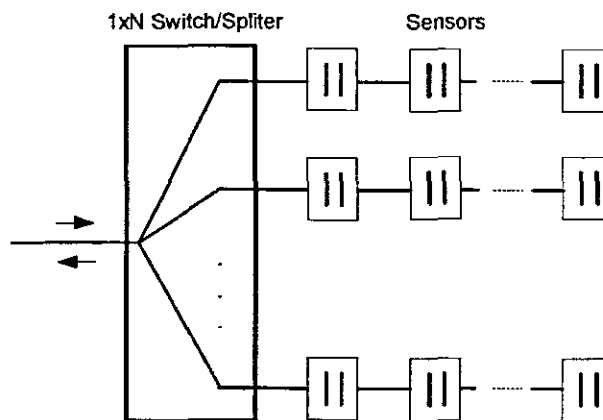
Figure 4 A hybrid star/serial topologies.

The topologies of sensor network are not dependent on the multiplexing schemes of signals from the sensors. For example, a sensor array in a serial topology can be multiplexed in TDM, FDM, CM schemes, and so can a sensor array in a star topology. In following subsections, different multiplexing schemes for fiber sensors will be discussed.

Many of the intrinsic and extrinsic sensors may be multiplexed offering the possibility of large numbers of sensors being supported by a single fiber optic line. The techniques that are most commonly employed are time, frequency, wavelength, coherence, polarization and spatial multiplexing.

Time Division Multiplexing (TDM)

In a Time division multiplexing (TDM) scheme, the sensors are sequentially addressed by injecting a pulsed input signal into the sensor network. The light transmitted by or reflected from different sensors will have different delays of time flight and allow individual sensor to be distinguished.

TDM scheme has been used in sensor networks with different topologies, such as serial topology, ladder topology, star topology etc. The requirement of sensor arrangement in a TDM system is that the signals from the different sensors have different delays. The most straightforward configuration for a TDM scheme is an OTDR based serial array working at reflective mode, as shown in figure 5. An OTDR contains a laser diode, a light modulator to generate a light pulse, a photodetector as well as a delayed gater to detect the time delay of the reflected light from sensors. The intensity, frequency or the phase shift of the reflected light pulses are detected to determine the measurands of interests.
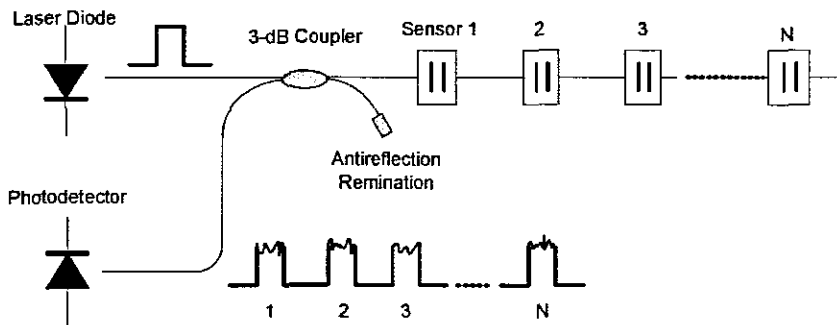
Figure 5 An OTDR based TDM sensor array.

TDM scheme has been used for the multiplexing of different sensors, such as microbend, interferometric and FBG sensors, working at either transmissive mode or reflective mode. TDM scheme has been used for the multiplexing of different sensors, such as microbend, interferometric and FBG sensors, working at either transmissive mode or reflective mode.

Time division multiplexing employs a pulsed light source launching light into an optical fiber and analyzing the time delay to discriminate between sensors. This technique is commonly employed to support distributed sensors where measurements of strain, temperature or other

parameters are collected. Figure 6 illustrates a time division multiplexed system that uses micro bend sensitive areas on pipe joints.
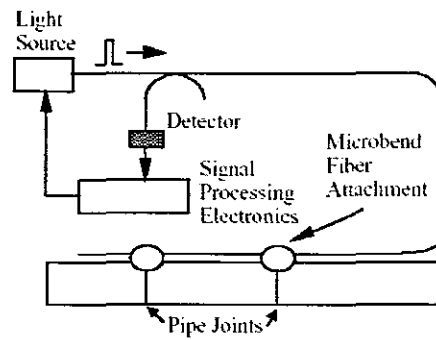
Figure 6 Time division multiplexing methods can be used in combination with microbend sensitive optical fiber to locate the position of stress along a pipeline.

As the pipe joints are stressed microbending loss increases and the time delay associated with these losses allows the location of faulty joints.

The entire length of the fiber can be made microbend sensitive and Rayleigh scattering loss used to support a distributed sensor that will predominantly measure strain. Other types of scattering from optical pulses propagating down optical fiber have been used to support distributed sensing, notably Raman scattering for temperature sensors has been made into a commercial product by York Technology and Hitachi. These units can resolve temperature changes of about 1 degreeC with spatial resolution of 1 meter for a 1km sensor using an integration time of about 5 minutes. Brillioun scattering has been used in laboratory experiments to support both strain and temperature measurements.

Frequency Division Multiplexing (FDM)

In a FDM scheme, signals from different sensors will have different frequencies. If the frequencies are optical frequencies, the multiplexing scheme is usually regarded as wavelength division multiplexed. Thus the frequency components in a FDM scheme are usually electrical signals with different frequencies.

FDM scheme usually use some modulation technique to modulate the light source periodically. Sinusoidal, sawtooth and triangle modulation are most common modulation schemes. Signals from different sensors have different frequencies due to the modulation of the light source. The different frequencies may stand for different physical meanings, which can be the carrier frequencies, positions of sensors, or optical path unbalance of sensors.

Dandrige et al. presented a FDM scheme based on phase carrier technique. The sensor network had a $J \times K$ matrix topology. Multiple laser light sources were frequency-modulated with different sinusoidal carrier frequencies. The measured signal from sensors contained multiple frequency components corresponding to different modulation carrier frequencies. The most attractive FDM scheme is the frequency modulated continuous wave (FMCW) based technique, which was originally developed for radar ranging, and then applied to laser ranging and measurement of optical sensors.

When FMCWtechnique is used in an optical fiber network, it is often called optical frequency domain reflectometry (OFDR). An OFDR is essentially a FMCW technique working at reflective mode. Both coherent OFDR and incoherent OFDR have been developed based on different modulation method of the light source and have been reported for multiplexing of intensity-modulated, interferometric, and FBG sensors.

A coherent FMCW usually modulate the optical frequency directly in a wavelength range from picometers to tens of nanometers. The light beams propagating through different optical paths will have different optical frequencies and will beat with each other when combined. The beating frequency is equal to the difference of optical frequencies of the two light beams and can be used to determine the optical path difference between the two light beams.

An incoherent FMCWmodulates the intensity of the light source instead of the optical carrier frequency, usually in a microwave frequency range of MHz-GHz. The intensity modulation is usually accomplished by modulating the driving current of a laser diode or the driving signal of an external optical modulator. The beating signal in an incoherent FMCW system comes from microwave frequencies instead of the optical frequencies in a coherent FMCW.

A typical FDM scheme of FMCW reflectometry based fiber sensor system is shown in figure 7. A coherent light source is linearly frequency modulated. A reference reflection point is used. The reflections from sensors will beat with the reflection of reference point. The reflections from different sensors will generate electrical signals with different frequencies. A spectrum analyzer is used to analyze the frequency components of the beat signals. The positions of the sensors can be determined by measuring the frequencies of electrical signals. The environmental parameters of interests can be determined by detecting the intensity of the light reflected from the sensors, which is related to the amplitude of the beating frequencies. Froggatt et al. presented a similar configuration for interrogation of FBG sensors for strain sensing. The reflection spectrum of each FBG sensor, instead of its intensity, was demodulated by inverse Fourier transforming the measured RF spectrum of

each sensor and concatenating the recovered sequences in continuous sweeps. The strain information was determined according to the reflection spectrum shift of FBG sensors.
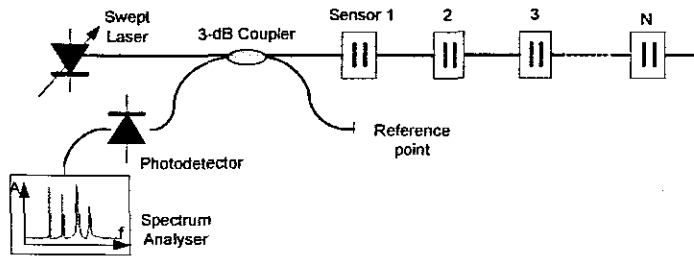
Figure 7 A FMCW based FDM sensor array

If the beating signal in a FMCW configuration comes from the two different light beams of an interferometer, then the beating frequency is characteristic to the OPD between the two light beams. Sensors with different OPDs will have different beating frequencies and can be multiplexed in a subcarrier frequency domain. Sakai et al presented a FMCW based FDM sensor system for Mach-Zehnder interferometric sensors in a transmissive mode in which the frequency-modulated light propagated through a series of unbalanced Mach-Zehnder interferometers and generated multiple frequency beating notes. Collins *et. al.* presented a FMCW based FDM scheme for Michelson interferometers in a star topologies.

A frequency division multiplexed system is shown in figure 8. In this example a laser diode is frequency chirped by driving it with a sawtooth current drive. Successive Mach-Zehnder interferometers are offset with incremental lengths (L-L1), (L-L2), and (L-L3) which differ sufficiently that the resultant carrier frequency of each sensor (dF/dt)(L-Ln) is easily separable from the other sensors via electronic filtering of the output of the detector.
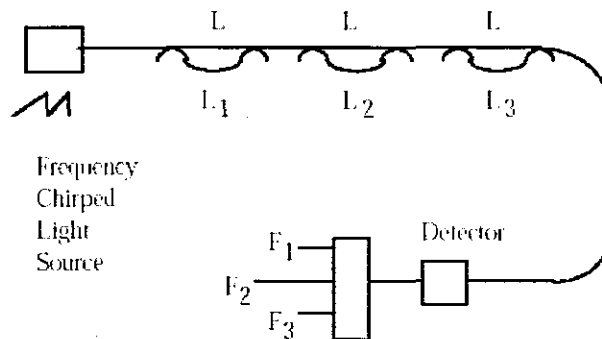
Figure 8 Frequency division multiplexing can be used to tag a series of fiber sensors, as in this case the Mach-Zehnder interferometers are shown with a carrier frequency on which the output signal ride.Wavelength Division Multiplexing (WDM)

Wavelength division multiplexing has been proven to be a powerful technique to increase the capacity of optical communication systems and has been widely deployed in long haul optical communication links and local optical networks.
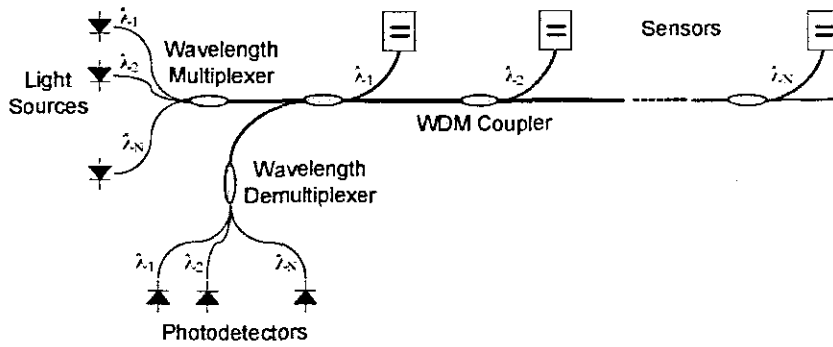
Figure 9 A wavelength division multiplexed sensor array

The application of the WDM technique is straightforward in a sensor network, in which different sensors can be designed to work in different wavelengths. An arrangement of a sensor array using the WDM scheme is shown in Figure 9. The light from a particular source can be directed to a particular sensor and then received by a particular photodetector. Although sharing a common fiber link, the sensor elements are independent on each other in wavelength domain by using WDM splitters, couplers and combiners. The evolution of the dense wavelength division multiplexing (DWDM) technique has made such optical components available in reasonable costs.

Another important WDM sensor interrogation scheme has been developed for FBG sensors, as shown in Figure 10. FBG sensors can be designed to reflect light at different wavelengths. When the sensor array is illuminated by a broadband light source, different FBG sensors will reflect different portions of lights with different wavelengths. An optical spectrometer can be used to monitor the central wavelength of each FBG sensor, and thus to determine the temperature and the strain. A tunable laser can also be used as the light source, while a photodetector is used as the detector instead of an optical spectrometer.
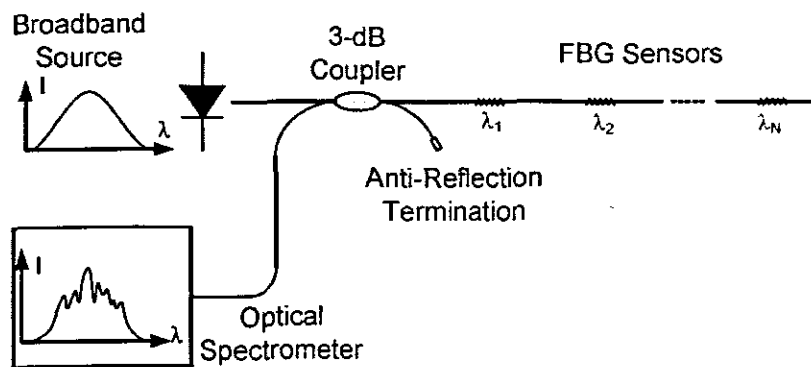
Figure 10 A WDM scheme for FBG sensors

Sensors in a WDM scheme need to be designed to work at different wavelengths, which may increase the complexity of sensor design and fabrication. Due to the limited availability of light bandwidth, the multiplexing capacity of a WDM scheme is usually limited to a small number. For example, when FBG sensors are interrogated in a WDM scheme, each FBG needs to occupy a certain bandwidth that may be as large as several nanometers. The total available bandwidth of the light source is usually tens of nanometers. Thus the multiplexing number is limited by the ratio of the source spectral width over the spacing between two neighboring Bragg wavelengths.

Wavelength division multiplexing is one of the best methods of multiplexing as it uses optical power very efficiently. It also has the advantage of being easily integrated into other multiplexing systems allowing the possibility of large numbers of sensors being supported in a single fiber line. Figure 11 illustrates a system where a broadband light source, such as a light emitting diode, is coupled into a series of fiber sensors that reflect signals over wavelength bands that are subsets of the light source spectrum. A dispersive element, such as a grating or prism, is used to separate out the signals from the sensors onto separate detectors.
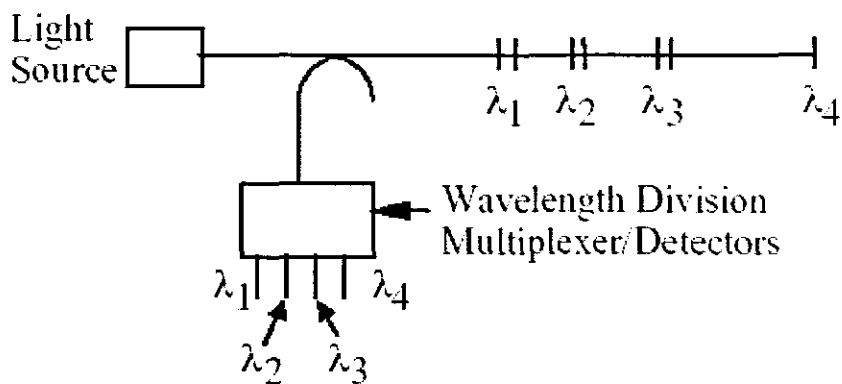
Figure 11 Wavelength division multiplexing are often very energy efficient. A series of fiber sensors are multiplexed by being arranged to reflect in a particular spectral band that is split via a dispersive element onto separate detectors.Coherence Multiplexing

Coherence multiplexing is another important interrogation scheme for interferometric sensor arrays by using the coherence properties of the light from an optical source with a short coherence length.

The core of the coherence-multiplexing scheme is the path-matched differential interferometric (PMDI) technique, which was first proposed by Al-Chalabi et al. In a PMDI detection scheme, a broadband light emitting diode (LED) or a superluminescent light emitting diode (SLED), whose coherence length, L_c, is usually in order of micrometers to sub-millimeters, can be used as the light source, a receiving interferometer with an optical path

imbalance of L_r is used to compensate the optical path imbalance, L_s, of a sensing interferometer. Both L_r and Ls are much larger than L_c. Thus either of the two interferometers alone will not give a significant interference fringe contrast. However, when L_r is arranged to be close to L_s, such that $|L_r-L_s|<<L_c$, the tandem combination of the two interferometers will form a PMDI device and give a significant interference fringe contrast.

In coherence multiplexed optical fiber sensor system, the path imbalance of each sensing interferometer is designed to be different from each other. One can use multiple receiving interferometers to path-match sensing interferometers simultaneously, as shown in Figure 12. One also can use a common receiving interferometer with tunable path imbalance to path-match sensing interferometers in series, as shown in Figure 13.

Coherence multiplexing is an elegant method for remotely interrogating a small numbers of interferometers including Mach-Zehnder, Michelson and Fabry-Perot sensors. However, as the number of multiplexed sensors increases, for the receiving interferometer, the light from unmatched sensing interferometers will give large intensity noise, thus signal to noise ratio for each sensor drops rapidly. Therefore, the multiplexing capacity of a coherence multiplexing system is usually limited to a small number.
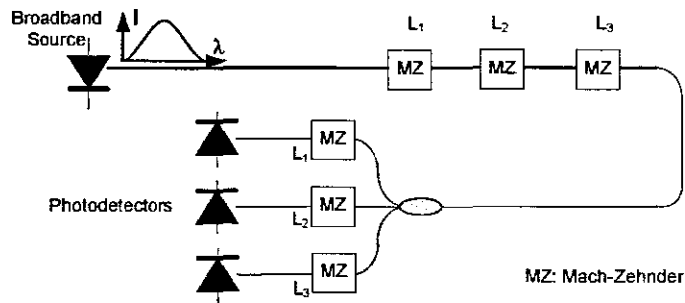
Figure 12 A CM scheme with multiple receiving interferometers
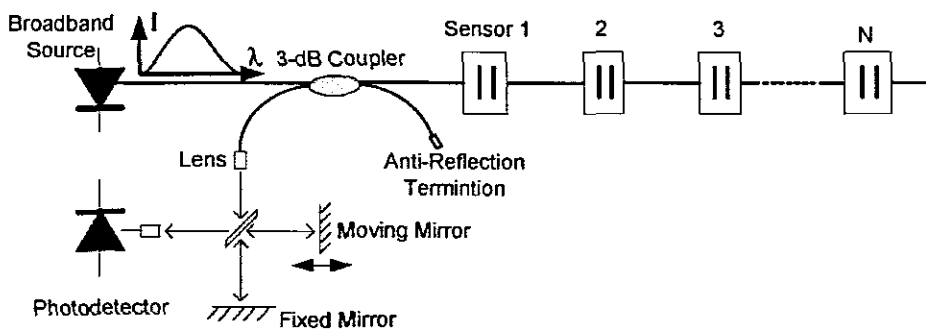
Figure 13 A CM scheme with a common receiving interferometer.

Light sources can have widely varying coherence lengths depending on their spectrum. By using light sources that have coherence lengths that are short compared to offsets between the reference and signal legs in Mach-Zehnder interferometers and between successive sensors, a coherence multiplexed system similar to figure 14 may be set up. The signal is

extracted by putting a rebalancing interferometer in front of each detector so that the sensor signals may be processed. Coherence multiplexing is not as commonly used as time, frequency and wavelength division multiplexing because of optical power budgets and the additional complexities in setting up the optics properly. It is still a potentially powerful technique and may become more widely used as optical component performance and availability continue to improve, especially in the area of integrated optic chips where control of optical path length differences is relatively straightforward.
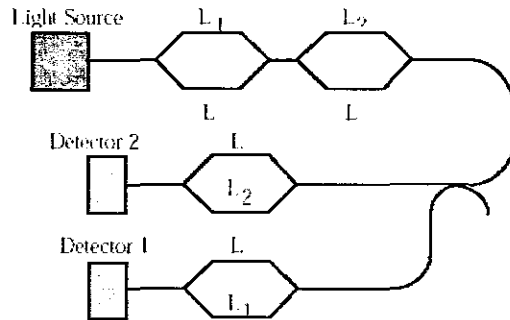
Figure 14 A low coherence light source is used to multiplex two Mach-Zehnder interferometers by using offset lengths and counterbalancing interferometers.

One of the least commonly used techniques is polarization multiplexing. In this case the idea is to launch light with particular polarization states and extract each state. A possible application is shown in figure 15 where light is launched with two orthogonal polarization modes; preserving fiber and evanescent sensors have been set up along each of the axes. A polarizing beam splitter is used to separate out the two signals. There is a recent interest in using polarization preserving fiber in combination with time domain techniques to form polarization based distributed fiber sensors. This has potential to offer multiple sensing parameters along a single fiber line.
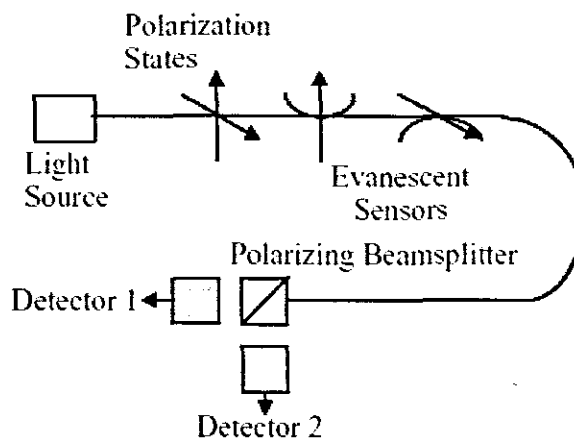
Figure 15 Polarization multiplexing is used to support two fiber sensors that access the cross polarization states of polarization preserving optical fiber.

Finally, it is possible to use spatial techniques to generate large sensor arrays using relatively few input and output optical fibers. Figure 16 shows a 2 by 2 arrays of sensors where two light sources are amplitude modulated at different frequencies. Two sensors are driven at one frequency and two more at the second. The signals from the sensors are put onto two output fibers each carrying a sensor signal from two sensors at different frequencies.
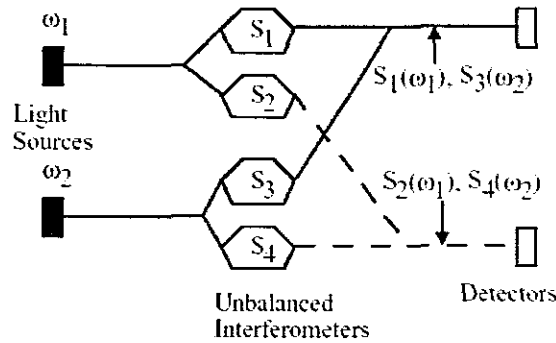
Figure 16 Spatial multiplexing of four fiber optic sensors may be accomplished by operating two light sources with different carrier frequencies and cross coupling the sensor outputs onto two output fibers.

This sort of multiplexing is easily extended to 'm' input fibers and 'n' output fibers to form 'm' by 'n' arrays of sensors as in figure 17.
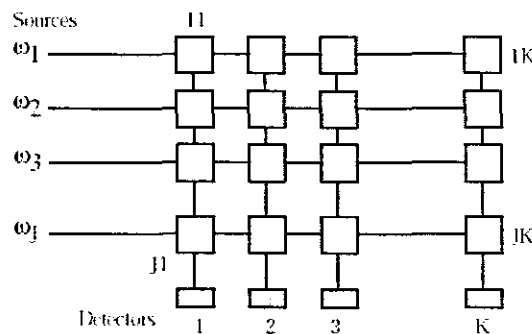
Figure 17 Extensions of spatial multiplexing the JK sensors can be accomplished by operating J light sources at J different frequencies and cross coupling to K output fibers.

All of these multiplexing techniques can be used in combination with one another to form extremely large arrays.

Other Multiplexing Schemes

There have been some other multiplexing schemes reported for optical fiber sensors, some of which include code-division-multiplexing (CDM) and spatial-division-multiplexing (SDM) schemes.

In a CDM scheme, the optical source is modulated using a pseudo-random bit sequence (PBRS) to generate a spread-spectrum signal. The locations of sensors are designed to be at delays that are multiple of the bit period. The received signals from the sensor array are then encoded by delayed versions of the PBRS optical pulses. Synchronous correlation detection technique is used to extract individual signals from different sensors. CDM schemes for interferometric sensors have been reported. CDM can be considered as a variant of conventional TDM. However, because a sequence of light pulses is used, stronger optical signals are produced at the output, thus the CDM method can provide better power budget than the TDM method.

In a SDM scheme, the light from a common source is split and directed to different locations for sensor interrogation. The sensors in a SDM scheme are addressed via different fiber links. The most advantageous features of the SDM method include a balanced power budget for each fiber link and totally free of crosstalk between sensors.

Hybrid Multiplexing

Each of the multiplexing schemes discussed above has its advantages and disadvantages. For example, TDM scheme has a large multiplexing capacity but heavy crosstalk between sensors in a serial topology. WDM has low crosstalk between sensors but a poor multiplexing capacity. Thus one can use a combination to take advantages of both of them. TDM/WDM hybrid multiplexing has been applied to interferometric sensors and FBG sensors. Some other hybrid multiplexing schemes have also been developed. Dandridge *et al.* introduced a J ×K scheme for the multiplexing of interferometric sensors. It is actually a combination of the SDM and the FDM scheme. Farahi *et al.* demonstrated a combination of the TDM and the FDM. Usually, the main purpose of a hybrid multiplexing scheme is to increase the number of sensors that can be multiplexed.

Appendix B: Code for Fiber Optical Read-out System Simulation

Matlab Programs for the Calculation Sensitivity, Fringe Contrast and Dynamic Range and Output Intensity
1) Un-guided F-P: Intensity & Sensitivity

```
n=1.0; % Rrefractive index inside the FPI cavity
nc=1.45; %Cladding index of the SMF
w0=1300; % Central wavelength
W0=5000; % Mode field radius of a SMF-28
alpha0=1.0; % Coupling efficiency
BW=200; % Total source spectral width
FWHM=35; % 3-dB bandwith of the source
dBW=FWHM/sqrt(8*log(2));
R1=0.3;
dR=0;
R2=R1*(1+dR); % Calculation of R2
Angle=0; % Mirror angular misalignment in degree
An=Angle*pi/180; % Mirror angular misalignment in rad
M=20; % Maximal cavity length over wavelength (l/w0)
m=M*13000+1; % Data points in cavity length
k=BW*10+1; % Data points in wavelength
S=zeros(m,2); % Sensitivity array
I=zeros(m,2); % Intensity array
for i=1:m % Cavityl length
l=w0*(i-1)/((m-1)/M);
x=0;
y=0;
for j=1:k % Wavelength integration
dw=1/((k-1)/BW);
w=w0-BW/2+(j-1)*dw;
f=(1/(sqrt(2*pi)*dBW))*exp(-(w-w0)^2/(2*dBW^2)); % Source spectrum -
Gaussian type
% Calculate Coupling Efficiency.
Z=2*l*w/(2*pi*nc*W0^2);
alpha=-
10*log10((1+4*Z^2)/((1+2*Z^2)^2+Z^2))+4.34*(l*tan(2*An)/W0)^2+4.34*(
pi*nc*W0*(2*An)
/w)^2;
C=10^(-alpha/10);
%Sensitivity calculation
x1=sqrt(C*R1*R2)*(1-R1)*(1-C*R2)*sin(4*pi*n*l/w);
x2=w*(1+C*R1*R2-2*sqrt(C*R1*R2)*cos(4*pi*n*l/w))^2;
x=x+8*pi*n*alpha0*f*(x1/x2)*dw;
%Intensity calculation
y1=R1+C*R2-2*sqrt(C*R1*R2)*cos(4*pi*n*l/w);
y2=1+C*R1*R2-2*sqrt(C*R1*R2)*cos(4*pi*n*l/w);
y=y+alpha0*f*(y1/y2)*dw;
end
S(i,1)=n*l/w0;
S(i,2)=x*1000; % Sensitivity. The factor 1000 is to convert the 1/nm
to 1/um
I(i,1)=n*l/w0;
I(i,2)=y; % Intensity of the FPI output
end
[AX,H1,H2]=plotyy(I(:,1),I(:,2),S(:,1),S(:,2),'plot');
xlabel('F-P Cavity Length (n*l/w0)')
```

```
set(get(AX(1),'Ylabel'),'String','Normalized FPI Intensity (I/I0)')
set(get(AX(2),'Ylabel'),'String','FPI Sensitivity (1/um)')
title('UnGuided Model')
```

2) Guided F-P: Fringe Contrast

```
w0=1300; %Central wavelength (nm)
BW=200; %Integration limit (nm)
FWHM=60; % Spectrum (Gaussian distribution)
delta=FWHM/sqrt(8*log(2)); %Spectrum width (1/e)
R1=0.4; %Reflectance of the fiber endface
R2=0.4; % Reflectance of the second mirror
n0=1.0; % Medium RI in the cavity
c=1.0; % Round trip coupling effeciency
airgap=zeros(0,31);
peak=zeros(0,31);
valley=zeros(0,31);
y=0;
for i=1:1:31
airgap(i)=(2*i-1)*w0/4;
for j=1:1:(10*BW+1)
d=1/10;
x=w0-BW/2+(j-1)*d;
f=(1/(sqrt(2*pi)*delta))*exp(-(x-w0)^2/(2*delta^2));
y1=R1+c*R2-2*sqrt(c*R1*R2)*cos(4*pi*n0*airgap(i)/x);
y2=1+c*R1*R2-2*sqrt(c*R1*R2)*cos(4*pi*n0*airgap(i)/x);
y=y+f*(y1/y2)*d;
end
peak(i)=y;
y=0;
end
y=0;
for i=1:1:31
airgap(i)=(2*i-2)*w0/4;
for j=1:1:(10*BW+1)
d=1/10;
x=w0-BW/2+(j-1)*d;
f=(1/(sqrt(2*pi)*delta))*exp(-(x-w0)^2/(2*delta^2));
y1=R1+c*R2-2*sqrt(c*R1*R2)*cos(4*pi*n0*airgap(i)/x);
y2=1+c*R1*R2-2*sqrt(c*R1*R2)*cos(4*pi*n0*airgap(i)/x);
y=y+f*(y1/y2)*d;
end
valley(i)=y;
y=0;
end
contrast=(peak-valley)./(peak+valley);
%plot(airgap/1000,peak,'-r',airgap/1000,valley,'--
b',airgap/1000,contrast,'-k')
plot(airgap/1000,contrast,'--k')
xlabel('F-P cavity length (micrometer)')
ylabel('Fringe contrast')
hold on
```

3) Guided F-P: Dynamic Range

```
n=1.45; % Rrefractive index inside the FPI cavity
nc=n*(1-0.005); %Cladding index of the SMF
w0=1300; % Central wavelength
```

```
W0=5000; % Mode field radius of a SMF-28
alpha0=1.0; % Coupling efficiency
BW=200; % Total source spectral width
FWHM=35; % 3-dB bandwith of the source
dBW=FWHM/sqrt(8*log(2));
Angle=6; % Mirror angular misalignment in degree
An=Angle*pi/180; % Mirror angular misalignment in rad
R1=0.3;
R2=0.3;
K=BW*100+1; % Data points in wavelength
M=2000; % Calculation points nearby the (Lmax,Smax) points in nm
N=58; % Peak points
DL=zeros(N,2);
DeltaL=zeros(N,1); % Initialize the Dynamic Range matrix
for i=1:N
L0=Lmax(i)*w0/n; % Lmax in nm
S0=Smax(i);
for j=1:M % Sensitivity calculation
l=L0+j/10;
x=0;
for m=1:K
dw=1/((K-1)/BW);
w=w0-BW/2+(m-1)*dw;
f=(1/(sqrt(2*pi)*dBW))*exp(-(w-w0)^2/(2*dBW^2)); % Source spectrum -
Gaussian
type
alpha=4.34*(pi*nc*W0*(2*An)/w)^2;
C=10^(-alpha/10); % Round trip coupling efficiency
%Sensitivity calculation
x1=sqrt(C*R1*R2)*(1-R1)*(1-C*R2)*sin(4*pi*n*l/w);
x2=w*(1+C*R1*R2-2*sqrt(C*R1*R2)*cos(4*pi*n*l/w))^2;
x=x+8*pi*n*alpha0*f*(x1/x2)*dw;
end
S=x*1000; % Sensitivity. The factor 1000 is to convert the 1/nm to
1/um
Error=abs((S-S0)/S0);
if Error > 0.5
DeltaL(i,1)=2*j/10; % Dynamic range in nm
break
end
end
end
DL(:,1)=Lmax;
DL(:,2)=DeltaL;
plot(Lmax,DeltaL(:,1))
```

4) Simulation of Output Intensity of Fiber Optical Interferometer

```
function varargout = fpisimulator(varargin)
% FPISIMULATOR M-file for fpisimulator.fig
%    FPISIMULATOR simulates Gaussian beam propagation through a
Fabry-Perot
%    interferometer with adjustable error angles.
%
%    The parameters are:
%    Screen Distance:    distance from 2nd mirror (infinitely thin)
to
%                        observation screen in mm
```

```
%    Mirror Spacing:      spacing between mirrors given by multiples
of
%                         wavelength
%    z:                   distance from position of minimal waist
radius
%                         (w0) to 1st mirror in mm
%    Reflectivity:        reflectivity of mirrors (between 0 and 1)
%    Refractive Index:    refractive index of medium in front of,
between
%                         and behind the mirrors
%
%    w0:                  minimal beam waist radius in mm
%    Wavelength:          wavelength of radiation in nm
%
%    Theta:               angle between incoming radiation and whole
%                         cavity (in x-direction) in angular seconds
%    Phi:                 x-angle deviation of 2nd mirror in angular
seconds
%    Rho:                 y-angle deviation of 2nd mirror in angular
seconds
%
%    Calculation-Window Width:   width of observation screen
%    Number of Pixels:           larger number means better
resolution but
%                                longer waiting times
%    Number of Rays:             number of simulated beam paths

% Version: 1.3
% Copyright: Birk Andreas 20060629


% Begin initialization code - DO NOT EDIT
gui_Singleton = 1;
gui_State = struct('gui_Name',       mfilename, ...
                   'gui_Singleton',  gui_Singleton, ...
                   'gui_OpeningFcn', @fpisimulator_OpeningFcn, ...
                   'gui_OutputFcn',  @fpisimulator_OutputFcn, ...
                   'gui_LayoutFcn',  [] , ...
                   'gui_Callback',   []);
if nargin && ischar(varargin{1})
    gui_State.gui_Callback = str2func(varargin{1});
end

if nargout
    [varargout{1:nargout}] = gui_mainfcn(gui_State, varargin{:});
else
    gui_mainfcn(gui_State, varargin{:});
end
% End initialization code - DO NOT EDIT

function fpisimulator_OpeningFcn(hObject, eventdata, handles,
varargin)
handles.output = hObject;
guidata(hObject, handles);
initialize_gui(hObject, handles);

function varargout = fpisimulator_OutputFcn(hObject, eventdata,
handles)
varargout{1} = handles.output;
```

```matlab
function abstand_CreateFcn(hObject, eventdata, handles)
if ispc && isequal(get(hObject,'BackgroundColor'),
get(0,'defaultUicontrolBackgroundColor'))
    set(hObject,'BackgroundColor','white');
end


function abstand_Callback(hObject, eventdata, handles)
handles.abstand=str2double(get(hObject,'String'));
if handles.abstand < 0
    handles.abstand=-handles.abstand;
end
guidata(hObject, handles);


function d_Callback(hObject, eventdata, handles)
handles.d=str2double(get(hObject,'String'));
if handles.d < 0
    handles.d=-handles.d;
end
guidata(hObject, handles);


function d_CreateFcn(hObject, eventdata, handles)
if ispc && isequal(get(hObject,'BackgroundColor'),
get(0,'defaultUicontrolBackgroundColor'))
    set(hObject,'BackgroundColor','white');
end


function z_Callback(hObject, eventdata, handles)
handles.z=str2double(get(hObject,'String'));
if handles.z < 0
    handles.z=-handles.z;
end
guidata(hObject, handles);


function z_CreateFcn(hObject, eventdata, handles)
if ispc && isequal(get(hObject,'BackgroundColor'),
get(0,'defaultUicontrolBackgroundColor'))
    set(hObject,'BackgroundColor','white');
end


function r_Callback(hObject, eventdata, handles)
handles.r=str2double(get(hObject,'String'));
if handles.r < 0
    handles.r=-handles.r;
end
guidata(hObject, handles);


function r_CreateFcn(hObject, eventdata, handles)
if ispc && isequal(get(hObject,'BackgroundColor'),
get(0,'defaultUicontrolBackgroundColor'))
    set(hObject,'BackgroundColor','white');
end


function theta_Callback(hObject, eventdata, handles)
handles.theta=str2double(get(hObject,'String'));
guidata(hObject, handles);


function theta_CreateFcn(hObject, eventdata, handles)
```

```matlab
if ispc && isequal(get(hObject,'BackgroundColor'),
get(0,'defaultUicontrolBackgroundColor'))
    set(hObject,'BackgroundColor','white');
end

function phi_Callback(hObject, eventdata, handles)
handles.phi=str2double(get(hObject,'String'));
guidata(hObject, handles);

function phi_CreateFcn(hObject, eventdata, handles)
if ispc && isequal(get(hObject,'BackgroundColor'),
get(0,'defaultUicontrolBackgroundColor'))
    set(hObject,'BackgroundColor','white');
end

function rho_Callback(hObject, eventdata, handles)
handles.rho=str2double(get(hObject,'String'));
guidata(hObject, handles);

function rho_CreateFcn(hObject, eventdata, handles)
if ispc && isequal(get(hObject,'BackgroundColor'),
get(0,'defaultUicontrolBackgroundColor'))
    set(hObject,'BackgroundColor','white');
end

function breite_Callback(hObject, eventdata, handles)
handles.breite=str2double(get(hObject,'String'));
if handles.breite < 0
    handles.breite=-handles.breite;
end
guidata(hObject, handles);

function breite_CreateFcn(hObject, eventdata, handles)
if ispc && isequal(get(hObject,'BackgroundColor'),
get(0,'defaultUicontrolBackgroundColor'))
    set(hObject,'BackgroundColor','white');
end

function pixel_Callback(hObject, eventdata, handles)
handles.pixel=str2double(get(hObject,'String'));
if handles.pixel < 0
    handles.pixel=-handles.pixel;
end
guidata(hObject, handles);

function pixel_CreateFcn(hObject, eventdata, handles)
if ispc && isequal(get(hObject,'BackgroundColor'),
get(0,'defaultUicontrolBackgroundColor'))
    set(hObject,'BackgroundColor','white');
end

function mult_Callback(hObject, eventdata, handles)
handles.mult=str2double(get(hObject,'String'));
if handles.mult < 0
    handles.mult=-handles.mult;
end
guidata(hObject, handles);
```

```
function mult_CreateFcn(hObject, eventdata, handles)
if ispc && isequal(get(hObject,'BackgroundColor'),
get(0,'defaultUicontrolBackgroundColor'))
    set(hObject,'BackgroundColor','white');
end


function w0_Callback(hObject, eventdata, handles)
handles.w0=str2double(get(hObject,'String'));
if handles.w0 < 0
    handles.w0=-handles.w0;
end
guidata(hObject, handles);


function w0_CreateFcn(hObject, eventdata, handles)
if ispc && isequal(get(hObject,'BackgroundColor'),
get(0,'defaultUicontrolBackgroundColor'))
    set(hObject,'BackgroundColor','white');
end


function lambda_Callback(hObject, eventdata, handles)
handles.lambda=str2double(get(hObject,'String'));
if handles.lambda < 0
    handles.lambda=-handles.lambda;
end
guidata(hObject, handles);


function lambda_CreateFcn(hObject, eventdata, handles)
if ispc && isequal(get(hObject,'BackgroundColor'),
get(0,'defaultUicontrolBackgroundColor'))
    set(hObject,'BackgroundColor','white');
end


function n_Callback(hObject, eventdata, handles)
handles.n=str2double(get(hObject,'String'));
guidata(hObject, handles);


function n_CreateFcn(hObject, eventdata, handles)
if ispc && isequal(get(hObject,'BackgroundColor'),
get(0,'defaultUicontrolBackgroundColor'))
    set(hObject,'BackgroundColor','white');
end


function calculate_Callback(hObject, eventdata, handles)
breite=1e-3*handles.breite;
pixel=round(handles.pixel);
abstand=1e-3*handles.abstand;
z=1e-3*handles.z;
w0=1e-3*handles.w0;
lambda=1e-9*handles.lambda;
n=handles.n;
d=handles.d*lambda;
r=handles.r;
theta=pi/648000*handles.theta;
phi=pi/648000*handles.phi;
rho=pi/648000*handles.rho;
mult=round(handles.mult);
k=2*pi*n/lambda;
c=sqrt(2/(pi*w0^2));
```

```
z0=n*pi*w0^2/lambda;
F=4*r/(1-r)^2;
t=1-r;
gr=max([theta phi rho]);
versatz=tan(gr*2*F)*abstand;
pixel2=round((breite+versatz)/breite*pixel*2);
Et=zeros(pixel2);
randfield=rand(2,mult)*(breite+versatz)-(breite+versatz)/2;
for N=1:mult
    x=randfield(1,N);
    y=randfield(2,N);
    for m=1:F
        xim=theta+m*2*phi;
        etam=m*2*rho;
        xm=x-m*2*d*tan(xim);
        ym=y-m*2*d*tan(etam);
        zm=z+m*2*d*2*1/sqrt((tan(xim))^2+(tan(etam))^2+1);
        w=sqrt(w0^2*(1+(zm/z0)^2));
        R=zm*(1+(z0/zm)^2);
        xd=xm+tan(xim)*abstand;
        yd=ym+tan(etam)*abstand;
        zd=zm+abstand*1/sqrt((tan(xim))^2+(tan(etam))^2+1); .
        ix=ceil(randfield(1,N)/breite*pixel+pixel2/2);
        iy=ceil(randfield(2,N)/breite*pixel+pixel2/2);
        xc=ceil(randfield(1,N)/breite*pixel+pixel2/2)-
(randfield(1,N)...
            /breite*pixel+pixel2/2);
        yc=ceil(randfield(2,N)/breite*pixel+pixel2/2)-
(randfield(2,N)...
            /breite*pixel+pixel2/2);
        xf=(randfield(1,N)/breite*pixel+pixel2/2)-
floor(randfield(1,N)...
            /breite*pixel+pixel2/2);
        yf=(randfield(2,N)/breite*pixel+pixel2/2)-
floor(randfield(2,N)...
            /breite*pixel+pixel2/2);
        A=t*r^m*w0/w*exp(-(xd^2+yd^2)/w^2)*exp(-i*(k*zd-
atan(zd/z0)))...
            *exp(-i*k*(xd^2+yd^2)/(2*R))*c;
        Et(iy-1,ix)=Et(iy-1,ix)+xf*yc*A;
        Et(iy,ix-1)=Et(iy,ix-1)+xc*yf*A;
        Et(iy-1,ix-1)=Et(iy-1,ix-1)+xc*yc*A;
        Et(iy,ix)=Et(iy,ix)+xf*yf*A;
    end
end
I=Et.*conj(Et);
I=I/sum(sum(I));
[zl,sp]=size(I);
I=I(floor(zl/2)-
floor(pixel/2)+1:floor(zl/2)+floor(pixel/2),floor(sp/2)-
floor(pixel/2)+1:floor(sp/2)+floor(pixel/2));
surf(I);
shading interp;
view(2);
assignin('base','Intensity',I);
P=angle(Et);
```

```
P=P(floor(zl/2)-
floor(pixel/2)+1:floor(zl/2)+floor(pixel/2),floor(sp/2)-
floor(pixel/2)+1:floor(sp/2)+floor(pixel/2));
assignin('base','Phase',P);
function initialize_gui(fig_handle, handles)
handles.breite=3;
handles.pixel=100;
handles.abstand=1000;
handles.z=100;
handles.w0=1;
handles.lambda=532;
handles.n=1;
handles.d=1000;
handles.r=0.3;
handles.theta=0;
handles.phi=0;
handles.rho=0;
handles.mult=3e5;
guidata(handles.figure1, handles);

function axes1_CreateFcn(hObject, eventdata, handles)
```

Appendix C: CoventorWare Introduction

CoventorWare can be described as a circularly connected series of modules. Designs may begin at different places in this flow, depending on whether the user chooses to design at the system or at the physical level. CoventorWare supports both system-level and physical approaches to designing MEMS and microfluidic devices. The system-level approach involves use of behavioral model libraries with a high-speed system simulator. The system-level design can be used to generate a 2-D layout for physical level verification. The physical approach starts with a 2-D layout and involves building a 3-D model, generating a mesh, and simulating using FEM or BEM solvers. Custom reduced-order macromodels can be extracted for use in system simulations. Finally, the verified 2-D layout can be transferred to a foundry for fabrication. CoventorWare has numerous options, including design libraries and a variety of 3-D physics solvers. Various entry and exit points allow import and export of files from and to other third-party software.

CoventorWare provides a comprehensive, integrated suite of tools for MEMS that enables rapid exploration of process and design options. The Architect suite allows system-level designers to simulate and rapidly evaluate multiple design configurations using a top-down, system-level approach. When the overall model has been sufficiently designed and analyzed, the layout can be extracted and viewed in the Designer's 2-D Layout Editor. This layout can then be combined with a process description to create a 3-D model, then meshed and resimluated using the analyzer's FEM and BEM solvers. The Integrator suite allows users to create custom macromodels from FEM/BEM meshes that can then be input to an Architect system model.

ARCHITECT
System-Level Design and Simulation

Design Entry

SCHEMATIC EDITOR

| Prepare System-Level Schematic | Run System-Level Simulations | Plot & Analyze Results |

Domain-Specific Parametric Model Libraries

Generate Layout

INTEGRATOR
Macromodel Extraction

Custom Macromodel Library

MACROMODELER

Extract Reduced-Order Models

MPD EDITOR

Material Properties Database

PROCESS EDITOR

Process Description

Design Entry

Foundry

LAYOUT EDITOR

Edit/View 2-D Masks

DESIGNER
Physical Device Design

MODEL BUILDER

Build 3-D Model

3rd party software

POST PROCESSOR

Plot Visualize Query Results

Pictures Movies

SOLVERS
Perform 3-D Simulations

| MEMS Physics | Fluidics Physics |

Set Up Solvers and Assign BCs

PREPROCESSOR

| Generate Mesh Name Parts and Surfaces | View 3-D Model |

ANALYZER
3-D Physical Simulation

Design Entry

Table C-1 Coventor Parametric Components Needed for Gyroscope Assembly

Symbol name	Symbol	Categories path	Part	Quantity
rigid_plate	Rigid Plate COVENTOR (1)	/Coventor Parts Library /Parametric Libraries /Electro-Mechanics /Rigid Plate	Rigid Plate	1
electrode	Cap E Electrode COVENTOR M (T)	/Coventor Parts Library /Parametric Libraries /Electro-Mechanics /Rigid Plate	Electrode	1
straight_comb_stator	Straight Comb with Stator COVENTOR (1) M	/Coventor Parts Library /Parametric Libraries /Electro-Mechanics /Rigid Plate	Straight Comb with Stator	1
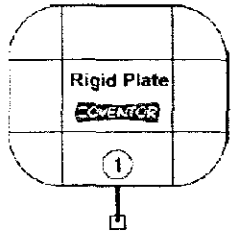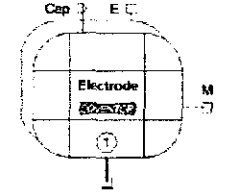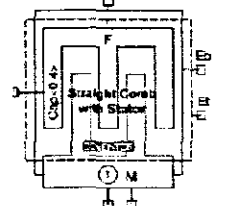
205

Table C-2 Parts Needed to Set Up Electrical Stimuli

Symbol name	Symbol	Categories Path	Quantity
gnd	Ground, (Saber Node 0)	/MAST Parts Library	7
v_sin	Voltage source, Sine v_sin amplitude:'req' frequency:'req'	/MAST Parts Library /Sources, Power, Ground /Electrical Sources/Voltage Sources	1
v_dc	Voltage Source, Constant Ideal DC Supply v_dc 'req'	/MAST Parts Library /Sources, Power, Ground /Electrical Sources/Voltage Sources	2
vcvs	Voltage Source, VCVS vp vcvs k:'req' vm	/MAST Parts Library /Sources, Power, Ground/Electrical Sources /Voltage Sources/Controlled Voltage Sources	1
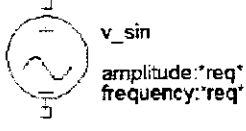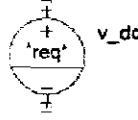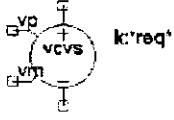
Appendix D: MEMS Fabrication Technology Introduction

a. Chemical Vapor Deposition (CVD)

In this process, the substrate is placed inside a reactor to which a number of gases are supplied. The fundamental principle of the process is that a chemical reaction takes place between the source gases. The product of that reaction is a solid material with condenses on all surfaces inside the reactor.

The two most important CVD technologies in MEMS are the Low Pressure CVD (LPCVD) and Plasma Enhanced CVD (PECVD). The LPCVD process produces layers with excellent uniformity of thickness and material characteristics. The main problems with the process are the high deposition temperature (higher than 600°C) and the relatively slow deposition rate. The PECVD process can operate at lower temperatures (down to 300° C) thanks to the extra energy supplied to the gas molecules by the plasma in the reactor. However, the quality of the films tend to be inferior to processes running at higher temperatures. Secondly, most PECVD deposition systems can only deposit the material on one side of the wafers on 1 to 4 wafers at a time. LPCVD systems deposit films on both sides of at least 25 wafers at a time. A schematic diagram of a typical LPCVD reactor is shown in the figure 1.
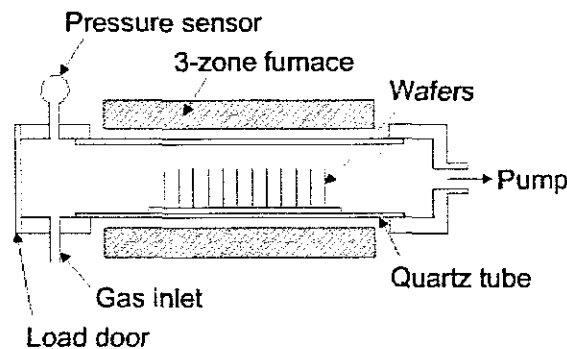
Figure 1 Typical hot-wall LPCVD Reactor.

CVD processes are ideal to use when you want a thin film with good step coverage. A variety of materials can be deposited with this technology; however, some of them are less popular with fabs because of hazardous byproducts formed during processing. The quality of the material varies from process to process, however a good rule of thumb is that higher process temperature yields a material with higher quality and less defects.

b. Electro-Deposition

This process is also known as "electroplating" and is typically restricted to electrically conductive materials. There are basically two technologies for plating: Electroplating and Electroless plating. In the electroplating process the substrate is placed in a liquid solution (electrolyte). When an electrical potential is applied between a conducting area on the substrate and a counter electrode (usually platinum) in the liquid, a chemical redox process takes place resulting in the formation of a layer of material on the substrate and usually some gas generation at the counter electrode.

In the electroless plating process a more complex chemical solution is used, in which deposition happens spontaneously on any surface which forms a sufficiently high electrochemical potential with the solution. This process is desirable since it does not require any external electrical potential and contact to the substrate during processing. Unfortunately, it is also more difficult to control with regards to film thickness and uniformity. A schematic diagram of a typical setup for electroplating is shown in the figure 2 below.

The electrodeposition process is well suited to make films of metals such as copper, gold and nickel. The films can be made in any thickness from ~1µm to >100µm. The deposition is best controlled when used with an external electrical potential, however, it requires electrical contact to the substrate when immersed in the liquid bath. In any process, the surface of the substrate must have an electrically conducting coating before the deposition can be done.
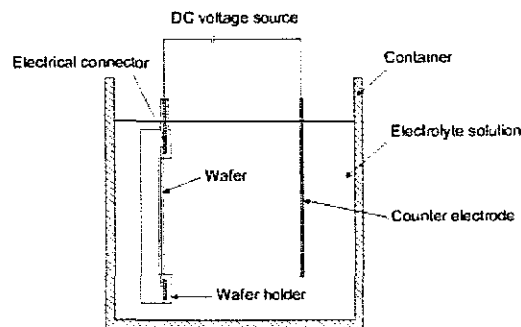
Figure 2 Typical setup for electrodeposition.

c. Epitaxy

This technology is quite similar to what happens in CVD processes, however, if the substrate is an ordered semiconductor crystal (i.e. silicon, gallium arsenide), it is possible with this process to continue building on the substrate with the same crystallographic orientation with the substrate acting as a seed for the deposition. If an amorphous/polycrystalline substrate surface is used, the film will also be amorphous or polycrystalline.

There are several technologies for creating the conditions inside a reactor needed to support epitaxial growth, of which the most important is Vapor Phase Epitaxy (VPE). In this process, a number of gases are introduced in an induction heated reactor where only the substrate is heated. The temperature of the substrate typically must be at least 50% of the melting point of the material to be deposited.

An advantage of epitaxy is the high growth rate of material, which allows the formation of films with considerable thickness (>100μm). Epitaxy is a widely used technology for producing silicon on insulator (SOI) substrates. The technology is primarily used for deposition of silicon. A schematic diagram of a typical vapor phase epitaxial reactor is shown in the figure 3 below.
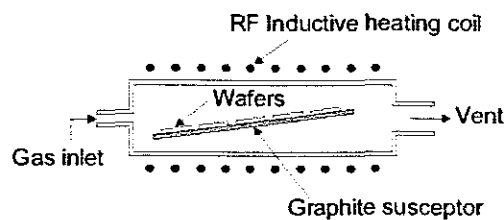
Figure 3 Typical cold-wall vapor phase epitaxial reactor.

This has been and continues to be an emerging process technology in MEMS. The process can be used to form films of silicon with thicknesses of ~1μm to >100μm. Some processes require high temperature exposure of the substrate, whereas others do not require significant heating of the substrate. Some processes can even be used to perform selective deposition, depending on the surface of the substrate.

d. Thermal oxidation

This is one of the most basic deposition technologies. It is simply oxidation of the substrate surface in an oxygen rich atmosphere. The temperature is raised to 800°C-1100°C to speed up the process. This is also the only deposition technology which actually consumes some of the substrate as it proceeds. The growth of the film is spurned by diffusion of oxygen into the substrate, which means the film growth is actually downwards into the substrate. As the thickness of the oxidized layer increases, the diffusion of oxygen to the substrate becomes more difficult leading to a parabolic relationship between film thickness and oxidation time for films thicker than ~100nm. This process is naturally limited to materials that can be oxidized, and it can only form films that are oxides of that material. This is the classical process used to form silicon dioxide on a silicon substrate. A schematic diagram of a typical wafer oxidation furnace is shown in the figure 4 below.

This is a simple process, which unfortunately produces films with somewhat limited use in MEMS components. It is typically used to form films that are used for electrical insulation or that are used for other process purposes later in a process sequence.
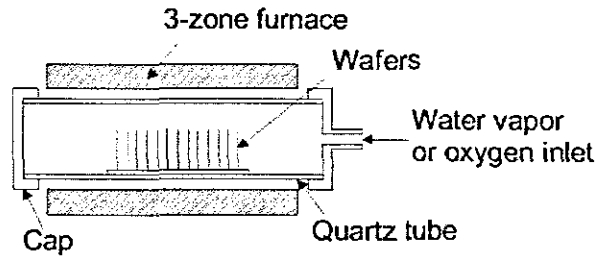
Figure 4 Typical wafer oxidation furnaces.

e. Physical Vapor Deposition (PVD)

PVD covers a number of deposition technologies in which material is released from a source and transferred to the substrate. The two most important technologies are evaporation and sputtering.

PVD comprises the standard technologies for deposition of metals. It is far more common than CVD for metals since it can be performed at lower process risk and cheaper in regards to materials cost. The quality of the films are inferior to CVD, which for metals means higher resistivity and for insulators more defects and traps. The step coverage is also not as good as CVD.

The choice of deposition method (i.e. evaporation vs. sputtering) may in many cases be arbitrary, and may depend more on what technology is available for the specific material at the time.

f. Evaporation

In evaporation the substrate is placed inside a vacuum chamber, in which a block (source) of the material to be deposited is also located. The source material is then heated to the point where it starts to boil and evaporate. The vacuum is required to allow the molecules to evaporate freely in the chamber, and they subsequently condense on all surfaces. This principle is the same for all evaporation technologies, only the method used to the heat (evaporate) the source material differs. There are two popular evaporation technologies, which are e-beam evaporation and resistive evaporation each referring to the heating method. In e-beam evaporation, an electron beam is aimed at the source material causing local heating and evaporation. In resistive evaporation, a tungsten boat, containing the source material, is heated electrically with a high current to make the material evaporate.

210

Many materials are restrictive in terms of what evaporation method can be used (i.e. aluminum is quite difficult to evaporate using resistive heating), which typically relates to the phase transition properties of that material. A schematic diagram of a typical system for e-beam evaporation is shown in the figure 5 below.
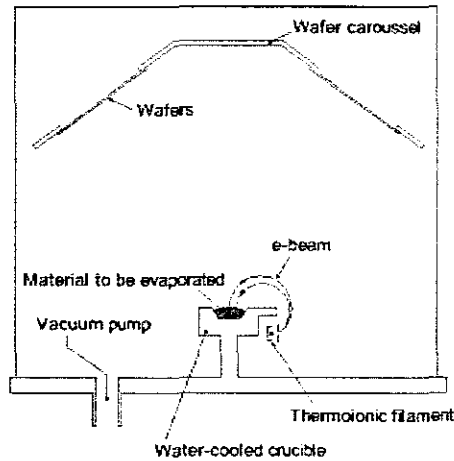
Figure 5 Typical system for e-beam evaporation of materials.

g. Sputtering

Sputtering is a technology in which the material is released from the source at much lower temperature than evaporation. The substrate is placed in a vacuum chamber with the source material, named a target, and an inert gas (such as argon) is introduced at low pressure. Gas plasma is struck using an RF power source, causing the gas to become ionized. The ions are accelerated towards the surface of the target, causing atoms of the source material to break off from the target in vapor form and condense on all surfaces including the substrate. As for evaporation, the basic principle of sputtering is the same for all sputtering technologies. The differences typically relate to the manor in which the ion bombardment of the target is realized. A schematic diagram of a typical RF sputtering system is shown in the figure 6 below.
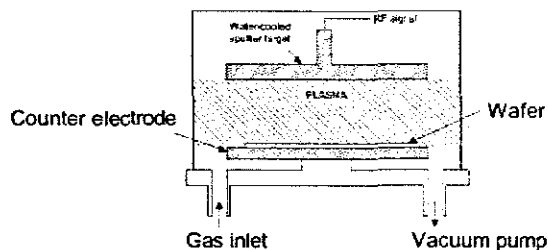
Figure 6 Typical RF sputtering system.

h. Casting

In this process the material to be deposited is dissolved in liquid form in a solvent. The material can be applied to the substrate by spraying or spinning. Once the solvent is evaporated, a thin film of the material remains on the substrate. This is particularly useful for polymer materials, which may be easily dissolved in organic solvents, and it is the common method used to apply photoresist to substrates (in photolithography). The thicknesses that can be cast on a substrate range all the way from a single monolayer of molecules (adhesion promotion) to tens of micrometers. In recent years, the casting technology has also been applied to form films of glass materials on substrates. The spin casting process is illustrated in the figure 7 below.

Casting is a simple technology which can be used for a variety of materials (mostly polymers). The control on film thickness depends on exact conditions, but can be sustained within +/-10% in a wide range. If you are planning to use photolithography you will be using casting, which is an integral part of that technology. There are also other interesting materials such as polyimide and spin-on glass which can be applied by casting.

BEFORE SPINNING   AFTER SPINNING
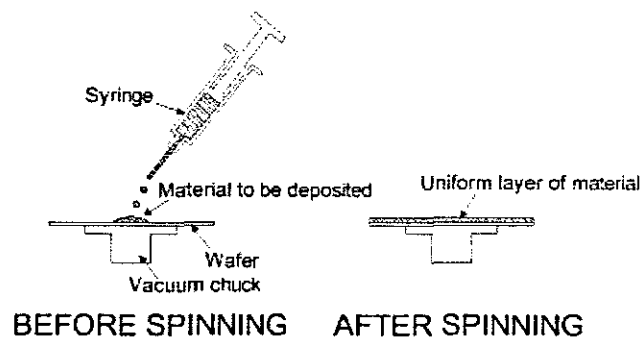
Figure 7 The spin casting process as used for photoresist in photolithography.

In the following, we will briefly discuss the most popular technologies for wet and dry etching.

a. Wet etching

This is the simplest etching technology. All it requires is a container with a liquid solution that will dissolve the material in question. Unfortunately, there are complications since usually a mask is desired to selectively etch the material. One must find a mask that will not dissolve or at least etches much slower than the material to be patterned. Secondly, some single crystal materials, such as silicon, exhibit anisotropic etching in certain chemicals. Anisotropic etching in contrast to isotropic etching means different etches rates in different directions in the material. The classic example of this is the <111> crystal plane sidewalls that appear when etching a hole in a <100> silicon wafer in a chemical such as potassium hydroxide (KOH). The result is a pyramid shaped hole instead of a hole with rounded

212

sidewalls with an isotropic etchant. The principle of anisotropic and isotropic wet etching is illustrated in the figure 6-19 below.

This is a simple technology, which will give good results if you can find the combination of etchant and mask material to suit your application. Wet etching works very well for etching thin films on substrates, and can also be used to etch the substrate itself. The problem with substrate etching is that isotropic processes will cause undercutting of the mask layer by the same distance as the etch depth. Anisotropic processes allow the etching to stop on certain crystal planes in the substrate, but still results in a loss of space, since these planes cannot be vertical to the surface when etching holes or cavities. If this is a limitation for you, you should consider dry etching of the substrate instead. However, keep in mind that the cost per wafer will be 1-2 orders of magnitude higher to perform the dry etching.

If you are making very small features in thin films (comparable to the film thickness), you may also encounter problems with isotropic wet etching, since the undercutting will be at least equal to the film thickness. With dry etching it is possible etch almost straight down without undercutting, which provides much higher resolution.

Wet etching is a blanket name that covers the removal of material by immersing the wafer in a liquid bath of the chemical etchant. Wet etchants fall into two broad categories; isotropic etchants and anisotropic etchants.

Isotropic etchants attack the material being etched at the same rate in all directions. Anisotropic etchants attack the silicon wafer at different rates in different directions, and so there is more control of the shapes produced. Some etchants attack silicon at different rates depending on the concentration of the impurities in the silicon (concentration dependent etching).

Isotropic etchants are available for oxide, nitride, aluminium, polysilicon, gold, and silicon. Since isotropic etchants attack the material at the same rate in all directions, they remove material horizontally under the etch mask (undercutting) at the same rate as they etch through the material. This is illustrated for a thin film of oxide on a silicon wafer in figure 8, using an etchant that etches the oxide faster than the underlying silicon (eg, hydroflouric acid).
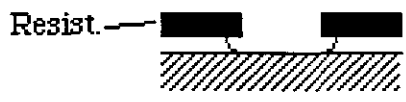
Figure 8 This illustrates the isotropic wet etching of a thin film of material. The photoresist is black, and the substrate yellow. The film is etched through, and the etching continues to further under-cut the mask.

Anisotropic etchants are available which etch different crystal planes in silicon at different rates. The most popular anisotropic etchant is potassium hydroxide (KOH), since it is the safest to use.

Silicon wafers are slices that have been cut from a large ingot of silicon that was grown from a single seed crystal. The silicon atoms are all arranged in a crystalline structure, so the wafer is monocrystalline silicon (as opposed to polycrystalline silicon mentioned above). When purchasing silicon wafers it is possible to specify that they have been sliced with the surface parallel to a particular crystal plane.

The simplest structures that can be formed using KOH to etch a silicon wafer with the most common crystal orientation (100) are shown in figure 9. These are V shaped groves, or pits with right angled corners and sloping side walls. Using wafers with different crystal orientations can produce grooves or pits with vertical walls.
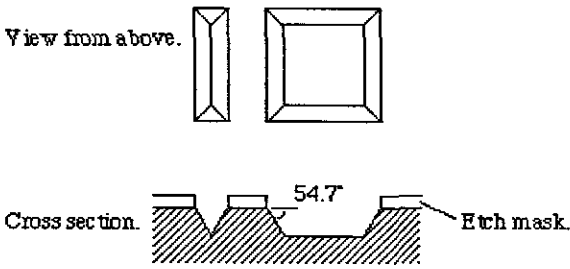
Figure 9 illustrates the Anisotropic wet etching of a thin film of material

Both oxide and nitride etch slowly in KOH. Oxide can be used as an etch mask for short periods in the KOH etch bath (ie., for shallow grooves and pits). For long periods, nitride is a better etch mask as it etches more slowly in the KOH.

The difference between anisotropic and isotropic wet etching is shown in figure 10.
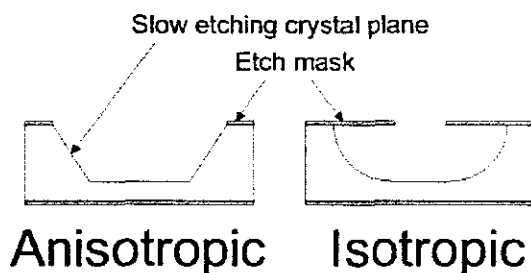
Figure 10 Difference between anisotropic and isotropic wet etching.

b. Dry etching

The most common form of dry etching for micromachining applications is reactive ion etching (RIE). Ions are accelerated towards the material to be etched, and the etching reaction is enhanced in the direction of travel of the ion. RIE is an anisotropic etching technique. Deep trenches and pits (up to ten or a few tens of microns) of arbitrary shape and with vertical walls can be etched in a variety of materials including silicon, oxide and nitride. Unlike anisotropic wet etching, RIE is not limited by the crystal planes in the silicon.

The dry etching technology can split in three separate classes called reactive ion etching (RIE), sputter etching, and vapor phase etching.

In RIE, the substrate is placed inside a reactor in which several gases are introduced. Plasma is struck in the gas mixture using an RF power source, breaking the gas molecules into ions. The ions are accelerated towards, and react at, the surface of the material being etched, forming another gaseous material. This is known as the chemical part of reactive ion etching. There is also a physical part which is similar in nature to the sputtering deposition process. If the ions have high enough energy, they can knock atoms out of the material to be etched without a chemical reaction. It is very complex tasks to develop dry etch processes that balance chemical and physical etching, since there are many parameters to adjust. By changing the balance it is possible to influence the anisotropy of the etching, since the chemical part is isotropic and the physical part highly anisotropic the combination can form sidewalls that have shapes from rounded to vertical. A schematic of a typical reactive ion etching system is shown in the figure 11 below.

A special subclass of RIE which continues to grow rapidly in popularity is deep RIE (DRIE). In this process, etch depths of hundreds of microns can be achieved with almost vertical sidewalls. The primary technology is based on the so-called "Bosch process", named after the German company Robert Bosch which filed the original patent, where two different gas compositions are alternated in the reactor. The first gas composition creates a polymer on the surface of the substrate, and the second gas composition etches the substrate. The polymer is immediately sputtered away by the physical part of the etching, but only on the

215

horizontal surfaces and not the sidewalls. Since the polymer only dissolves very slowly in the chemical part of the etching, it builds up on the sidewalls and protects them from etching. As a result, etching aspect ratios of 50 to 1 can be achieved. The process can easily be used to etch completely through a silicon substrate, and etch rates are 3-4 times higher than wet etching.

Sputter etching is essentially RIE without reactive ions. The systems used are very similar in principle to sputtering deposition systems. The big difference is that substrate is now subjected to the ion bombardment instead of the material target used in sputter deposition.

Vapor phase etching is another dry etching method, which can be done with simpler equipment than what RIE requires. In this process the wafer to be etched is placed inside a chamber, in which one or more gases are introduced. The material to be etched is dissolved at the surface in a chemical reaction with the gas molecules. The two most common vapor phase etching technologies are silicon dioxide etching using hydrogen fluoride (HF) and silicon etching using xenon diflouride (XeF2), both of which are isotropic in nature. Usually, care must be taken in the design of a vapor phase process to not have bi-products form in the chemical reaction that condense on the surface and interfere with the etching process.

The first thing you should note about this technology is that it is expensive to run compared to wet etching. If you are concerned with feature resolution in thin film structures or you need vertical sidewalls for deep etchings in the substrate, you have to consider dry etching. If you are concerned about the price of your process and device, you may want to minimize the use of dry etching. The IC industry has long since adopted dry etching to achieve small features, but in many cases feature size is not as critical in MEMS. Dry etching is an enabling technology, which comes at a sometimes high cost.
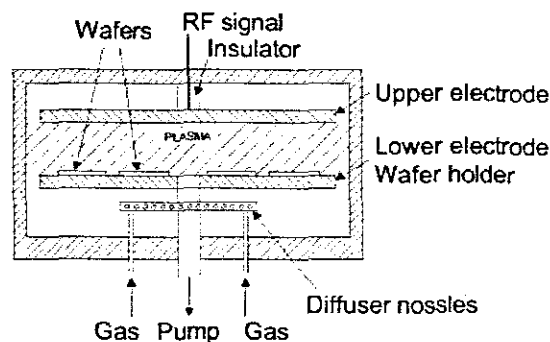
Figure 11 Typical parallel-plate reactive ion etching system.

Deep X-ray Lithography and Mask Technology

Deep X-ray lithography allows structures of any lateral design with high aspect ratios to be produced, i.e., with heights of up to 1 *mm* and a lateral resolution down to 0.2 *μm*.

The walls of these structures are smooth and parallel to each other. The very sophisticated structures of this type can be produced lithographically only by a highly penetrating, intense, and parallel X-radiation supplied by a synchrotron.

The structural information is compiled by means of a CAD system and then stored on a mask meeting the special requirements of hard X-radiation; the „transparent" carrier of the mask is a very thin metal foil (e.g. titanium, beryllium), while the absorbers consist of a comparatively thick layer of gold. Synchrotron radiation is used to transfer the lateral structural information into a plastics layer, normally polymethylmethacrylate (PMMA), by „shadowing". Exposure to radiation modifies the plastic material in such a way that it can be removed with a suitable solvent, leaving behind the structure of the unirradiated plastic (the "shadowed areas") as the primary structure. The development process and the ensuing electroforming process impose stringent requirements on the process technology because of the high aspect ratios and the resultant narrow, deep grooves in the structure.

a. Electroforming

The spaces generated by the removal of the irradiated plastic material can be filled with metal by electroforming processes. In this way, the negative pattern of the plastics structure is generated as a secondary structure out of metals, such as nickel, copper and gold, or alloys, such as nickel-cobalt and nickel-iron. This technique is used to produce microstructures for direct use, but also tools made of nickel and nickel alloys for plastics molding.

b. Plastics Molding

Plastics molding is the key to low-cost mass production by the LIGA process. The metal microstructures produced by deep X-ray lithography and electroforming are used as molding tools for the production of faithful replicas of the primary structure in large quantities and at low cost.

Vacuum embossing of plastics is the main technique used to mold microstructures. Micro vacuum embossing has been advanced in important respects in MEMS fabrication technology and now represents an interesting alternative to injection molding for special applications.

217

The materials used in plastics molding range from thermoplastics with very special optical properties (plexiglass=PMMA, polycarbonate) to materials particularly resistant to chemicals (epoxy phenol resins, polyvinylidene fluoride (PVDF), and other fluoropolymers) to polymers of high temperature resistance (such as polysulfones, polyether ketones).

The embossing technique allows microstructures of metals or plastics to be made directly on top of the appropriate electronic evaluation circuit, i.e., to be integrated in a quasi-monolith without changing their electronic properties. The enormous advantage of this integration technique lies in the combination of the LIGA technique with silicon microelectronics as well as micromechanics in manufacturing industrial products. In this way, microsystems can be produced which avoid, on the one hand, the drawbacks of inflexible monolithic integration and, on the other hand, the high costs of hybrid structures.